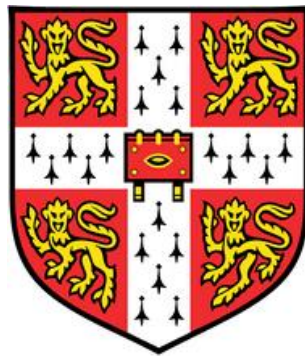


# **Dynamic distributed monitoring of masonry railway bridges**



**Samuel Cocking**

Department of Engineering

University of Cambridge

This dissertation is submitted for the degree of

*Doctor of Philosophy*



To my family



# Declaration

I hereby declare that this thesis is the result of my own work and includes nothing which is the outcome of work done in collaboration except where this is specifically indicated in the text. It is not substantially the same as any that I have previously submitted, nor is it concurrently being submitted, for any other degree, diploma, or other qualification at the University of Cambridge, or at any other University or similar institution. This thesis contains fewer than 65,000 words, excluding the bibliography, and 131 figures.

Samuel Cocking

June 2021

# Dynamic distributed monitoring of masonry railway bridges

Samuel Cocking

## Abstract

Novel sensing technologies – for instance, fibre-optic Fibre Bragg Grating (FBG) sensors – offer engineers new means to study the dynamic distributed behaviour of complex structures, such as masonry arch bridges. These bridges, which are common features of many European transport networks, are often ageing structures, with complex histories of damage and repair work. Furthermore, their material properties and non-visible geometry may be challenging, if not impossible, to ascertain, creating uncertainty in the reliability of computational analyses.

Particularly in light of the financial and environmental costs of their replacement, and the contributions that many of these bridges make to our shared architectural and industrial heritage, it is increasingly urgent to improve our understanding of the structural behaviour of masonry arch bridges under their real working loads. As these bridges undergo many cycles of loading, which may directly drive their deterioration, their response in working conditions is often more important than an understanding of their collapse behaviour, which can be studied using established methods such as limit state analysis.

In this thesis, Structural Health Monitoring is used to gain new insights into the behaviour of masonry arch bridges and viaducts. Part 1 includes an initial study in which the outputs of simplified finite element models are compared against previously gathered FBG monitoring data, describing the response of a damaged masonry viaduct under applied train loading. It is found that the impact of damage on the viaduct response is primarily local, while common ‘single-point’ measurements, such as the crown vertical displacements, can be well matched by the simplified models. Furthermore, relative contributions from each of the main structural components of the viaduct, towards its overall SLS performance, are quantified.

The remainder of the thesis is concerned with the monitoring of a case study structure: a recently repaired, skewed, masonry arch railway bridge. FBGs are used to monitor the dynamic behaviour of this bridge in detail – in particular, the in-plane strain response and the movements across cracks, including both opening and shearing movements across a key separation crack between the arch barrel and a spandrel wall. The sensitivity of these responses to a range of

---

external variables – namely train speed, ambient temperature, time of day, and date – is presented. Trains travelling between approximately 80 and 90 mph are observed to induce a local strain response that is up to 15% higher than that of slower trains, although this effect is only present close to the arch crown, where loads are most concentrated at the extrados. The trend with time-of-day follows anticipated passenger behaviour. Trains at peak commute times result in higher magnitude and lower statistical spread in the bridge response; hence, comparing trains recorded at these times allows for variable passenger loading to be normalised.

The in-plane flow of force throughout the skewed arch is also measured and visualised, using a novel ‘FBG strain rosette’ implementation that monitors the arch principal strains. These force flow distributions, experimentally mapped in detail for the first time for a skewed masonry arch, are highly consistent across many train events, suggesting a common response to different types of train loading. Separately, videogrammetry is used to measure the out-of-plane, vertical displacements of the arch. The distribution of these movements is used to fit a simplified beam model of the transverse bending component of the arch response.

This structural monitoring is part of a broader, collaborative study, trialling a large range of different monitoring technologies at the case study bridge. A practical evaluation of these various technologies is presented in this thesis; despite the larger initial costs for an FBG system, the many measurement locations and high quality of data afforded by this technology meant that it compared favourably with more established approaches. In another collaboration, existing laser scan analysis methods for masonry arch bridges have been extended to skewed arches, and employed to study the historic, distributed deformation of this bridge. It is shown that the current deformed geometry could have been caused by small support movements at the obtuse corners of the arch abutments, which are consistent with past hypotheses in the literature regarding the behaviour of skewed masonry arch bridges.

Much of this thesis is concerned with the analysis and interpretation of data collected through on-site monitoring of the case study bridge, carried out over a six-month period. Since this time, the FBG system at the bridge has been adapted for autonomous, remote sensing. The necessary improvements to the system are presented, covering both the equipment installed at the bridge and the accompanying data processing strategies, which now allow for automated data categorisation, analysis, and visualisation. Following this, the long-term data gathered to date is analysed. These data reveal further trends – in particular, linking the bridge response to ambient temperature. Lower temperatures lead to a larger magnitude response – potentially due to thermal contraction of the masonry causing existing cracks throughout the bridge to open, and thus increasing the potential for movements to occur under applied loads.

# Acknowledgements

First of all, I am extremely grateful to my supervisor, Professor Matthew DeJong, for his support, encouragement, and guidance throughout the past several years. Matt's enthusiasm for this research, the opportunities he has given me, and the great example that he sets for all his students, have made this project possible and been a continual source of motivation for me.

Secondly, I want to thank Dr James Talbot for acting as my supervisor since Matt's return to the United States, and for his helpful advice on numerous occasions. Likewise, I am grateful to Dr Mohammed Elshafie and Professor Campbell Middleton, who at various points have been my graduate advisor, and to my tutor at Clare College, Dr Maciej Dunajski. As I write this, it is approaching ten years since I first arrived at Clare to begin my undergraduate degree. The warm atmosphere at Clare and the wonderful people I have met there, as well as at other colleges, have greatly enriched my time at Cambridge.

There are many others at the Department of Engineering and the Centre for Smart Infrastructure and Construction to whom I owe thanks. In particular, I have benefited from the advice and support of Dr Haris Alexakis and Professor Sinan Acikgoz, whose expertise and generosity with their time has improved this project in many ways. I am thankful to the entire CSIC family – including Dr Farhad Huseynov, Paul Fidler, Dr Cedric Kechavarzi, Jason Shardelow, and Peter Knott – for all of their help, and for making CSIC such a great place to work. I am also grateful to Alistair Ross and the team at the CUED workshops, who have always been an absolute pleasure to work with.

The monitoring component of my research would not have been possible without the support of Sam De'Ath, at Network Rail, and the help of AECOM, where I owe particular thanks to Dave Kite, Daniel Thompson, Andrew Mercer, Matthew Audley, and Nathan Lander. Collaborating on this monitoring installation has been great fun.

Elements of my research have either involved or led to enjoyable collaborations with other students, and I want to acknowledge and thank Daniel Brackenbury, Simon Ye, Carlo Olivieri, and Austin Chen in particular.

I have enjoyed getting to know many others in the research community – at Cambridge, further afield at conferences, and at the International Summer School on Historic Masonry Structures. Anjali, Tim, and Daniele also deserve a special mention, for making our office such a fun place to work as I was beginning my PhD, although I could easily add the entire Structures Research Group to this list.

Finally, I want to thank the family and friends who have been there for me throughout this journey. Without my family – especially my parents, sister, and grandparents – I could not be where I am today. I love them dearly, and this thesis is dedicated to them. Over the past several years, and houses, I have also had the best housemates that I could have hoped for, keeping me sane, laughing, and well-fed as I have slowly completed this thesis. I will always be thankful to Nate and Em, Phil and Alina, and, most of all, to Ross – for his love and support, and for inspiring me in many ways.

# Table of contents

## Part 1 Introduction

<b>1</b>	<b>Introduction.....</b>	<b>19</b>
1.1	Background.....	19
1.2	Research topics and questions.....	20
1.2.1	Simplified modelling of masonry arch bridges.....	21
1.2.2	Detailed monitoring of masonry arch bridges.....	21
1.2.3	The behaviour of skewed masonry arch bridges.....	23
1.4	Thesis outline.....	24
<b>2</b>	<b>Literature review.....</b>	<b>27</b>
2.1	Arch bridge construction.....	27
2.1.1	The history of masonry bridge construction.....	27
2.1.2	Historic material properties.....	28
2.2	Behaviour of masonry arch bridges.....	29
2.2.1	Testing of scale models.....	29
2.2.2	ULS behaviour of arch bridges.....	30
2.2.2.1	Behaviour of masonry arches.....	30
2.2.2.2	Importance of additional structural components.....	32
2.2.3	SLS behaviour of arch bridges.....	33
2.2.3.1	Behaviour of masonry arches.....	33
2.2.3.2	Importance of additional structural components.....	34
2.2.4	Fatigue of masonry arch bridges.....	35
2.2.5	Assumptions regarding the flow of force.....	36
2.2.5.1	Skewed masonry arch bridges.....	36
2.2.5.2	Interactions between structural components.....	38

---

2.3	Structural monitoring of masonry arch bridges .....	39
2.3.1	Monitoring the response of bridges to loading.....	39
2.3.1.1	Distributed, dynamic sensing methods used in this thesis.....	39
2.3.1.2	Other examples of dynamic monitoring .....	40
2.3.2	Monitoring to determine bridge properties.....	42
2.4	Computational analysis of arches .....	43
2.4.1	Finite element method (FEM) .....	43
2.4.1.1	Assumptions for simplified analyses.....	43
2.4.1.2	Complex analyses .....	43
2.4.1.3	Modelling of dynamic behaviour .....	44
2.4.2	Discrete element method (DEM).....	45
2.4.3	Examples of other modelling approaches.....	45
2.4.4	Probabilistic and statistical methods .....	46
2.5	Assessment of arch bridges .....	47
2.5.1	Assessment of damage .....	47
2.5.2	Assessment of arches in their working conditions .....	47
2.5.2.1	Practical guidance for assessment .....	47
2.5.2.2	Assessment under working conditions .....	48
2.5.2.3	The persistence of the MEXE method.....	49
2.6	Summary.....	49
<b>3</b>	<b>Comparison of modelling and monitoring for a masonry rail viaduct.....</b>	<b>53</b>
3.1	Introduction .....	53
3.1.1	Choice of modelling approach.....	53
3.1.2	Scope of study .....	55
3.2	Background: the Marsh Lane Viaduct.....	56
3.2.1	Overview of the viaduct .....	56
3.2.2	Monitoring data .....	59
3.2.3	Data used in this study.....	61
3.3	Methodology: finite-element modelling.....	63
3.3.1	Overview .....	63
3.3.2	Assumed input parameters.....	66

3.3.3	Boundary conditions .....	68
3.4	Results.....	70
3.4.1	Comparison of monitoring data and modelling results.....	70
3.4.2	Contributions of structural components to overall behaviour.....	71
3.5	Discussion .....	76
3.5.1	Comparison of monitoring data and modelling results.....	76
3.5.2	Contributions of structural components to overall behaviour.....	79
3.5.3	Further comments on the finite element simulations .....	81
3.6	Conclusions.....	82

## **Part 2 Monitoring a skewed masonry bridge**

<b>4</b>	<b>Monitoring methodology and evaluation of technologies.....</b>	<b>87</b>
4.1	Introduction.....	88
4.1.1	Introduction to the CFM-5 bridge.....	88
4.2	Development of the monitoring installation .....	93
4.3	The FBG installation at CFM-5 .....	94
4.3.1	Introduction to the FBG sensors .....	96
4.3.2	Development of the new FBG clamps .....	97
4.3.3	Preliminary data processing approach for the FBG data .....	99
4.3.3.1	Data cleaning.....	99
4.3.3.2	Obtaining the peak-to-peak strain response.....	101
4.3.3.3	Categorising the monitoring data.....	102
4.4	Videogrammetry monitoring at CFM-5.....	104
4.4.1	Overview of videogrammetry and the on-site monitoring approach ..	104
4.4.2	Processing approach for the videogrammetry data.....	108
4.4.2.1	Strategies adopted from FBG data processing.....	108
4.4.2.2	Compensating for environmental effects .....	108
4.4.2.3	Correcting for the choice of reference frame .....	111
4.5	Practical evaluation of the sensing technologies.....	112
4.6	Laser scan analysis of historic bridge deformation.....	115

---

4.6.1	Overview of the LiDAR post-processing strategy .....	117
4.6.2	Comparison with standard mechanisms .....	119
4.6.3	Results and discussion .....	120
4.6.3.1	Potential historic deformation mechanisms.....	122
4.7	Conclusions .....	124
<b>5</b>	<b>Dynamic structural behaviour of the arch bridge.....</b>	<b>127</b>
5.1	Introduction .....	127
5.1.1	Overview of the relevant FBGs .....	127
5.1.2	Impact of arch curvature on FBG measurements .....	130
5.2	Typical strain and displacement distributions in the bridge.....	133
5.2.1	Arch intrados: longitudinal strains .....	134
5.2.2	South-east longitudinal crack: crack opening displacements .....	138
5.2.3	South spandrel crack: crack opening and pumping displacements ....	139
5.3	Statistical overview of the longitudinal strain distributions .....	143
5.4	Variability of the longitudinal strain distributions .....	150
5.5	Variability of crack opening displacements .....	154
5.6	Conclusions .....	157
<b>6</b>	<b>The flow of force in the skewed arch .....</b>	<b>159</b>
6.1	Measurement and visualisation of force flow in the arch.....	159
6.1.1	The FBG strain rosettes .....	159
6.1.1.1	Calculating the general strain state in an FBG rosette.....	161
6.1.1.2	Symmetry in the bridge response .....	164
6.1.2	Mapping principal strains in the arch .....	171
6.1.2.1	The principal strain response for Class 185 trains.....	171
6.1.2.2	Variability of this response to different train loads .....	172
6.1.3	Mapping other strain states in the arch.....	178
6.1.3.1	Strains aligned with the skewed span direction.....	179
6.1.3.2	Strains aligned with the square span direction .....	180
6.2	Out-of-plane behaviour of the arch .....	181
6.2.1	Visualising vertical dynamic displacements of the arch crown line ..	181
6.2.2	Derivation of displacement and strain profiles along the crown line .	184

6.2.3	Evaluation of the fitted displacement and intrados strain profiles.....	194
6.2.3.1	Modifications of the fitted beam model.....	199
6.3	Conclusions.....	201

### **Part 3 Long-term monitoring of the skewed masonry bridge**

<b>7</b>	<b>An autonomous FBG sensing system .....</b>	<b>207</b>
7.1	On-site changes for long-term, autonomous FBG sensing .....	207
7.2	Data-processing strategies for long-term FBG data.....	209
7.3	Trains recorded during long-term FBG monitoring.....	213
7.4	Summary .....	214
<b>8</b>	<b>Analysis of the long-term FBG data.....</b>	<b>217</b>
8.1	Introduction.....	217
8.2	The instantaneous dynamic strain response in the arch .....	217
8.3	The peak-to-peak dynamic strain response in the arch .....	220
8.3.1	Trains on the north track .....	221
8.3.2	Trains on the south track.....	224
8.4	The peak dynamic crack movements .....	225
8.4.1	Trains on the south track.....	225
8.4.2	Trains on the north track .....	232
8.5	The principal strain response in the arch .....	238
8.6	Conclusions.....	245

### **Part 4 Conclusions**

<b>9</b>	<b>Conclusions.....</b>	<b>249</b>
9.1	Summary of main findings.....	249
9.2	Scientific contributions .....	252
9.3	Practical applications .....	253
9.4	Future work.....	254

---

<b>References.....</b>	<b>257</b>
Related publications by the author .....	266
<b>Appendix A Long-term FBG data: Northern Rail trains.....</b>	<b>269</b>
A.1 The instantaneous dynamic strain response in the arch.....	269
A.2 The peak-to-peak dynamic strain response in the arch .....	272
A.2.1 Trains on the north track.....	272
A.2.2 Trains on the south track .....	274
A.3 The peak dynamic crack movements.....	276
A.3.1 Trains on the south track .....	276
A.3.2 Trains on the north track.....	280
A.4 The principal strain response in the arch .....	284
<b>Appendix B Long-term FBG data: CrossCountry trains.....</b>	<b>289</b>
B.1 The instantaneous dynamic strain response in the arch.....	289
B.2 The peak-to-peak dynamic strain response in the arch .....	292
B.2.1 Trains on the north track.....	292
B.2.2 Trains on the south track.....	294
B.3 The peak dynamic crack movements.....	296
B.3.1 Trains on the south track.....	296
B.3.2 Trains on the north track.....	300
B.4 The principal strain response in the arch .....	304



# **Part 1**

## **Introduction**



# Chapter 1

## Introduction

### 1.1 Background

Masonry arch bridges feature significantly on transport networks in the United Kingdom and other countries. Across Europe, railways alone contain an estimated 200,000 masonry arch bridges (Brencich and Morbiducci, 2007). In the UK, roughly 40-50% of the bridge spans on roads and railways are masonry arches (Augusthus-Nelson et al., 2016), with a total of approximately 70,000 structures (Armstrong et al., 1995b). This includes more than 25,000 arch spans on the UK railways (Gilbert et al., 2016).

These are ageing structures. The vast majority have typically been in continuous operation for between 100 and 150 years, and some are even older. The Skerne Bridge in Darlington, which used to feature on the UK £5 note, opened in 1825 and is the oldest railway bridge in continuous use in the world.

The length of these working lives and the changing nature of modern vehicular loading – particularly for rail – has often led to damage (Acikgoz et al., 2018a). It is important that this damage is understood so that the bridges can be properly maintained. Many are located at important points on passenger and freight routes, and their continued smooth operation carries considerable social and economic significance. Even if their heritage value is ignored, the economic cost of replacing these bridges would be exorbitant. Adjusting Network Rail estimates (from Gilbert et al., 2016) for inflation up to 2020, it would cost approximately £25 billion to replace all masonry arch bridges on the UK railway network.

The behaviour of these bridges close to collapse is relatively well understood. A range of established theoretical approaches exist to study this Ultimate Limit State (ULS) in varying levels of detail, from simplified limit analysis tools (Harvey, 1988; Gilbert and Melbourne,

1994), based on the work of Heyman (1982), through to more advanced approaches such as the Finite Element Method (FEM) and Discrete Element Method (DEM). These can be applied to model detailed aspects of bridge behaviour, such as the interactions of different structural components or soil-structure interaction within a bridge, which may affect its ULS performance (e.g., in Forgács et al, 2019b; Sarhosis et al., 2019b). These advanced studies offer valuable research contributions, but the methods are often too complex and costly for regular application in asset management.

For this reason, quick, simplified assessment approaches are still the norm for asset management purposes, except for certain highly significant, unusual, or damaged structures which warrant an increased scale of analysis. Frequently, simplified assessments will suggest that masonry arch bridges do not have sufficient capacity to carry higher ratings of train loading, leaving asset managers with little choice but to implement speed or weight restrictions. This is despite the fact that the full impact of train speed on masonry arch bridges remains unclear. Increasing the understanding of their structural behaviour under working conditions – i.e., at the Serviceability Limit State (SLS) – will allow such decisions to be made in greater context and may even allow for assessment guidelines to be revised.

SLS behaviour is more complex and less well understood than the ULS case, yet it is behind a substantial majority of the observed defects requiring intervention and repair. This creates a major challenge for asset managers, and when a bridge exhibits signs of damage or deterioration it is understandable that there may be little choice other than to use blunt instruments, such as speed and weight restrictions or extensive repair works. There is the risk that inappropriate asset management decisions may be made, with potential consequences such as repair works not being properly tailored to the structures they seek to benefit. Such interventions may introduce changes in the stiffness profile of a masonry bridge, giving rise to new load paths that either exacerbate current damage or lead to new damage arising in another location. Even when interventions do not actively harm a bridge, uncertainty remains as to how long they may remain effective.

## **1.2 Research topics and questions**

The SLS behaviour of masonry arch bridges remains an active research area. Some computational studies have investigated this behaviour; however, this is also a prime opportunity to deploy Structural Health Monitoring (SHM). Monitoring data can provide useful insights into the real-world SLS behaviour of these structures, improving our fundamental

---

understanding, and offer validation to complex analyses, where uncertainty in the results may otherwise persist.

Parts 2 and 3 of this thesis present results from the detailed field monitoring of a case study structure: a single span, skewed, masonry arch bridge showing signs of past damage, which were the target of repair work in 2016. In order to validate the success of this intervention, and track the bridge's structural condition over time, monitoring of its live load response under working loads was commissioned by the asset owners, Network Rail. This monitoring has been carried out in collaboration between the author, at the Centre for Smart Infrastructure and Construction (CSIC) at the University of Cambridge, and AECOM, as described in Cocking et al. (2019b).

The following research topics are considered in this thesis.

### **1.2.1 Simplified modelling of masonry arch bridges**

Capitalising on previous FBG monitoring of the Marsh Lane viaduct in Leeds, by Acikgoz et al. (2018a), Chapter 3 of this thesis compares the results of simplified linear elastic analyses to these monitoring data. Prior to monitoring, repair work at the viaduct had addressed its historic damage. This damage may be expected to cause nonlinearities in the bridge response but, if behaviour is stable following the intervention, then it is possible that masonry in relatively undamaged regions of the bridge may yet behave linear-elastically.

The key research questions addressed by this work are:

1. To what extent does detailed monitoring data, describing the dynamic response of a masonry arch viaduct under working loads, agree with the results of simplified, linear elastic, finite element analysis?
2. What are the relative contributions of the various structural components, which make up a masonry arch viaduct, towards the overall SLS response?
3. Do the modelling results suggest any potential areas of focus for future monitoring studies?

### **1.2.2 Detailed monitoring of masonry arch bridges**

SHM is used in asset management to observe and track metrics describing structural behaviour. The aim is not necessarily to gain a deep understanding of each structure through monitoring, but rather to identify any changes in behaviour which could be emblematic of the onset or progression of damage, thus warranting further inspection or assessment. Identification of

specific damage, and prescription of remedies such as repair works, remains likely to be based on visual inspection. For this reason, SHM strategies in the UK to date have tended to be centred on simplified, single-point measurements that can be taken to be representative of the overall condition of a larger portion of a structure, or even its entirety.

Network Rail commonly use a deflection pole system to measure vertical displacements of the arch crown, under train loading. It is assumed that, as damage progresses, the magnitude of this dynamic response will increase. However, by the time this damage, which may be occurring far from the arch crown, has progressed sufficiently to influence the crown vertical deflections, it may already be quite significant and require an appreciable intervention to remedy. Furthermore, the deflection pole method is not practical for bridges in inaccessible locations, such as those spanning rivers or deep valleys. It may also necessitate costly and disruptive road closures, and therefore does not lend itself to continuous long-term monitoring.

In contrast to this, remote sensing technologies typically only require access to the bridge for installation and maintenance. Conventional point sensors such as strain gauges and Linear Variable Displacement Transducers (LVDTs) can be deployed in this way, as well as a range of more emergent sensing technologies. In this thesis, the primary sensors used are Fibre Bragg Gratings, a fibre-optic monitoring technology enabling efficient dynamic monitoring at numerous points across a structure (Acikgoz et al., 2018a). FBGs can be used in isolation, or in conjunction with other sensors as part of a complementary monitoring system. A number of SHM studies have made use of FBGs but these have only recently been applied to monitor masonry structures (for instance, in Acikgoz et al., 2018a; Acikgoz et al., 2019a; Alexakis et al., 2019a). The project described in this thesis is believed to be the first application of FBGs to study a skewed masonry arch bridge.

Videogrammetry has also been used to study the distributed vertical displacements of the arch. However, this approach can be highly sensitive to environmental effects and ambient vibrations, when used in the field, which can compromise data quality. This thesis presents an overview of the equipment setup and post-processing developed to mitigate this issue, followed by interpretation of the processed data.

The following research questions are addressed:

1. Can new implementations of FBGs be developed, which increase the range of structural behaviour that they can be used to monitor?
2. Can the full strain state, including the principal strains, be measured, and visualised across the extent of the arch bridge?

3. To what extent is the measured dynamic response of the bridge consistent over many loading cycles, and to what extent is it sensitive to external variables (e.g., train speed, ambient temperature)?
4. Considering a range of practical factors, how do established monitoring technologies compare with more emergent technologies, such as FBGs and videogrammetry?
5. Which monitoring technologies offer the most viable alternatives to the current Network Rail deflection pole method?

### **1.2.3 The behaviour of skewed masonry arch bridges**

In the case study structure, considered in Parts 2 and 3 of this thesis, the arch was built skew to allow the railway tracks above it to span over an existing road. The bridge crosses this road at an angle of  $64^\circ$ , meaning that the arch has a skew angle of  $26^\circ$ .

The impact of skew on structural behaviour can be unclear and increase its complexity. While it seems intuitive for the span direction of a square arch to be aligned with its longitudinal axis, the preferred load path in a skewed arch is not as clear. The bridge width may influence whether it spans along the square or skewed span direction (McKibbins et al., 2006; Network Rail, 2006). It is generally considered that the behaviour of skewed arches is significantly three-dimensional, and this has been observed in computational analyses (Forgács et al., 2018a; Forgács et al., 2018b), while previous monitoring of skewed masonry arch bridges does exist (Harvey, 2013) but is very limited.

In this thesis, detailed FBG and videogrammetry sensing data are analysed to offer new insights into the three-dimensional response of skewed masonry arch bridges to their working loads.

Specific research questions are as follows:

1. To what extent can the historic deformations of the skewed masonry arch be explained?
2. What is the detailed, three-dimensional response of the skewed masonry arch bridge under its current train loads – including both the in-plane flow of force through the arch barrel and the out-of-plane vertical displacements – and is this measured response consistent with its anticipated behaviour?
3. Similarly, what are the detailed, dynamic responses across cracks in the skewed masonry arch bridge?

## 1.4 Thesis outline

Part 1 of this thesis begins with this introduction, stating the background and motivation for the project and the main research questions that have been addressed. This is followed by Chapter 2, a review of relevant available literature. Chapter 3 then presents the modelling study of the Marsh Lane viaduct.

Parts 2 and 3 are concerned with field monitoring of the case study structure: the CFM-5 railway bridge in North Yorkshire, UK. Chapter 4 describes the development of the monitoring installation, including the design of novel implementation strategies for the FBGs; an overview of the general data processing strategies that were adopted; a practical evaluation of the various sensors used; and a desk study utilising laser scan data to investigate historic deformations and support movements of the skewed masonry arch.

Following this, in Chapter 5, strain data from the FBGs are used to investigate the typical, dynamic response of the skewed arch. In particular, the longitudinal strain distribution and movements across cracks are studied in detail. The consistency of this response is considered by examining the statistical distribution of data for many different train events. The large number of measured trains also allows for investigation of the sensitivity of the response to a range of factors, including the train speed, ambient temperature, and time of day – which is used as a proxy for the precise applied loading, by factoring in expectations of passenger behaviour at various times.

In Chapter 6, a novel FBG strain rosette implementation is used to study the distribution of principal strains – and, hence, the in-plane flow of force – throughout the skewed arch barrel. Strain states in which the normal strains are aligned with the skewed span and square span directions are also investigated. Again, the consistency of response between different train events is studied. Following this, the processed videogrammetry data are used to characterise the out-of-plane, vertical displacements of the arch barrel. A simplified beam model is introduced to describe transverse bending and is fitted to the experimental data. This leads to insights into the support conditions at the edges of the arch barrel – in other words, the separation cracks between the arch barrel and the spandrel walls – the improvement of which was one of the key objectives of the recent repair work.

Part 3 begins with Chapter 7, which presents the adaptation of the FBG installation for long-term, autonomous monitoring. This necessitated changes to the data processing strategies outlined in Chapter 4, which are also described.

Chapter 8 presents an analysis of all FBG data gathered to date at the CFM-5 bridge. This includes the initial six months of on-site monitoring, as well as remote monitoring from July 2020 up to the end of April 2021. Between these periods, there were changes in the rolling stock used on the main passenger route over CFM-5; this new train loading is clearly identifiable in the data. Further trends in the expanded data set – in particular, relating the bridge response to ambient temperature – are studied. Data corresponding to trains on other passenger routes are plotted separately and included in Appendices.

Lastly, Part 4 summarises the main findings of this thesis and concludes with possible avenues for future research.

A number of conference and journal papers have been written, based on the research that is described in this thesis, and further publications are planned. These are summarised at the end of the References.



# Chapter 2

## Literature review

This chapter presents pertinent results from the available literature, although the size and history of the field of masonry arch bridge research mean that this cannot be exhaustive. The focus here, where necessary, is on brick masonry railway bridges. A brief overview of arch bridge construction and materials is given first, followed by a discussion of behaviour. This includes findings from laboratory testing of scale models; an overview of behaviour in ULS and SLS conditions; investigations into arch bridge fatigue; and studies and assumptions regarding the flow of force. Structural field monitoring of masonry arch bridges is then considered, followed by computational analyses. The last part of this chapter deals with arch bridge assessment.

### 2.1 Arch bridge construction

#### 2.1.1 The history of masonry arch bridge construction

The ideal shape of a masonry arch under static loads has been known for centuries and was eloquently captured in Hooke's description of an inverted chain. This gave rise to early rules on arch geometry, including specifications of rise-to-span ratios and preferable schemes for varying the arch thickness, which have since been investigated by modern researchers (Brencich and Morbiducci, 2007). Much historical information remains from the early period of masonry arch bridge construction, which has been examined by modern civil engineering historians (e.g., Ruddock, 2000). A recent review by Sarhosis et al. (2016) gives a useful overview of the history of masonry arch bridge construction and research.

Practical guidance is available for asset engineers tasked with inspecting and maintaining these bridges today (e.g., Network Rail, 2006; McKibbins et al., 2006). This is based on an understanding of historic construction techniques, designs, and materials used in the building

of masonry arch bridges, as well as common types of damage which may arise over their long working lives.

The typical structural elements which make up a masonry arch bridge are shown in Figure 2.1 (after McKibbins et al., 2006).

Figure removed for copyright reasons. Copyright holder is CIRIA.

*Figure 2.1: Structural elements of a typical masonry arch railway bridge, after McKibbins et al. (2006)*

### **2.1.2 Historic material properties**

A principal source of uncertainty when analysing historic masonry arch bridges is the specification of material properties. While corresponding data for new materials – which may be expected to have reasonably uniform properties – is easy to find, there is significant variation between historic masonry structures, as well as within individual structures. This variation is primarily due to material deterioration over time, although there is also more spread in the likely initial values of these properties. Fortunately, many tests have been carried out on samples of historic masonry, giving feasible values which may be used in an initial analysis, in the absence of specific test data for an individual bridge.

Based on flat-jack tests, Bergamo et al. (2015) suggest a value of 4.16 GPa for the Young's Modulus of historic brick masonry. Recommendations by the Italian seismic design code are slightly lower, in the range 1 to 3.6 GPa, but can be conservative since this code assumes a certain level of damage has already occurred (Eucentre, 1987). Material properties from a wide range of tests on historic masonry are compiled in the online Masonry Database, MADA, and these suggest a likely range of 1 to 5 GPa, although values as high as 10 GPa are occasionally reported (Augenti, Acconcia, and Parisi, 2012).

Furthermore, material properties will not be uniform over an entire bridge, due to the variable quality of historic construction materials and the typically uneven distributions of damage. For instance, tests on the Tanaro Bridge in Italy, built in 1866, found that the Young's Modulus of its masonry varied between 1.2 and 5 GPa at different locations (Brencich and Sabia, 2008). Similar distributions will occur for other properties.

Clearly, this likely variation means that the use of a single, averaged value of, say, the Young's Modulus in structural calculations may well yield flawed results. While this may be a necessary simplifying assumption, in order to make the calculations tractable, its ramifications must be recalled during the interpretation of results.

## **2.2 Behaviour of masonry arch bridges**

### **2.2.1 Testing of scale models**

There is a history of static tests on scale model arch bridges, which forms an important part of 20<sup>th</sup> Century masonry arch research. The tests carried out at the Bolton Institute are frequently referenced; these involved a set of single span masonry arch bridges, with spans of either 3 m or 5 m (Melbourne and Gilbert, 1995), as well as a set of multispan bridges, each with three spans of 3 m each (Melbourne, Gilbert, and Wagstaff, 1997). Although the majority of masonry arch bridges are less than 5 m in span (Brencich et al., 2006), these are modest spans by the standards of many railway bridges.

Recently it has been suggested by Brencich and Riotto (e.g., in 2016a, 2016b) that these tests do not apply proper scaling laws, and that therefore the results cannot be generalised to larger bridges without overpredicting the strength of their masonry. Brencich and Riotto have performed both static (2016a) and dynamic (2016b) experiments on model bridges and proposed scaling laws that may be used to relate their results to bridges of a different size. However, it is important that the bridge geometry is otherwise consistent. For instance, results from a scale model of a shallow arch bridge – i.e., a low ratio of the arch rise,  $r$ , to span,  $s$  –

cannot be used to predict behaviour of a deep arch. In particular, the mode of failure may be different; Brencich and Riotto observed some material crushing close to the failure of their shallow ( $r/s = 0.2$ ) model arch, before a fourth hinge was able to form, but negligible crushing and a clear, classical 4-hinge mechanism during the failure of a deeper ( $r/s = 0.3$ ) model arch. Note that clear mechanism failures were also observed during the collapse of the Bolton ( $r/s = 0.25$ ) model arches (Melbourne and Gilbert, 1995; Melbourne, Gilbert, and Wagstaff, 1997), which may support Brencich and Riotto's claim that these test results would effectively overpredict material strength if used to estimate the behaviour of larger-scale bridges.

More research is needed to fully establish the importance of model scaling, particularly for contributions to overall bridge behaviour resulting from structural components other than the arch, such as the arch-backfill interaction. In the meantime, this highlights the importance of collecting detailed monitoring data on the response of real-world, full-scale masonry arch bridges. Such data can lead directly to insights into bridge behaviour and, ultimately, will be necessary to validate any improved model scaling laws.

## **2.2.2 ULS behaviour of arch bridges**

### **2.2.2.1 Behaviour of masonry arches**

Simplified analysis of masonry arch bridges may often ignore the spandrel walls and soil fill. Instead, the Ultimate Limit State of the bare arch is considered. Unlike elastic methods, a limit analysis does not require the same depth of knowledge regarding material properties and initial stresses, which may be difficult or impossible to establish. Heyman popularised the limit analysis of masonry arches as an extension of plasticity theory (Heyman, 1982).

Heyman argued that arches fail through the formation of a hinged collapse mechanism. Having assumed that the compressive strength of masonry would be far higher than any likely stresses, it follows that stability instead of strength will govern failure. Heyman's assumptions – of infinite compressive strength, negligible tensile resistance, and no possibility of sliding (i.e., mortar-initiated) failure between the blocks – would be adopted by many researchers to come, although in time more general solutions were formulated that allowed these assumptions to be relaxed.

Limit analysis lies at the heart of the most popular commercial analysis programs for masonry arches, such as ARCHIE (Harvey, 2017) and LimitState:RING (Gilbert, 2017). These are widely used in arch bridge assessment.

This approach suggests that failure is governed by the eccentricity of the thrust line from the centroidal axis. When this eccentricity is great enough to bring the thrust line outside of the arch ring then a hinge is formed, with four hinges resulting in a collapse mechanism for a single arch span. Conservatively, failure may be said to occur when the first hinge is formed and knowing that the maximum allowable eccentricity is half of the arch depth allows the failure surface to be drawn as a function of axial force  $P$ . This is shown in Figure 2.2 (after Carr et al., 2013).

Heyman was primarily concerned with the analysis of masonry arches in buildings and monuments, rather than masonry arch bridges. In this context, his assumptions were often found to be reasonable and removing them only affected a small number of cases. For example, Boothby examined the possibility of mortar-initiated failures and found that in most cases these would give rise to another equilibrium state before eventually leading to a classical hinge-based mechanism, as Heyman predicted (Boothby, 1997). It is less apparent, however, that these assumptions will apply to masonry arch bridges. Here, the presence of significant backfill above the arch as well as heavy vehicles, especially for rail, can give rise to high loads. As a result, the stresses within the arch may begin to approach the compressive strength of masonry.

Allowing for finite compressive strength gives a maximum axial force which further defines the failure surface. Following the notation used by Carr et al. this critical force is  $P_0 = bh\sigma_0$ , where  $\sigma_0$  is the compressive strength of masonry,  $b$  is the arch width and  $h$  is its depth. Similarly, the critical moment is  $M_0 = \frac{1}{8}bh^2\sigma_0$ , assuming a simple rectangular stress distribution over the compression half of the arch when this maximum moment is realised (Carr et al., 2013). From this, the equations for the failure surface may be written. The simple case for infinite compressive strength is:

$$M = \frac{Ph}{2} \quad (2.1)$$

If the compressive strength is taken to be finite, then the failure surface may be written as:

$$M = 4M_0 \left[ \left( \frac{P}{P_0} \right) - \left( \frac{P}{P_0} \right)^2 \right] \quad (2.2)$$

This equation for the yield surface is quoted by Carr et al. and is described in more detail in an earlier paper by Boothby (2001). A similar result is obtained by Clemente, Occhiuzzi, and Raithel (1995).

Figure removed for copyright reasons. Copyright holder is Elsevier.

*Figure 2.2: Failure surface for masonry, showing the two cases of infinite and finite compressive strength, after Carr et al. (2013)*

#### **2.2.2.2 Importance of additional structural components**

Thus far, the focus has been on the masonry arch itself. However, it is important to consider the other structural components that make up the overall bridge. For example, up to approximately two thirds of the ultimate load capacity of these structures may be due to stabilising effects from the arch-fill and arch-spandrel interactions, though the precise figure depends on the bridge geometry and typology (Brencich, Cassini, and Pera, 2016).

Assumptions are often made during analysis regarding load distribution through the fill. It was found in scale models, tested statically in laboratory conditions, that load distribution was only significant at lower loads and that close to the ultimate capacity of the bridge its impact was minimal (Brencich, Cassini, and Pera, 2016). It was also found that when the load was applied to the top of the fill rather than at the fill-barrel interface, such that load distribution through the fill was permitted, then the response of the test structure was more ductile.

In some studies, the initial presence of full connectivity between arch barrel and spandrel walls has been found to increase the ultimate failure load of single-span masonry arch bridges by as much as 72%, through inhibiting the formation of hinges in the barrel (Boothby, Domalik, and Dalal, 1998; Fanning, Boothby, and Roberts, 2001). The corresponding increase for multi-span bridges has been reported to be 30% (Melbourne, Gilbert, and Wagstaff, 1997; Fanning, Boothby, and Roberts, 2001), although this value is based on scale model tests and so its applicability to significantly larger bridge spans is uncertain (Brencich and Riotto, 2016a). The

positive impact provided by spandrel walls, as well as that provided by the soil fill, is seen to be greater for deeper arches than it is for shallower ones.

Different numbers and patterns of hinges will arise in single span and multi-span bridges, eventually leading to collapse mechanisms – unless local crushing causes failure before the formation of the final hinge. For a single arch, four hinges are needed to give rise to an asymmetric mechanism, or five hinges for a symmetric mechanism if the loading pattern dictates that failure will occur this way. However, for multi-span bridges, interaction between spans makes the behaviour more complicated. A total of seven hinges are required to give rise to a mechanism failure in this case, and the interaction effect between spans leads to a reported 70% loss of capacity when compared to an analogous single span bridge (Brencich and De Francesco, 2004b). However, this study ignored the effect of spandrel walls, so this predicted loss of capacity may be conservative.

In a rare example of a load test to failure, a historic bridge was observed to fail through crushing of the barrel directly below the point of application of the load, while a classical four-hinge mechanism had been predicted (Leon and Espejo, 2007). In this particular case, it was concluded that the presence of rigid backing acted to increase the effective arch thickness, removing the possibility of a stability-based failure, and allowing the development of high compressive stresses which eventually led to crushing. This study highlights the importance of gathering reliable construction information, wherever possible, on masonry arch bridges before trusting in the results of any calculations. Rigid backing, such as concrete, is often added between the arch ring and soil fill but is difficult to detect without potentially invasive tests.

## **2.2.3 SLS behaviour of arch bridges**

### **2.2.3.1 Behaviour of masonry arches**

Most existing research considers the ULS behaviour of masonry arch bridges. However, it will be the behaviour under working loads that drives deterioration, making it increasingly important to understand the Serviceability Limit State in detail.

The behaviour of masonry can be simplified by considering it to be linear elastic up to an infinite compressive strength, while the tensile strength is zero (Heyman, 1982). A slightly more sophisticated model could recognise both the tensile and compressive strengths of masonry and assume that intermediate behaviour is linear elastic with Young's Modulus  $E$  (Aita, Barsotti, and Bennati, 2017a, 2017b). This relationship is then as follows, with  $\sigma_t$  usually assumed to be zero:

$$\sigma_{\theta} = \begin{cases} \sigma_c & \text{when } \epsilon_{\theta} \leq \epsilon_c, \\ E\epsilon_{\theta} & \text{when } \epsilon_c < \epsilon_{\theta} < \epsilon_t, \\ \sigma_t & \text{when } \epsilon_{\theta} \geq \epsilon_t, \end{cases} \quad (2.3)$$

The assumption of linear elastic behaviour is either true or approximately true in the case of relatively undamaged masonry arch bridges; a rule of thumb suggests that while deflections are less than 1 mm this remains a safe assumption (Fanning, Boothby, and Roberts, 2001). The extent of damage should also be considered, as this will increase the nonlinearity of bridge behaviour. Nonetheless, for bridges with reasonably low damage and applied vehicle loads that are not excessive, this suggests that linear elastic modelling may be an acceptable starting point for SLS analysis.

### 2.2.3.2 Importance of additional structural components

Under service conditions, it has been observed that significant load distribution occurs through the soil fill (Brencich, Cassini, and Pera, 2016). Further distribution can also happen in the arch barrel itself (Harvey, Tomor, and Smith, 2005). It is argued that load distribution within the barrel gives rise to a ‘zone of thrust’ as opposed to the classical line of thrust, and that the minimum size of this zone is governed by the need to keep stresses below the relevant compressive limits. This has immediate consequences for any analysis that assumes an effective width of the arch, since transverse distribution through the arch ring means that a more substantial portion of the structure than previously appreciated will be involved in carrying the applied loads.

Transverse effects also influence the SLS response. Their impact is amplified for bridges with thin arch rings or high spandrel walls, both of which increase the disparity in stiffness between the arch and the spandrels. Displacements are observed to be higher at the bridge centreline than they are close to the spandrel walls (Fanning, Boothby, and Roberts, 2001). In other words, transverse bending occurs because stiffness is higher at the edges of the barrel when full connectivity exists with the spandrel walls. Bulging or leaning spandrels can be a sign that transverse effects are significant.

Spandrel wall separation is a common defect, and, in some cases, transverse tie bars are installed in an attempt to restore connectivity. These interventions are not always successful but can lead to significant improvements in residual bridge capacity (Fanning, Boothby, and Roberts, 2001).

Lastly, interactions between spans can define the response of multi-span bridges and viaducts (Acikgoz et al., 2018a). Span opening is a good indicator of the condition of these structures. This will be significantly less notable for single span bridges, although in cases where

deterioration has taken place it may still be possible to measure deflections at the abutments (Fanning, Boothby, and Roberts, 2001).

#### **2.2.4 Fatigue of masonry arch bridges**

A review of research into masonry fatigue is given by Laterza, D'amato, and Casamassima (2017), who then apply the stress-life curve method to estimate the residual service life of a historic masonry arch bridge. Several papers have also been published as a result of a significant research campaign into the fatigue of masonry arch bridges, led by Adrienn Tomor (Wang et al., 2013; De Santis and Tomor, 2013; Tomor and Verstryngge, 2013; Tomor, De Santis, and Wang, 2013; Koltstida, Tomor, and Booth, 2014). This area has also been researched by Matthew Gilbert (e.g., in Gilbert, 2009).

Key types of damage, including ring separation, longitudinal cracking, and, in particular, spandrel wall separation cracks, were found to occur under high-cycle fatigue loading. In addition, long-term distortion of bridge geometry was reported. Significant similarities were established between fatigue behaviour and creep, but fatigue limits remained hard to define for masonry. Instead, the key findings of Tomor's study were fed into parallel research into a Permissible Limit State (PLS) for use in assessment. This is discussed further in section 2.5.2.2.

Cyclic load tests were carried out in laboratory conditions, on a 3 m span masonry arch bridge, by Augusthus-Nelson et al. (2016). Cyclic 'travelling wave' loads were applied by five actuators spaced equally along the span, at progressively higher magnitudes. Deterioration was noted once peak loads rose above 70 kN, when hairline cracks began to appear. Above 80 kN, severe damage was observed. The stiffness of the bridge was measured between each loading cycle and was found to steadily decrease until peak loads reached 90 kN. Beyond this, the stiffness decreased far more rapidly, until failure occurred at roughly 140 kN. From these results, it was concluded that loads under 50% of the ultimate failure load may not cause permanent damage. This supports the proposal, seen in several cases in the literature, that 50% of the ULS load can be used as an estimate of the allowable SLS load for masonry arch bridges (Gilbert et al., 2016; Melbourne et al., 2013; Highways Agency, 2001).

The deterioration of brick masonry beams under cyclic loading has recently been studied by Alexakis, Liu, and DeJong (2020), using Acoustic Emission (AE) sensors. Statistical analysis of the AE data allowed identification of the different damage stages and modes, during a range of deterioration processes – such as micro- and macro-cracking, material crushing, and shear failures – which ultimately led to the collapse of the beams. In related, ongoing field research, AE sensing has also been used to track damage propagation in a masonry arch viaduct (Alexakis

et al., 2019a; 2019b). This has the potential to lead to better understanding of the general fatigue response of masonry arch bridges and viaducts, under repeated application of their working train loads.

## 2.2.5 Assumptions regarding the flow of force

### 2.2.5.1 Skewed masonry arch bridges

Skewed bridges are built when it is necessary for the road or railway they carry to cross an obstacle at an angle other than  $90^\circ$ . This results in the longitudinal span direction no longer being perpendicular to the abutments, so that the planform of the arch is a parallelogram. In contrast, the planform of a square-spanning arch is rectangular. Different construction methods have been used in the building of skewed masonry arches, as shown schematically in Figure 2.3 (after McKibbins et al., 2006). This figure includes construction with the masonry bedding planes parallel to the arch springings (Figure 2.3(a)), which is the typical construction pattern used for square-spanning arches. While this method may still be used for arches with low skew, the presence of notable skew is likely to lead to the use of either the helicoidal (Figure 2.3(b)) or orthogonal (Figure 2.3(c)) methods.

Forces are typically assumed to flow in the square span direction of masonry arches, as this offers the shortest load path to the abutments. This remains the assumption for skewed arches when these are wide enough for a subset of the arch barrel to form an effective square-spanning arch, which bounds its assessed effective width (Network Rail, 2006).

Figure removed for copyright reasons. Copyright holder is CIRIA.

*Figure 2.3: Construction methods for skewed masonry arches, after McKibbins et al. (2006)*

For skewed arches that are thinner than this, the preferred load path is uncertain. In this case, the capacity may be assessed as the lower result of separate 2D analyses that assume the arch to span in, respectively, the square and skewed span directions (Network Rail, 2006). However, this is a simplification intended to expediate assessment. The true behaviour of skewed masonry arch bridges is known to be complex and three-dimensional, warranting a full, 3D analysis (McKibbins et al., 2006). Harvey (2004) gives an interesting discussion of this problem and suggests several hypotheses for skewed arch behaviour, which require validation through monitoring of real bridges. Note that an analysis of laser scan data presented later, in section 4.6.3.1, supports one of Harvey's hypotheses in this paper.

Sarhosis et al. (2014) have used DEM to study the cracking and collapse behaviour of a set of skewed masonry arches. Increased skew was observed to lead to a more highly three-dimensional response, which in turn led to failure at lower loads. However, in these arches the block joints were parallel to the springings (as in Figure 2.3(a)), which is not common for significantly skewed arches and may affect the applicability of these results.

More recent DEM analysis by Forgács et al. has produced interesting predictions of the behaviour of skewed masonry arches (2018b) and arch bridges (2018a; 2019a) close to collapse. In particular, it was predicted that the line of thrust would follow the shortest available span, leading to load concentrations in the obtuse corners of the arch, and the collapse behaviour was highly three-dimensional. Helicoidal construction (see Figure 2.3(b)) was observed to give significantly better performance than arches whose block joints were parallel to their springings (see Figure 2.3(a) and compare with Sarhosis et al. (2014) above).

It is important to note, however, that these studies have not specifically investigated the impact of the boundary conditions at the arch abutments, which are modelled as rigid supports. This is an unrealistic assumption for many real-world arch bridges (see Harvey, 2004, and the later discussion in section 4.6.3.1) and may affect the validity of these findings.

Experimental work exploring the preferred load paths in skewed masonry arch bridges is very rare. Figure 2.4 shows the result of one investigation, by Harvey (2013), into the behaviour of a shallow skewed arch. On the left is an FE-generated analysis of static load distribution through the arch, for a concentrated applied load, while on the right are deflection data against which this distribution was verified. Harvey's analysis suggests that the locus of peak displacements – and hence, presumably, peak thrust – is aligned with the square span direction, while that of the centroid of the distributed thrust, over the arch width, follows the skewed span direction. More experimental work on skewed masonry arch bridges – ideally on full-scale, real-world

bridges, under dynamic working loads applied at track or road level – is needed, in order to fully investigate the behaviour of these complex structures.

Figure removed for copyright reasons. Copyright holder is ICE Publishing.

*Figure 2.4: Example of finite element analysis of the load distribution through a skewed arch bridge (left) and corresponding vertical deflection measurements (right) for a statically loaded, skewed bridge, after Harvey (2013)*

### **2.2.5.2 Interactions between structural components**

Many masonry arch bridges contain regions of rigid backfill above the bridge piers or abutments, between the arch haunches and the soil fill. The rigid backfill is typically constructed using concrete or rubble masonry and can consequently have significant stiffness. Furthermore, in some cases, voids are present above this solid backfill, as opposed to soil fill (Harvey, 2012). Particularly in the case of multi-span bridges and viaducts, these rigid regions can, if present, greatly alter the overall behaviour. Considering this, Harvey proposes that each of these regions – containing the stiffer backfill, the skewback, and the adjacent portions of the arch barrels – be considered as one rigid block, which can rotate on the top of the pier or abutment on which it rests (Harvey, 2012; Harvey and Harvey, 2017). This has the result of reducing the true span distance of the arch, which now effectively spans only between these two rigid blocks, rather than the full distance between the piers or abutments.

However, this formulation does not allow for the lack of tensile strength at the arch-backfill interface. These two portions may separate from one another, as was observed in monitoring data for the Marsh Lane viaduct (Acikgoz et al., 2018a). Furthermore, it was concluded in the same study that spreading of the relieving arches in the piers was causing the pier masonry on either side of the relieving arches to rotate outwards. Instead of the viaduct behaving uniformly

over its width, this pier rotation led to separate rigid body movements developing over its two halves. The overall response mechanism at this viaduct, consequently, included rigid body movements of a larger-than-expected number of regions, some of which moved collectively at certain points in the response and independently at others.

The findings at the Marsh Lane viaduct highlight that, even after the formation of clear visible cracks on the exterior surfaces of a masonry arch bridge, the response mechanism may be highly complex. Detailed, distributed measurements are likely to be necessary to confidently identify these mechanisms.

## **2.3 Structural monitoring of masonry arch bridges**

### **2.3.1 Monitoring the response of bridges to loading**

Structural Health Monitoring can provide useful insights into the actual behaviour of masonry arch bridges under their service loads. Here, dynamic monitoring is of primary interest, but static techniques may also be useful to investigate long-term deformation of these structures. Note that, although dynamic monitoring is needed to capture the bridge response to travelling live loads, the response itself has been found to be pseudo-static (Acikgoz et al., 2018b).

Distributed methods, such as fibre-optic (FO) sensing and videogrammetry, are well suited to examining the global response at many points across the extent of a structure. However, these tend to produce large volumes of data, and so point sensors may, in some cases, be more practical for long-term monitoring.

Furthermore, combining AE sensing (see section 2.2.4) with dynamic displacement or strain monitoring can potentially form the basis of early-warning structural alert systems for masonry arch bridges and viaducts. As described by Alexakis et al. (2019a; 2019b; 2020), such an alert system would have major practical applications in the asset management of these ageing structures. This is a significant motivating factor behind the development of novel SHM procedures for masonry arch bridges, such as those described in this thesis.

#### **2.3.1.1 Distributed, dynamic sensing methods used in this thesis**

From Chapter 4, this thesis presents a detailed monitoring campaign at a skewed masonry arch railway bridge. The primary technologies employed in this study are fibre-optic FBGs, used to measure the dynamic strain response in the bridge, and videogrammetry, used to study the out-of-plane movements of the arch.

The necessary theory behind these technologies is presented later, in the relevant methodology sections in Chapter 4. General overviews of FBG and videogrammetry sensing are presented in sections 4.3 and 4.4, respectively.

A useful summary of the videogrammetry method is given by Acikgoz et al. (2018b), including typical sources of measurement errors which must be corrected for, either by using an appropriate equipment setup during monitoring, or through post-processing of the displacement measurements.

This research project is believed to be the first example of FBG monitoring of a skewed masonry arch. Although FBGs are an established technology, particularly in experimental research, previous examples of FBG monitoring of masonry structures are rare. Acikgoz et al. (2018a) used FBGs to monitor two damaged arches of a masonry railway viaduct, and a revised installation at the same structure has since been developed by Alexakis et al. (2019a; 2019b; 2021). Separately, Acikgoz et al. (2019b, 2021) have used FBG sensing alongside laser scan data to evaluate distributed strain and displacement profiles of a historic masonry church that was expected to experience tunnelling-induced settlements.

### **2.3.1.2 Other examples of dynamic monitoring**

Previous studies have used other monitoring technologies to investigate the dynamic response of masonry arch bridges – for instance, to assess their modal properties. Dynamic tests on a subset of the Bolton Institute arch bridges (see section 2.2.1) concluded that loaded arches, perhaps unsurprisingly, display different modal properties to unloaded arches, and that the original modal properties are recovered upon unloading (Armstrong et al., 1995a). However, the behaviour is more nuanced than may initially be expected because, further to the simple addition of mass, the stiffness of the soil fill is stress dependent and therefore changes under this extra applied load.

In a subsequent study on the same model bridges, modal data were post-processed to yield the dynamic stiffness, which was then used to determine the degree of connectivity between the arch barrel and the spandrel walls (Armstrong, Sibbald, and Forde, 1995b). The dynamic stiffness is the ratio between an applied dynamic force and its resulting displacement and is frequency dependent; it is, in other words, the inverse of the structure's transfer function. At zero frequency, this will correspond to the distribution of static stiffness over the bridge.

It was observed that, in a bridge with connectivity between the arch barrel and spandrels, there was a roughly quadratic distribution of dynamic stiffness across its transverse cross-section.

This was not observed in a separate bridge, which exhibited spandrel wall separation; here, the transverse dynamic stiffness was approximately constant. Both cases, however, showed a roughly quadratic distribution of dynamic stiffness in the longitudinal direction. Typical distributions for these two bridges, with and without spandrel wall separation, are reproduced in Figure 2.5 (after Armstrong, Sibbald, and Forde, 1995b). Note that the left- and right-hand distributions in this figure correspond to different model geometries with arch spans of 3 m and 5 m, respectively. Because of this, comparison of the stiffness values between the two cases is not informative.

Figure removed for copyright reasons. Copyright holder is Elsevier.

*Figure 2.5: Distributions of dynamic stiffness measured at the intrados of two model masonry arch bridges, showing the case of spandrel wall connectivity on the left and spandrel wall separation on the right, after Armstrong, Sibbald, and Forde (1995b)*

Dynamic testing of the 19<sup>th</sup> Century Tanaro Bridge during its demolition showed an interesting feature of the arch-spandrel interaction. While spandrels remained fully connected, it was observed in the mode shapes that multiple spans were involved in the response. However, once the spandrels had been removed, the mode shapes were found to occur at lower frequencies and only involve appreciable movements of the loaded span (Brencich and Sabia, 2008). The results for the first natural frequency are reproduced in Figure 2.6.

Figure removed for copyright reasons. Copyright holder is Elsevier.

*Figure 2.6: Comparison of the first mode shapes measured over two spans of the Tanaro Bridge, (a) when spandrels remained present, and (b) after spandrels had been removed, after Brencich and Sabia (2008)*

In the studies mentioned above, accelerometers were used to measure the dynamic responses. These have yielded useful results for the scale model bridges studied by Armstrong et al. (1995a; 1995b) and the partly demolished bridge investigated by Brencich and Sabia (2008). However, when it is also desired to identify the dynamic displacements, traditional accelerometers may struggle to accurately capture this response, for operational masonry arch bridges under their service loads. Having said this, studies using recently developed, low-noise accelerometers have identified dynamic displacements on a par with FBGs (Alexakis et al., 2019a).

### **2.3.2 Monitoring to determine bridge properties**

Various techniques can be used to ascertain the material properties of masonry bridges. For instance, flat-jack testing can obtain in-situ stresses and identify the Young's Modulus (Arède et al., 2016). This technique is also described in detail by Bergamo et al. (2015).

Properties of infill materials can be found using Ménard pressuremeters (Arède et al., 2016). However, since this requires the drilling of boreholes in the bridge, the destructive nature of these tests may not always be acceptable. Cores that are extracted in order to create these boreholes can provide further useful information, for example through triaxial or shear tests.

Although these approaches can, where permissible, allow for material properties to be quantified, best practice dictates that measurements should be taken at a sufficient number of locations across the bridge extent, in order to account for the variable quality of historic construction materials. Even then, as discussed in section 2.1.2, the use of averaged material

properties in any further analysis will belie their true, variable distributions over the bridge. In cases where this variation is significant, the quality of analysis results may become dubious.

An increasingly common technique for inspecting the internal structural geometry of masonry bridges is ground-penetrating radar (GPR). This can detect internal spandrel walls, if any are present (Bergamo et al., 2015). Other useful information can also be obtained, such as the top level of any rigid backfill (Arède et al., 2016). Contrasting with these investigations of internal construction, laser scanning is an effective way of obtaining detailed information on the external geometry (Riveiro, DeJong, and Conde, 2016).

## **2.4 Computational analysis of arches**

### **2.4.1 Finite element method (FEM)**

#### **2.4.1.1 Assumptions for simplified analyses**

An assumption of linear elasticity is sometimes justifiable when modelling the SLS behaviour of arch bridges. Specifically, this may be a safe assumption when deflections are small and damage is minimal (Fanning, Boothby, and Roberts, 2001), but its applicability outside of these conditions is uncertain.

Nonlinear elastic models can be used but entail greater computational expense and running time. Furthermore, they require more input parameters to characterise behaviour and so are more sensitive to parameter uncertainty.

#### **2.4.1.2 Complex analyses**

Detailed modelling can include the nonlinear aspects of material behaviour, such as zero resistance to tensile stresses and a finite compressive strength. For instance, a study by Domede, Sellier, and Stablon (2013) uses a solid mechanics approach – specifically, the Drucker-Prager failure criteria – to model cracks. Drucker-Prager modelling of cracks is commonly found in the literature.

The internal soil fill can be modelled indirectly, as horizontal forces applied to the arch, or directly, for instance as a Mohr-Coulomb cohesive-frictional material which cannot resist tension (Cavicchi and Gambarotta, 2007). Interface elements can be used to model the interaction between the fill and the arch (Fanning and Boothby, 2001).

Further examples of masonry arch bridge modelling in the literature include 3D nonlinear analysis by Milani and Lourenço (2012), examining square and skewed bridges, and mesoscale modelling developed by Zhang et al., who investigated various aspects of behaviour, including

the skew effect (2016; 2017) and the interactions between the arch and adjacent fill and spandrels (2018).

These studies also happen to have been validated against experimental data from the previously discussed test programme at the Bolton Institute. The continued use of the Bolton data in recent analytical work highlights the lack of availability of other detailed experimental data, particularly for larger span skewed arch bridges.

#### **2.4.1.3 Modelling of dynamic behaviour**

A number of finite element (FE) approaches allow for dynamic behaviour to be modelled. For instance, a fibre beam formulation has been developed by de Felice (2009), which has been extended to allow nonlinear dynamic analysis of masonry arch bridges under seismic loads (De Santis and de Felice, 2014).

Gibbons used 3D finite element models to investigate the dynamic behaviour of several masonry arch railway bridges (Gibbons, 2014). Experimental data were used to fine-tune the FE results by varying the damping ratio of the model; good agreement was observed for both the mode shapes and natural frequencies. 3% damping was ultimately found to be a reasonable value for these historic bridges. This agrees with the average damping value identified by Bayraktar, Türker, and Altunisik (2015).

Using these models, Gibbons ran transient analyses and compared the results against calculations based on codes EN 1991-2 (CEN, 2003) and UIC 776-1R (UIC, 2006). It was found that both codes, which use simplified beam-based models, grossly overpredicted the dynamic amplification factors. The actual factors were always less than 10% for the three bridges considered, compared with code predictions in the range 47% to 121%, depending on train speed. A maximum train speed of 125 mph is considered by the codes; even when using a speed of 250 mph Gibbons found that the predictions from her finite element models did not result in the dynamic amplification factor exceeding 30% (Gibbons, 2014).

Improvements on these simplified beam models have since been developed by Smith and Acikgoz (2019). In their study, a curved beam model is proposed as a better approximation of a masonry arch bridge.

### **2.4.2 Discrete element method (DEM)**

Discrete element modelling is an alternative to FEM which is well suited to studying the collapse of masonry structures. For instance, in a study by Dimitri and Tornabene (2015), DEM and FEM were used to investigate the dynamic seismic response of masonry arches and found to obtain very similar predictions of the collapse mechanisms and loads. DEM analysis by Forgács, Sarhosis, and Adany (2018a; 2019a) has identified features of the collapse behaviour of skewed masonry arch bridges (see section 2.2.5.1). A novel DEM formulation of the soil backfill region has also been proposed by Sarhosis, Forgács, and Lemos (2019a; 2019b).

Numerous other applications of DEM exist in the literature, particularly for dry-stone masonry structures. Examples include the work by Lemos (2007), DeJong and Vibert (2012), McInerney and DeJong (2014), Costa et al. (2015), and Forgács et al. (2017). Large displacements, which may lead to separation and recontact of masonry regions, are ideally suited for modelling with DEM. However, for the majority of masonry arch bridges remaining in service, distributed material deformation and cracking may be likelier forms of damage. These can be more challenging to model with DEM.

### **2.4.3 Examples of other modelling approaches**

Other approaches may idealise the arch as a one-dimensional beam. This can be formulated as a series of nonlinear ordinary differential equations for dynamic analysis, as was done by Aita, Barsotti, and Bennati (2017a; 2017b). This approach has since been explored in more depth, for the static case (Barsotti and Bennati, 2017).

Cazzani et al. (2016) define an elastic numerical model of a bare arch in which the geometry is defined using non-uniform rational B-splines (NURBS), a mathematical technique first developed for computer-aided design; their analysis model can be directly imported from a drawing file. Geometry and displacements are assigned using NURBS and the elastic model is based on a curved Timoshenko beam (Cazzani, Malagù, and Turco, 2016; Chiozzi et al., 2016).

An iterative procedure for modelling a masonry arch has also been proposed by Brencich and De Francesco (2004a; 2004b; see also Brencich et al., 2006). In this approach, a limit is placed on the compressive strength of masonry, beyond which the behaviour is plastic with further constraints placed on the allowable strains. Above these strain limits, material crushing occurs.

Useful overviews of the development of various modelling approaches for masonry arch bridges are given by Gibbons (2014) and Sarhosis et al. (2016).

Recently, a new equilibrium solution has been developed using membrane equilibrium analysis (MEA) to consider the arch barrel as a membrane structure. This efficient solution allows for a biaxial stress state to be modelled within the arch, hence capturing the three-dimensional nature of its response. Early results, obtained by applying this method to a square-spanning masonry arch viaduct, have yielded a higher capacity than other, traditional 2D methods (Olivieri, Fortunato, and DeJong, *in press*). It is hoped to extend this method to skewed arches in future work, by leveraging the monitoring results presented later in this thesis.

#### **2.4.4 Probabilistic and statistical methods**

Probabilistic methods can address uncertainty in the analysis of masonry arch bridges, for example regarding input parameters like the Young's Modulus, the boundary conditions, and the choice of computational model. These methods identify the most likely parameter values or models by considering the likelihood that these are correct, given certain monitoring data representing the real-world structure and its response.

For example, Hacıfendioğlu, Başağa, and Banerjee (2017) used Monte Carlo simulations to address parameter uncertainty in an FE analysis of a historic masonry arch bridge. This study investigated the types of statistical distributions used to capture parameter uncertainty and found negligible differences in the results. Based on this, it is most appropriate to use normal distributions, which also offer the simplest approach. Furthermore, it was found that variation of the Young's Modulus caused significant differences to emerge in the model output, while the same impact was not observed after variation of the material density. A separate study by Moreira, Matos, and Oliveira (2017), which used Bayesian updating to reduce statistical uncertainty in measured bridge properties, similarly identified that normal distributions offered the best representations for these properties.

Recent sensitivity analysis by Tubaldi et al. (2020) has investigated the material parameters whose uncertainty has the greatest impact on the results of complex analytical modelling. It was found that the results were particularly sensitive to the properties of the soil backfill.

Separately, statistical methods, of various complexities, may be used in the processing of large data sets collected through long-term monitoring. Examples of some of the approaches used to do this are given by Alexakis et al. (2019a; 2019b; 2020; 2021).

---

## **2.5 Assessment of arch bridges**

### **2.5.1 Assessment of damage**

Cracking is the most common form of damage that masonry arch bridges can suffer. Longitudinal separation cracks can appear between the arch and spandrels, where there is a significant difference in relative stiffness. Cracks may also be found in the arch, typically below railway tracks or following the bridge centreline, for bridges that carry two lines of traffic. In some cases, these cracks extend into the piers or abutments. Transverse cracks may appear as well; often these arise close to the top of the rigid backfill, where again there is a change in stiffness. Cracks may also appear on the spandrel walls, at this vertical level.

Bulging of the spandrels or wing walls is common and may be accompanied by cracking. Remedial works may take the form of tie rods through the bridge, when the issue affects the spandrels, or soil anchors for the case of wing walls.

Some degree of damage can often be tolerated without significant impact on the performance of the bridge. As a result, a framework is needed against which damage can be rated. One such procedure was commissioned by UIC, the International Union of Railways (Martin-Caro and Lopez, 2016). Under the UIC framework, the severity of damage dictates the level of assessment which must be performed. If the damage is substantial, then assessment must consider the SLS case.

### **2.5.2 Assessment of arches in their working conditions**

#### **2.5.2.1 Practical guidance for assessment**

Various practical guidance has been compiled to aid asset managers in the assessment of masonry arch bridges. A number of simplifications are used to expedite assessment, although these vary between documents. For instance, the permissance of 2D analyses for skewed bridges by Network Rail (2006) is contrasted by McKibbins et al. (2006) with different approaches taken by other agencies, such as Highways England.

While the complex behaviour of masonry arch bridges is acknowledged in this guidance, it is also noted that the results of any detailed analyses may be sensitive to uncertain material properties. Instead, emphasis is placed on visual inspection, qualitative assessment by experienced engineers, and simplified analysis techniques whose results may be easier to justify. However, such analyses will tend to focus on the collapse of bridges in ULS conditions, rather than directly considering deterioration under SLS loads.

### 2.5.2.2 Assessment under working conditions

Recently a Permissible Limit State has been proposed for use in assessment, as an alternative serviceability limit. This corresponds to the maximum repeatable loading that a masonry arch bridge can sustain without inducing permanent deterioration (Gilbert et al., 2016; Augustus-Nelson et al., 2016).

Laboratory tests on masonry arch bridges with 3 m spans have demonstrated progressive damage, beginning when peak applied loads exceeded 50% of the ultimate failure load; significant loss of stiffness was reported when loads rose above 65% of this ultimate capacity (Augustus-Nelson et al., 2016). Based on this, the PLS load limit could be given as 50% of the ULS load. However, since the test bridges did not have spandrels, these limit loads may well be above the point at which spandrel separation would occur on a previously undamaged bridge. Furthermore, given their 3 m spans, the results may need to be scaled before being applied to larger bridges (see the earlier discussion in section 2.2.1).

Previous guidance includes the proposal in UK highway bridge assessment code BD21 that the maximum SLS load should be half of the calculated failure load at ULS (Highways Agency, 2001), in strong agreement with the more recent PLS proposals. Other tests have also indicated that significant deflections only seem to arise for loads above 50% of the failure load (Carr et al., 2013). Carr et al. propose that SLS failure of masonry arches could be defined as the point at which the first hinge is formed. Since at least four hinges are required to form a mechanism, this should provide a conservative limit.

SLS load rating of masonry arch bridges has also been developed by Boothby; this has since been updated to allow a more sophisticated treatment of the material behaviour (Boothby, 2001; Boothby and Fanning, 2004).

PLS is included in another recently developed assessment framework, the ‘Sustainable Masonry Arch Resistance Technique’, or ‘SMART’ (Melbourne et al., 2013; Melbourne, Wang, and Tomor, 2007). The ‘SMART’ framework aims to classify appropriate assessment procedures for different subsets of masonry arch bridges, based on their typology and current condition, and encourages more onerous cases to be assessed in greater detail. For example, it promotes the use of probabilistic methods to reduce parameter and output uncertainty.

### 2.5.2.3 The persistence of the MEXE method

Another assessment procedure that is still sometimes used to evaluate the capacity of masonry arch bridges is the semi-empirical Military Engineering Experimental Establishment (MEXE) method. This method builds on simplified elastic analyses performed by Pippard (summarised in Pippard, 1948) to produce a tool for rapid assessment of masonry arch bridges. Summaries of its development are given by Heyman (1982) and Gibbons (2014). McKibbins et al. (2006) provide a useful overview of Pippard's key assumptions, which are carried through to the MEXE method.

For many years, the MEXE method has been used as an initial – and, in some cases, the only – assessment stage for masonry arch bridges. An updated version, the modified MEXE method, persists in modern guidance documents (e.g., in Network Rail, 2006). This is despite the emergence of fundamental concerns about the method (Hughes and Blackler, 1997; Harvey, 2005) and known issues regarding its performance for certain categories of masonry arch bridge, such as those with short spans (McKibbins et al, 2006). The opaqueness of the semi-empirical approach means that it is difficult to identify the root causes of uncertainty in its results, even in cases where it is generally believed to be unconservative (Gibbons, 2014).

Furthermore, because the MEXE method can be highly sensitive to modification factors, which allow for the user to employ their 'engineering judgement' of a masonry arch bridge's condition, it is quite possible for two analysts to produce markedly different results for the same bridge. This may be of particular concern if the method is used by an inexperienced engineer. Because of this, the MEXE method should not be recommended for use.

The continued popularity of the MEXE method in spite of these concerns highlights the need for other, more reliable methods of rapid arch bridge assessment. The development of simplified modelling and assessment tools to meet this need will require a strong evidence base for their validation, ideally including monitoring data of the performance of real-world bridges.

## 2.6 Summary

This chapter has presented an overview of the available literature on masonry arch bridge research. Given the size of the field, this is not exhaustive. However, a number of key themes can be identified.

From the discussion of historic bridge construction, it is clear that the significant variation in material properties between and within masonry arch bridges presents a key challenge for meaningful analysis. Further research into and refinement of methods that seek to capture the

realistic distribution of these properties is required. It is possible that these could capitalise on statistical methods such as Bayesian updating, in which case separate methods for capturing detailed, distributed bridge condition data will also be needed.

The complex behaviour of masonry arch bridges involves contributions from various structural components and depends on the detailed bridge condition. Although progress has been made in identifying these contributions through laboratory tests, which are also commonly used as benchmarks in modelling studies, it seems likely that the scale of these model bridges may have some impact on their behaviour. Therefore, it will be important to complement these studies through further, detailed experimental campaigns that monitor real-world masonry arch bridges. Emergent monitoring technologies offer exciting opportunities in this area. Measuring distributed behaviour over the full structural extent is of particular interest.

Fatigue of masonry arch bridges under repeated application of their working loads is a potentially significant concern. Ongoing work seeks to establish rational load limits that will mitigate this issue. It is likely that this work will also benefit from the collection of long-term monitoring data that track any changes in bridge condition under real-world loading.

Appropriate analysis techniques depend on the conditions being studied. Valuable results have been obtained using many different formulations, of varying complexity. In certain limited situations, even linear elastic analyses may be beneficial, although it may be difficult to establish whether a given bridge satisfies these constraints. Experimental data provide an important benchmark for evaluating different analysis techniques; therefore, this is another area in which new sources of detailed, distributed measurements of bridge behaviour may provide a valuable contribution.

In particular, gaps in the current knowledge exist for skewed masonry arch bridges. Despite the existence of rules of thumb for their assessment, and prevalent hypotheses regarding their behaviour, the pool of experimental data describing these bridges is very limited.

In order to meet the practical needs of asset engineers, convenient assessment tools will be required to replace the unreliable MEXE method. Any new approaches should have a defensible theoretical basis and be validated against real-world bridges, to inspire confidence in their use. In addition to simplified assessment tools, there is a growing awareness of the role of Structural Health Monitoring in asset management and it is likely that, in the coming years, this discipline will become increasingly data centric.

Contributions made in this thesis either leverage or are directly concerned with detailed, distributed monitoring of masonry arch bridges. In Chapter 3, FBG data previously gathered by Acikgoz et al. (2018a) are used to evaluate a series of linear elastic models of a masonry arch viaduct, leading to the SLS contributions of various structural components being identified. Following this, in Chapter 4 onwards, a significant monitoring campaign at a single-span skewed masonry arch bridge is presented. A variety of novel implementations of FBGs are outlined; practical considerations of the various monitoring technologies are discussed; and the detailed data are interpreted to reveal new insights into the dynamic behaviour of this skewed bridge.



# Chapter 3

## Comparison of modelling and monitoring for a masonry rail viaduct

Linear elastic finite-element analysis is sometimes used in the assessment of masonry arch bridges under service loads, despite the limitations of this method. Specifically, linear elastic analysis can be sensitive to material properties, geometry, and support settlements, while also allowing the development of tensile stresses that may be unrealistic for masonry structures. However, even though linear elastic methods remain appealing for their simplicity, it is rare to evaluate their output against experimental data.

In this chapter, detailed strain and displacement monitoring data for a masonry arch viaduct are used to evaluate a series of independently developed linear elastic simulations of this structure. Although uncertainties in input parameters mean the magnitude of modelling results cannot be presumed accurate, the simulated response pattern was found to agree reasonably well with monitoring data in regions of low damage. However, more damaged regions produced a markedly different local response. Comparisons between the simulations revealed useful conclusions regarding common modelling assumptions, namely the importance of modelling backing material, spandrels, and foundation stiffness, to capture their influence on the arch response.

### 3.1 Introduction

#### 3.1.1 Choice of modelling approach

The choice of analysis type should be informed by the fundamental behaviour of masonry structures and, in particular, by both the current damage state of the structure under consideration and the magnitude of its loading with respect to the ultimate collapse load. For

example, although limit state techniques are well established and allow for good understanding of the collapse behaviour of masonry structures, they cannot provide information on the response under low magnitude working loads.

Masonry gravity structures tend to have significant dead loads, leading to compressive stresses. This is before the application of their live loads, which may themselves elicit either compressive or tensile stresses. This compressive baseline due to dead loads allows for the safe operation of masonry structures because, even after live loads are applied, resultant stresses should remain compressive. Furthermore, as long as these loads are not too high in magnitude, stress-strain behaviour may be assumed to be linear elastic.

However, there are several factors that can cause damage and affect the baseline stress, meaning that any estimate of this baseline is highly uncertain. This can happen independently of any applied loading. The inherent weakness of historical lime mortars means that minor cracking can easily arise, for example, when centring is struck following the construction of an arch. Cracking such as this does not necessarily mean that the arch is in danger, and the overall behaviour should remain effectively linear elastic even if some minor cracks are present. In the case of large settlements, however, larger cracks may occur in the masonry, which will have an influence on its 'initial' state of stress. This level of damage will have an impact on the subsequent response of the structure to loading.

Detailed analysis of the dynamic response of masonry arch structures with a significant amount of existing damage, such as major cracking, would require the use of complex three-dimensional nonlinear computational models. Numerous examples of complicated finite-element analyses exist in the literature (see section 2.4.1.2). Alternatively, discrete element modelling may be used (see section 2.4.2).

For asset management of masonry arch bridges, it is often impractical to employ these complex procedures. Instead, typical assessments may only address safety at the Ultimate Limit State. ULS conditions can be investigated through a simplified limit state analysis, and the collapse loads related back to working conditions by means of an adequacy factor, but serviceability behaviour is not explicitly considered in this approach. However, because the response under working loads will drive the deterioration of these structures, it is warranted to examine serviceability behaviour directly. Indeed, the concerns of asset managers are often serviceability issues, such as large deflections, progressive cracking, or a lack of transverse load transfer.

When an asset engineer is concerned about the performance of a bridge, they may commission monitoring to gauge the current level of response and to track any changes in behaviour over

time. For example, in the United Kingdom, Network Rail sometimes measures vertical deflections at the arch crown under the action of train loads. In these cases, it would be useful to know typical values for arch crown deflections for a given linear elastic bridge as a point of comparison. The influence of previous and emerging damage on the bridge can then be observed by comparing monitoring data to simulations.

### 3.1.2 Scope of study

In this study, the severity of the case study viaduct's current condition was investigated by comparing the true, monitored response of the 'as-is' viaduct against a simulated pre-damage response corresponding to its original linear elastic behaviour, produced using FE models of the undamaged 'as-built' viaduct. The structure under consideration is the Marsh Lane viaduct, located in Leeds, UK. Monitoring data had previously been gathered that illuminated its structural response under operational loads (Acikgoz et al., 2018a).

This study is concerned with the evaluation of FE simulations with respect to the monitoring data, rather than interpretation of the monitoring data themselves. Specifically, linear elastic FE modelling results are compared to monitoring data in order to evaluate:

1. The extent to which the real behaviour deviates (both in displacement and strain distribution) from an undamaged elastic response. It is hypothesized that these deviations represent nonlinearities that could indicate the extent and location of damage to the viaduct.
2. The relative importance of modelling each structural component (such as spandrel walls, backing material between the arch haunches, and relieving arches in the piers). This is evaluated by comparing FE models with different levels of complexity against one another, as well as against monitoring results. From this, conclusions are drawn regarding the importance of common modelling assumptions for masonry arch bridges.

Other researchers have investigated the relative importance of these structural components experimentally for the ULS case and suggested percentage increases of the ULS capacity that result from the inclusion of features such as fully connected spandrel walls and the arch-backfill interaction (Boothby et al., 1998; Fanning et al., 2001; Brencich, Cassini, and Pera, 2016). However, this computational study focuses on SLS conditions.

## **3.2 Background: the Marsh Lane viaduct**

### **3.2.1 Overview of the viaduct**

In previous research, the service response of the Marsh Lane viaduct has been monitored by Acikgoz et al. (2018a). The viaduct dates from the 1860s and has a total of 93 arch spans. Arches 37 and 38 are the two considered in detail in this study because they show the most damage and so were the focus of the monitoring installation. The location of these arches is shown in Figure 3.1, which is adapted from a Network Rail map (Network Rail, 2013).

All main components of the superstructure are built using the conventional brickwork and weak lime mortar of the time. The only exceptions are the skewbacks, which consist of stone blockwork, and the internal backing above the piers. The composition of the backing is not known but is believed to be either concrete or rubble masonry. Above this lies the soil backfill and ballast supporting the rails. Drawings of the substructure do not exist; however, taking account of typical construction details for the period, the most likely case is concrete strip foundations underneath each pier.

The viaduct – shown in Figure 3.2, with key dimensions given in Figure 3.3 – shows signs of deterioration from its long working life, which has given rise to visible deflections under live load. Prior to monitoring, Network Rail commissioned repair work to address this damage; this included the fitting of tie bars through the spandrel walls and the filling in of the relieving arches with concrete. These repairs aimed to arrest development of significant existing cracks in the arch soffits, primarily located near the arch haunches but in some cases extending toward the arch crown. This latest intervention seems to have had a positive impact because the rate of propagation of cracks close to the arch haunches has since declined. This has been noted in recent inspections of the bridge and, more recently, has been confirmed through Acoustic Emission monitoring (Alexakis et al., 2019b). However, deflections remained visible following these interventions, and so monitoring was conducted in order to understand the key drivers of this behaviour.

Figure removed for copyright reasons. Copyright holder is Network Rail.

*Figure 3.1: Map view showing the location of Arches 37 and 38 of the Marsh Lane viaduct (adapted from Network Rail, 2013)*

Figure 3.4 indicates the key damage affecting Arches 37 and 38 on either side of their shared pier. Pronounced longitudinal cracks spring from just above the pier relieving arches and extend up to the third points of the arch spans. Transverse cracks are also present and consistently occur close to the tops of the arch haunches, at a vertical level corresponding to the height of internal rigid backing. Further longitudinal cracking is found on the soffits along the interfaces between the arch barrels and the spandrel walls, and this is supplemented by horizontal cracking on the spandrel walls themselves. Finally, it is worth noting that hammer tapping on the arch soffit did not indicate appreciable ring separation. The detailed damage at the Marsh Lane viaduct is documented in Acikgoz et al. (2018a) and has been studied in detail through comprehensive laser scanning, which suggests that settlement of the pier between Arches 37 and 38 could explain the increased severity of the damage affecting these arch spans (Ye et al., 2018).



Figure 3.2: View of the Marsh Lane viaduct (taken by Matthew DeJong)

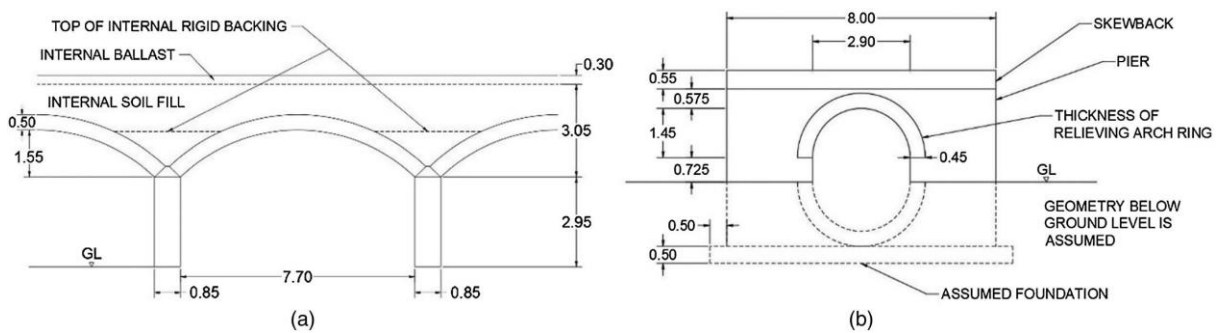


Figure 3.3: (a) Main span elevation of the Marsh Lane viaduct; and (b) typical pier geometry as viewed along the global longitudinal direction (with key dimensions in metres)

---

### 3.2.2 Monitoring data

Details of the monitoring scheme were presented by Acikgoz et al. (2018a) and will only be summarised briefly here. The installation used FBG sensors, embedded in fibre-optic cables, to measure in-plane strains at various locations on the arch soffit and piers of the two adjacent spans of Arches 37 and 38, whereas digital image correlation with commercial video cameras was used to capture displacements and rigid body rotations (Acikgoz, DeJong, and Soga, 2018b).

FBGs measured strain along two longitudinal lines on each monitored arch barrel; the lines were positioned to lie directly underneath the centrelines of the two railway tracks. Each line recorded data at eight locations, labelled S1–S8 and distributed symmetrically across the arch intrados, in addition to the pier-to-pier span opening. Separate FBGs measured transverse strains in the arch barrel, as well as pier strains.

The locations of the longitudinal FBG monitoring lines, which are of most relevance to this study, are indicated in Figure 3.5. This figure shows the monitoring locations on the arch soffits as viewed from ground level. The notation in this study is such that as the train passes over each barrel, S1 is the first FBG that the leading axle passes above and S8 is the last, irrespective of the direction in which the train is traveling. The approximate locations of the rail tracks are also shown in Figure 3.5, with dotted lines.

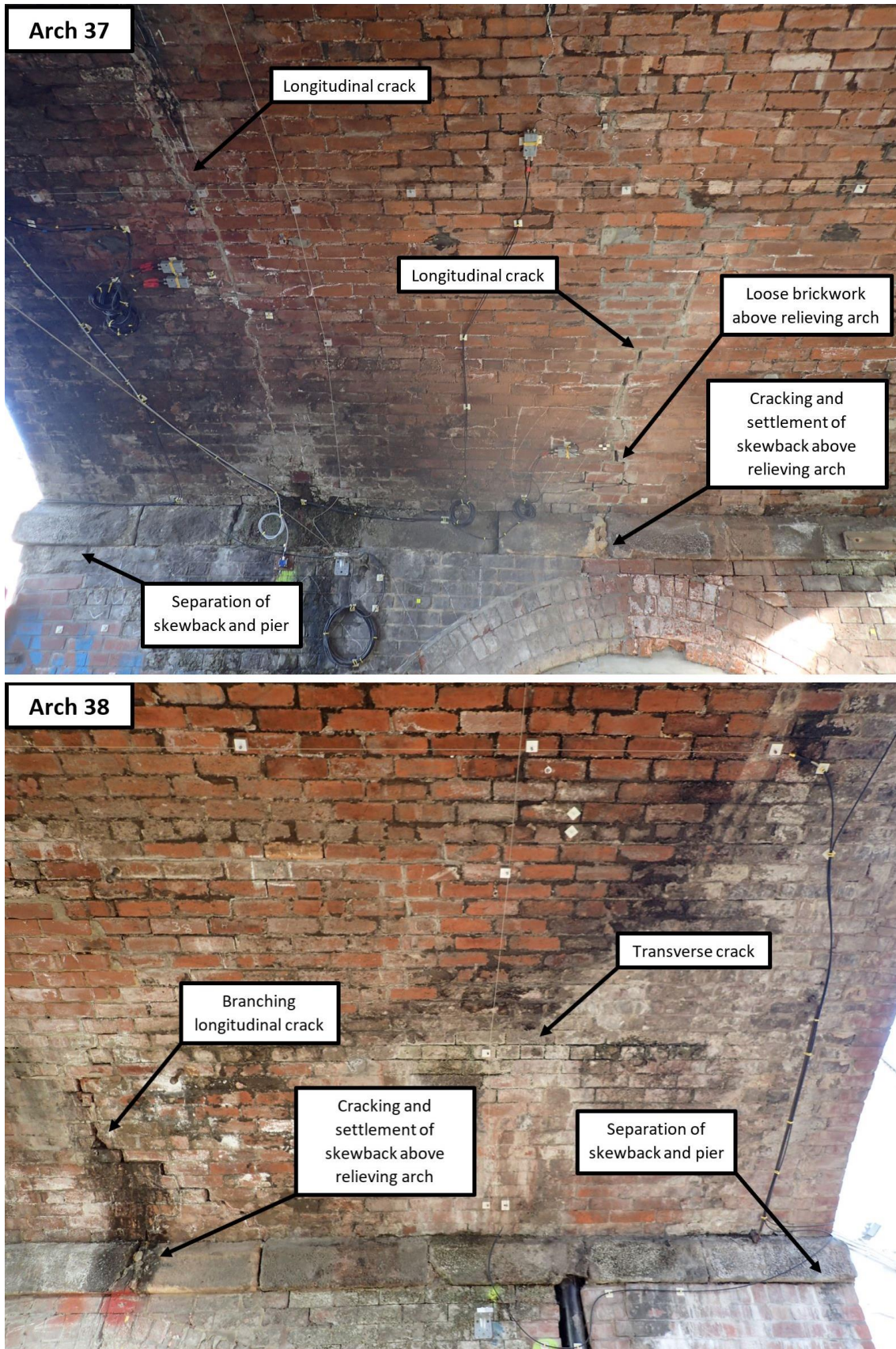


Figure 3.4: Overview of key damage affecting Arches 37 and 38 of the Marsh Lane viaduct

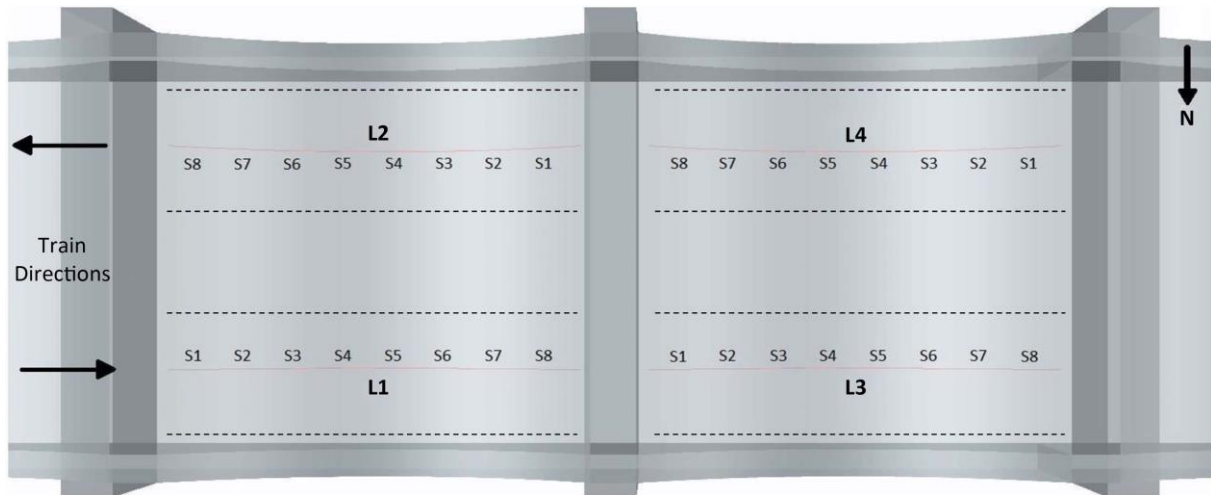


Figure 3.5: Locations of FBGs, labelled S1–S8, along the four longitudinal monitoring lines L1–L4

### 3.2.3 Data used in this study

From the monitoring data, two representative data sets were chosen for use in this study. These captured the response of the viaduct under a three-carriage Class 185 train, traveling east in one data set and west in the other. This allowed investigation of the responses of both halves of the viaduct, which were expected to be similar. Class 185 trains were the most common loading experienced by the viaduct; furthermore, their long wheelbase of 16 m, which is the distance between the bogie centres of each carriage, is approximately twice the span length of the viaduct arches and therefore caused the most significant span opening response. These dynamic loads, as the trains travelled over the viaduct, were found to result in a pseudo-static response that was repeatable with little variation between trains, suggesting only minor variation in live loads due to different passenger levels (Acikgoz et al., 2018a; 2018b). Typical axle loads for Class 185 trains were applied in the models: 32.2 t for the leading bogie of each carriage and 34.4 t for the rear bogie.

Comparisons between monitoring data and finite-element simulations were made for the span-to-span opening displacement, crown vertical displacement, crown in-plane strain, and barrel in-plane strains at Points S1–S8. The in-plane strains offered the most insight into the overall mode of deformation of the arches and the variation of this mode between current real behaviour and the ‘pre-damage’ FE models.

An example of the monitored span opening response is shown in Figure 3.6. Here, responses from all four longitudinal monitoring lines are shown, both for the case where trains are passing directly overhead (Figure 3.6, top row), as well as the response that is measured when trains pass on the other track (Figure 3.6, bottom row). The response is considerably larger for northern monitoring lines L1 and L3, where significant damage is concentrated. In these signals, peaks correspond to span opening, which occurs when axle loads are applied directly above the span; meanwhile, troughs correspond to span contraction, which occurs when the train is positioned such that axle loads are only applied to the adjacent spans either side of the arch under consideration. This interaction effect between adjacent spans is visualized later in Figure 3.8; however, spans that are further away are found to have a negligible impact. Here, and in later figures,  $\Delta\text{WP} - \text{EP}$  is used to denote pier-to-pier span opening and is measured by a single FBG that is clamped between the tops of the two piers.  $\tau$  is a normalised time, determined by identifying the two largest peaks of the response, which correspond to the leading and rear bogies of the train, and then equalizing the time between these peaks. This allows the evaluation of multiple data sets, from trains with different speeds, within the same plot.

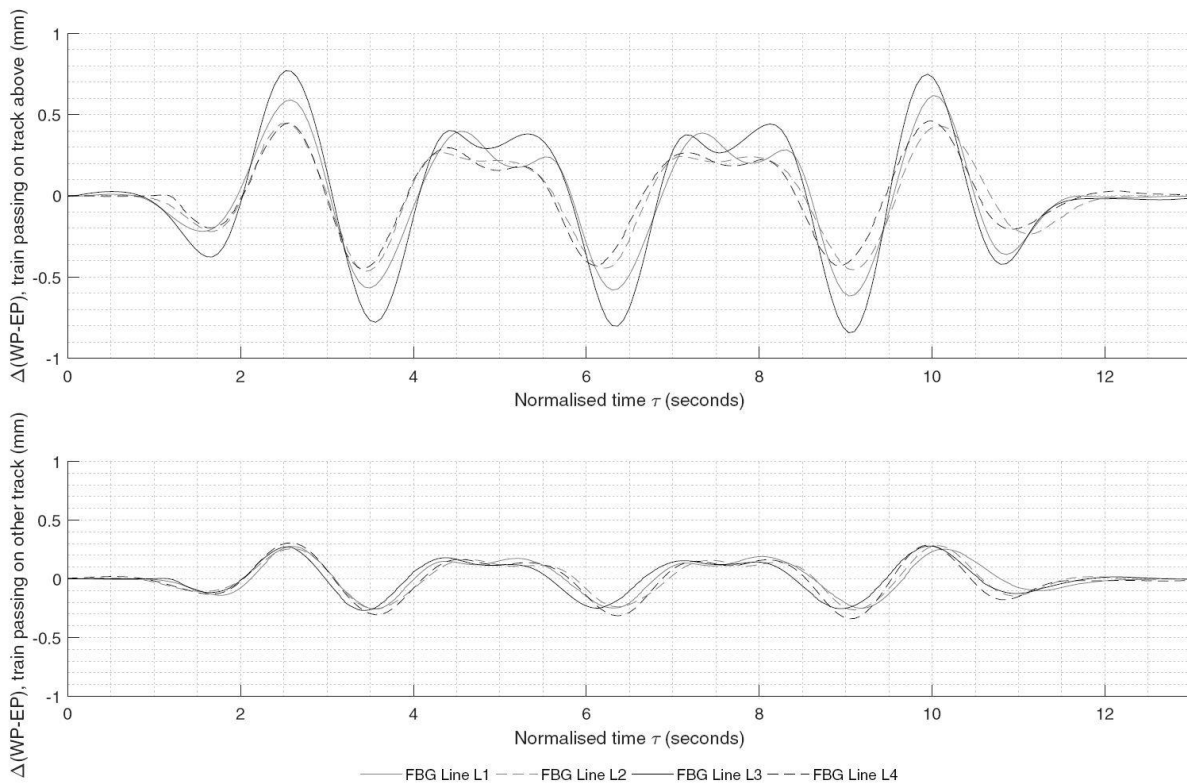


*Figure 3.6: Typical span-to-span opening as measured by FBG sensors at the Marsh Lane viaduct, for the cases when (top) trains are passing on the track directly above the FBG sensors; and when (bottom) trains are passing on the opposite track*

### 3.3 Methodology: finite-element modelling

#### 3.3.1 Overview

A series of FE models of the viaduct were built using Abaqus FEA software, each including progressively more structural detail for the superstructure of the viaduct. This allowed the relative stiffness contributions of each major structural component to be assessed. These models are shown in Figure 3.7:

1. A basic model of the piers and arches.
2. Model 1 with spandrel walls added.
3. Model 2 with rigid backing modelled up to the underside of the soil fill.
4. Model 3 with relieving arches added to the piers.

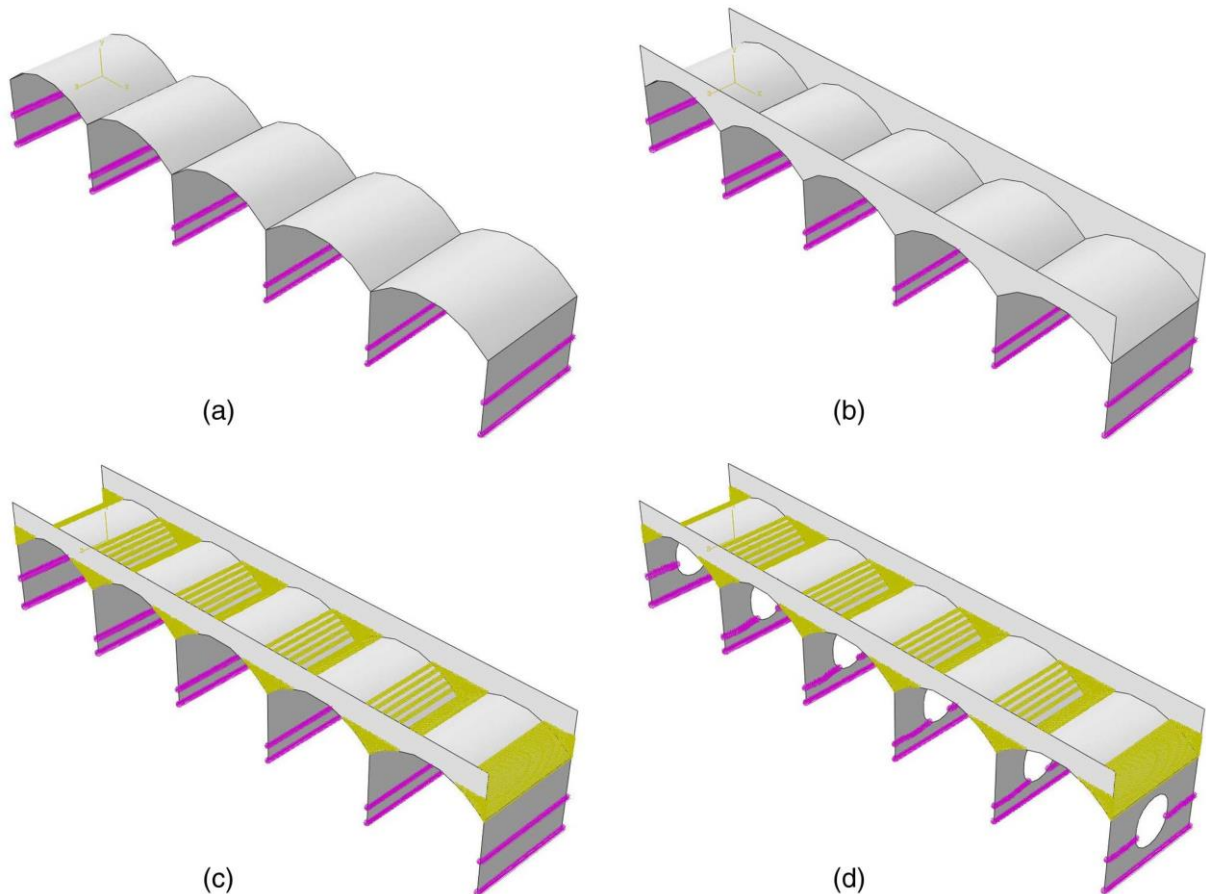


Figure 3.7: Views of the four FE models: (a) Model 1; (b) Model 2; (c) Model 3; and (d) Model 4

In Model 1, the dead loads of the spandrel walls and backing material have been applied to the arches but these components are not explicitly modelled. In this way, the arches respond independently to the applied loads, as might be expected for a heavily damaged viaduct that has lost continuity between these components as a result of significant cracking. The exclusion of spandrel walls and backing from models of damaged arch bridges is not unusual as a simplifying assumption. However, this may lead to an overestimation of the SLS response.

In Models 2 and 3, these structural components have been explicitly modelled and assumed to have full connectivity with the arches. In this way, the overestimation of response may be avoided. However, the assumption of full connectivity is not realistic for damaged viaducts, which typically exhibit some degree of separation cracking between these structural components. Based on typical construction details for the time, it was assumed that the backing material above the piers was either concrete or rubble masonry and therefore provided significant stiffness compared to the adjacent soil. Therefore, the backing was modelled indirectly by rigidly tying the arch haunches together across the top of their shared pier.

In FE Model 4, relieving arches in the piers have been included. These had the effect of reducing the stiffness of the piers, which could potentially lead to larger span-to-span opening displacements.

In reality, there is likely to be partial connectivity between the arches and their adjacent structural components. The measured, true response of the bridge has been compared with the limiting cases of these simplified models to see which, if any, is most representative.

In each of these models, homogeneous continuum shell elements (types S3R and S4R) were used to represent the masonry. Five integration points were specified across the thickness of each element. Surface strains were extracted from the extreme integration point at locations of interest on the arch intrados. When rigid ties were included, these were achieved using slave-master node relationships.

Each model consisted of five arch spans. The outer two arches existed purely to apply boundary conditions without influencing the results at the central span, which were compared against monitoring data. Live loads were applied pseudostatically to the central three spans in order to capture the interaction effects of adjacent spans on the central arch.

Dead loads were modelled in an initial analysis step before the application of live loads. These live loads, which in reality are traveling point loads applied by the train axles to the tracks, were modelled directly at the arch extrados in the FE models. Following distribution through the

---

backfill, each axle load becomes spread out into a patch load that acts over a region of the masonry arch. This load is then transferred from the backfill into the arch as a pressure, which acts in the normal direction of the arch. By applying the train loads directly as normal pressures, it was possible to avoid modelling the soil backfill material explicitly in the FE simulations.

Distribution was calculated separately, assuming a half-angle of distribution of  $15^\circ$  through the ballast and  $30^\circ$  through the fill. These values come from Network Rail guidance (Network Rail, 2006). Although this guidance also allows for possible distribution through the sleepers, this has been neglected here. These calculations were repeated for nine distinct locations corresponding to salient points of the span-to-span opening response. The nine analysis steps are shown in Figure 3.8, along with the corresponding locations of axle loads at these times. In particular, there is clear repetition in the span-to-span opening response, which allows these nine analysis steps to describe any Class 185 train with an arbitrary number of carriages.

The three distinct components of the response correspond to bogie locations shown in the three rows of the grid in Figure 3.8. The top row (Steps 1–3) shows the leading bogie of the train, which produces the peak span opening at the start of the response; by reversing the order of these analysis steps, they can also represent the rear bogie of the train, which produces a similarly large span opening displacement at the end of the response. The remaining analysis steps correspond to points at which there is interaction between two bogies. The second row (Points 4–6) represents the case when the leading and rear bogies of an individual carriage are applied to the two spans either side of the arch under consideration, resulting in span closing. In the third row, the rear bogie of one carriage interacts with the leading bogie of the carriage behind it, giving rise to the characteristic double peak described by Points 7–9.

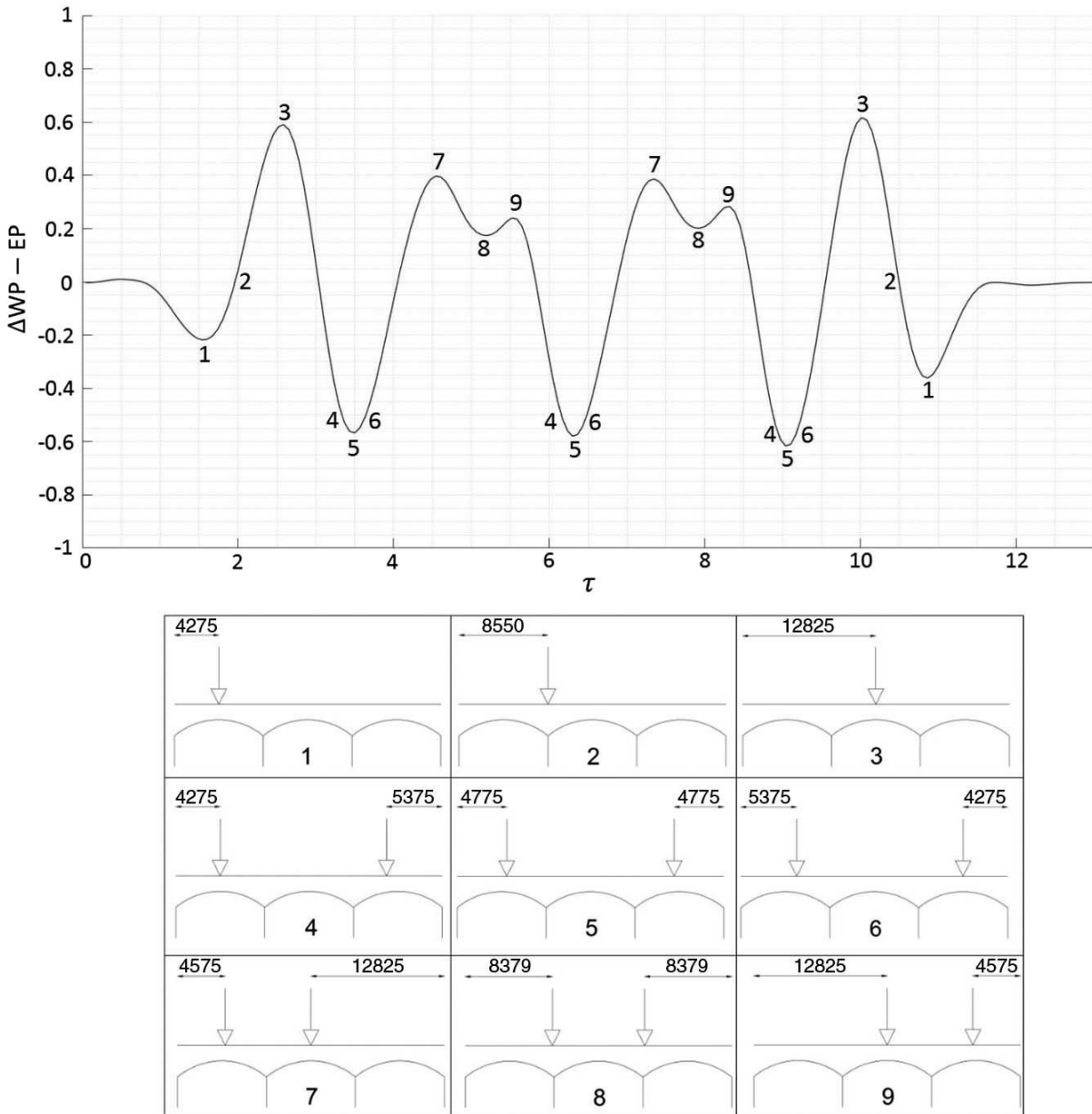


Figure 3.8: Nine analysis steps used in the finite element calculations, plotted on a smoothed pier-to-pier response, with corresponding axle locations given below (with dimensions in millimetres).

### 3.3.2 Assumed input parameters

It was not possible to perform in-situ material testing at the Marsh Lane viaduct, so input parameters had to be estimated. This is often the case when a masonry arch bridge is to be modelled, and as a result there can be high uncertainty in the output of any computational simulation. The following assumptions for this study were arrived at by investigating the likely

values and comparing them primarily to the  $\Delta WP - EP$  signal. Later, the simulation data were compared to other signals, which were not involved in the calibration of the model.

Likely values of the Young's modulus and density of masonry were taken from the literature (Eucentre, 1987; Augenti et al., 2012). Upper values from the most probable ranges were specified, representing the maximum possible stiffness that a simplified linear elastic model could offer.

The soil springs were calculated using the empirically fitted Wolf's equations for embedded foundations (Wolf, 1994). These are summarised in Equations (3.1) to (3.3) below.

$$K_r = \frac{G_{soil}b^3}{1-\nu_{soil}} \left[ 3.73 \left( \frac{l}{b} \right)^{2.4} + 0.27 \right] \left[ 1 + \frac{e}{b} + \frac{1.6}{0.35 + \left( \frac{l}{b} \right)^4} \left( \frac{e}{b} \right)^2 \right] \quad (3.1)$$

$$K_h = \frac{G_{soil}b}{2-\nu_{soil}} \left[ 6.8 \left( \frac{l}{b} \right)^{0.65} + 2.4 \right] \left[ 1 + \left( 0.33 + \frac{1.34}{1 + \frac{l}{b}} \right) \left( \frac{e}{b} \right)^{0.8} \right] \quad (3.2)$$

$$K_v = \frac{G_{soil}b}{2-\nu_{soil}} \left[ 3.1 \left( \frac{l}{b} \right)^{0.75} + 1.6 \right] \left[ 1 + \left( 0.25 + \frac{0.25b}{l} \right) \left( \frac{e}{b} \right)^{0.8} \right] \quad (3.3)$$

To express these equations in terms of the soil Young's modulus, the Shear modulus  $G_{soil}$  can be substituted as follows.

$$G_{soil} = \frac{E_{soil}}{2(1+\nu_{soil})} \quad (3.4)$$

In these equations,  $2b$  is the foundation's length and  $2l$  is its width. Rotation is assumed to occur about the 'length' axis. The embedment from ground level to the underside of the foundation is denoted by  $e$ . The values  $E_{soil}$  and  $\nu_{soil}$  are the Young's modulus and Poisson's ratio for the soil, respectively.

The vertical soil spring  $K_v$ , originally calculated using Equation (3.3), was recalibrated based on observations of vertical pier deflection under load. It was found that Wolf's equations under-predicted this stiffness. Unfortunately, there was no available information against which the other two soil springs could be recalibrated; therefore, the original values resulting from Wolf's equations were kept in these cases. It is recognised that these may also be underestimates of the true spring stiffnesses.

For the Marsh Lane viaduct, the assumed geometry below ground level is as shown in Figure 3.3(b). The foundation dimensions and embedment were estimated based on guidance from Network Rail. The foundations were taken to be 0.5-m-deep concrete strips that extended

beyond the plan dimensions of the piers by 0.5 m in all directions. The embedment was found by assuming that inverse relieving arches existed immediately below ground level, giving an overall embedment of 2.4 m below ground level.

Table 3.1 summarises the values of input parameters that were ultimately used. For the soil springs, Table 3.1 presents individual stiffness values that describe the global response of each embedded pier; this is the form that is yielded by Wolf's equations. However, in the FE models, these are then distributed over a row of springs, one at each node along the length of the pier.

*Table 3.1: Assumed values of input parameters used in the finite element simulations*

<b>Parameter:</b>	<b>Assumed Value:</b>
Young's Modulus of masonry, $E_{masonry}$	5 GPa
Poisson's ratio of masonry, $\nu_{masonry}$	0.2
Density of masonry, $\rho_{masonry}$	1600 kg/m <sup>3</sup>
Young's Modulus of soil, $E_{soil}$	250 kPa
Poisson's ratio of soil, $\nu_{soil}$	0.3
Soil vertical spring $K_v$	984x10 <sup>6</sup> N/m
Soil horizontal spring $K_h$	2.30x10 <sup>6</sup> N/m
Soil rotational spring $K_r$	12.5x10 <sup>6</sup> Nm

### 3.3.3 Boundary conditions

The model was restrained against longitudinal and vertical translation at the outer two arch barrels, along their furthestmost springing lines. The outer edges of the spandrel walls were also restrained against longitudinal translation, as well as against rotation about the global vertical axis. These conditions represent the restraint provided by the rest of the viaduct superstructure and are illustrated in Figure 3.9. No site investigations into the foundations and soil conditions exist at the Marsh Lane viaduct, beyond a qualitative assessment which rated the soil as a sandy clay. This was used to estimate likely values of its properties (see Table 3.1).

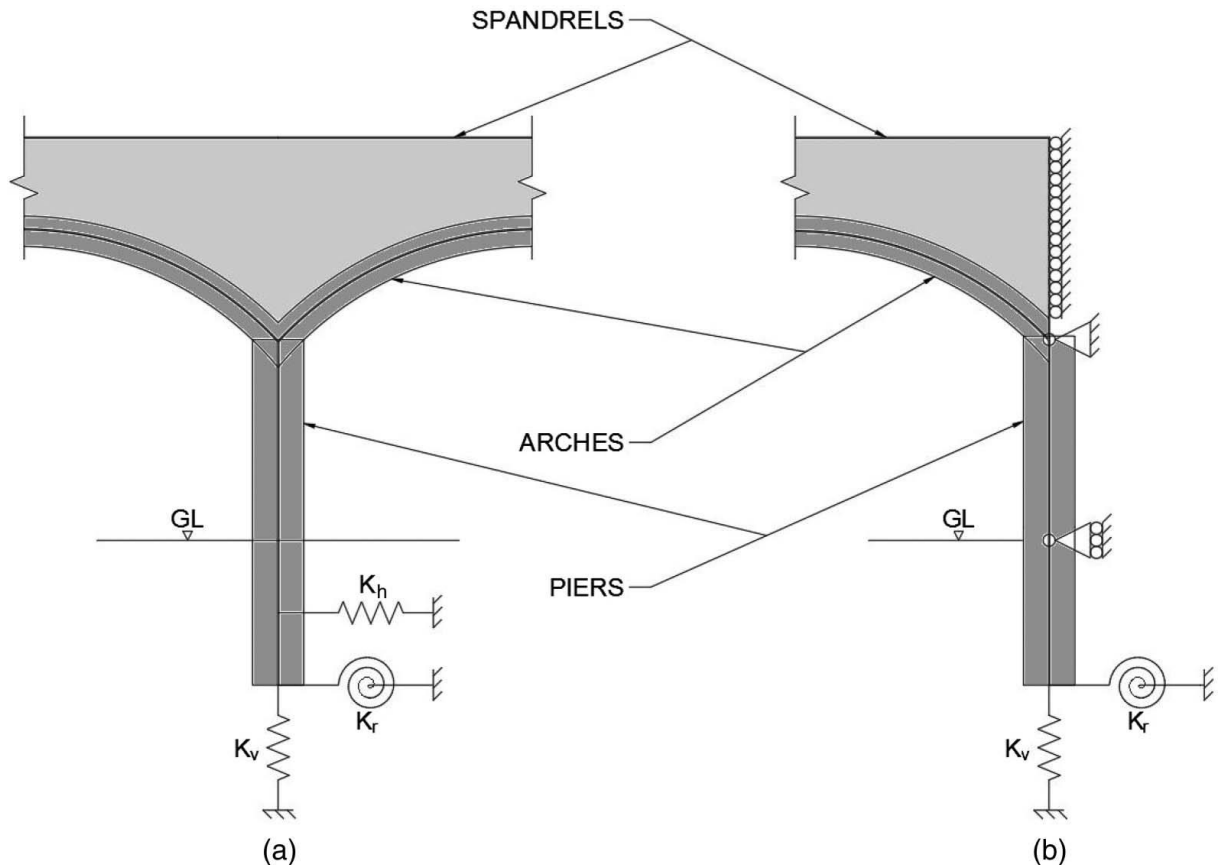


Figure 3.9: Boundary conditions and soil springs, as applied to (a) interior piers; and (b) outer piers in the FE models

The vertical soil springs, of total stiffness  $K_v$ , were distributed along the pier bases. The horizontal springs were distributed along a line of nodes at the mid-depth of the embedded region; these had a combined total stiffness of  $K_h$ . However, on the outer piers, these springs were replaced by ground-level pins, preventing any horizontal movement. These pins, although not physical, were required as a boundary condition to achieve physically acceptable behaviour of the outer piers; because the superstructure was not modelled beyond these piers, they tended to deflect outward unrealistically before the pins were included. Furthermore, all the pier bases were restrained against rotation about the global transverse axis by rotational springs. For each pier, these springs had total stiffness  $K_r$ , but, once again, these were modelled by distributing this stiffness over the length of the pier.

Figure 3.9 illustrates these boundary conditions and soil springs. Additionally, and not shown in Figure 3.9, the pier bases were restrained against rotation about the global vertical and longitudinal axes. Furthermore, the centre points of each pier base were pinned against

translation in the transverse direction. This transverse boundary condition was kept to a single point because it was not desirable to over-constrain the model.

The impact of these boundary conditions was assessed by comparing pier-to-pier deflections over the central span of two model versions, one with five spans and another with seven. The results are shown later in Figure 3.13(b), which compares the span-to-span opening response of two versions of Model 4. The difference in results is negligible. This suggests that, when five spans are modelled, the boundary conditions are already far enough removed from the central span that they do not influence the results. Similar checks yielded the same results for the other three finite element models.

## **3.4 Results**

### **3.4.1 Comparison of monitoring data and modelling results**

Throughout model development, pier-to-pier span opening was used to compare the results of finite element models against the monitored behaviour of the real viaduct. Figure 3.10 shows a typical pier-to-pier response, as measured by FBG sensors, and compares this against results for FE Models 1–4.

Having developed the models against the benchmark of the pier-to-pier response, agreement between the linear elastic FE simulation and the monitoring data was investigated for other parameters. Figure 3.11 compares vertical displacements at the arch crown from FE Model 4 against values that were observed using digital image correlation (Acikgoz et al., 2018b). Similarly, in-plane crown strain is also shown in Figure 3.11; the measured values here were obtained from FBG data. For completeness, the earlier comparison for pier-to-pier span opening is also included. In this figure, the modelling results are compared against monitoring data for all longitudinal lines, denoted L1–L4 as in Figure 3.5.

Figure 3.12 then compares the in-plane barrel strains at FBG monitoring locations S1–S8. Strains from the FE analysis were averaged over the same 1-m gauge lengths that the FBGs used and measured in the same longitudinal planes.

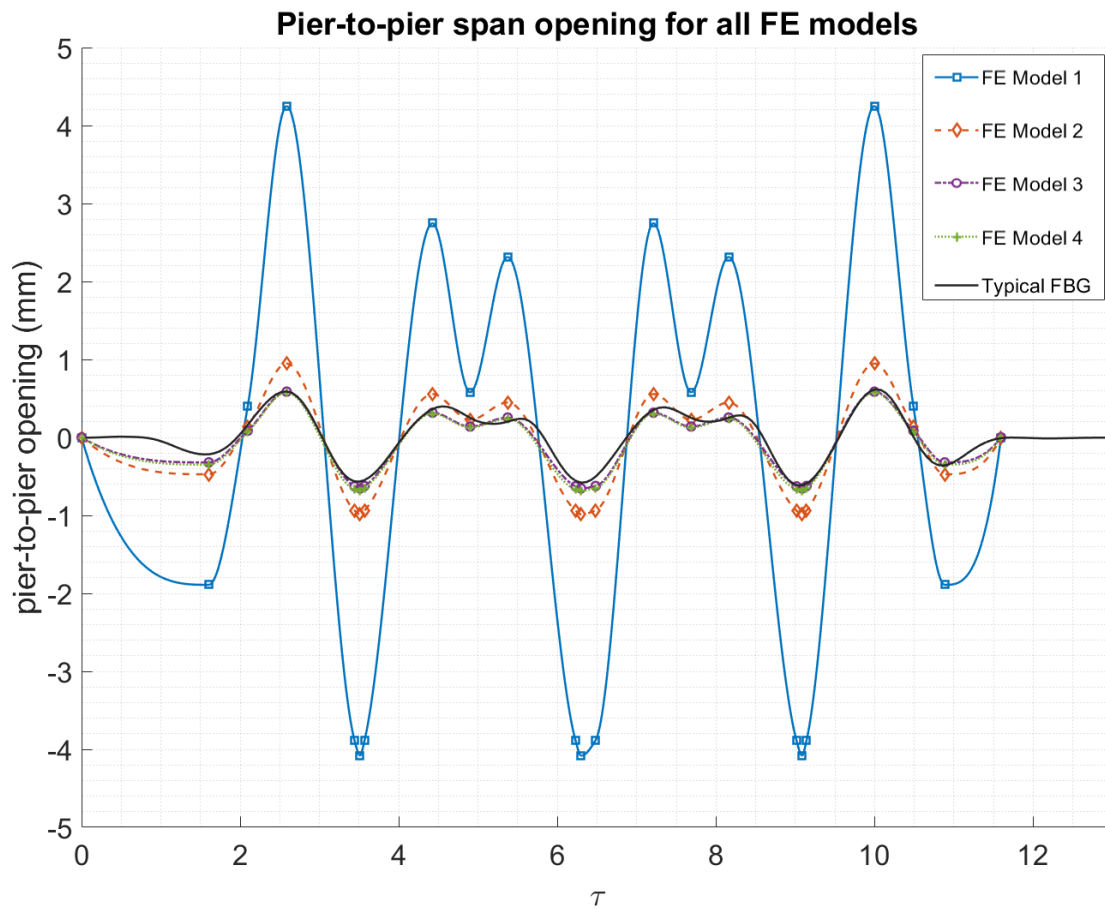


Figure 3.10: Comparison of pier-to-pier span opening between typical FBG data and FE analysis models

### 3.4.2 Contributions of structural components to overall behaviour

Based on the information contained in Figure 3.10, which compared the pier-to-pier response for the four FE models against FBG monitoring data, it is possible to ascertain the relative resistance that was provided by each of the models against pier-to-pier opening.

The final FE model was chosen as a benchmark of 100% resistance because it contained all key structural components; other models were compared against this. Because the linear elastic models will scale equally if different input parameters are used, this comparison between models is independent of the parameters that were used in this case. In effect, this gives the relative contributions of the various structural components to overall serviceability behaviour. These results are given in Table 3.2.

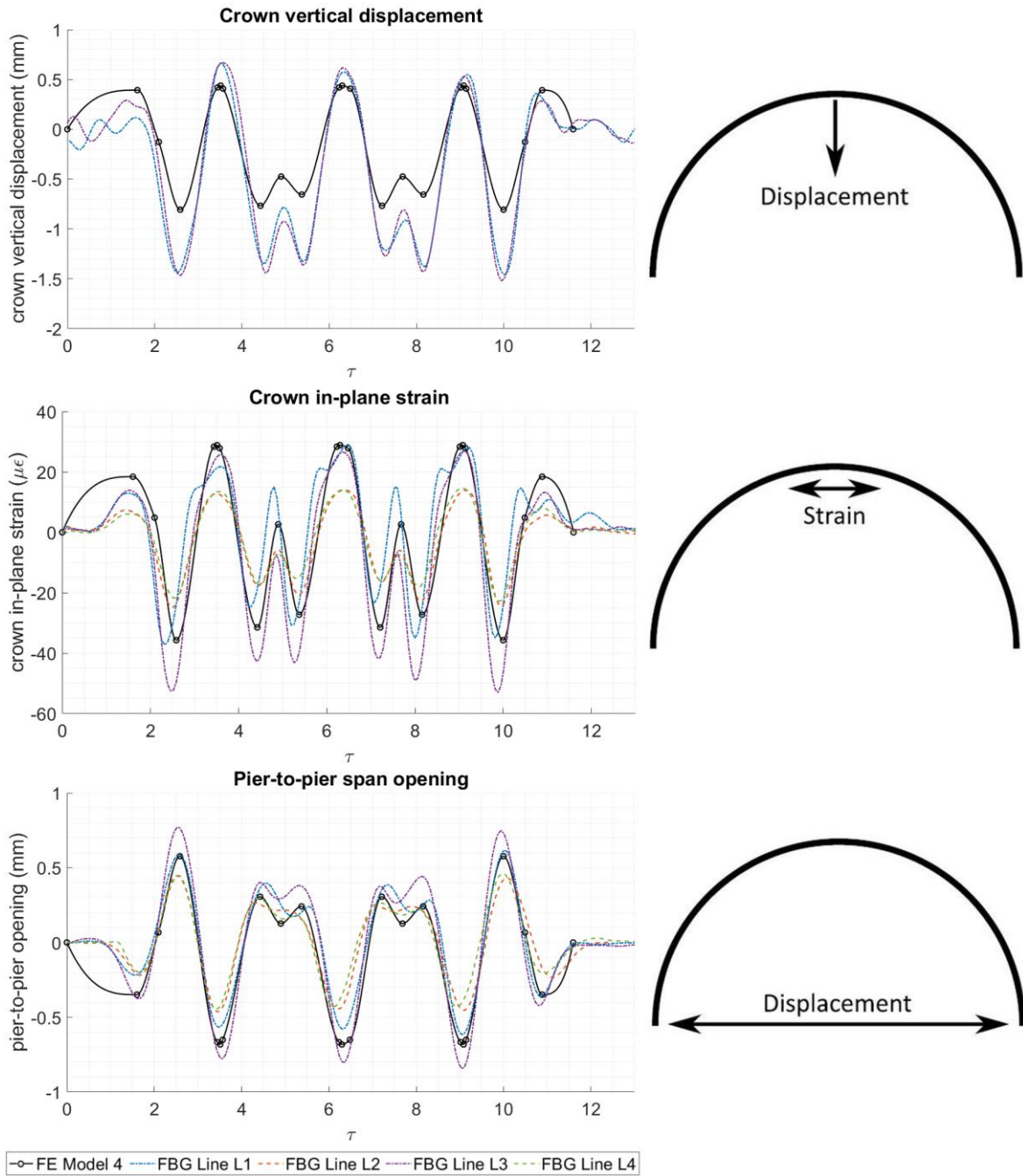


Figure 3.11: Comparison between FE Model 4 and monitoring data for crown vertical displacement, crown in-plane strain, and pier-to-pier span opening

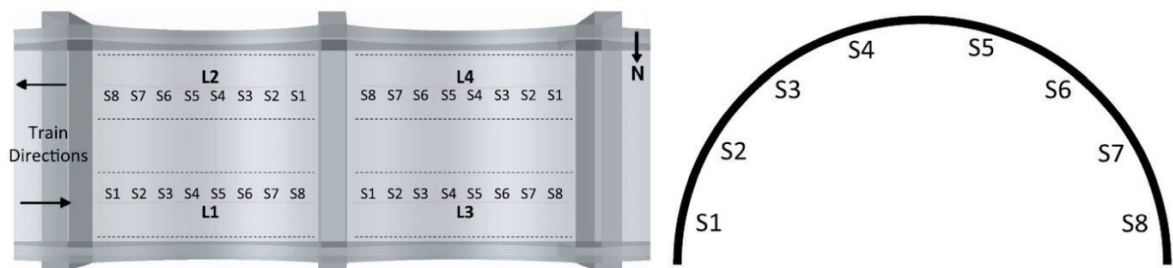
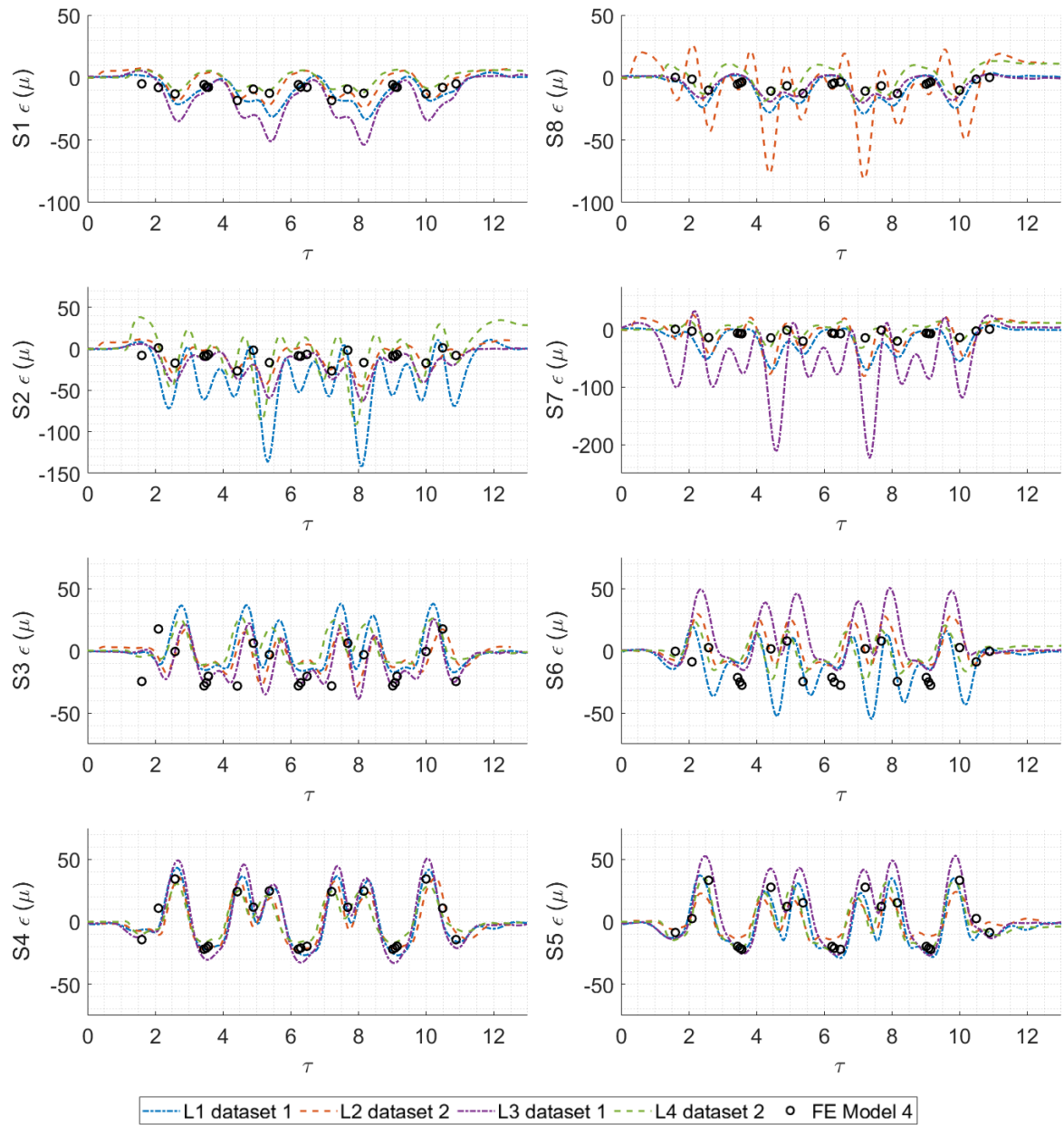


Figure 3.12: Comparison of in-plane barrel strain distributions between FE Model 4 and FBG data; symmetric locations from the two halves of the arch are shown side by side

The final FE model can also be compared against the measured FBG response, as in Table 3.2, which indicates the current resistance provided by the real structure. A reduction in this resistance is seen as a result of the damaged state of the viaduct. However, to obtain the true value of this reduction would require that the FE analysis used precisely correct input parameters, which cannot be confirmed.

Figure 3.13(a) shows the impact that varying the soil spring boundary conditions has on the pier-to-pier span opening response of FE Model 1. In calculating the soil springs, the material properties of soil used were as shown in Table 3.1; these values are based on the description of the soil as a sandy clay. Wolf's equations also require knowledge of the embedment and dimensions of the foundations, which were not known from record drawings and so had to be estimated (see section 3.3.2).

Figure 3.13(b) summarises a check of the remaining boundary conditions, as described earlier. To arrive at this figure, identical boundary conditions were applied to the outermost spans of models containing five and seven arch spans, and the responses of the central spans were then compared to FBG data.

*Table 3.2: Resistance against pier-to-pier span opening deflections, as provided by the various finite element models and the real viaduct*

<b>Model</b>	<b>Model 1</b>	<b>Model 2</b>	<b>Model 3</b>	<b>Model 4</b>	<b>Real Viaduct</b>
Structural elements added in this model	Piers, arches, and soil springs (basic model)	Spandrel walls	Rigid backing above arch haunches	Relieving arches (final model)	---
Contribution to global resistance from additional element(s)	13%	48%	39%	0%	---
Cumulative global resistance to deformation	13%	61%	100%	100%	91%

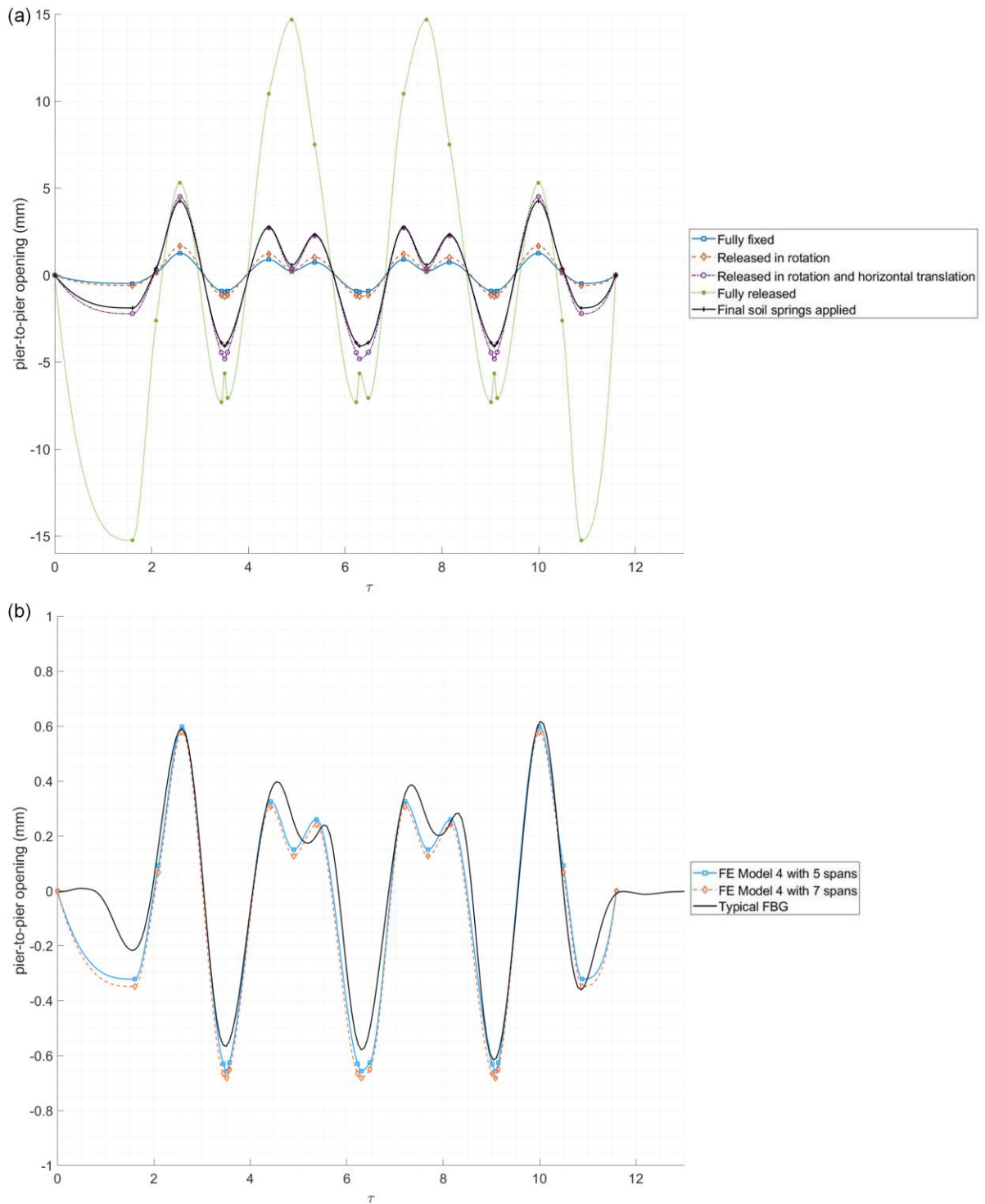


Figure 3.13: (a) Impact of varying soil spring stiffnesses on the pier-to-pier opening response of FE Model 1; and (b) the difference in pier-to-pier opening responses for versions of FE Model 4 containing five and seven spans

## 3.5 Discussion

### 3.5.1 Comparison of monitoring data and modelling results

Given the existing damage to the viaduct, some nonlinearity is unquestionably present in its real behaviour. Furthermore, variation exists between the various monitored spans due to uneven distribution of damage, and so a linear elastic model will agree better with some measurements than others. On top of this, uncertainty in some input parameters for the FE simulations means that comparing magnitudes between FE output and monitoring data is not always informative. However, varying these parameters will only affect the magnitude of the linear elastic results, not their pattern. It is by searching for similarity, or the lack thereof, in the pattern of the response that interesting conclusions can be drawn. Where there is significant difference, this indicates that damage has led to a different mode of response. This can potentially be useful in estimating the regions of critical damage, because these should be the regions in which the largest deviation from the linear elastic mode of response is seen to occur.

First inspection of Figure 3.10 would suggest that the monitored pier-to-pier response at Marsh Lane can be well reproduced in pattern by a linear elastic model that includes sufficient structural detail. Furthermore, both Models 3 and 4 produce responses that are very similar in magnitude to the FBG measurements, whereas Models 1 and 2 are much less stiff, and as a result significantly overpredict the magnitude of displacements. This is important because the linear elastic models are intended to simulate the viaduct before the advent of any significant damage, which would result in a loss of stiffness. Therefore, models that suggest a notably larger magnitude of response than is seen in the FBG data cannot be physically correct.

Because the highest reasonable estimated values of input parameters were used throughout all FE models, it appears that Models 1 and 2 do not include sufficient structural information and that only by including the effects of both spandrel walls and rigid backing can the true scale of the response be emulated. Even if the soil springs were underestimated, the ‘fully fixed’ response of Figure 3.13(a) would not give the necessary decrease in magnitude that is required for Model 1 to produce physically sensible results.

The key remaining uncertainties in the FE models are the masonry Young’s modulus and horizontal and rotational soil springs  $K_h$  and  $K_r$ , which could not be calibrated onsite. The FE models have all used a value of 5 GPa for the masonry Young’s modulus. In general, historic masonry can have a Young’s modulus in the range 1–10 GPa, though it is unlikely for 5 GPa to be exceeded (Augenti et al., 2012). However, the low value of 1 GPa would imply extensive damage. The Italian seismic design code recommends a value of 3.6 GPa for historic masonry

that may be damaged; this is a more likely lower bound (Eucentre, 1987). After factoring in the additional constraint that FE Model 4 must produce a response that is no larger in magnitude than that observed in the monitoring data, the required lower bound increases to roughly 4.6 GPa, which is very close to the 5 GPa that has been used.

The estimated stiffnesses of the soil springs correspond to lower bounds of their likely values. However, the vertical soil spring  $K_v$  was found to increase substantially upon calibration, and it is not unreasonable to assume that the remaining springs  $K_h$  and  $K_r$  have been similarly underestimated. Because the recalibrated vertical spring is comparable to fully fixing the pier bases in vertical translation, this suggests that the true soil conditions could approach the limiting case of fully fixed pier bases.

In Figure 3.10 onward, interpolation between the discrete results from FE analysis is achieved using a shape-preserving piecewise cubic interpolation. This approach was found to best preserve smoothness in the simulated response while minimizing any unphysical oscillation. This allowed for simpler visual comparison of the modelling output and the measured patterns of response, although all numerical comparisons only make use of the point measurements obtained directly from the FE models. However, interpolation has not been carried out for the barrel in-plane strains in Figure 3.12; the patterns of response seen in the FBGs here have changed significantly and there are now different salient points, so that interpolation between the FE analysis steps would no longer be meaningful.

In Figure 3.11, the variation between the monitored response at the four locations, L1–L4, immediately highlights the uneven distribution of damage across the viaduct, which means that the response no longer maintains the symmetry that would be anticipated in an ideal structure. In particular, there is a pronounced difference in response between the north (L1 and L3) and south (L2 and L4) sides of the viaduct; the response on the north side is consistently larger in magnitude, and this corresponds to its higher damage level relative to the south side (Ye et al., 2018). Given this, it makes sense that the FE simulations reliably show greater similarity to monitoring data for the south side, given that they are a closer representation of the less damaged regions of the viaduct.

Figure 3.12 considers the strain distribution over the arch barrel. The clearest disagreement occurs when strain is measured across a transverse crack; this is the case for FBG line L1 at Point S2 and for L3 at Point S7. Line L2 also crosses a transverse crack at Point S8, though this is less severe. Other than this, FE results show a reasonable proximity to monitoring data,

particularly over the central region of the arch and for lines L2 and L4, which measure the response of the less-damaged southern half of the viaduct.

In general, there is less clear similarity in strain response patterns, between the FE simulations and monitoring data, than there was for the parameters examined in Figure 3.11. This is compounded by the fact that analysis Steps 1–9, which were chosen based on the pier-to-pier span opening response, no longer necessarily represent salient points for the strain distribution at all points of the arch. The best similarity in pattern is obtained over the central region of the arch, particularly at Points S4 and S5, where the response is close to the characteristic traces seen in Figure 3.11. However, at points closer to the arch haunches, the response no longer seems to exhibit this form.

Having said this, there is less disagreement when only the response over the southern half of the viaduct is considered. Examining Points S1 and S8, peak strains of  $-10$  to  $-20 \mu\epsilon$  are well matched, though the relaxation when load is removed is not predicted and a transverse crack colours the results for line L2 at Point S8. It is possible that relaxation under the removal of load would be better predicted by a model that accounted for the possibility of a cracked interface between the arch haunches and rigid backing, but this was not possible while working within linear elastic limitations. Likewise, at Points S2 and S7, simulated peak strains of  $-20$  to  $-30 \mu\epsilon$  show reasonable consistency with the least-damaged line, which is L2 for Point S2 and L4 for Point S7.

For brevity, Figure 3.12 only presents strains from Model 4. The strain distributions from Models 1–3 were found, through least-squares error minimization, to have worse agreement in pattern relative to the FBG data. This suggests that Model 4 is the linear elastic simulation that most closely resembles the true distribution of deformation throughout the arch barrel, although that does not mean that Model 4 is correct. What can be said, however, is that this indicates that the true response mode involves some degree of interaction between the arch barrel and both the spandrel walls and rigid backing material. When these interaction effects are not modelled, the corresponding simulated strain pattern deviates further from the true response. Even though it is incorrect for Model 4 to assume full connectivity of these structural components, this has a smaller impact than not modelling them at all.

Furthermore, in order for the strain results from Models 1–3 to approach the monitoring data in magnitude, unrealistically high values of masonry Young's modulus would have to be used in the FE analysis. It is therefore concluded that Model 4 represents the best linear elastic approximation of the real mode of deformation.

Despite the sensitivity of the local strain distribution to damage, which can affect its response pattern, it is noteworthy that the parameters considered in Figure 3.11 show roughly the same pattern even when there is significant difference in the extent of damage between the two halves of the viaduct. However, because the measurement locations of these parameters are not close to the damaged regions of these arches, it is perhaps not surprising that the damage has had little impact on the patterns of these measurements. There is little cracking near the arch crown, where vertical displacement and in-plane strain were monitored, and although there has been significant deterioration of the arch haunches, this was not picked up in the pier-to-pier measurements because these were taken between the skewbacks.

Although these are common measurements for asset engineers to prescribe – and are seen as characteristics that can give an impression of the ‘global’ response of the overall arch – it follows that they may not be the most effective. Interpretation of the magnitudes of these measurements is only meaningful if it can be carried out against a benchmark, which could either be measurements prior to damage or a finite element model with fully accurate input parameters. Because it is frequently impractical to ascertain these parameters, which were shown in this study to significantly affect the output of FE simulations, measurement of ‘global’ arch characteristics such as these will often remain opaque until their repetition allows for the tracking of changes.

However, if the monitoring location were to be revised to a point where damage is more commonly seen in masonry arch bridges, then the pattern of the measured response, as well as the magnitude, could offer some useful information about the severity of any nonlinearities. Because damage is often seen on the arch intrados close to the vertical level of rigid backing, due to the sudden step change in stiffness at this level, potential contenders for future ‘single point’ monitoring could well be the third or quarter point of the span, as opposed to the arch crown. In particular, strain measurements at these locations are likely to be illuminating and warrant investigation in future work.

### **3.5.2 Contributions of structural components to overall behaviour**

The contributions to global resistance against deformation under serviceability loads are shown in Table 3.2 for the various structural components. Often, simplifying assumptions will be made during analysis of masonry arch bridges and viaducts. For example, an ‘effective width’ model may neglect the positive effects of the spandrel walls. Table 3.2 shows the size of the contribution that would be neglected in this case if such a calculation were to be performed under serviceability conditions. Likewise, the presence of rigid backing material above the arch

haunches provides a further stabilizing effect that increases the global resistance of the structure to deformation.

The values of Table 3.2 are in rough agreement with other results in the literature, which give corresponding ULS predictions of contributions from these components (Boothby et al., 1998; Fanning et al., 2001; Brencich, Cassini, and Pera, 2016). One point in particular is worth noting: the contribution of spandrel walls is higher under service conditions than it seems to be at ULS. When a multi-span masonry arch bridge is at its ultimate capacity, Fanning et al. (2001) suggested that a contribution toward this capacity of 30% comes from the spandrel walls. The results of this study suggest that the contribution of spandrel walls is 48% in serviceability conditions, a significant increase. In all likelihood, this is because partial spandrel wall separation can be expected to occur before the ultimate capacity is reached, so that, by this point, the effectiveness of the spandrel walls will have been reduced.

Another interesting observation is that the inclusion of relieving arches in Model 4 does not lead to a more flexible response, despite the reduction in pier stiffness that this results in. Instead, it can be concluded that the response is more sensitive to the stiffness of the spandrel walls and rigid backing. A marginal reduction in pier stiffness has a negligible impact because the piers already offer little resistance against flexural deformation.

Figure 3.13(a) summarises the work that was done to investigate parameter variation in the uncertain soil springs. For very soft springs in all degrees of freedom, the pattern of span opening is no longer properly replicated. There is, therefore, a minimum amount of restraint which must be applied to the pier bases before the modelled behaviour will capture the true span-to-span response of the real viaduct. Additionally, springs of this softness are unlikely to be realistic because these would be far softer than the stiffnesses suggested by Wolf's equations.

The response under the applied soil springs was very similar to that obtained by releasing the pier bases in rotation and horizontal translation. In other words, the recalibrated vertical soil springs, in combination with horizontal and rotational springs calculated using Wolf's equations, produced a very similar outcome to simply fixing the pier bases in vertical translation alone. This is perhaps not surprising, given that the recalibrated vertical springs were considerably stiffer than their horizontal and rotational counterparts. The most likely implication is that the qualitative ground investigations underestimated the soil conditions or that the assumed embedment was underpredicted. However, in the absence of more definite information, it was decided to continue using the current estimates because these at least constitute a safe lower bound on the true conditions.

It can also be concluded that the overall response is reasonably insensitive to pier rotational springs because releasing the pier bases in rotation causes only a small change compared to pier bases that are fully fixed. This also indicates that the pier-to-pier span opening is insensitive to the precise mode of response of the piers, which must behave in double curvature bending when their bases are fully fixed but will freely rotate as rigid bodies once this degree of freedom is released. This is most likely a consequence of the pier height, which is very large compared to the movements imposed on the piers by span opening and closing.

However, even if the true soil stiffnesses approached the ‘fully fixed’ upper bound, this could at most cause a fourfold increase in the global resistance to pier-to-pier span opening. Meanwhile, Model 1 has seven times less global resistance to this response than is observed in the FBG data. As a result, despite the spandrel separation cracks that are present on the Marsh Lane viaduct, which may well also extend across the arch-backing interface, it is impossible to achieve the observed structural resistance to deformation without including some effect from either or both the backing and spandrel walls.

Figure 3.13(b) examines the impact of the boundary conditions that were enforced on the outer spans of the FE simulations. These boundary conditions themselves are artificial but were implemented to account for the continuity of the viaduct beyond the modelled spans. Results were only extracted for the central span of the model, so it is necessary that this span be sufficiently removed from the outer boundary conditions. In the figure, a comparison is made between models containing five and seven spans. The responses show negligible difference, so it can be concluded that, in both models, these boundary conditions were sufficiently remote from the central span that they did not influence the results in this region of interest. Although Figure 3.13(b) considers FE Model 4, similar results were achieved when earlier models were investigated in the same way. As a result, it was decided to consider only five spans in the FE models because this reduced computation time.

### **3.5.3 Further comments on the finite element simulations**

Based on these findings, FE Model 4 appears to offer the closest approximation of real behaviour that can be achieved using a linear elastic model. However, it also assumes full connectivity of the various structural components, which may not be realistic and warrants further discussion.

The assumption of full connectivity can be investigated by examining stresses at the arch-spandrel interface. At the lower edges of the spandrel walls, these are in the range +0.25 to -1 MPa; negligible tensile strength means that this is sufficient to cause separation cracks between

the arch and spandrels. Such cracks are observed at the viaduct. It is not possible to investigate any radial tensile stresses within the arch at the arch-backing interface because the backing has not been explicitly modelled and the arch is composed of shell elements, with the corresponding assumption that stresses in the radial – that is, the out-of-plane – direction are zero.

Although there is no visible evidence of inter-ring shear failure at the Marsh Lane viaduct, and the presence of interlocking header bonds should increase shear resistance and mitigate the possibility of inter-ring shear cracking, this can be further investigated in the output of FE Model 4. In this model, there was not much variation of shear stress over the depth of the arch, which is four brick rings in thickness. For the majority of the arch, extreme shear stresses were in the range  $\pm 0.2$  MPa, with linear variation of shear stress over the depth of the arch. However, close to the spandrel walls, this range increased to  $\pm 0.3$  MPa.

The Italian code for historic masonry suggests a maximum value of shear resistance of 0.18 MPa for full brickwork with lime mortar (Eucentre, 1987). It therefore follows that typical values of extreme shear stress are at the limit that can be resisted by historic masonry brickwork and exceed this limit close to the spandrel walls so that separation of the arches from the spandrels might be expected. However, at the inter-ring interfaces over the arch depth, shear stresses are consistently below this limit. This aligns with the visible evidence on site, where there is cracking between the arch and the spandrels but not between the individual arch rings.

From this, it can be concluded that FE Model 4 exhibits some nonphysical behaviour. The inability to transmit tensile stresses between the arch and spandrels means that its estimations of deflections under load are lower bounds on the true response. The real behaviour lies between the limiting cases of Models 1 and 4. Within the limits of linear elastic methods, the similarity in response pattern for Model 4, at least for parts of the arch with low damage, suggests that it offers a better simulation than other, more simplified models.

### **3.6 Conclusions**

In this study, linear elastic finite-element models were compared with the actual service response of a masonry arch railway viaduct under its operational loads, which had previously been evaluated using monitoring technologies (for more details, see Acikgoz et al., 2018a and 2018b).

Because of parameter uncertainty, it was necessary to make reasonable assumptions about the material properties, nonvisible geometry, and boundary conditions. With these in place, it was found that the output of FE simulations was similar in pattern to typical monitoring data for

---

common ‘global’ arch measurements, such as the vertical crown displacements and pier-to-pier span opening displacements. Although there was also similarity in magnitude for the more detailed models, uncertainty remains with regard to the input parameters and, as such, conclusive interpretation of the response magnitude is not possible.

‘Local’ measurements of the distribution of barrel in-plane strains offered less similarity in pattern between modelling and monitoring results; however, this is to be expected given the damaged condition of the viaduct and indeed suggests that there may be potential to exploit these ‘local’ measurements in the future for more insightful monitoring of these structures. In this context, linear elastic analysis provided a useful simplification of the pre-damage behaviour, against which local measurements could be evaluated to gauge the severity, and the extent of impact, of any damage in cases where more thorough modelling is impractical. However, it is important to emphasise that the magnitude of these FE simulations is very difficult to verify; this is the case for more complex analyses as well as linear elastic methods.

For the Marsh Lane viaduct in particular, it was found that the transverse cracking damage caused a local change in strain response patterns, and, to a lesser degree, global changes, such as an increase in vertical crown displacements. Regions with low visible damage displayed a pattern of response similar to the linear elastic idealisation, which suggests that they do indeed remain healthy.

Furthermore, this study has quantified the relative contributions to global serviceability behaviour that come from the various structural components making up a masonry arch viaduct. The results demonstrate that although neglecting major structural components may be a useful and conservative assumption for ULS assessment, these components must be considered when evaluating SLS behaviour.



## **Part 2**

# **Monitoring a skewed masonry bridge**



# Chapter 4

## Monitoring methodology and evaluation of technologies

A significant proportion of the research presented in this thesis consists of a monitoring campaign at the CFM-5 skewed masonry arch railway bridge in North Yorkshire, UK, and interpretation of the resulting strain and deflection data. This chapter presents an introduction to the bridge and outlines the development and installation of the monitoring scheme.

The installation presented here forms part of a larger study, carried out in collaboration with AECOM. During this study, several technical reports have been co-authored with AECOM for Network Rail (Wood, Cocking, and DeJong, 2017; Thompson, Cocking, and DeJong, 2018; and Thompson et al., 2019). These reports cover the development and installation of the monitoring systems, and practical evaluation of the various technologies used – parts of which are also presented in this chapter. Parts of this chapter have also been reported in Cocking, Thompson, and DeJong (2019), and in Cocking, Ye, and DeJong (2019).

The reports also cover data processing and initial interpretation, which is presented in more detail over the following chapters. Basic data processing, necessary for all data sets, is included in this chapter. However, further processing necessary for interpreting specific aspects of the installation is covered in the relevant sections of the subsequent chapters.

## **4.1 Introduction**

Skewed masonry arch railway bridges are common, yet their structural behaviour under typical working loads can be difficult to determine, including the impact of the skew angle on this behaviour, and any gradual changes due to degradation. The work presented here aims to address this problem through detailed monitoring of a damaged – albeit recently repaired – skewed masonry arch railway bridge in the UK.

A comprehensive Structural Health Monitoring system was installed, including arrays of fibre-optic FBGs providing distributed sensing data over a large portion of the bridge. Videogrammetry was also used to investigate the distribution of vertical deflections across the arch barrel. These technologies were deployed at the bridge by the author, alongside an installation of conventional point sensors which was undertaken by AECOM. The combined project was in response to the asset owner Network Rail's aspiration to explore a greater range of technologies that could be used to monitor their stock of ageing masonry arch bridges.

The FBG and videogrammetry monitoring data are used here to investigate the typical dynamic structural response of the skewed bridge, in detail, and to quantify the sensitivity of this response to a range of variables. It is observed that the dynamic bridge response is sensitive to the time of day, which is a proxy for passenger loading, to the train speed, and to temperature. It is also observed that the sensitivity of the response to these variables can be local, in that the response can differ throughout the bridge and be affected by existing local damage. Identifying these trends is important to distinguish additional damage from other effects.

The monitoring data are also used to evaluate some typical assumptions regarding bridge behaviour – in particular, the flow of force through skewed arches. This is achieved through the measurement and visualisation of principal strains across the arch soffit, using a new design of FBG strain rosette. Measurements from these rosettes are compared both against other monitoring data, captured using videogrammetry, and the results of simplified calculations. Assumptions of symmetry in the arch response are also investigated.

### **4.1.1 Introduction to the CFM-5 bridge**

The bridge considered in this study is a single span, skewed masonry arch railway bridge in North Yorkshire, UK. Completed in 1868, it carries a range of passenger and freight rail traffic, on two tracks. Its construction is a brick masonry arch barrel, with the bricks laid helicoidally following the skew span direction, supported by stone blockwork skewbacks, abutments, and wing walls. The spandrel walls and parapets are also built using stone blocks. The skew angle

is approximately  $26^\circ$ . An elevation view of this bridge – designated CFM-5 by Network Rail – is shown in Figure 4.1.

The main signs of damage at CFM-5 are separation cracks between the brick arch barrel and stone spandrel walls, and an additional longitudinal crack in the south-eastern quadrant of the arch soffit. This crack is located roughly underneath the centreline of the southern track and extends from the arch springing by just over 3 metres, approximately following the skewed span direction. In addition to these cracks, some cracking and bulging of the spandrel walls has been reported, as well as bulging of the south-western and north-eastern wing walls, adjacent to the acute corners of the skewed arch. In 2016, soil anchors were fitted in these wing walls, ten new tie rods were installed through the spandrel walls to constrain the arch in its transverse direction, and the cracks were comprehensively stitched using steel rods. Visible signs of this damage and intervention work are shown in Figure 4.2, and the extent of the tie rods can also be seen in the elevation view of Figure 4.1. The new tie rods were installed to replace previous ones, which had been found to be ineffective in preventing further expansion of the spandrel separation cracks. Pattress plates for the previous tie rods can still be seen in Figure 4.1 and in the right-hand photograph of Figure 4.2. These are smaller and a lighter colour than those for the new tie rods.



*Figure 4.1: Upside elevation view of the CFM-5 bridge, looking north*

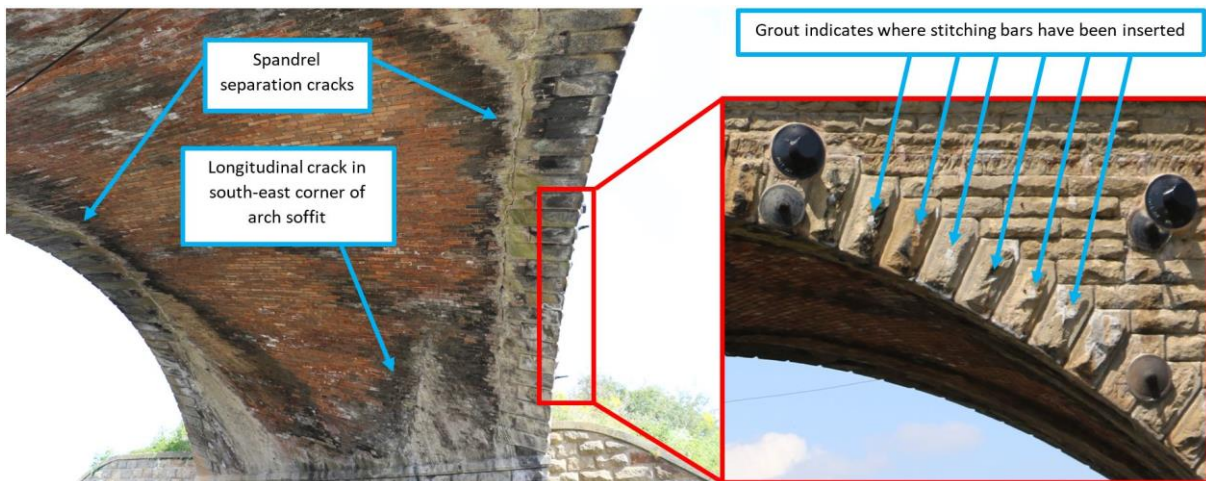


*Figure 4.2: Views of the arch soffit and south spandrel at the CFM-5 bridge, with key cracks and signs of past interventions highlighted*

Based on visual observations from before and after this repair work, the 2016 intervention was successful in reducing the growth of cracks and the liveliness of the bridge response. In particular, the arch barrel had previously displayed visible vertical deflections under train loading, relative to the spandrel walls. The formation of separation cracks between the arch barrel and the spandrel walls, which may be expected given the likely step change in stiffness between these structural components, gives rise to this phenomenon, termed an ‘arch pumping’ response. Without the significantly higher stiffness of the spandrel walls to restrain its movements, the arch barrel is able to undergo much larger live load deflections, as indicated in Figure 4.3. These larger dynamic deflections are believed to cause progressive deterioration of the bridge, over many cycles of loading. Therefore, preventing further arch pumping, by improving connectivity between the arch barrel and spandrel walls, was a key objective of the 2016 intervention.

However, the extensive nature of these repairs, in which the cracks were stitched at frequent intervals, was motivated by significant uncertainty regarding the bridge’s structural response to live loads. It is therefore unclear to what extent this intervention was proportionate to the scale of the problems at this bridge, and for how long it will continue to remain effective. This led to a desire from the asset managers to instigate regular condition monitoring of the bridge. Specifically, this monitoring needed to track any increases in the magnitude of the bridge response, which could indicate the return or progression of damage.

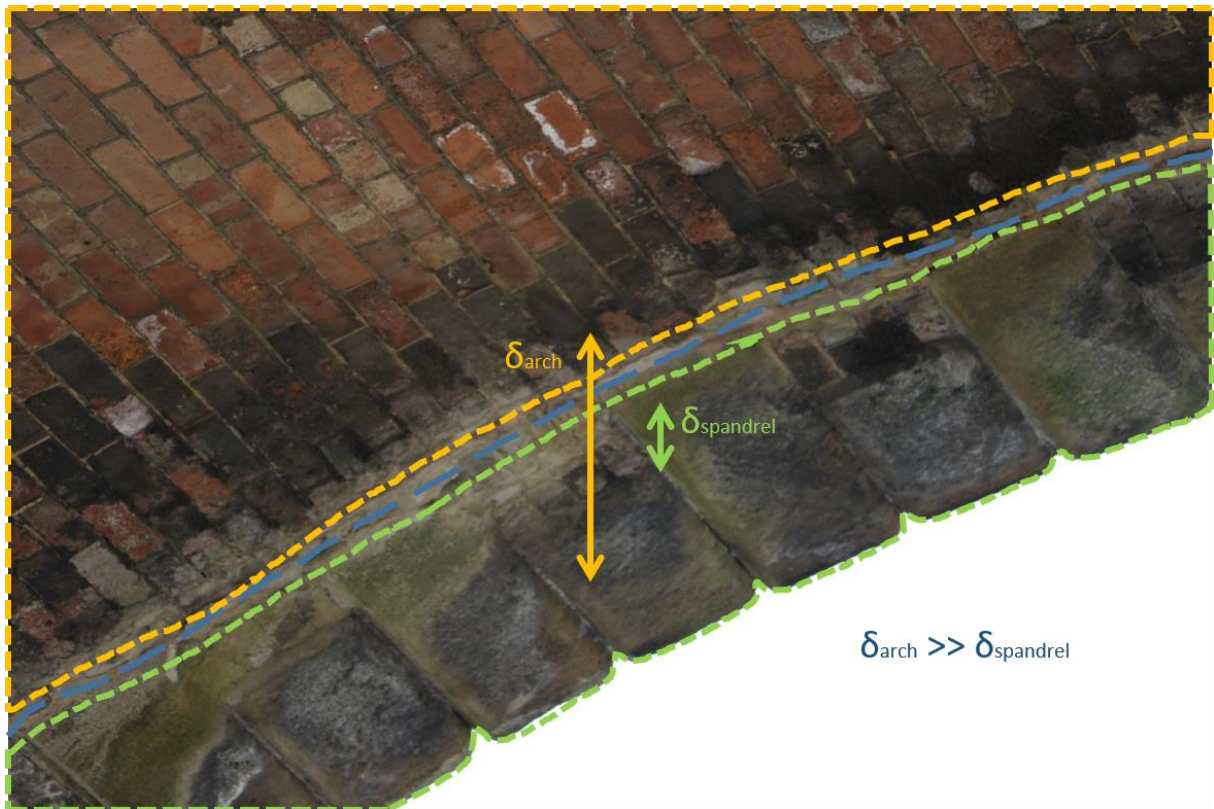


*Figure 4.3: Annotated view of the spandrel separation crack at the CFM-5 bridge, illustrating the 'arch pumping' phenomenon in which the arch barrel detaches from the spandrel wall and moves independently of it under live loads*

At the time of writing, Network Rail's usual approach for SHM of masonry arch bridges is deflection pole monitoring of the vertical dynamic deflections at the crown. As shown in Figure 4.4, poles containing LVDTs are temporarily installed between the ground and the arch soffit – typically at points along the crown line, underneath the rail tracks – and log displacement measurements as trains pass over the bridge. This method requires direct access to the underside of the arch, throughout the monitoring period, and suitable ground conditions to constrain the pole. As a result, deflection poles cannot be used to monitor bridges that span rivers or other inaccessible terrain and may be disruptive when used at bridges that span roads or railway lines, if these cannot readily be closed. Measurement frequency can also be an issue since, when bridges are damaged or their condition is uncertain, Network Rail may prescribe continuous, monthly monitoring until remedial work can be undertaken.



*Figure 4.4: View of deflection pole monitoring at CFM-5, with poles installed underneath both rail tracks (after Thompson et al., 2019)*

CFM-5 crosses a busy, rural road that is used by lorry freight and so, when this road is closed to facilitate deflection pole monitoring, the 38-mile diversion shown in Figure 4.5 is necessary in order to provide an appropriate alternative route for this traffic. These considerations meant that monthly deflection pole monitoring was not feasible at CFM-5. They also made it an ideal structure at which to trial other monitoring technologies, which could allow measurements to be recorded at the bridge while the road below remained open.

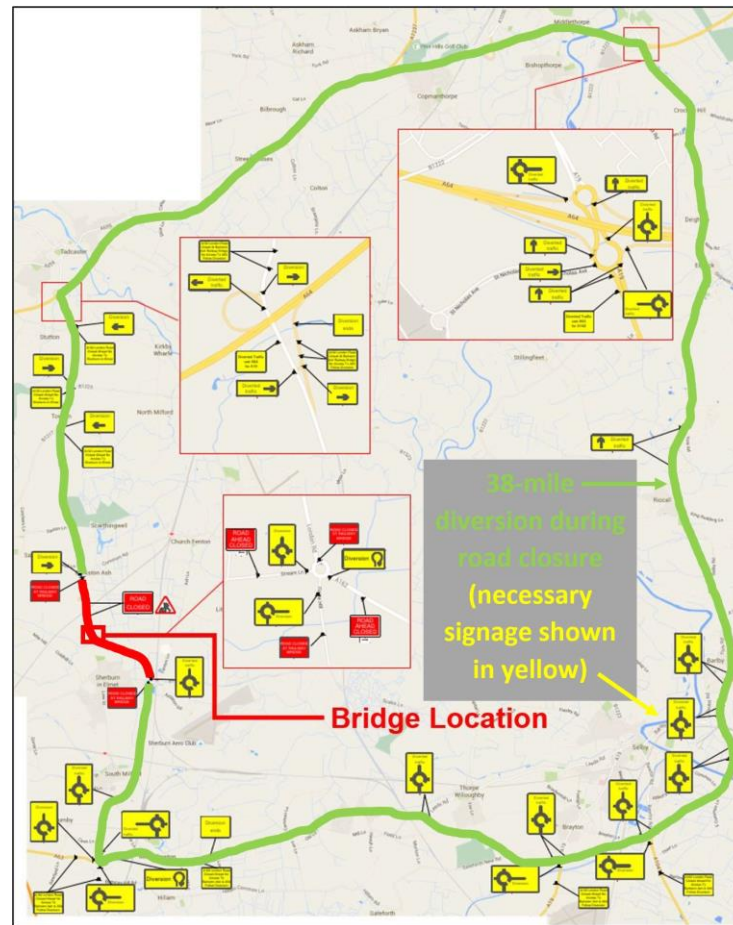


Figure 4.5: Schematic of the road diversion required to facilitate deflection pole monitoring at the CFM-5 bridge (adapted from unpublished figure by Daniel Thompson)

## 4.2 Development of the monitoring installation

Drawing on relevant archive drawings, inspection reports, available literature, and visual inspection of CFM-5, a desk study (Wood, Cocking, and DeJong, 2017) proposed a range of sensing technologies and measurable parameters which could form the basis of a monitoring installation at this bridge. This was followed by an initial monitoring survey in which a laser scan of the bridge geometry was captured, and the magnitude of live load response was studied using laser vibrometry.

Vibrometry had the advantage of being a purely remote technology, requiring no devices or targets to be attached to the structure. Its main drawback was that movements could only be measured in the direction of its line of sight, whereas the response at the bridge was expected to be three dimensional. While it could theoretically replace deflection pole monitoring of vertical arch displacements, this would require the vibrometer to be sited underneath the bridge

(similarly to the deflection poles in Figure 4.4) and so would not solve the access issues associated with this method. Therefore, laser vibrometry was not considered a viable long-term solution for monitoring the bridge. However, using vibrometry measurements taken from a number of vantage points, initial estimates of the magnitude of movements were made that informed the design of a monitoring installation. For instance, these measurements were used to verify the proposed gauge lengths for various sensors and identified locations of interest for monitoring.

The monitoring installation presented to Network Rail (Thompson, Cocking, and DeJong, 2018) is summarised in Figure 4.6. The author proposed the use of FBGs and videogrammetry to obtain distributed measurements of the in-plane strains and vertical displacements, respectively. This required the installation of fibre-optic cables and videogrammetry targets on the arch soffit. Alongside this, AECOM installed a range of point sensing technologies across the arch. Other than ambient temperature data, only results from FBG and videogrammetry monitoring are presented here. A comparison of the different methods used at CFM-5, including the point sensors, was given in Cocking, Thompson, and DeJong (2019). Key findings from this are presented later, in section 4.5.

### **4.3 The FBG installation at CFM-5**

FBGs were installed in a variety of configurations at this bridge. In particular, the installation included the first deployments of two new FBG implementations, developed by the author and first reported in Cocking et al. (2019a; 2019b; and 2019c). In the first of these, FBGs monitor both in-plane and out-of-plane crack displacements, in order to measure the ‘pumping’ response between the arch barrel and the south spandrel wall. The second is an FBG strain rosette, made possible by a new clamp designed by the author. This allows FBGs to be installed in triangular rosettes, measuring the full strain state at numerous locations across the arch soffit.

In the following chapters, the novel FBG implementations used at the case study bridge will be described in detail, followed by analysis and interpretation of six months of monitoring data recorded between September 2018 and February 2019. Note that different subsets of the FBGs are discussed in Chapters 5 and 6, and the numbering conventions used to refer to these sensors are introduced in the relevant chapters (see, respectively, Figures 5.1 and 6.1). Long-term data, recorded by an autonomous FBG sensing system that was installed at the bridge in July 2020, are discussed later in Part 3 of this thesis.

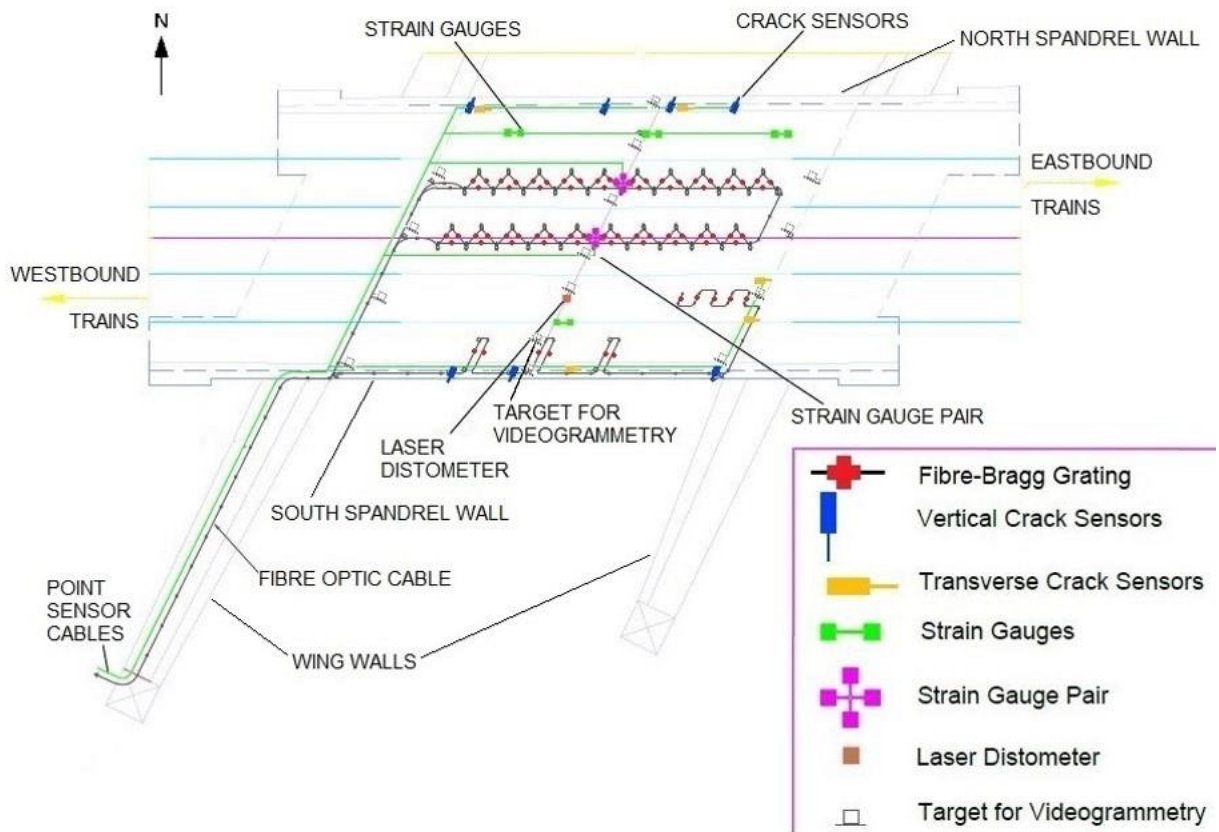


Figure 4.6: Installation plan showing the proposed locations of sensors at the CFM-5 bridge

During installation of the sensors, the size of the brackets used for AECOM's vertical crack sensors meant that, at the southern arch crown, it was not possible to site the FBGs along the south spandrel crack in the planned locations shown in Figure 4.6. Instead, these sensors were shifted to the east so that FBGs were now placed either side of the arch crown, at the  $5/12$  and  $7/12$  points, and at the eastern quarter point (instead of the third point, as originally planned). Separately, more FBGs were ultimately installed along the south-eastern longitudinal crack, allowing for measurements to be taken at 0.5-metre intervals along its length and just ahead of the crack tip. Results from these sensors are discussed in Chapter 5 and the final, as-installed locations of these FBGs are shown in Figure 5.1.

### 4.3.1 Introduction to the FBG sensors

The FBGs used in this installation were manufactured by FBGS, and a model sm130 Micron Optics FBG interrogator was used to record measurements. Custom-made clamps were manufactured by L&C Precision Engineering and used to install the fibre-optic cables on the bridge. The measurement noise achieved by this monitoring system was  $1 \mu\epsilon$ , ideal for capturing the small magnitudes of movements at this masonry arch bridge. By pre-straining the FBGs during installation, so that they are under tension when the bridge is unloaded, both compressive and tensile strains could be measured. This pre-strain was applied by hand and was of the order of several hundred microstrain, an order of magnitude above the compressive strains to be measured.

A combination of thermal and mechanical strain will make up the overall total measured strain and, furthermore, changes in temperature can cause the refractive index of the glass core inside the fibre to vary. Therefore, the true mechanical strain is related to the measured shift in Bragg wavelength by Equation (4.1), in which  $\Delta\epsilon_m$  is the change in mechanical strain,  $k$  is a strain calibration coefficient for the fibre,  $\frac{\Delta\lambda}{\lambda_0}$  is the ratio of the measured change in wavelength to the original Bragg wavelength for the grating,  $\Delta T$  is the change in temperature, and  $\alpha$  is a coefficient accounting for thermal effects. Calibration of the FBGs installed at CFM-5, under known displacements, identified that their calibration constant was  $k = 0.78$ .

$$\Delta\epsilon_m = \frac{1}{k} \left( \frac{\Delta\lambda}{\lambda_0} - \alpha\Delta T \right) \quad (4.1)$$

In reality,  $\alpha$  captures a range of thermal and thermo-optic effects which influence the fibre-optic cable and the structure being monitored (Majumder, 2008). Consequently, it is necessary to compensate for thermal strains in static FBG monitoring. However, when only short dynamic events are being measured, changes in thermal strain can be neglected. In this study, temperature variation during dynamic events was assumed to be negligible, but temperatures were still recorded in order to account for possible thermal effects within the bridge. These ambient temperature measurements were logged by separate points sensors, distributed by AECOM across the bridge, and then averaged to give a single value for each train event.

The total allowable number of FBGs is limited by the wavelength range of the FBG interrogator. Each FBG is etched to have its own Bragg wavelength. These wavelengths need to be sufficiently separated so that the individual gratings can always be distinguished during monitoring. In this study, four fibre-optic cables, each with a maximum of 20 FBGs, were used.

The sampling frequency was set as 1 kHz throughout the period of monitoring described in Chapters 4 to 6. Note that, in later, long-term monitoring of the bridge – described in Part 3 of this thesis – the sampling frequency was decreased to 250 Hz. This was done to maximise the storage space available for monitoring data on the site PC.

### 4.3.2 Development of the new FBG clamps

Fibre-optic cables housing the FBGs were connected to the arch soffit using aluminium clamps, and pre-strained to no less than  $500 \mu\epsilon$  so that both compressive and tensile movements in the bridge could be recorded. A clamp design originally developed several years earlier at CSIC (see, for example, Acikgoz et al., 2018a) was used for standard installation of the FBG cables in longitudinal lines, and across cracks to measure crack opening in the plane of the arch barrel. Two drilled connections per clamp, using expanding masonry plugs, fixed the clamps to the bridge and ensured that they would not rotate relative to the masonry once they had been secured.

Two new clamping arrangements were developed, innovating on the original CSIC design, in order to measure new types of movement at the CFM-5 bridge. Photos of the FBG installation at CFM-5 which highlight the new clamp designs are shown in Figure 4.7.

In one of these new implementations, two FBGs are installed in a pair across a crack that, under load, is anticipated to undergo both in-plane crack opening and out-of-plane crack shearing movements. Here, one FBG is installed as usual across the crack, with its fibre axis parallel to the direction of expected in-plane crack opening. The adjacent FBG in the pair is inclined relative to this direction. This is achieved by clamping the two end points of its gauge length to angled brackets of different lengths, which are in turn fixed to the bridge soffit on either side of the crack. In this way, the inclined fibre measures components of both the crack opening and shearing displacements. Using measurements from both of the FBGs in a pair, the two components of movement at this location can be decoupled from one another and the magnitudes of shearing displacements identified.

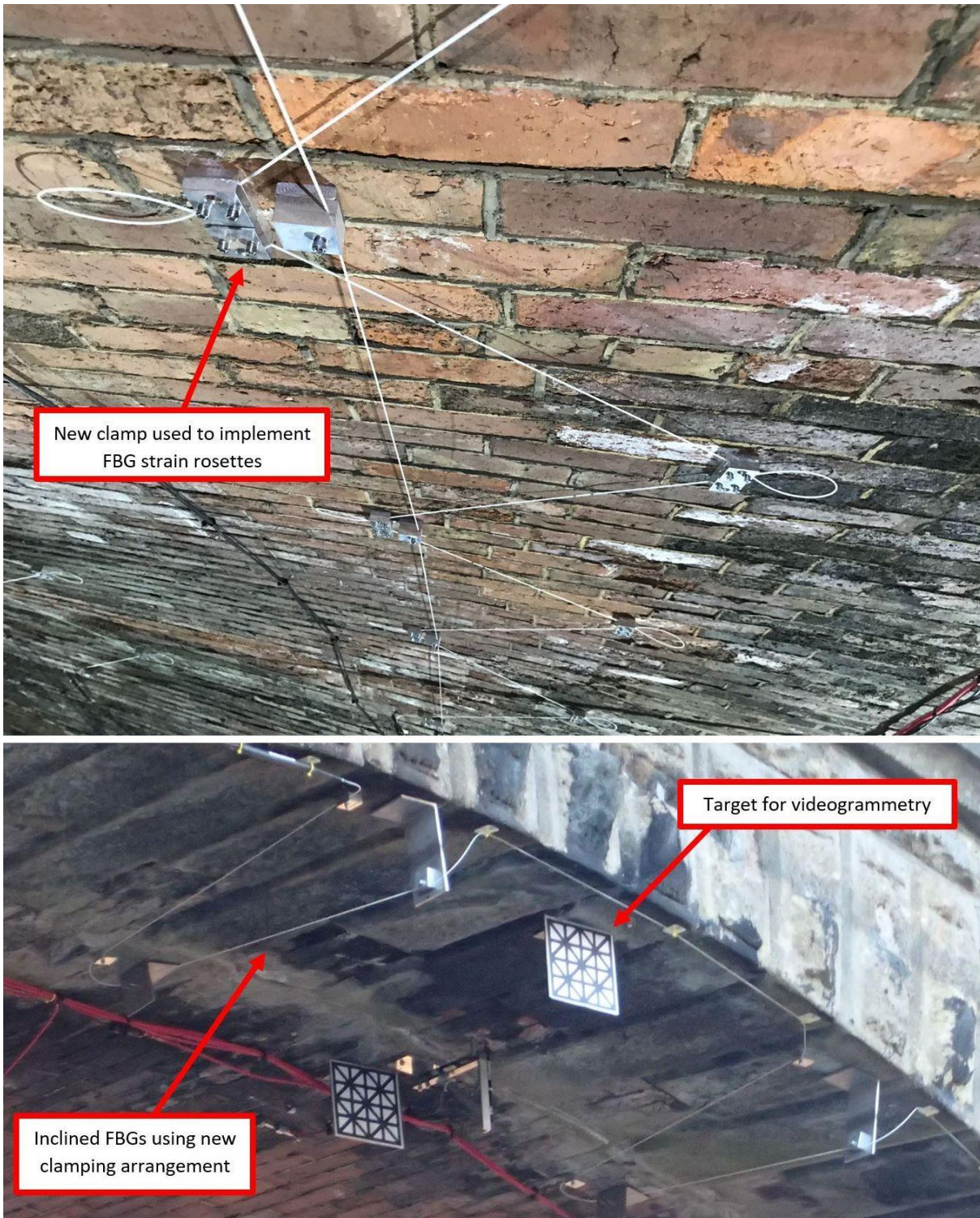


Figure 4.7: Photos from the sensor installation at CFM-5, highlighting the new FBG clamps used for the triangular strain rosettes and inclined FBGs across the south spandrel crack, as well as the new target design used for videogrammetry

At CFM-5, these ‘FBG pairs’ have been installed at three points along the separation crack between the arch barrel and south spandrel wall. The full methodology for calculating shearing movements using these FBGs is presented in Chapter 5, in section 5.1.1. Tracking the evolution of peak shear movements across this crack allows for the effectiveness of the 2016 repair work in reducing these ‘arch pumping’ movements to be evaluated over time, which was identified to be of significant practical importance earlier in section 4.1.1.

The second new clamp type allows for an FBG cable to be installed in a zigzag, or sawtooth, formation. When one of these sawtooth lines of FBGs is positioned next to a conventional longitudinal FBG array, the result is a line of triangular FBG strain rosettes (see Figure 4.7). Fibres installed using these sawtooth clamps subtend an angle of  $90^\circ$  at each clamp, such that the fibres making up each rosette form the edges of an isosceles triangle of  $0.25 \text{ m}^2$  area. The measurements recorded by a rosette are an average, over their area, of the intrados strain state, and can be resolved to yield the in-plane normal and shear strains in any chosen orientation. The methodology for calculating these strains is presented in Chapter 6, in section 6.1.1.1.

Since the fibre-optic cables for this project had FBGs spaced at regular, 1 m intervals, this resulted in a longitudinal line of FBGs with 1 m gauge lengths, while the adjacent sawtooth line needed gauge lengths of 0.707 m in order to construct each rosette as an isosceles triangle. Conveniently, this left 0.293 m for the loop at each clamp, which was compatible with the  $\sim 50$  mm minimum radius of curvature permitted by the fibre before (a) losses of light from the glass core would be induced, and (b) the fibre would potentially reach levels of bending stress that could result in the fracture of the glass core.

### **4.3.3 Preliminary data processing approach for the FBG data**

#### **4.3.3.1 Data cleaning**

The raw output from the Micron Optics FBG interrogator is a set of strain time histories, which are calculated from each grating’s wavelength shifts using Equation (4.1) (see section 4.3.1). High frequency measurement noise is present in these time histories and although typically it has a magnitude of only  $\pm 1 \mu\epsilon$ , this can occasionally be as high as  $\pm 5 \mu\epsilon$ . The magnitudes of intrados strains are small but typically an order of magnitude higher than this noise – even at locations close to the arch haunches, where significant load dispersion occurs through the fill material before forces are applied to the arch extrados, and arch strains are resultingly lower.

Despite the difference in magnitude between measurement noise and peak strain response, noise can still obscure some features of the time histories. To mitigate this, the first stage of processing the strain data is to pass these through a low pass filter. An equiripple filter with

upper cut-off frequency  $f_{stop} = 10$  Hz was designed using the inbuilt `fdesign.lowpass` function in MATLAB. This was found to perform well in removing high frequency noise, while leaving the key peaks in the signals well defined.

Figure 4.8 compares raw and filtered strain time histories at the western haunch and close to the arch crown, during the passage of a typical Class 185 passenger train. Note that in the raw time histories, plotted in red solid lines, the two axles at each bogie are observed to produce clear individual peaks in the response close to the arch crown, where minimal load dispersion can occur, while these peaks are merged in the response at the arch haunch. The filtered time histories are plotted as black dashed lines. In the filtered signal at the arch crown, the individual axle peaks are still distinguishable but are less prominent. At the arch haunch, the filtered and raw signals are very similar, other than a slight – and approximately uniform – shift in time.

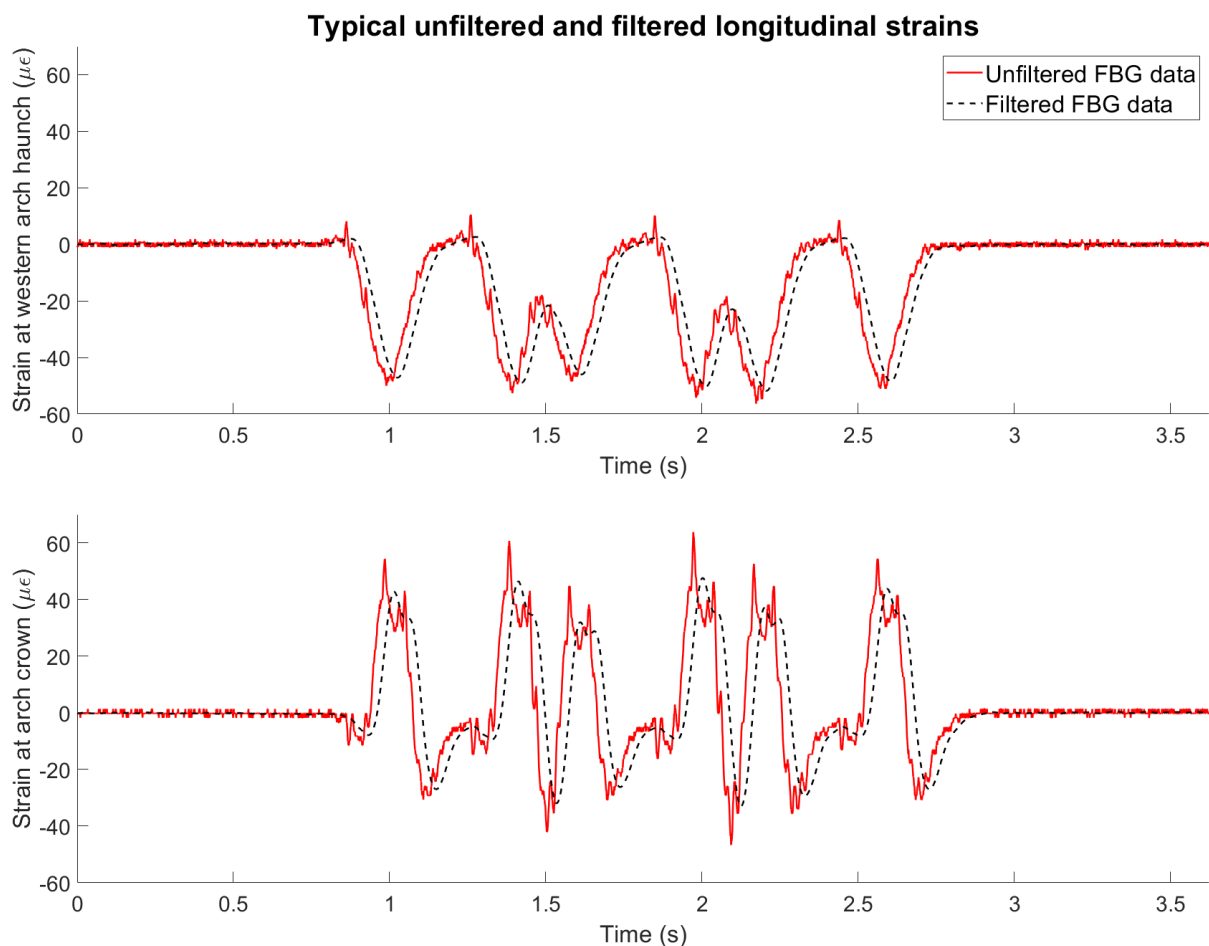


*Figure 4.8: Longitudinal strains at the arch crown and western haunch, for a typical 3-carriage Class 185 passenger train, showing both raw FBG data and the same data after high frequency noise has been removed using a low-pass filter*

### 4.3.3.2 Obtaining the peak-to-peak strain response

In order to compare the evolution of the strain response over many train events, the maximum peak-to-peak strain responses of all FBGs are computed, for each time history. This is accomplished using the following algorithm:

1. Using the inbuilt `findpeaks` function in MATLAB,
  - a. Identify all peaks in the strain time history.
  - b. Identify all troughs in the strain time history, by reflecting the time history in the horizontal axis and then identifying peaks.

In both cases, the minimum peak separation is specified based on the known separation of axles on the same bogie, for each train class, and assuming a maximum possible train speed of 100 mph. Therefore, only the maximum response under each bogie is included in the peak-to-peak calculation. Note that the permissible line speed at this bridge is 90 mph, and later it is observed that the instantaneous train speeds do not exceed 95 mph for the available FBG data set (see section 5.4), so 100 mph is a reasonable upper bound on the train speed. A minimum peak height is also specified but this is tailored to each FBG, since the patterns of response and magnitudes of important peaks vary spatially over the bridge. For instance, note in Figure 4.8 that the response at the arch haunch is almost entirely compressive (i.e., strains take predominantly negative values), whereas notable tensile and compressive strains are observed at the arch crown.

2. Identify the timestamps of all peaks and troughs.
3. Combine peaks and troughs, and their associated timestamps, into a single table and sort this by time.
4. Using the inbuilt MATLAB function `diff`, find the differences between adjacent peaks and troughs in this table.
5. Save the maximum peak-to-peak response for this given FBG and data file.

Once data has been categorised into groups based on common characteristics such as the train class (see section 4.3.3.3), this algorithm is used to calculate peak-to-peak strains for each FBG across all data files in a given group. These peak-to-peak strains can then be plotted to investigate potential trends over time or sensitivities to variables of interest, although in some cases, such as measurements across cracks, it is more meaningful to first convert strains to displacements by multiplying by the gauge length between clamps.

#### 4.3.3.3 Categorising the monitoring data

FBG monitoring data have been categorised by a number of variables, to allow for analysis of groups sharing common properties. Firstly, data were grouped according to train class. Each Train Operating Company (TOC) which runs routes crossing the CFM-5 bridge uses a known fleet of train stock. These fleets are each comprised of one or more train classes, models of which share common geometry and axle loads – including a known range of potential passenger loading for various occupancy levels – and limits on their potential numbers of carriages. For the period of monitoring considered in this section of this thesis – corresponding to data gathered between September 2018 and February 2019 – the following train classes were in operation for the three main TOCs whose routes cross CFM-5:

- First TransPennine Express, the most frequent route to operate passenger trains over CFM-5, used a fleet of Class 185 trains.
- Northern Rail operates a range of train classes, of which Class 150 is believed to have been the most common.
- CrossCountry operates a range of train classes, of which Class 220, 221, and 222 were the most common over this period. These have similar properties and could not always be distinguished during monitoring, and so for simplicity all these trains are classified here as Class 222.

During on-site monitoring at CFM-5, observation notes were kept which detailed the classes and number of carriages of each recorded train. These notes were later verified against publicly available train timetable data, compiled by AECOM and shared with CSIC. Using these notes, the FBG data were manually sorted by train class and assigned a number of carriages, the latter of which was confirmed by peak counting of the time history data.

Train direction was calculated by comparing the magnitudes of peak longitudinal strains measured by FBGs beneath the north track and the bridge centreline. Trains which passed on the north track produced a larger strain response in FBGs directly beneath the loaded track than they did in FBGs under the bridge centreline, while the opposite pattern was the case for trains passing on the south track. Using this approach, the assignment of train direction was automated. Note, also, that all eastbound trains passed on the north track (the DOWN line) and all westbound trains on the south track (the UP line), as shown earlier in Figure 4.6.

Train speed was calculated using the strain time history data for longitudinal FBGs located either side of the arch crown, aligned with both the north track and overall bridge centrelines. For this group of four FBGs, the time elapsed between the first and last peaks in the time history,

together with the known length of the overall train – based on the train class geometry and number of carriages – was used to compute the train speed. Extreme speed values, further than one standard deviation from the group mean, were then excluded – as these likely arose from potential errors in identifying either the first or last peak in the strain time history – and the mean speed based on calculated values at the remaining FBGs was then assigned to that train.

Ambient temperature was measured by point sensors installed by AECOM. These recorded hourly temperatures at a number of points distributed across the bridge. These values were averaged and interpolated to give an approximate ambient temperature at the times each train was recorded. Most data were recorded during night-time shifts, during which temperatures remained reasonably constant. However, during daytime shifts (in September 2018) there were notably larger changes in temperature throughout the periods of monitoring. It is recognised that this therefore means the temperatures assigned to these data files are more uncertain.

Information on the date and time of recording was assigned automatically, based on the timestamp of the FBG file. Table 4.1 gives a summary of all FBG data recorded at CFM-5 between September 2018 and February 2019, grouped by month, train class, and direction. Note that data were recorded over four days in September 2018 in order to verify the success of the sensor installation, which had just been completed. In subsequent months, data were gathered on individual day trips.

*Table 4.1: Summary of the train events recorded by FBG monitoring at CFM-5, during the 2018–2019 monthly monitoring*

<b>Train Class (&amp; Route):</b>	<b>Passing on track:</b>	<b>Sept 2018:</b>	<b>Oct 2018:</b>	<b>Nov 2018:</b>	<b>Dec 2018:</b>	<b>Jan 2019:</b>	<b>Feb 2019:</b>	<b>Total:</b>
Class 185 (First Trans Pennine)	North	70	16	15	11	8	9	129
	South	66	13	14	11	10	9	123
Class 150 (Northern Rail)	North	19	5	4	6	6	6	46
	South	19	4	3	6	4	4	40
Class 222 (Cross Country)	North	18	4	5	2	3	2	34
	South	20	2	4	4	1	3	34
<b>Overall total:</b>								<b>406</b>

## 4.4 Videogrammetry monitoring at CFM-5

### 4.4.1 Overview of videogrammetry and the on-site monitoring approach

At CFM-5, videogrammetry enabled measurement of out-of-plane deflections of the arch, under train loading. An Imetrum Dynamic Monitoring Station (DMS) videogrammetry system was used, comprising either one or two high definition, high-speed cameras synchronised to a controller PC which logged measurements using proprietary Video Gauge software (Imetrum, 2021). In this software, one or more reference frames were defined within the camera's field of view and calibrated using known dimensions. The software automatically transformed movements in the camera image plane to the desired measurement reference frame and converted the units of displacements from pixels to millimetres. Virtual targets were created in the software, at specified locations within the field of view where displacement measurements were desired; the output from Video Gauge was a set of target displacements within the user-defined reference frame(s). These measurements were then exported from Video Gauge for further post processing and analysis in MATLAB, using custom scripts.

In reality, physical videogrammetry targets were also installed on the bridge, in the locations where virtual targets were later overlaid in Video Gauge. These physical targets were designed specifically for this project to have a high-contrast pattern that was large enough to be clearly visible from the location of the camera during monitoring. Targets were installed using a similar connection detail to the FBG clamps discussed in section 4.3.2, with the correct orientation to face the camera. The locations of targets on the arch soffit, and of the camera used for 2D videogrammetry, are shown in Figure 4.9. The target pattern can be seen in Figure 4.7.

Lines of targets were installed along the crown line and arch springings. However, movements at the arch springings were consistently below the level of measurement noise – which had a typical magnitude of 0.5 to 1.0 mm in the raw exported data from Video Gauge, dropping to 0.1 to 0.3 mm after post-processing in MATLAB. Because of this, only results from the targets along the arch crown line are considered here. Targets along the crown line were installed on both spandrel walls, on the edges of the arch barrel immediately adjacent to the spandrel separation cracks, underneath the centrelines of the north and south tracks, and at the longitudinal centreline of the bridge (see Figure 4.9).

The Digital Image Correlation (DIC) method used in videogrammetry is well established and has been used extensively in recent years, especially in laboratory-based experimental research. A useful overview of the method is given by Acikgoz et al. (2018b), which includes a rarer example of structural field monitoring using videogrammetry. The algorithms used by the

Video Gauge software are not evaluated here and given the proprietary nature of the software it is not clear precisely how the claimed sub-pixel resolution of measurements is obtained. Acikgoz et al. (2018b) found that various sources of errors can have a significant impact on the quality of videogrammetry measurements, especially in the field, and suggest potential mitigations for these. A number of these mitigations have been used at CFM-5. Most errors can be compensated for, using either an optimal equipment setup or appropriate post-processing strategies, but lens radial distortions and out-of-plane movements (normal to the camera image plane) were identified as notable residual contributors to measurement errors.

At CFM-5, errors due to lens radial distortion have been mitigated by using a sufficiently large focal length lens (no less than 25 mm) and positioning the camera a sufficient distance away from the bridge (at least 20 m), so that it may reasonably be assumed that straight lines in the real-world geometry remain straight in the camera image plane. In Acikgoz et al. (2018b), an 8 mm focal length lens and full utilisation of the image plane for measurements resulted in deformations of straight lines that were visible in the camera footage and, at most, a 4% measurement error close to the edges of the image. In their study, applying a simple model to correct for lens radial distortion was found to yield negligible improvements in measurement errors. Therefore, it has been assumed that the improved camera setup at CFM-5 is sufficient to negate any potential errors here, due to lens radial distortion.

Out-of-plane movements were investigated, and found to be minimal at this bridge, through the initial use of 3D videogrammetry. During this, two cameras were used to take measurements and a full, 3D coordinate system was calibrated using known dimensions of the bridge. Figure 4.9 shows the approximate location of the primary camera, south of the south-west wing wall; this was later used as the only camera during 2D monitoring. The secondary camera was positioned near to the end of the south-east wing wall, on the other side of the road. This was done during a daytime road closure, so that synchronisation cables could be laid across the road to connect the two cameras.

Using 3D videogrammetry, it was not possible to identify any transverse components of movement – i.e., movements approximately in the direction of line of sight of the primary camera (see Figure 4.9). If present, these were below the level of measurement noise. Furthermore, negligible movements were observed in the other horizontal – i.e., bridge longitudinal – direction. Only vertical deflections of the crown line targets could be discerned above the measurement noise. As a result, it was concluded that the response predominantly consisted of vertical deflections of the arch barrel, which 2D videogrammetry would be sufficient to capture.

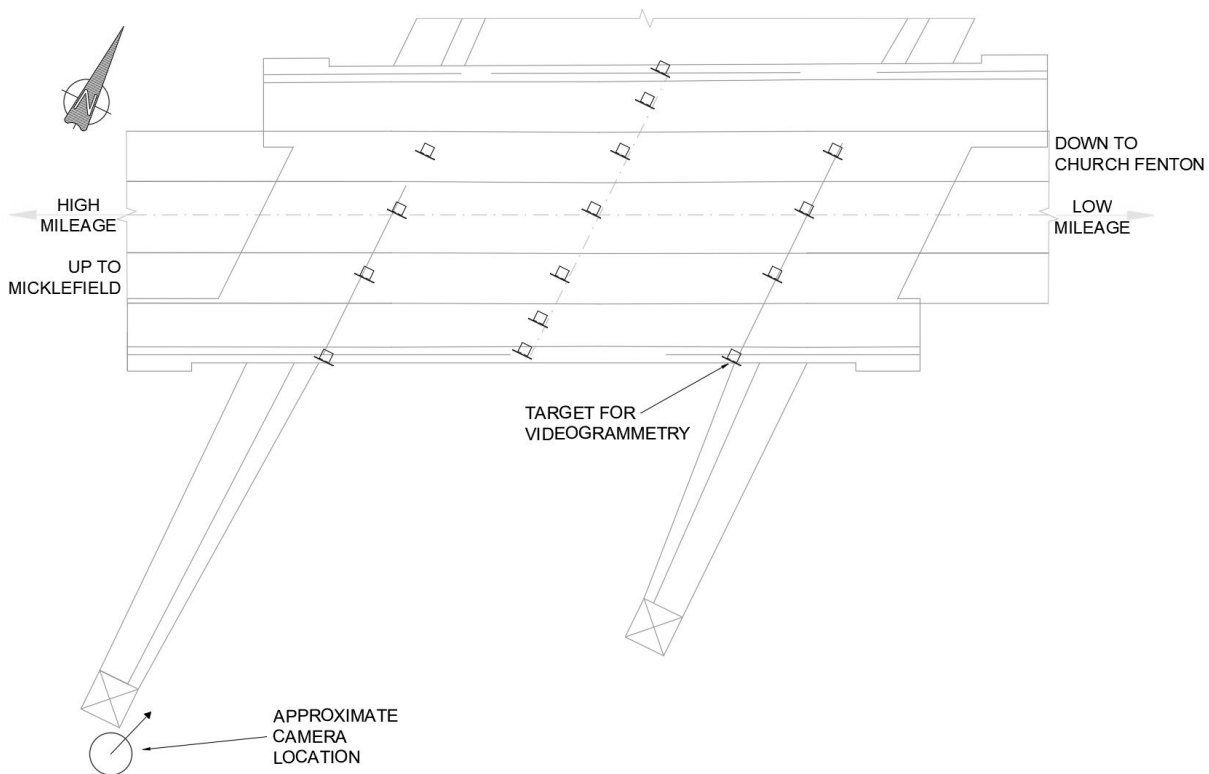
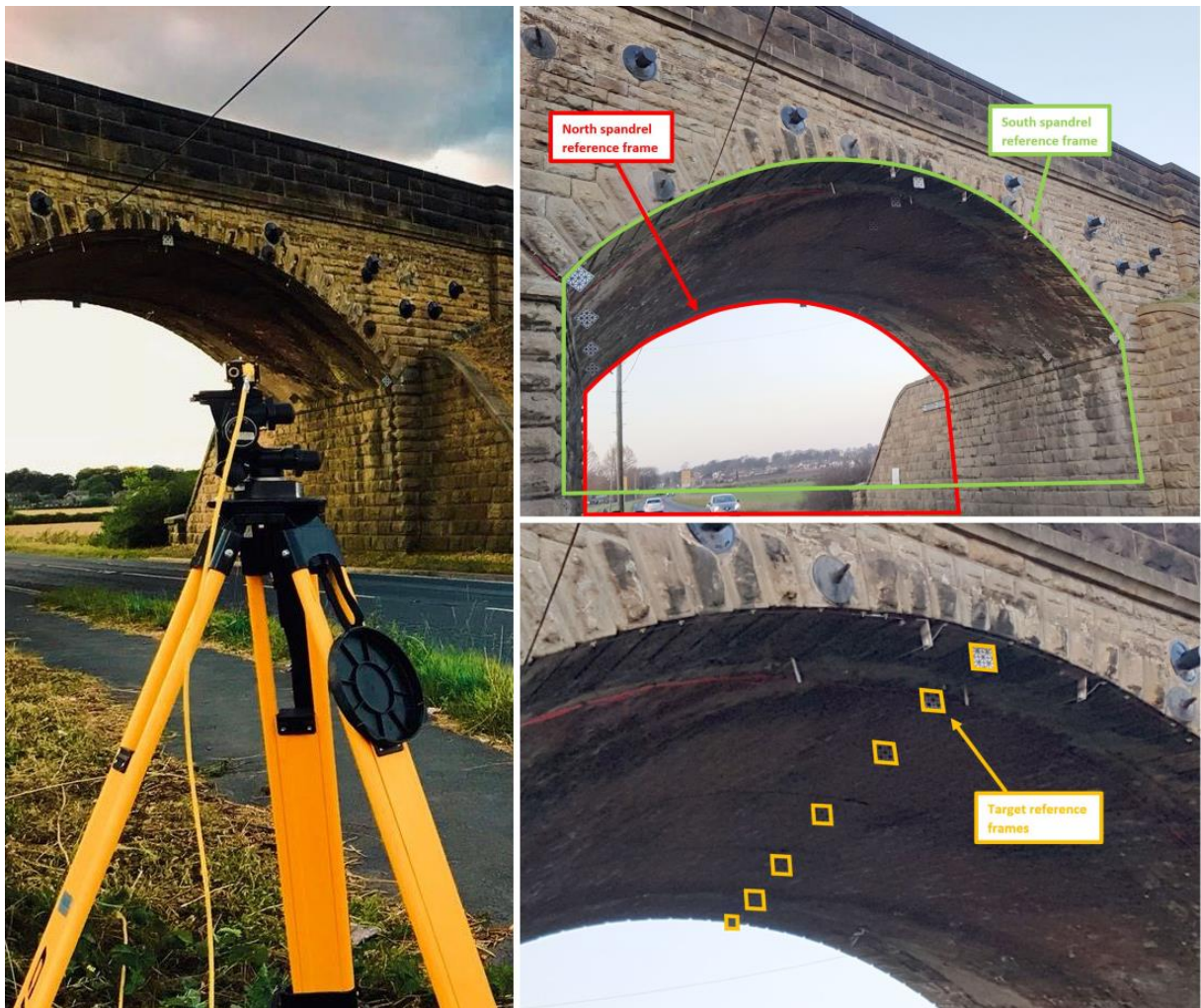


Figure 4.9: Plan view of CFM-5 showing the installed targets (not to scale) and approximate location of the camera used for 2D videogrammetry monitoring

Throughout the period of 2D videogrammetry monitoring, out-of-plane movements were measured using other technologies, such as FBGs, and found to remain negligibly low, compared to the in-plane videogrammetry measurements of interest. Specifically, as is discussed later in section 5.2.3 of Chapter 5, FBGs at the south spandrel separation crack recorded transverse movements of the arch barrel, relative to the spandrel wall, which did not exceed 0.1 mm in magnitude and were often considerably smaller than this.

An advantage of 2D videogrammetry is that calibration is less sensitive to errors than the 3D case, making it easier to carry out on site. However, it still requires detailed knowledge of structural dimensions. This was achieved at CFM-5 through laser scanning, although the precise specification of points of known geometry in the camera image remained challenging. Errors induced from this mismatch, between known points in the laser scan and selected points in the camera image, were minimised by favouring calibration settings that factored in parallel and perpendicular lines in the bridge geometry, over ones in which a larger number of discrete points had to be specified (Acikgoz et al, 2018b). Clear corners and edges were used, where possible, as these were easier to identify in the camera image.

Here, only vertical displacement data measured using 2D videogrammetry are considered. Monthly 2D videogrammetry measurements were taken at CFM-5, between September 2018 and February 2019. The camera view during 2D videogrammetry, and schematics of the various reference frames that were trialled, are shown in Figure 4.10. To begin with, a 25 mm lens was used, through which the entire arch span could be seen in the camera's field of view. This allowed measurements to be taken for targets along the crown line and at both arch springings. Reference frames were calibrated at the south and north spandrel walls, and measurements from these compared. The setup was used between September and December 2018.



*Figure 4.10: View of the south elevation of CFM-5 from the videogrammetry monitoring location, and schematics of the reference frames defined at the north and south spandrel walls (used in January 2019) and for each target (used in February 2019)*

After it had been concluded that useful measurements could not be extracted for the arch springings, even after post-processing, a 75 mm lens was adopted. This concentrated the field of view on the crown line targets. In January 2019, the same approach of calibrating reference frames at the south and north spandrel walls was used. However, this now led to discernible differences in the two sets of measurements. This could be due either to calibration errors – since it was more challenging to calibrate both of these reference frames in the reduced field of view – or to the increased accuracy of measurements now that a smaller field of view gave each of the crown line targets a higher pixel density. This increase in pixel density resulted in an effective reduction of measurement noise, in terms of metric units. To address this, in February 2019, individual reference frames were calibrated for each of the targets (see Figure 4.10), using their known geometry. The efficacy of the different reference frames is evaluated in Chapter 6, in section 6.2.1.

## **4.4.2 Processing approach for the videogrammetry data**

### **4.4.2.1 Strategies adopted from FBG data processing**

In the same way as the FBG data, raw exported displacements from the Video Gauge software were first filtered in MATLAB, to remove noise. Noise was observed at a significantly broader range of frequencies in the videogrammetry data, and so the upper cut-off frequency was revised to  $f_{stop} = 2.75$  Hz. This was chosen to be just above the highest expected rate of the cyclic train axle loading.

In order to account for various, mostly environmental, effects, further stages of post-processing were required for the videogrammetry data, as detailed in the following sections. After these, peak-to-peak displacements were obtained using the algorithm described for FBG data in section 4.3.3.2. Data were then sorted according to train class, direction, and date, using the same processes as were described for FBG data in section 4.3.3.3.

### **4.4.2.2 Compensating for environmental effects**

The increased range of noise observed in the videogrammetry data is likely due to a combination of various environmental effects. Most significantly, changing light conditions can cause significant drift in displacement readings over a period of only seconds. If left uncorrected, this drift can sometimes be large enough to obscure the displacement response to train loading completely. It can be seen in Figure 4.10 that there is a significant amount of unobstructed sky in the background of the camera images, due to the exposed location of the bridge. Sudden changes in light intensity in this background – for instance, when the sun emerged from behind a cloud – could lead to such overexposure in the image that the algorithm

---

would lose some targets, and so the displacement time histories for these targets would terminate partway through the train event.

Video Gauge provides an autoexposure algorithm that attempts to compensate for universal changes in light conditions in the camera image. This was used – with the consequence that the sampling frequency of measurements was limited to 50 Hz – and was observed to improve the quality of some but not all measurements. At CFM-5, targets are distributed over a large area of the structure and, as such, are differently affected by changes in light conditions, meaning that a universal autoexposure algorithm cannot correctly compensate in all cases.

To further mitigate the impact of changing light conditions, it was decided to perform videogrammetry monitoring overnight and uniformly illuminate the bridge using floodlights. Note that this decision was taken after the 3D videogrammetry trial, which was done during a daytime road closure. Night-time monitoring led to significant improvements, although it could not eliminate all changes in light levels. Some vehicles, particularly lorries, would sometimes cast shadows or reflect floodlighting onto the arch soffit as they passed beneath the bridge. This would appear as a transient, non-uniform drift in the displacement data, which could not easily be removed in post-processing.

Where it was felt that this drift was sudden or severe enough to potentially affect the accuracy of peak-to-peak displacement calculations, compromised data files were excluded from further analysis. This affected a reasonably high proportion of data recorded with the 25 mm lens, which had a field of view encompassing the entire arch soffit. However, a far smaller proportion of data files were compromised when the 75 mm lens was used, and the field of view only covered the crown line targets. It is possible that this is a result of the 75 mm lens increasing pixel density at locations of interest, giving rise to improved performance of the DIC algorithms. Alternatively, it may be that, by limiting the field of view to a relatively small portion of the arch soffit, the autoexposure algorithm was better able to compensate for changing light conditions.

Separately, movements of the camera may occur due to wind loading, since the site is exposed, or ground-borne vibrations originating from rail or road traffic – although the distance of the camera from the bridge, which was always at least 20 m, greatly reduces the chance of vibrations from trains reaching the tripod. These movements can be removed from the displacement time histories, either by monitoring an additional point that is known to remain stationary or by calculating relative displacements for two targets of interest.

At CFM-5, stationary points on the wing walls were initially used to provide this baseline reading. However, since no artificial targets had been installed in these locations, the effectiveness of this method was limited by the minimal texture of the stone blockwork construction. A better baseline was ultimately obtained by averaging displacements recorded at the targets installed on the north and south spandrel walls. It had been established, by this point, that movements of the spandrel walls were negligible under train loading, which makes sense due to their significantly increased stiffness relative to the arch barrel. Figure 4.11 shows a set of vertical displacement time histories for the targets distributed along the crown line, including the average baseline recorded at the spandrel walls. This baseline has been subtracted from the time histories in the other subplots.

In Figure 4.11, note that there is some residual noise which still dominates the response where magnitudes of displacement are low. However, using the strategies described above, the response on the loaded side of the arch is now clearly visible. By comparing peak-to-peak displacements between train events, rather than absolute peak values, the impact of this residual noise is further reduced.

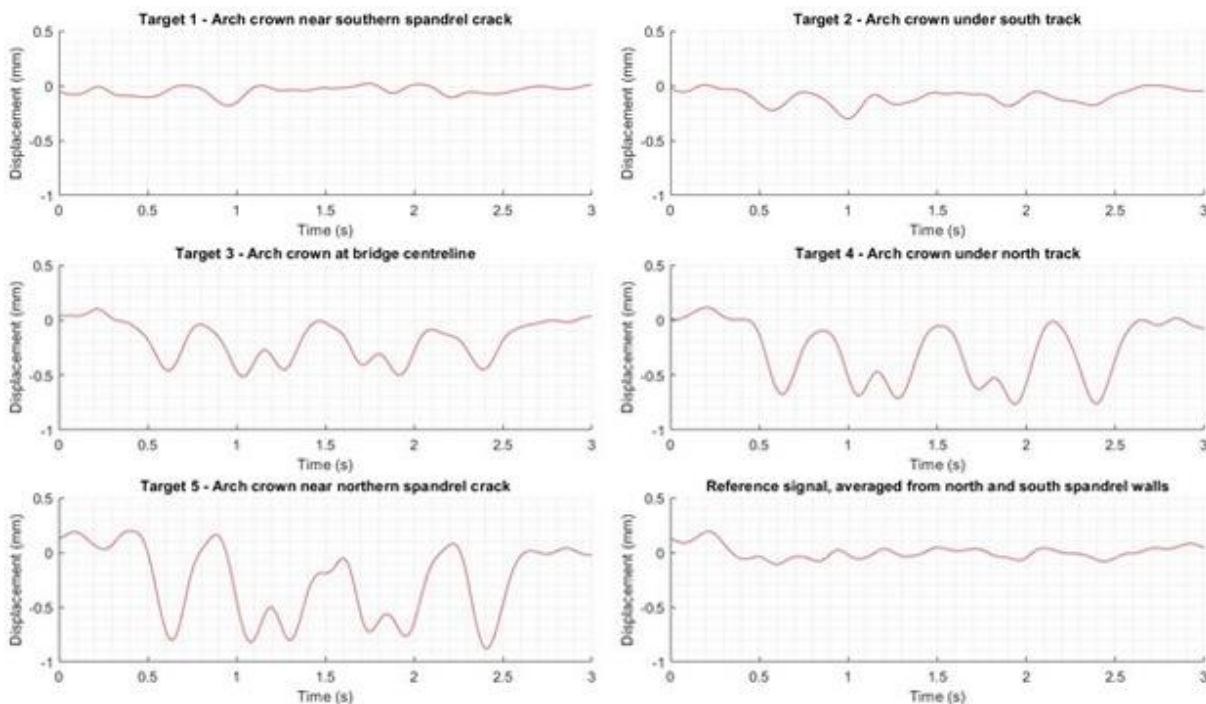


Figure 4.11: Typical processed time history of vertical deflections along the arch crown line, measured using videogrammetry, for a typical 2-carriage Class 150 passenger train

Because of the significantly improved performance of videogrammetry monitoring using the 75 mm lens, only data captured using this approach – in January and February 2019 – will be analysed further in this thesis. Table 4.2 gives an overview of the trains that were recorded in these months, grouped by train class and the track on which they passed over the bridge.

*Table 4.2: Summary of the train events recorded by videogrammetry monitoring at CFM-5, during January and February 2019*

<b>Train Class:</b>	<b>Passing on track:</b>	<b>Jan 2019:</b>	<b>Feb 2019:</b>	<b>Total:</b>
Class 185	North	5	11	16
	South	8	9	17
Class 150	North	5	7	12
	South	4	6	10
Class 222	North	3	3	6
	South	1	2	3
Overall total:				64

#### **4.4.2.3 Correcting for the choice of reference frame**

In Figure 4.10, the reference frames used to calculate displacements in the camera footage were presented. In February 2019, individual reference frames were generated for each of the artificial targets installed on the crown line, which runs along the depth of the bridge. However, displacement data recorded in January 2019 were measured in only two reference planes, defined at the north and south spandrel walls. Measurements at all targets along the crown line were generated in both reference frames.

In the January 2019 data, it was necessary to account for the fact that targets (other than those on the spandrel wall in question) were not located at the same distance from the camera as the reference frames initially used to calculate their displacements. Each pixel represents a greater amount of physical space at points further away from the camera; thus, a smaller number of pixels is needed to represent the same arch span distance at the north spandrel wall than at the south spandrel wall. Therefore, when Video Gauge performs calculations in the north spandrel reference frame, the size and displacements of targets towards the south side of the bridge are progressively overpredicted. The opposite is true for targets towards the north side of the bridge when these are considered in the south spandrel reference frame.

To correct for errors in the south spandrel reference frame, a simple multiplicative factor  $C_{depth}$  is applied to the displacement time histories:

$$C_{depth} = 1 + s \left( \frac{d_{target} - d_{S\_spandrel}}{d_{N\_spandrel} - d_{S\_spandrel}} \right) \quad (4.2)$$

Here,  $s = 0.3552$  is a scaling factor accounting for the different number of pixels required to represent the same distance at the north and south spandrel walls; this was evaluated using Video Gauge. The distances from the camera to the south spandrel wall, north spandrel wall, and target in question are, respectively,  $d_{S\_spandrel}$ ,  $d_{N\_spandrel}$ , and  $d_{target}$ . Errors induced in the north spandrel reference frame can also be accounted for, by dividing these measurements by  $C_{depth}$ .

## 4.5 Practical evaluation of the sensing technologies

A practical evaluation of the different monitoring technologies that have been used at CFM-5 was given in Thompson et al. (2019) and, in condensed form, in Cocking et al. (2019b). In this, data produced by different technologies were directly compared and the sensors were appraised against a variety of criteria, such as measurement resolution, noise, and sampling frequency. The sensitivity of sensors to environmental effects, and the complexity of sensor installation, operation, and data post-processing, were also considered. A summary of the main findings is presented here.

As discussed in section 4.2, fibre-optic and videogrammetry monitoring at CFM-5 were performed alongside further monitoring by AECOM, who installed a significant number of point sensors across the arch. These included Vibrating Wire Strain Gauges (VWSGs), measuring in-plane strains of the arch barrel, and crack sensors, containing LVDTs. These were installed to measure either crack opening or shearing displacements. VWSGs had gauge lengths of 165 mm while LVDTs had a gauge length of approximately 150 mm, although all movement recorded by these sensors was assumed to be concentrated in the crack response. AECOM also installed a laser distance meter, underneath the south track at the arch crown, to investigate this as a potential alternative to deflection pole monitoring. This measured absolute movements of the arch, with respect to the ground, using a laser targeted at the central line of the roadway below.

A comparison of measurements taken by the different monitoring technologies, during the passage of a typical, 4-carriage Class 222 passenger train, are given in Figure 4.12. Each subplot shows data captured at different locations across the bridge, where multiple technologies were

installed in close proximity. Figures 4.12(a) and 4.12(b) compare strain measurements taken by FBGs and VWSGs. Excellent agreement is observed at the north track centreline (Figure 4.12(b)); however, at the bridge centreline (Figure 4.12(a)) FBG strains are significantly higher than data from the corresponding VWSG. This is believed to be due to the difference in sensor gauge lengths – 1 m for the FBG compared to 0.165 m for the VWSG – and suggests that there is some concentration of strain outside of the region monitored by the VWSG. This result highlights the value of using a sufficient number of sensors to properly capture the full strain distribution. This is particularly important for structures such as masonry arch bridges, where a degree of nonlinearity may be expected in their behaviour and complex, local damage can sometimes lead to an unexpected structural response to loads.

Figures 4.12(c) and 4.12(d) compare vertical displacements recorded by FBGs, AECOM's crack sensors, and – at the arch crown (Figure 4.12(d)) – videogrammetry. Good agreement is observed but there are, in general, differences in the reported peak displacements. At the arch third point (the quarter point, for the FBG pair), in Figure 4.12(c), displacements from FBGs are approximately 0.14 mm larger than those from the LVDT crack sensors. Closer to the crown (Figure 4.12(d)), FBGs produce peak displacements that are approximately 0.09 mm below those of the LVDTs and 0.1 mm above those generated by videogrammetry.

All methods shown in these plots calculate displacements relative to the spandrel wall. According to manufacturer data, they should all have sufficiently high resolution and low noise to accurately capture these peak displacements – although it is noted that the LVDTs have a repeatability of only 0.125 mm and the noise of videogrammetry measurements was sometimes found to be as high as 0.3 mm, due to environmental effects on site.

A likely contributing factor is that it was not possible to install devices at the spandrel wall directly adjacent to each other. This can be seen in Figure 4.7, which shows a photograph of the devices installed at the south spandrel separation crack. Although the videogrammetry targets and LVDT crack sensor are approximately aligned with the arch crown, the former measure displacements of the arch barrel at a point slightly further away from the separation crack. In Chapter 6, it is shown that arch vertical displacements increase towards the spandrel separation crack on the loaded half of the bridge. Therefore, it is possible that the difference in these readings in Figure 4.12(d) reflects real bridge behaviour. The FBGs, meanwhile, were installed approximately 1 m to the side of LVDT crack sensors. Shearing displacements were seen to vary significantly along the length of the spandrel wall crack, rising towards the crown, and so this difference in the placement of sensors may be sufficient to explain their disagreement.

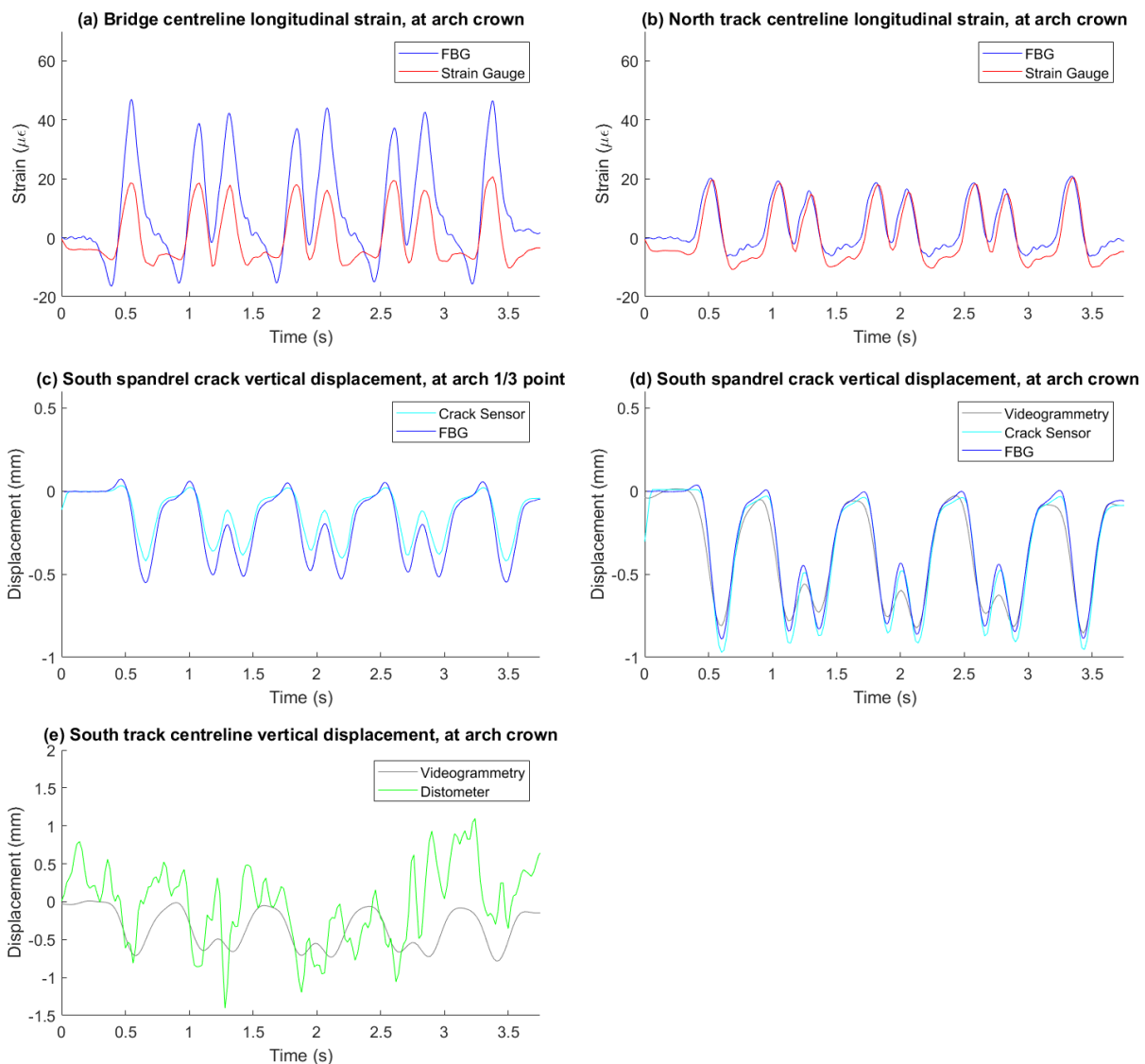


*Figure 4.12: Comparison of measurements taken with the various sensing technologies at CFM-5, during the passage of a typical 4-carriage Class 222 passenger train*

Lastly, in Figure 4.12(e), vertical displacement data are shown at the south track centreline for videogrammetry and the laser distometer. It is clear that the distometer cannot accurately capture the displacement time history and that its measurements are dominated by noise. This is believed to be due to the reflectivity and smoothness of the road central line being poorer than expected. It is also assumed, in this technique, that movements of the arch crown are wholly vertical, with no rotation of the arch barrel at this point. Even very small rotations could potentially alter the laser path enough to have a large adverse effect on measurement quality.

It was possible – on one occasion in September 2018, during a road closure in which 3D videogrammetry was also deployed – to directly compare the performance of the monitoring installation with deflection pole monitoring, which was performed at CFM-5 by AMEY. Videogrammetry and AECOM’s LVDT crack sensors were both found to yield measurements whose magnitudes were very slightly below those of the deflection pole data. This may be at least partly explained by both videogrammetry and the LVDTs measuring displacements of the arch barrel relative to the spandrel wall, whereas the deflection poles measured absolute movements of the bridge relative to the ground. Additionally, it is important to note that this monitoring was done during the day, and so there was sometimes significant drift in the videogrammetry data due to changing light conditions. For this reason, it is more informative to compare peak-to-peak displacements (rather than absolute displacements) between the technologies. Doing this, videogrammetry data with lower noise (due to environmental effects) perform similarly to LVDTs, relative to the deflection pole method (Thompson et al., 2019).

Table 4.3 summarises various characteristics of the sensing technologies used at CFM-5. These include physical properties of the sensors, such as sampling frequency and typical magnitudes of measurement noise in the field, together with practical considerations that are of relevance to practicing asset managers and engineers. For instance, the ease of installation may be critical at structures, such as CFM-5, which require disruptive and expensive road closures in order for devices to be installed. Likewise, the complexity of processing the raw data that are supplied by the monitoring system may have a significant impact on the labour costs associated with using these sensors in industrial applications. As may perhaps be expected, data processing is more onerous for FBG and videogrammetry monitoring, which are less established outside of research. Not mentioned in Table 4.3 is the additional complexity of matching remotely recorded data to specific train events. AECOM developed algorithms for this purpose, which successfully matched the majority of data to publicly available train timetable information.

## **4.6 Laser scan analysis of historic bridge deformations**

The laser scan gathered during the initial monitoring survey of CFM-5 (see section 4.2), was recorded in collaboration with Daniel Brackenbury (PhD student at the Cambridge University Engineering Department (CUED)). A point cloud resulting from this is shown in Figure 4.13. In addition to using this laser scan to validate the true geometry of the bridge – which was useful, for example, when calibrating the videogrammetry monitoring system on site – the laser scan has also been studied further. This analysis was done in collaboration with Simon Ye (PhD

student at CUED), in order to investigate long-term historic deformations of the arch geometry, and results were presented in Cocking et al. (2019c).

*Table 4.3: Practical characteristics of the various sensing methods used at CFM-5*

<b>Sensing technology:</b>	<b>Sampling frequency:</b>	<b>Typical noise:</b>	<b>Sensitivity to environmental effects (e.g., temperature, light conditions, wind)</b>	<b>Ease of installation:</b>	<b>Complexity of data processing:</b>
FBG	1 kHz	$\pm 1 \mu\epsilon$ (raw)	FBG sensors not sensitive to environmental effects; FBG interrogator exhibits problems at temperatures below $+5^\circ\text{C}$ .	Simple installation procedure for fibre-optic cables, with a short installation time for each sensor.	FBG strains can be visualised with minimal post-processing. Automated scripts allow rapid calculation of further results.
Videogrammetry	50 Hz	$\pm 0.5\text{-}1.0$ mm (raw); $\pm 0.1\text{-}0.3$ mm (filtered)	Highly sensitive to changing light conditions and camera vibrations, although data can be processed to remove some effects.	Artificial targets have a quick installation time (similar to FBGs). Calibration before monitoring may be time intensive.	Post-processing is needed to remove environmental effects before the quality of measurements can be established.
LVDT crack sensors	50 Hz	$\pm 0.5 \mu\text{m}$ (raw)	Operational range of $-30$ to $+125^\circ\text{C}$ .	Simple installation procedure using anchor resin.	Measurements can be visualised with minimal post-processing.
Vibrating wire strain gauges	50 Hz	$\pm 0.5 \mu\epsilon$ (raw)	Operational range of $-20$ to $+80^\circ\text{C}$ .	Setting of the resin increases installation time.	N/A. Signal-to-noise ratio is too poor to allow for meaningful post-processing.
Laser distometer	50 Hz	$\pm 1$ mm (raw)	Operational range of $-40$ to $+65^\circ\text{C}$ .		

Specifically, historic deformations are evaluated by comparing the detailed point cloud data against inferred reference geometries, such as planes and cylinders, which are fitted as estimates of the intended, ‘as-built’ geometry of the bridge, prior to the onset of any damage. Discrepancies between the point cloud of the bridge and this estimate of its original form are expressed as error maps, and used to quantify settlements which could have led the bridge to adopt its current, deformed state.

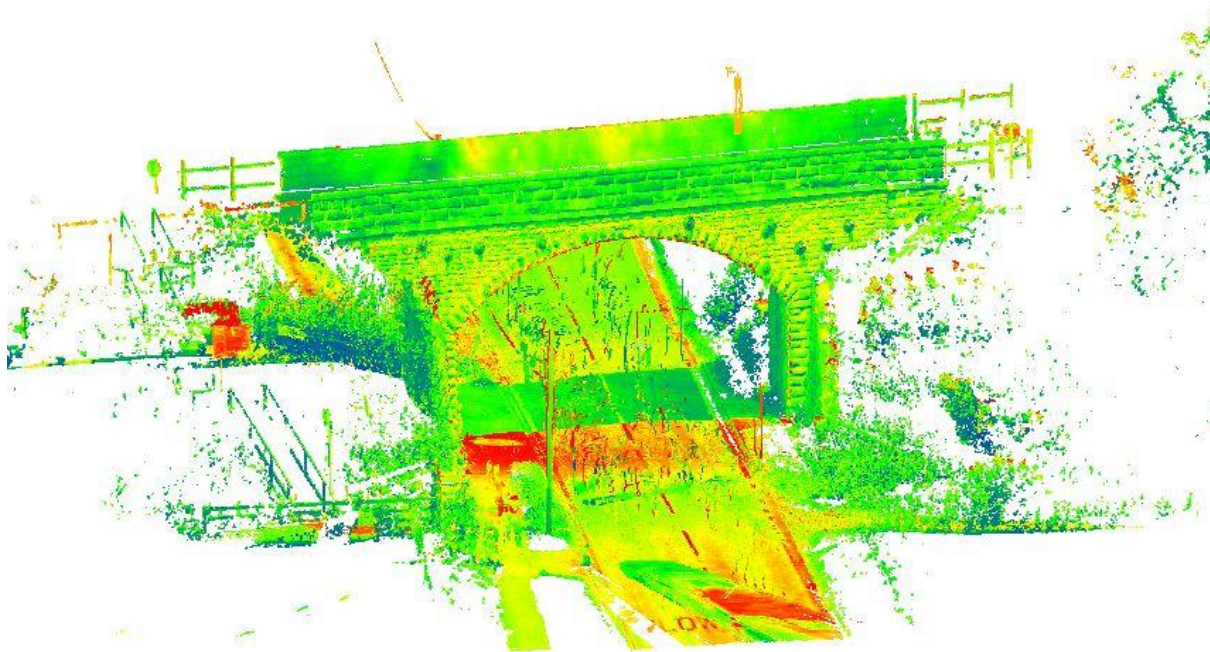


*Figure 4.13: The laser scan point cloud of bridge CFM-5, showing the south elevation*

Furthermore, these discrepancies, generated from the actual point cloud, can be compared against the theoretical discrepancies that would result from the most common theoretical deformation mechanisms, such as span opening or closing, or differential settlements. Inspection of the discrepancy features reveals which mechanisms are permissible, and the associated long-term movements are then inferred using the methodology developed by Ye et al. (2018).

#### **4.6.1 Overview of the LiDAR post-processing strategy**

Detailed point cloud data for CFM-5 were captured by Daniel Brackenbury, as noted above, using a FARO Focus 3D laser scanner. This LiDAR technology allowed for accurate

assessment of the ‘as-is’ geometry of the bridge. After segmentation of the point cloud to leave only the arch barrel, as shown in plan view in Figure 4.14, the remaining data were used to generate a best-fit cylinder representing the intended, ‘as-built’ form of the arch. An error map of deformations from this assumed original geometry was then created, by plotting the discrepancies between the real arch and the best-fit cylinder. It can be shown that the arch barrel is a cylindrical shell, where the axis of the cylinder is parallel with the bridge abutments (see section 5.1.2 for a fuller discussion of this).

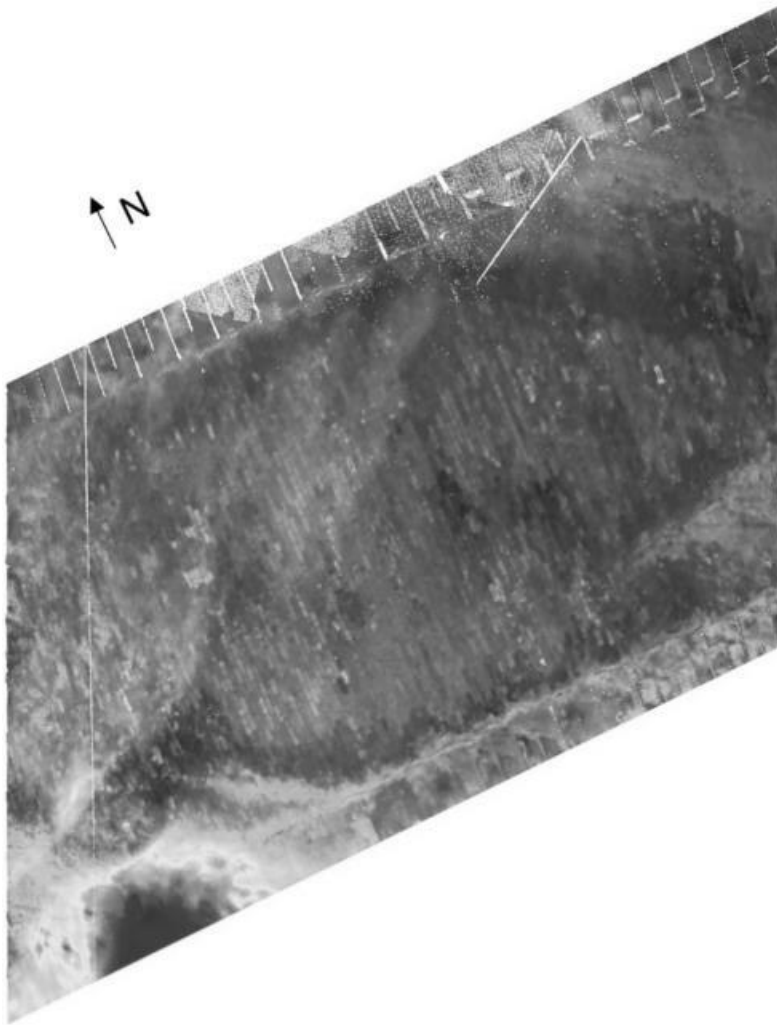


*Figure 4.14: Plan view of the arch barrel point cloud, following segmentation of this region (image by Simon Ye, after Cocking et al. (2019c))*

Individual ‘2D’ slices of the point cloud, as shown in Figure 4.15, were also analysed, against theoretical circular (or elliptical) segments which describe the assumed reference geometry. Because the axis of the best-fit cylinder is parallel with the bridge abutments, slices in the

skewed span direction will be elliptical whereas slices in the square span direction will be circular. Originally, slices were taken in both the square and skewed span directions for further investigation. However, it was found that slices in the skewed span direction were mostly dominated by noise and could not be resolved into a sensible deformation mechanism. Therefore, only the slices in the square span direction will be presented here.

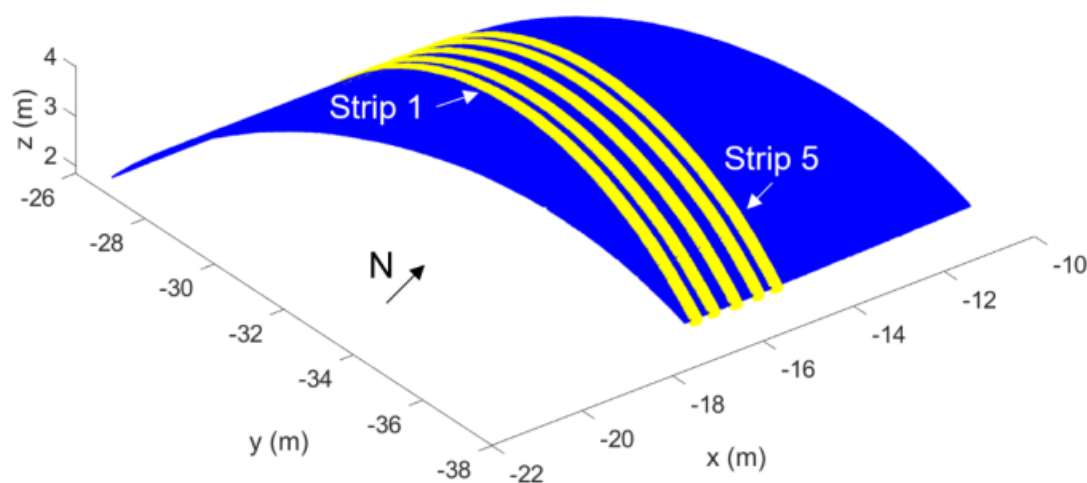


Figure 4.15: Slices analysed in the square span direction (image by Simon Ye, after Cocking et al. (2019c))

#### 4.6.2 Comparison with standard mechanisms

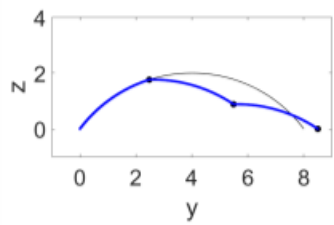
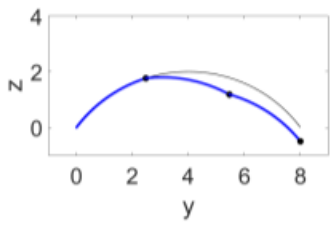
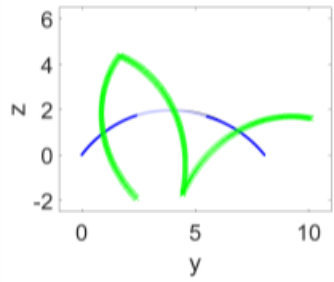
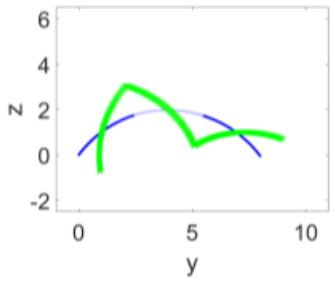
Once a slice has been compared with its best-fit circular geometry, the resulting error map, with discrepancies magnified to aid visualisation, can be compared against error maps of standard arch mechanisms that would result from common long-term deformations, such as span opening or closing or differential support settlement. Inspection of the error maps reveals which mechanisms are compatible with the deformed geometry. These permissible mechanisms can then be fitted against the actual error map to infer the likely magnitudes of support movements. Previous work has established that this method can produce informative results for masonry arch bridges and viaducts (Ye et al., 2018). However, this is the first time that the method has been extended to skewed arch bridges.

Although the database contains several standard mechanisms for arch deformation, only two were found to be feasible for the data slices analysed at CFM-5. These are two partial asymmetric mechanisms for span opening and for relative settlement of one abutment, respectively. These mechanisms are presented in Table 4.4.

### 4.6.3 Results and discussion

As stated in section 4.6.1, the original ‘as-built’ geometry of the arch barrel is assumed to be approximately cylindrical, with the axis of this cylinder aligned with the square transverse direction. Additionally, it can be assumed that the axis of this cylinder was intended to lie in a horizontal plane, although a combination of construction processes and differential settlements may ultimately result in this not being the case.

Table 4.4: Permissible historic deformation mechanisms (images by Simon Ye, after Cocking et al. (2019c))

Mechanism:	Span opening	Settlement of right support
Schematic diagram*		
2D error map**		
<p>* In schematic diagrams: black line = ideal shape, blue line = schematic distorted shape, black dot = plastic hinge.  ** In 2D error maps: alternating colours (dark and light blue) = distorted shape, green = distorted geometry (magnified 100 times) with respect to the fitted shape.</p>		

For this reason, it is informative to consider two cases when fitting a best-fit cylinder to the point cloud data. The first case assumes that the best-fit cylinder will have its axis lying in a horizontal plane, while the second assumes that either the span was not built level, or the barrel has rotated as part of its deformation history. These cases correspond respectively to the error maps in Figures 4.16(a) and 4.16(b), which plot the difference between the point cloud data and the best-fit cylinder for either case.

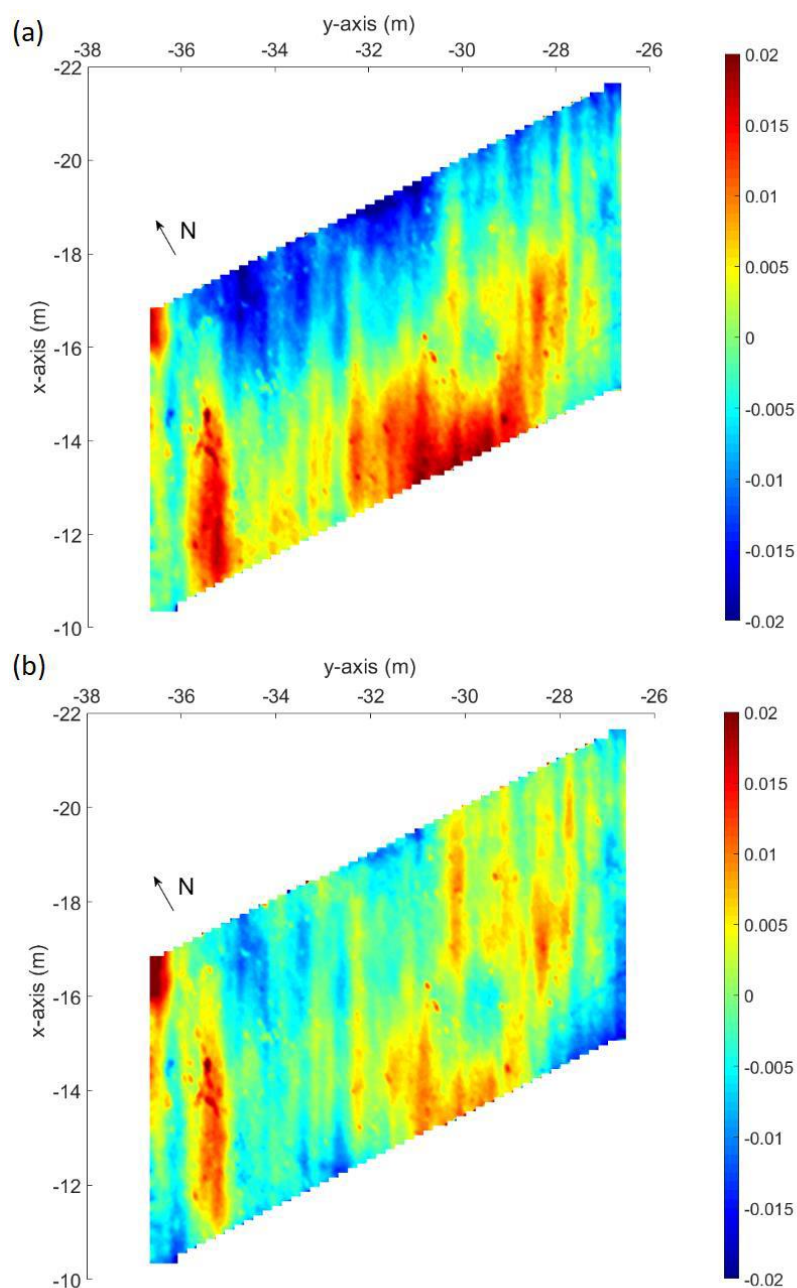


*Figure 4.16: Best-fit cylinders for the CFM-5 arch barrel, for (a) a cylinder that is constrained to have its axis in a horizontal plane, and (b) a cylinder with no constraints applied; colour bar values in m: positive values (red) signify upwards movement, negative values (blue) signify downwards movement (image by Simon Ye, after Cocking et al. (2019c))*

It can be seen in Figure 4.16(a) that the error map is dominated by rotation of the barrel. In Figure 4.16(b), after the rotation has been accounted for, deformation bands can be more easily identified and are consistently oriented with the square transverse direction. The axis of the

best-fit cylinder for Figure 4.16(b) is inclined by  $0.02^\circ$  from the horizontal, corresponding to a variation in elevation of approximately 23 mm across the width of the bridge.

Next, the analysis of individual slices from the point cloud is considered. As previously mentioned, only slices aligned with the square span direction were found to give sensible results, which were sufficiently consistent between strips. This is in keeping with the error map of Figure 4.16(b) in which deformation bands are aligned with the transverse of this direction. Five slices were analysed, the locations of which were shown in Figure 4.15.

#### **4.6.3.1 Potential historic deformation mechanisms**

The error maps in Figure 4.17 correspond to viewing the arch from the south and perpendicular with the square span direction. These suggest a partial asymmetric mechanism with movements occurring at the western abutment. Two possibilities exist which could produce error maps of this type. As indicated previously in Table 4.4, these correspond to either span opening, resulting from outwards horizontal movement of the western skewback, or to vertical settlement of this skewback. In practice, the true deformations could also be the result of a combination of both mechanisms.

It can also be seen from Figure 4.17 that the error maps show a larger response towards the north of the bridge, indicating larger arch deformations and associated support movements towards the north end. Fitting the two potential mechanisms to Strips 3 and 5 produces Figure 4.18, in which the first column corresponds to results for arch spreading and the second column to results for differential settlement.

The likely support movements that give the theoretical error maps in Figure 4.18 are presented in Table 4.5. The data indicate that the current geometry of the bridge could be caused by differential movement of the western skewback (between Strips 3 and 5) of either 1 cm, if only horizontal abutment movement occurred, or 3 cm, if only vertical abutment settlements occurred. These predictions assume that each mechanism acts alone and so provide upper limits on the potential differential movements in each direction. Note that this LiDAR analysis can predict likely settlements to within approximately 0.5 centimetres. This is because the measured point cloud data, on which these predictions are based, are accurate to within several millimetres.

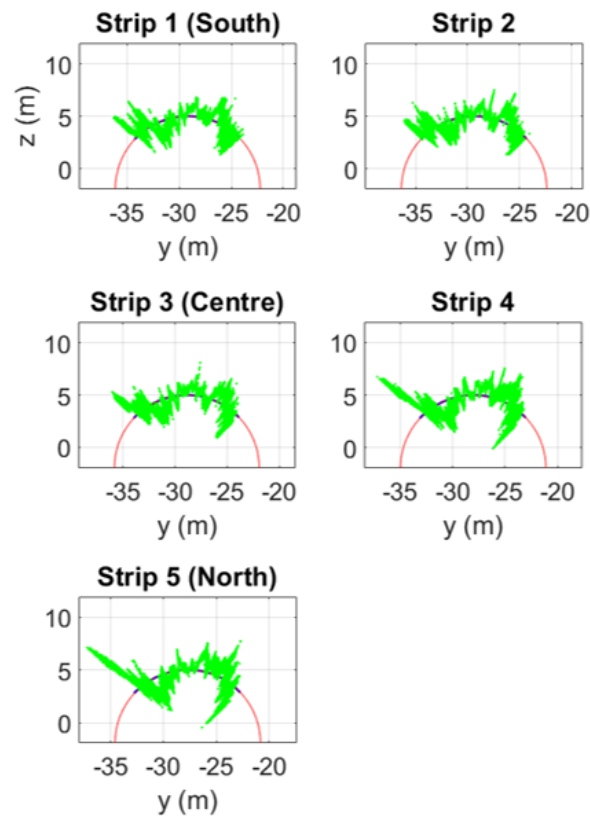


Figure 4.17: 2D error maps of the point cloud slices (image by Simon Ye, after Cocking et al. (2019c))

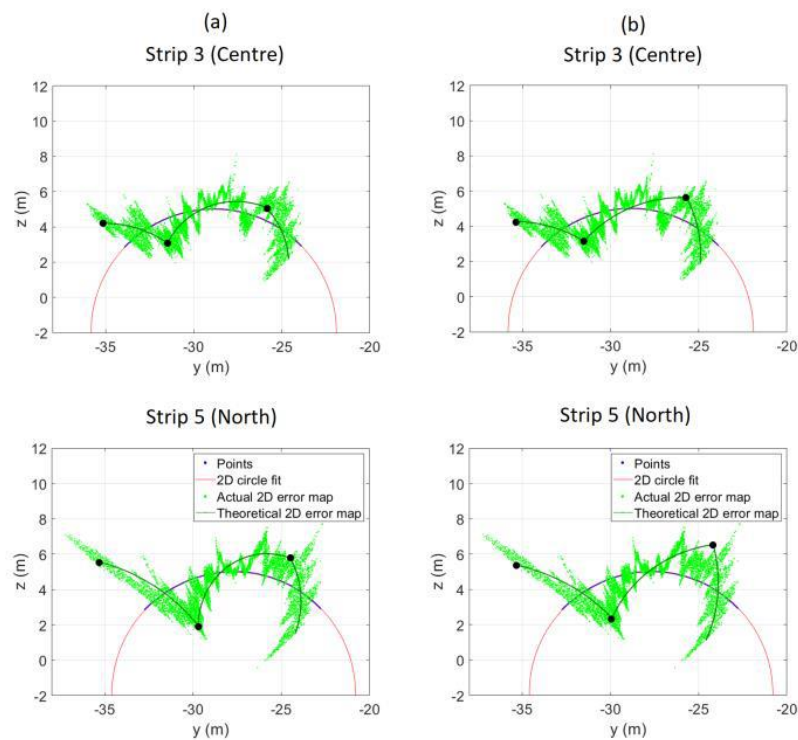


Figure 4.18: Fitted theoretical mechanisms for (a) arch spreading and (b) relative vertical settlement of the western skewback (image by Simon Ye, after Cocking et al. (2019c))

While it cannot definitively be concluded whether the abutment movement was vertical or horizontal, the potential of horizontal movement to explain the results seems more feasible. The typical assumption that an arch preferably spans square would lead to a larger thrust at the north-west corner of the arch than along the rest of the length of the western skewback. This increased thrust could reasonably have caused a local horizontal movement of the north-western corner, enabling load redistribution of the thrust. This could provide an explanation of the small tensile strains seen currently in the north-western corner of the bridge (discussed later, in section 6.1.2). These strains could be an indication of transverse bending, which would provide an alternative load path if the structure had previously begun to yield in this region.

Note that this finding agrees with the hypothesis by Harvey (2004) that, given the significant plan stiffness of masonry arches, only very minor abutment movements at the obtuse corners – resulting from the off-centre thrusts applied by a skewed arch initially spanning square – would be required in order for the arch behaviour to change such that it spanned skew.

Lastly, the likely support movements estimated for the mechanism of differential vertical settlement are significantly higher than those for span opening. While the latter could feasibly be realised through the deformation history of the bridge, the former could most likely only be achieved if the as-built geometry already deviated from the assumed reference geometry.

*Table 4.5: Predicted support movements at the western skewback*

<b>Mechanism:</b>	<b>Horizontal movement (arch spreading)</b>	<b>Relative vertical settlement</b>
Predicted movement at Strip 3 (Centre)	1 cm	4 cm
Predicted movement at Strip 5 (North)	2 cm	7 cm

## 4.7 Conclusions

In this chapter, the CFM-5 bridge has been introduced. An overview of its construction, existing damage, and recent repair work was first presented, which provided the motivation for regular condition monitoring. Given the uncertainty surrounding the evolution of this historic damage, repair work was notably extensive, and it was critical to track the effectiveness of this intervention in arresting further progression of damage over time. It was also noted that the location of this bridge, which spans a busy, rural road used by lorry freight, meant that it was

impractical to use Network Rail's standard approach of deflection pole monitoring, as each shift using this technique would require disruptive road closures. As a result, this bridge became the focus of a detailed SHM campaign, which sought to examine potential alternatives to the deflection pole method, looking particularly at remote and automated monitoring technologies.

This monitoring installation was developed collaboratively between the asset owner Network Rail, AECOM, and the Centre for Smart Infrastructure and Construction at the University of Cambridge. The process of developing the installation was described, with particular focus paid to the technologies deployed by the author: fibre-optic monitoring, using Fibre Bragg Gratings, and videogrammetry. New clamp designs were introduced to allow novel implementations of the FBGs, which could now monitor an increased range of parameters at the bridge. New target designs were also created to aid videogrammetry monitoring. The field set-up of videogrammetry camera equipment was then presented, which was important in order to minimise potential errors in this approach.

Basic post-processing strategies for the FBG and videogrammetry data were presented, in order to clean the data – including the removal of environmental effects, in the case of videogrammetry data – and categorise them for detailed analysis. This analysis is the subject of the following Chapters 5 and 6, and further, application-specific post-processing is described in the relevant sections of these chapters.

A comparison of the various monitoring technologies deployed at CFM-5, by both the author and AECOM, was then presented. This incorporates a discussion of measurement quality, including the direct comparison of data obtained in adjacent locations on the bridge with different technologies, and an overview of practical considerations likely to be of relevance to asset managers and engineers looking to use these technologies outside of the research domain.

Lastly, a research study was described in which laser scan data were utilised to investigate historic, long-term deformations of the bridge geometry. In this, laser scan data were used to generate a best-fit approximation of the original structural geometry, and distortions of the current geometry relative to this original form were visualised as error maps. Using an existing library of error maps resulting from common arch deformation mechanisms (Ye et al., 2018), permissible support movements that could have caused the current, deformed state of the arch at CFM-5 were quantified and assessed. Plausible support movements in the square span direction were identified. These could indicate a historic load path with thrusts oriented in this direction, prior to the yielding of these supports which potentially led to load redistribution and the onset of the live load response currently observed at the bridge.



# Chapter 5

## Dynamic structural behaviour of the arch bridge

### 5.1 Introduction

This chapter examines detailed distributions of the longitudinal strains, and crack opening and shearing displacements, under typical train loading at the CFM-5 bridge. Statistical distributions of the longitudinal strain response are also considered and found to demonstrate remarkable consistency across a large number of train events, for a given train class. This is the case for both instantaneous strains, occurring when train axles reach key locations along the bridge span, and for the maximum peak-to-peak strains in the overall response.

Sources of variability in these responses are considered, such as train speed and the time of day. The latter is a proxy for passenger levels and hence the precise axle loading applied by a train. Strain amplification for trains travelling at high speeds is observed only for FBGs located close to the arch crown, where there is less fill material between the arch and track and therefore loads are more concentrated. Furthermore, some variability in crack opening responses to ambient temperature is also observed.

#### 5.1.1 Overview of the relevant FBGs

Of the 74 FBGs that were installed on the arch soffit at CFM-5, 34 are discussed in this chapter. Results for the remainder of the FBG installation are presented separately in Chapter 6. The installation locations of the FBG sensors which will be discussed in this chapter are shown in Figure 5.1. Key accompanying dimensions are given in Table 5.1. Values for the thickness of the arch barrel and the depth of ballast and fill material are based on inspection reports and

could not be independently verified in this study. The FBGs in Figure 5.1 monitor three key regions of the bridge:

1. FBGs L1 to L20 were installed in two longitudinal lines of ten FBGs each along the arch intrados, directly underneath the centreline of the north track and the overall bridge centreline. There are no visible signs of damage in this region, and so these sensors are used to investigate the general structural behaviour of a skewed masonry arch railway bridge. Specifically, in this chapter, the sensitivity of this longitudinal response to various parameters is investigated in detail. These FBGs were installed with gauge lengths of 1 m.
2. FBGs SE1 to SE8 measure the in-plane crack opening of the south-eastern longitudinal crack. These FBGs were installed with gauge lengths of 0.5 m, and at 0.5 m intervals along the length of the crack. In this way, FBG SE1 is located at the crack root, FBG SE7 is located at the crack tip, and FBG SE8 is located just ahead of the crack tip in masonry that is not currently visibly cracked.
3. FBGs SS1 to SS6 were installed in pairs, in three locations along the south spandrel separation crack. These locations were either side of the arch crown, at the  $\frac{5}{12}$  and  $\frac{7}{12}$  points of the arch span, as well as the eastern  $\frac{1}{4}$  point. A schematic of a typical FBG pair is shown in Figure 5.2. It can be seen that one fibre is installed in the in-plane transverse direction of the arch, to measure pure crack opening, while the second fibre is inclined so that it measures both crack opening and crack shearing, or ‘pumping,’ in the vertical direction. With the data from both sensors, it is possible to calculate the relative vertical movement across the crack (i.e., movements parallel to  $c$  in Figure 5.2). These readings were validated against other measurement technologies which recorded the relative vertical displacements directly (see section 4.5, and Cocking et al., 2019b).

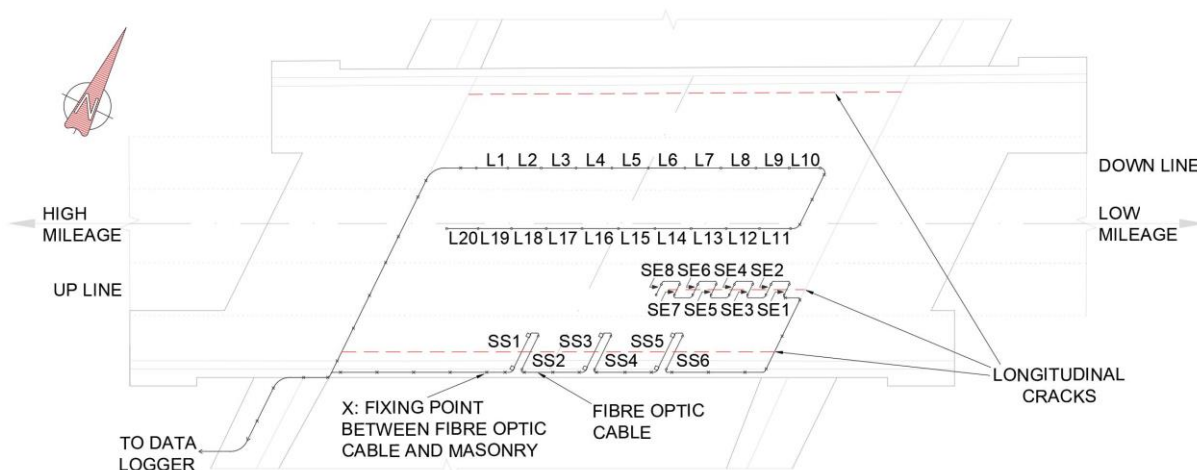
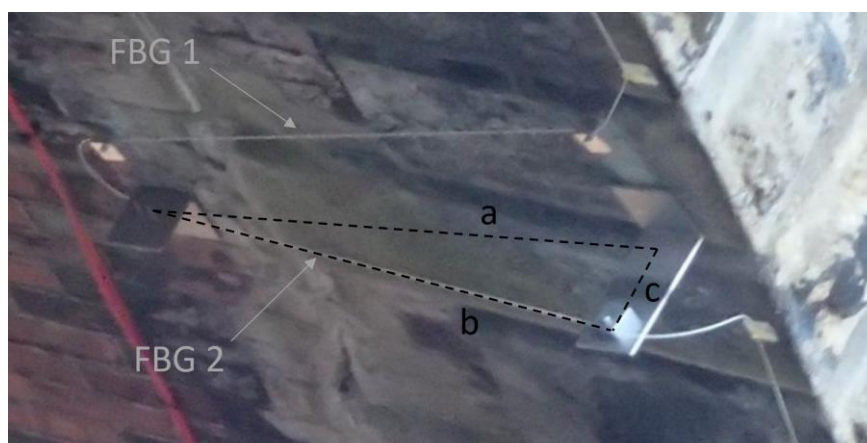


Figure 5.1: Plan view of the arch soffit at CFM-5, showing the FBGs relevant to this chapter



a: parallel to FBG 1

b: parallel to FBG 2

c: parallel to desired measurement

Figure 5.2: A typical 'FBG pair' installed at the south spandrel separation crack

Using the notation in Figure 5.2, the fibre measuring pure crack opening has a gauge length of  $a = 1\text{m}$ . This fibre is parallel to the transverse direction of the arch barrel, while one end of the second fibre in this pair is displaced by  $c = 150\text{mm}$ . As a result, the gauge length of this second fibre is  $b = \sqrt{a^2 + c^2} = 1.011\text{m}$ . Relative movements across this spandrel separation crack are known to be small in magnitude, such that there is negligible change to the interior angles of this triangle.

Therefore, as movements across the crack occur, the new side lengths of this triangle are given by Equation (5.1):

$$(b + \Delta b)^2 = (a + \Delta a)^2 + (c + \Delta c)^2 \quad (5.1)$$

Here,  $\Delta c$  corresponds to the vertical, out-of-plane, displacements of the arch barrel relative to the spandrel wall. This is of interest but cannot be directly measured.  $\Delta a$  and  $\Delta b$  correspond to the axial extensions of the fibres in these two directions (see Figure 5.2) and can hence be related to the measured FBG strains by Equations (5.2) and (5.3) below.  $\Delta a$  is also the in-plane component of the crack opening movements.

$$\epsilon_a = \frac{\Delta a}{a} \quad (5.2)$$

$$\epsilon_b = \frac{\Delta b}{b} \quad (5.3)$$

Rearranging Equation (5.1) and substituting for  $\Delta a$  and  $\Delta b$  results in Equation (5.4), a quadratic in  $\Delta c$  in which all else is known. Solving this for each instance in time yields the dynamic ‘pumping’ displacements of the arch barrel relative to the spandrel wall.

$$\Delta c^2 + 2c \cdot \Delta c + [c^2 + a^2(1 + \epsilon_a)^2 - b^2(1 + \epsilon_b)^2] = 0 \quad (5.4)$$

### 5.1.2 Impact of arch curvature on FBG measurements

FBGs L1 to L20, installed in the skewed longitudinal direction of the bridge, are clamped to the arch soffit such that their gauge length, along the fibre axis, is always 1 m. It is worth considering whether the curvature of the arch barrel in this direction – which means that the corresponding arclengths for sections of masonry between two adjacent clamps are slightly greater than 1 m – causes any appreciable errors in the FBG strains, which are measured along their fibre axes. Upon computing these arclengths, however, the impact is found to be small.

The arch barrel is a circular cylindrical shell with its axis oriented along the square transverse direction (the dashed line parallel to North in Figure 5.1). This cylinder has radius  $R_{sq}$  which is given by:

$$R_{sq} = \frac{h}{2} + \frac{L_{sq}^2}{8h} \quad (5.5)$$

Here,  $h$  is the arch rise – the height of the crown above the springings – and  $L_{sq}$  is the square span. Values for  $h$  and  $L_{sq}$  are given in Table 5.1; using these,  $R_{sq}$  is found to be 6875 mm.

Equation (5.5) results from viewing the arch along the cylinder axis. From this perspective, the arch is a circular arc whose end points also define a chord of length  $L_{sq}$ ; hence  $h$  is the sagitta.

This arc also defines a sector of angle  $\theta$ , given by:

$$\tan \frac{\theta}{2} = \frac{L_{sq}/2}{R_{sq}-h} \quad (5.6)$$

Table 5.1: Key dimensions at bridge CFM-5

Dimension:		Value:
Bridge width (square span direction)		9.44 m
Bridge width (skew span direction)		8.46 m
Bridge span (square span direction), $L_{sq}$		10.61 m
Bridge span (skew span direction), $L_{sk}$		11.83 m
Skew angle, $\alpha$		26°
Height of arch springings (above ground)		3.92 m
Arch rise, $h$		2.50 m
Arch thickness		0.457 m
Depth of fill and ballast at the crown, between arch extrados and sleepers		0.352 m
FBG gauge lengths	Longitudinal FBGs (L1 to L20)	1 m
	FBGs across the south-eastern crack (SE1 to SE8)	0.5 m
	FBGs at the south spandrel crack measuring crack opening (SS1, SS3, SS5) – $a$ in Figure 5.2	1 m
	FBGs at the south spandrel crack measuring relative vertical displacements (SS2, SS4, SS6) – $b$ in Figure 5.2	1.011 m

$\theta$  is found to be  $101^\circ$ , or 1.763 rad. From this, the arclength,  $s_{sq}$  – in other words, the curved length of a slice of the arch in the square span direction – can be simply found:

$$s_{sq} = R_{sq}\theta \quad (5.7)$$

This gives  $s_{sq} = 12119$  mm.

It is slightly more complicated to evaluate a slice of the arch in the skew span direction. Such a slice can be precisely defined by the intersection of the circular cylinder with a plane oriented to its axis at an angle  $\beta = 90^\circ - \alpha$ . For CFM-5,  $\alpha = 26^\circ$  and hence  $\beta = 64^\circ$ . This intersection will be an ellipse, of eccentricity  $e = \cos \beta = 0.44$ . Its semi-major axis is  $a = \frac{R_{sq}}{\sin \beta} = 7650$  mm, while its semi-minor axis is  $b = a\sqrt{1 - e^2} = 6870$  mm.

Points on the ellipse can be defined in  $x, y$  coordinates, where  $-b \leq x \leq b$  and  $y = b\sqrt{1 - \frac{x^2}{a^2}}$ .

The coordinates corresponding to the locations of two adjacent FBG clamps also have the following constraint, based on the gauge length of the fibre between them:

$$\sqrt{(x_{i+1} - x_i)^2 + (y_{i+1} - y_i)^2} = 1000 \text{ mm} \quad (5.8)$$

The arclength between these two points on the ellipse can be found by numerically evaluating the following incomplete elliptic integral of the second kind:

$$s = -b[E(z|m)]_{z_i}^{z_{i+1}} \quad (5.9)$$

Here,  $\cos z_i = \frac{x_i}{a}$  and  $m = 1 - \frac{a^2}{b^2}$ .

Using this integral to evaluate the curved length of an arch slice in the skew span direction gives  $s_{sk} = 13226$  mm. Note that if the slice had been approximated as circular, following the approach in Equations (5.5) to (5.7), then this would have yielded  $s_{sk} = 13198$  mm, an error of 0.21%.

Starting from the FBG clamp at the arch crown ( $x_0 = 0, y_0 = b$ ) and enforcing the constraint in Equation (5.8), the coordinates of the FBG clamps on one side of the arch can be identified, and the arclengths between these clamps evaluated using Equation (5.9). The results are presented in Table 5.2.

The critical FBGs are those closest to the arch haunches, where the curvature of the arch is highest: FBGs L1, L10, L11, and L20 in Figure 5.1. The sections of masonry at these FBGs all have an arclength of 1.0007 m, only 0.07% higher than the FBG gauge length. The impact of

arch curvature is therefore small enough to neglect. For comparison, placing a clamp incorrectly by 1 mm during installation would give rise to a 0.1% error in the longitudinal strains calculated by the FBGs on either side of this clamp.

*Table 5.2: Locations of FBG clamps on one side of the skewed arch span, and the elliptical arclengths between them*

Clamp x coordinate (mm):		Clamp y coordinate (mm):		Arclengths (mm):	
$x_0$	0	$y_0$	6870		
$x_1$	998.3	$y_1$	6811.3	$s_1$	1000.6
$x_2$	1982.7	$y_2$	6635.3	$s_2$	1000.6
$x_3$	2939.0	$y_3$	6342.8	$s_3$	1000.6
$x_4$	3852.3	$y_4$	5935.4	$s_4$	1000.7
$x_5$	4706.8	$y_5$	5415.8	$s_5$	1000.7

## 5.2 Typical strain and displacement distributions in the bridge

Monitoring data were recorded for a range of passenger trains, on each monthly monitoring shift between September 2018 and February 2019. The data were categorised by train class and direction, which corresponded to the track on which the train had passed over the bridge. Information was then assigned to each data file to represent the date and time of the measurement, the ambient temperature (measured by other point sensors), and the train speed (calculated using the FBG data themselves, as described earlier in section 4.3.3.3). This allowed different groupings of data to be analysed, to better investigate the sensitivity of the strain response to individual variables while minimising the influence of other variables. The variables considered in this analysis were train speed, ambient temperature (to investigate the impact of any seasonality on the response, through thermal expansion or contraction of the bridge), time of day (which was used as a proxy for passenger loading, by differentiating between peak and off-peak trains), and date (to investigate any potential long-term trends, or deterioration of the bridge over time).

In the following sections, results for Class 185 trains are presented and discussed. These have been chosen as representative SLS loading for CFM-5, since they are the most common train class to pass over this bridge.

### 5.2.1 Arch intrados: longitudinal strains

A typical distribution of longitudinal strains along the arch intrados, as a Class 185 train passes over the bridge on the northern track, is shown in Figure 5.3. In this figure, plots for the individual FBG responses are arranged so that the direction of travel of the train is from the top to the bottom of the overall figure, with the train travelling directly above the FBGs in the left-hand column. Thus, the train passes first over FBG L1 and last over FBG L10, as it travels east. Note that, after FBG L10, the fibre-optic cable returns westward along the centreline of the bridge, so that FBG L20 is the first to detect the passage of a train on the northern track and FBG L11 is the last. This sequence can also be seen in the FBG installation plan in Figure 5.1.

The FBG strain data shown in Figure 5.3 onwards have been processed using a low-pass filter, to remove high-frequency noise in the signals (see section 4.3.3.1). For FBGs close to the arch crown – such as FBGs L5, L6, L15, and L16 – where there is less potential for load distribution to occur through the backfill before loads are transmitted into the arch, it is still possible to identify the individual axles on each bogie of the train. For FBGs in other locations, these axles tend to merge into a single peak corresponding to each bogie. In such locations, the time history of the strain response is composed of single peaks at the start and end of the response, corresponding to the first and last bogies of the train, with intermediate double peaks in which the rear and leading bogies of adjacent carriages are both visible.

Throughout the figures, tensile strains are plotted as positive while compressive strains are negative. Note that the measured strains are purely the result of dynamic train loading and do not include the substantial, pre-existing compressive strains caused by the dead load of the bridge.

Using the monitoring data for this typical train event, the instantaneous strain distributions across all longitudinal FBGs can be plotted for times of interest. Examples are shown in Figure 5.4, with distributions included that correspond to the critical axle load of the train from Figure 5.3 being applied above FBGs: (a) L18, the western third point, (b) L16, just west of the arch crown, (c) L15, just east of the arch crown, and (d) L13, the eastern third point. These responses – corresponding to progressive instances in time during the passage of this train – are plotted, respectively, as dotted, dot-dashed, dashed, and solid lines, whose colour varies progressively from black to light grey.

In each case, a bulb of positive, tensile strains is observed in the vicinity of the applied load, with compressive strains either side of this bulb. This observation supports the notion that a potential load path for these applied forces is through arching action in this longitudinal

direction. Furthermore, the instantaneous intrados strain distributions in Figure 5.4 are consistent with the anticipated thrust lines for concentrated loads applied at locations (a) to (d) along the span, which are also shown schematically in Figure 5.4. Close to the applied load the thrust line will pass nearer to the arch extrados, so that strains at the intrados are tensile. Outside of this region, the thrust line will be nearer to the intrados, and intrados strains will therefore tend to become compressive.

The distributions in Figure 5.4 also demonstrate that the largest tensile strains occur close to the arch crown when loads are applied directly overhead: the symmetric loading case. This is to be expected because close to the crown there is the least backfill material between the arch and the track and therefore the least opportunity for load distribution to occur before the load path enters the arch. The largest compressive strains, meanwhile, are observed on either side of the arch at times when loads are applied on the opposite side: the asymmetric loading case. Again, this is to be expected, as the asymmetric loading case will cause the thrust line to pass closer to the intrados in the locations where peak compressive strains are observed (see schematic thrust lines (a) and (d) in Figure 5.4).

The largest peak-to-peak strains are observed at the arch  $1/3$  points. This can also be seen later in Figure 5.9, which plots the statistical distribution of peak-to-peak strains for all available data.

When trains pass on the northern track, the largest magnitude response is observed in FBGs L1 to L10, located directly underneath the active track. Although the pattern of strains along the bridge centreline is very similar, the strain magnitudes here are reduced; they are in the range of 50-90% of the values observed in corresponding FBGs under the north track centreline.

Although not included here, the longitudinal distributions that are obtained for trains passing on the southern track are, once again, similar other than a reduced strain magnitude. In this case, the largest strain magnitudes are observed in FBGs L11 to L20 along the bridge centreline, with the corresponding strains in FBGs L1 to L10 presenting magnitudes approximately 45-55% of those measured along the bridge centreline.

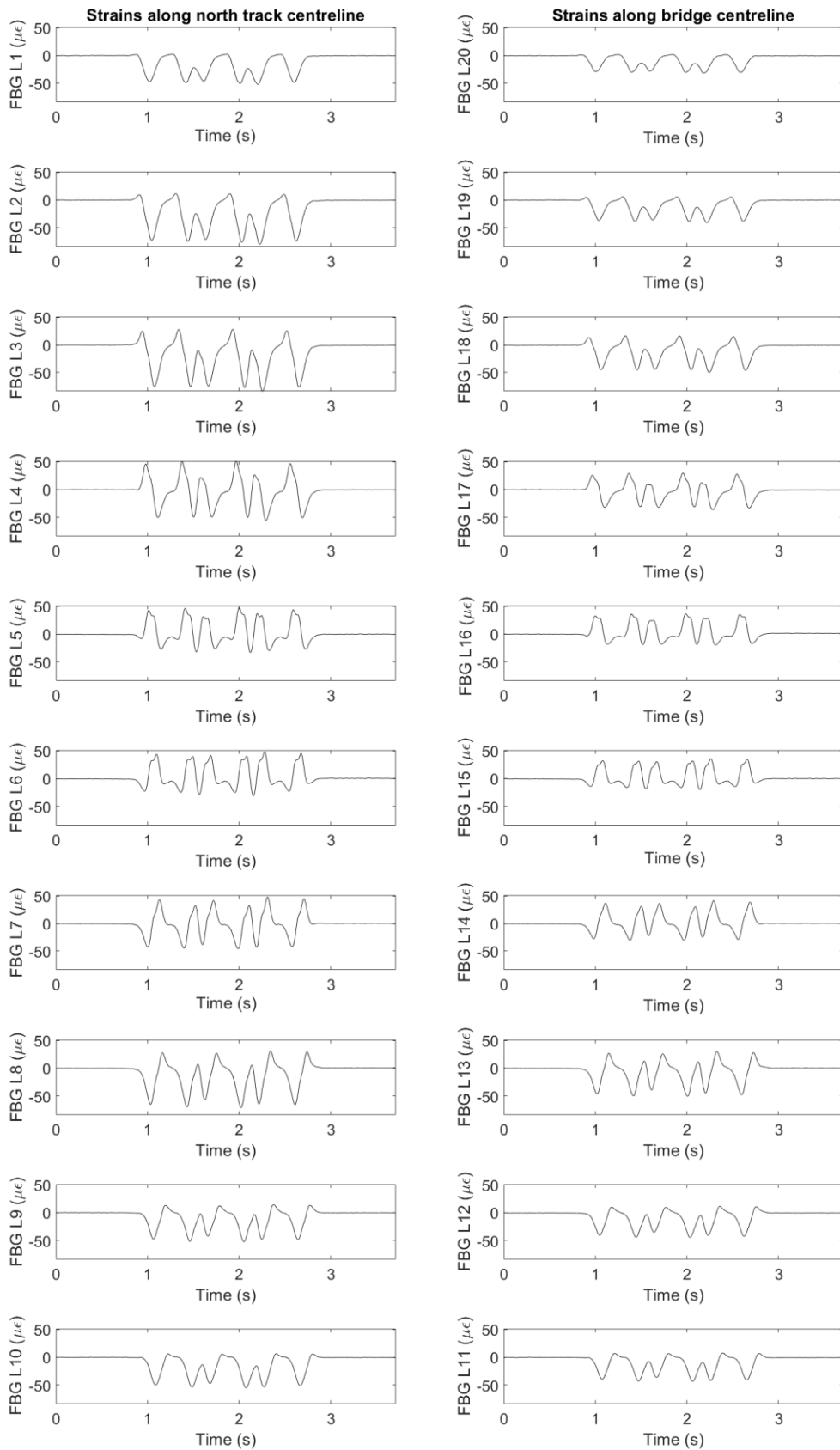


Figure 5.3: Typical time histories of the longitudinal strains at the arch intrados, for a Class 185 train passing on the northern track (tensile strains are positive; compressive strains are negative)

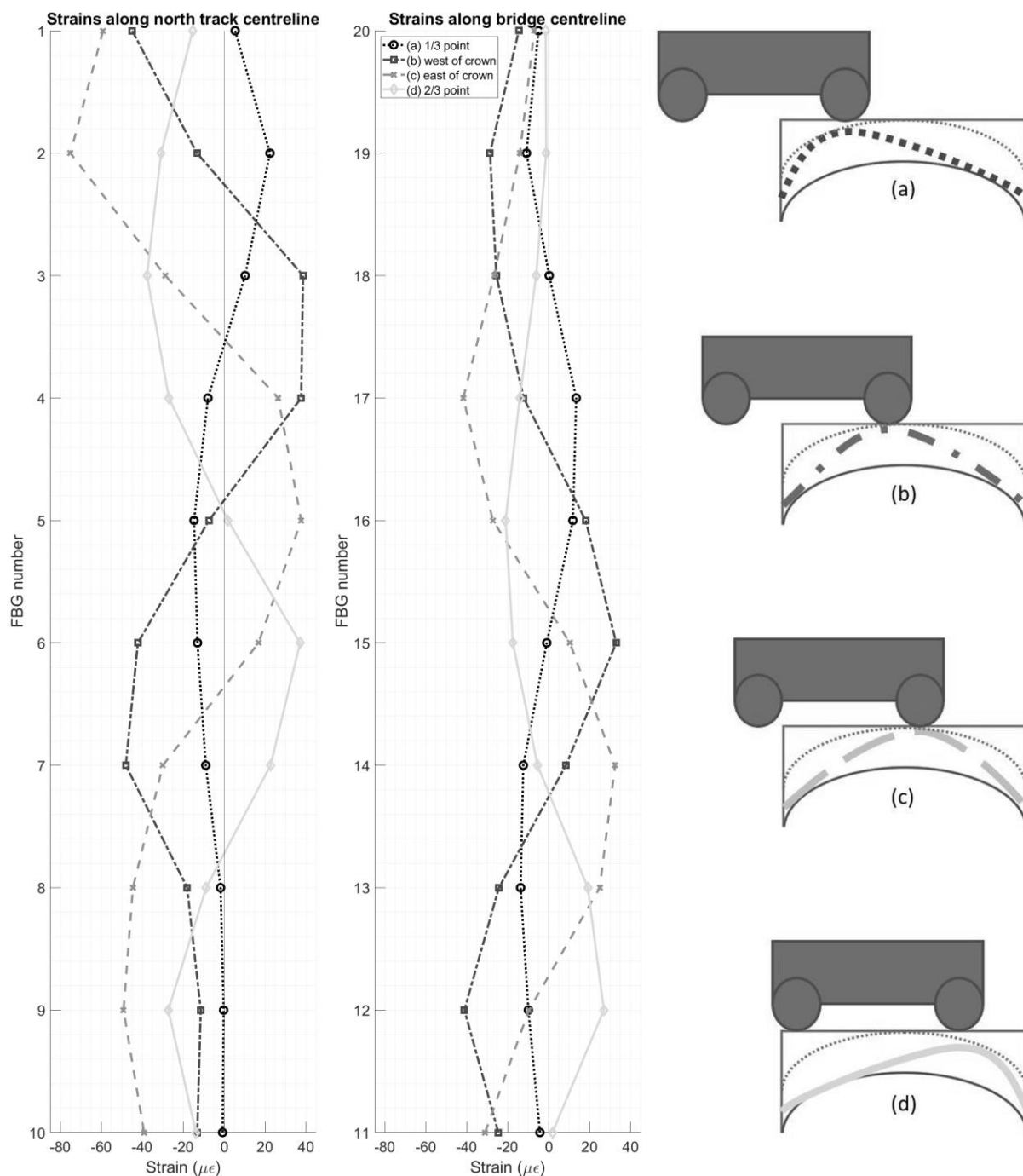


Figure 5.4: The instantaneous longitudinal strain responses observed at the arch intrados when the leading axle of a typical Class 185 train passes above key locations along the arch span, and schematics of the anticipated thrust lines in the arch bridge for point loads applied in these locations, namely (a) the western third point, (b) west of the arch crown, (c) east of the arch crown, and (d) the eastern third point

### 5.2.2 South-east longitudinal crack: crack opening displacements

Figures 5.5(a) and 5.6(a) show typical time histories of crack opening displacements at the south-eastern longitudinal crack, as a Class 185 train passes on the south and north track, respectively. Figures 5.5(b) and 5.6(b) show schematics of these crack opening distributions overlaid on photographs of the crack. These represent the relative shapes of the distributions while the magnitudes of movements have been exaggerated, although the schematics in Figures 5.5(b) and 5.6(b) are plotted at the same scale.

In Figures 5.5(a) and 5.6(a), crack opening is positive and crack closing is negative. In both of these figures a ‘football-shaped’ distribution is observed along the crack length, with the response being largest over the central portion of the crack. FBGs SE1 and SE7 are located at the root and tip of the crack respectively, while FBG SE8 is located ahead of the crack tip. Magnitudes of peak-to-peak movements are similar at FBGs SE1 and SE8, and only slightly larger at FBG SE7, although the ratio of tension to compression is higher at the crack tip than it is at the crack root.

The crack opening movements occur relatively simultaneously along the crack length, as trains pass over the bridge. The largest crack opening responses take place when train axles are at the eastern  $\frac{1}{3}$  point, above the crack. This gives rise to the distributions shown with black bars in Figures 5.5(b) and 5.6(b), for trains travelling on the south and north tracks, respectively. Conversely, when axles reach the western  $\frac{1}{3}$  point, peaks in crack closing are observed. For trains on the south and north tracks, these take the form of the distributions shown with white bars in Figures 5.5(b) and 5.6(b) respectively. While, in both cases of crack opening and closing, the peak response is observed over the central region of the crack, it is also observed in Figures 5.5(b) and 5.6(b) that crack opening results in generally larger movements over the top half of the crack, while crack closing leads to larger movements over the lower half of the crack.

Comparing each FBG between Figures 5.5 and 5.6, the magnitudes of peak-to-peak crack opening remain similar regardless of the track on which trains are travelling. However, in Figure 5.5, for a train travelling on the south track directly above the crack, movements over the upper half of the crack are primarily tensile and the crack is opening, while movements over the lower half of the crack are primarily compressive and the crack is closing. When trains pass on the northern track, as in Figure 5.6, movements at the crack are almost entirely compressive, at all points along its length.

It is of interest that the lower half of the crack displays primarily compressive movements regardless of whether a train is passing directly overhead or on the other side of the bridge. This could suggest that compressive thrusting into the abutment and obtuse corner of the arch dominates the response in this region, where the fill depth is large and therefore local transverse bending is negligible. It is also interesting that tensile movements ahead of the crack tip are not negligible when trains are passing directly overhead, as seen for FBG SE8 in Figure 5.5. For these load locations, the response in this region of the arch is consistent with transverse sagging bending. Tracking the evolution of these movements over the long term will provide insight into whether the crack is stable or still growing, with the potential for any changes to be detected before they are observable in visual inspections of the bridge.

### **5.2.3 South spandrel crack: crack opening and pumping displacements**

In each of the measurement locations across the southern spandrel wall crack, monitored by FBGs SS1/SS2, SS3/SS4, and SS5/SS6, strains have been converted to give relative displacements of the arch barrel compared to the spandrel wall. Here, these are presented in two orthogonal directions: in-plane crack opening in the transverse direction of the arch barrel, and out-of-plane vertical ‘pumping’ displacements (i.e., crack shearing). Crack opening and upwards vertical movements are plotted as positive, while crack closing and vertical downwards movements are plotted as negative. The high stiffness of the spandrel walls limits their vertical deflection. This was confirmed by the fact that the vertical displacements of the arch barrel relative to the spandrels agreed well with absolute vertical displacements of the arch relative to the ground (see section 4.5, and Cocking et al., 2019b).

Figures 5.7 and 5.8 show typical crack opening and relative vertical displacements at the three monitoring locations, for Class 185 trains passing on the southern and northern tracks, respectively. The top rows of these – Figures 5.7(a) and 5.8(a) – show that the separation crack always opens, in the transverse direction, when trains pass on the southern track and closes when trains pass on the northern track. The magnitudes of these movements are very small, below 0.1 mm for trains on the southern track and below 0.05 mm for trains on the northern track.

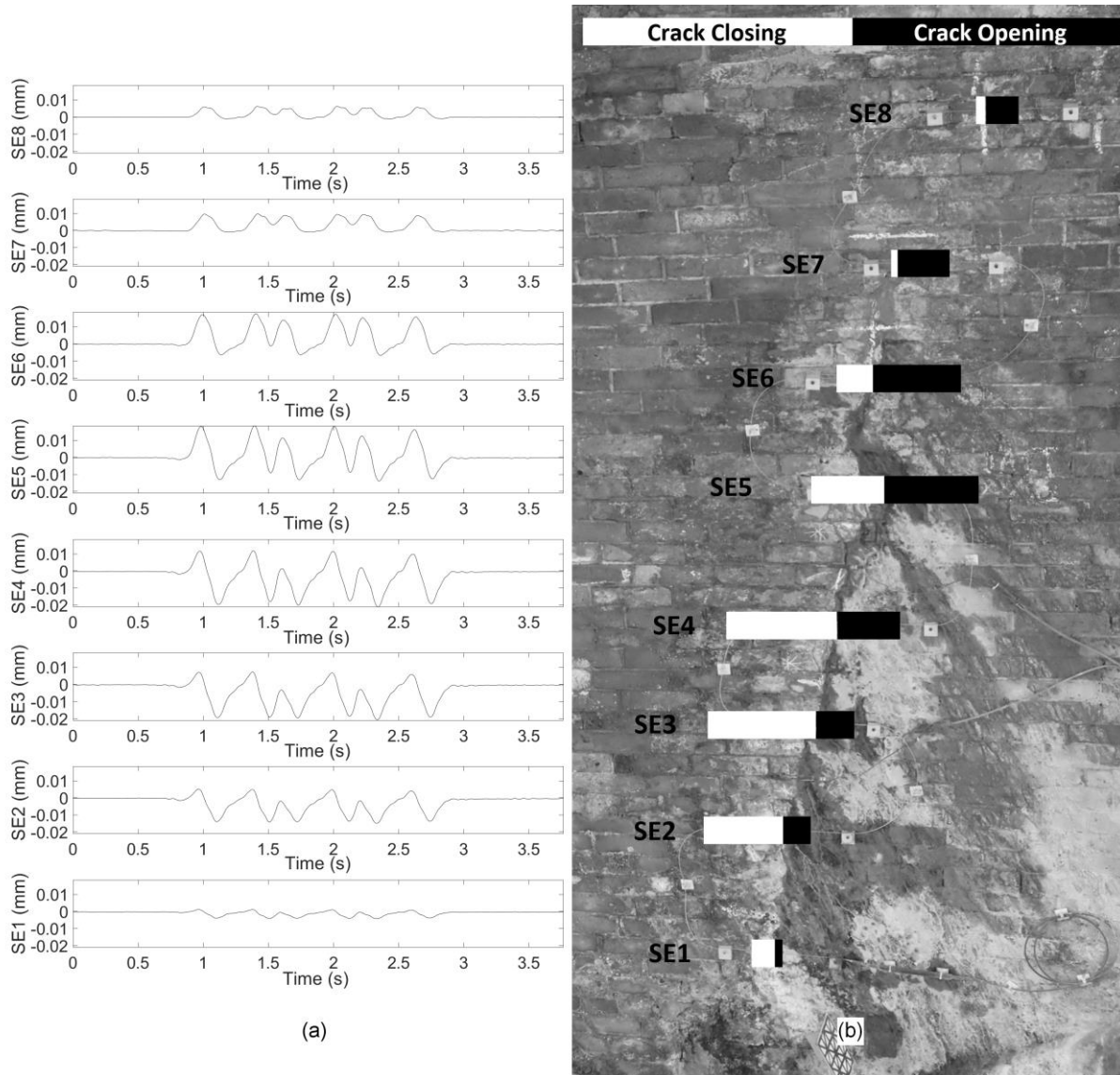


Figure 5.5: (a) Typical time histories of the crack opening displacements at the south-eastern longitudinal crack, for a Class 185 train passing on the southern track, and (b) schematic showing the 'football-shaped' distribution of these peak-to-peak crack opening displacements

The magnitudes of the vertical pumping displacements – shown in the second rows of Figures 5.7(a) and 5.8(a) – are always substantially larger, with peak-to-peak pumping displacements of approximately 1 mm for trains on the southern track and 0.15 mm for trains passing on the northern track.

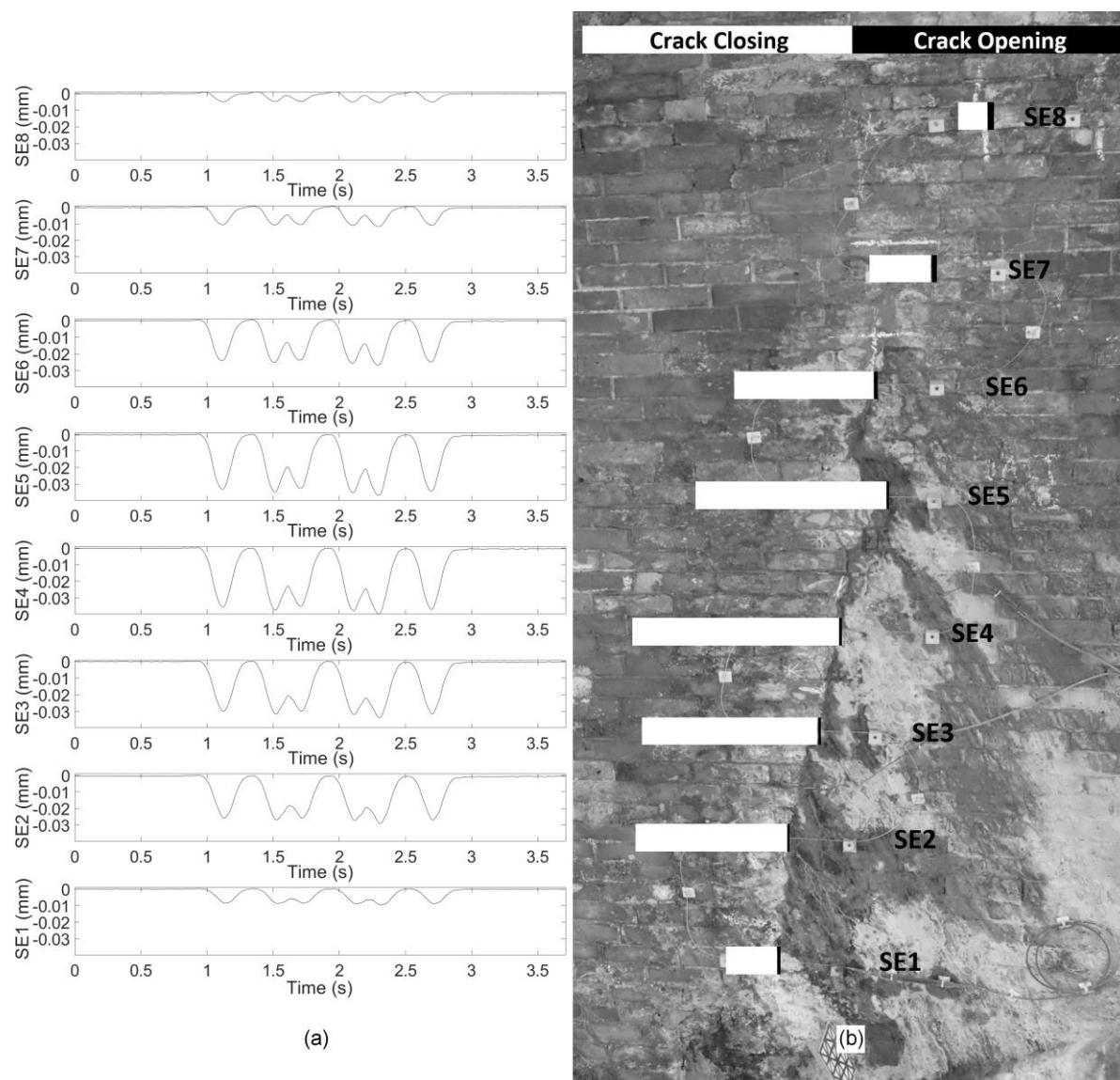


Figure 5.6: (a) Typical time histories of the crack opening displacements at the south-eastern longitudinal crack, for a Class 185 train passing on the northern track, and (b) schematic showing the 'football-shaped' distribution of these peak-to-peak crack opening displacements

These patterns of response are visualised in Figures 5.7(b) and 5.8(b), which are schematics showing the compressive and tensile components of the peak-to-peak displacements. The convention for plotting these displacements is shown in the top-left of Figures 5.7(b) and 5.8(b): crack opening displacements, which occur in the transverse direction of the bridge, are shown with horizontal bars, while the relative pumping displacements are shown with vertical bars. For crack opening displacements, as with Figures 5.5(b) and 5.6(b), these schematics show crack opening movements in black and crack closing movements in white. For relative vertical displacements, peak upwards movements of the barrel relative to the spandrel are shown in

black, while peak downwards movements are shown in white. The monitored regions of the crack interface are indicated by grey circles. Note that the schematics in Figures 5.7(b) and 5.8(b) use two distinct scaling factors, because of the significant difference between the magnitudes of response for the two cases. The figures are internally consistent; however, bar lengths between figures should not be directly compared.

For trains passing on the southern track, as in Figure 5.7, the vertical component of the response at the separation crack is dominated by downwards movement of the arch barrel relative to the spandrel wall. However, small upwards movements are seen in the responses at all three monitored points on the crack, corresponding to instances in time when axle loads are applied to the opposite side of the arch span. Magnitudes of movement are largest in the central region of the crack, peaking for FBG SS4 to the east of the arch midspan, although interestingly the response is not symmetric on the two sides of the crown (at FBGs SS2 and SS4).

A different pattern is observed when trains pass on the northern track. In this case, shown in Figure 5.8, movements at FBG SS4, just to the east of the arch crown, are notably smaller than those observed on either side, at SS2 and SS6, and there are appreciable upwards movements of the southern edge of the arch barrel relative to the spandrel wall. The response to the west of the arch crown (at FBG SS2, shown in the bottom-left subplot of Figure 5.8(a)) demonstrates that application of axle loads at a corresponding point along the arch span still leads to downwards movement of the arch relative to the spandrel wall, but upwards movements occur in the ‘troughs’ between these peaks. The response at the eastern quarter point (at FBG SS6) is more notably dominated by upwards movements, occurring at the same times as the peak downwards movements are observed at the arch crown (particularly at FBG SS2).

The crack does not shear simultaneously along its length. With the exception of FBG SS6 for trains on the north track, as described above, the peak vertical response is a downwards deflection occurring when an axle load is applied at a corresponding point along the arch span. Peak vertical deflections at each monitored location, for the trains in Figures 5.7 and 5.8, are given in Table 5.3.

The values in Table 5.3 highlight that the response is not symmetric on either side of the arch crown, and that different patterns of response arise depending on the track on which the train is travelling. When trains pass on the southern track and loading is applied close to the midspan of the arch, this causes asymmetric downwards movement of the points on either side of the arch crown and either a modest downwards deflection or a small uplift of the eastern quarter point, depending on which side of the arch crown the axle load is applied. Loads applied at the

eastern quarter point cause a peak downwards deflection at the corresponding point along the crack (SS6), decreasing downwards deflections towards the arch crown (SS4), and some uplift of the opposite side of the crown (SS2).

For trains on the northern track, loading close to the midspan causes an asymmetric response at the southern arch crown (SS2 and SS4) but a consistent uplift at the eastern quarter point (SS6). The magnitude of this uplift is approximately double that of the downwards deflection observed at this point when axle loads are applied to the eastern side of the north track. Furthermore, this asymmetric loading case causes upwards movement at the arch midspan, with larger upwards deflections observed on the opposite side of the crown (SS2).

Planned future work includes computational modelling of this skewed arch bridge; it will be particularly interesting to compare the modelled distributions of arch displacements to these detailed monitoring data.

### **5.3 Statistical overview of the longitudinal strain distributions**

The following plots present a statistical summary of all longitudinal strain data recorded for Class 185 trains passing on the northern track. Figure 5.9 summarises the peak compressive, peak tensile, and peak-to-peak strain responses at each longitudinal FBG. Note that, in keeping with earlier figures, compressive strains are plotted as negative while tensile strains are positive. Figure 5.10 summarises the variation of the instantaneous strain responses as the leading axles of each train reach certain key locations along the arch span. These locations are the same as those for which a typical instantaneous strain response was plotted in Figure 5.4.

In both Figures 5.9 and 5.10, the top rows plot the strains measured by FBGs L1 to L10 underneath the north track centreline, while the bottom rows plot strains for FBGs L11 to L20 along the bridge centreline.

These figures use boxplots (Tukey, 1977; McGill et al., 1978) to represent the statistical distribution of strains at each FBG. Median values of strain are shown as black dots in white circles. These circles are within solid boxes which represent the interquartile ranges, although for data sets with very low statistical dispersion these boxes are not always visible. Whiskers extend beyond the boxes by a distance of 1.5 times the interquartile range. The few outliers beyond these whiskers have been omitted for clarity. Solid lines between adjacent boxplots connect the median values.

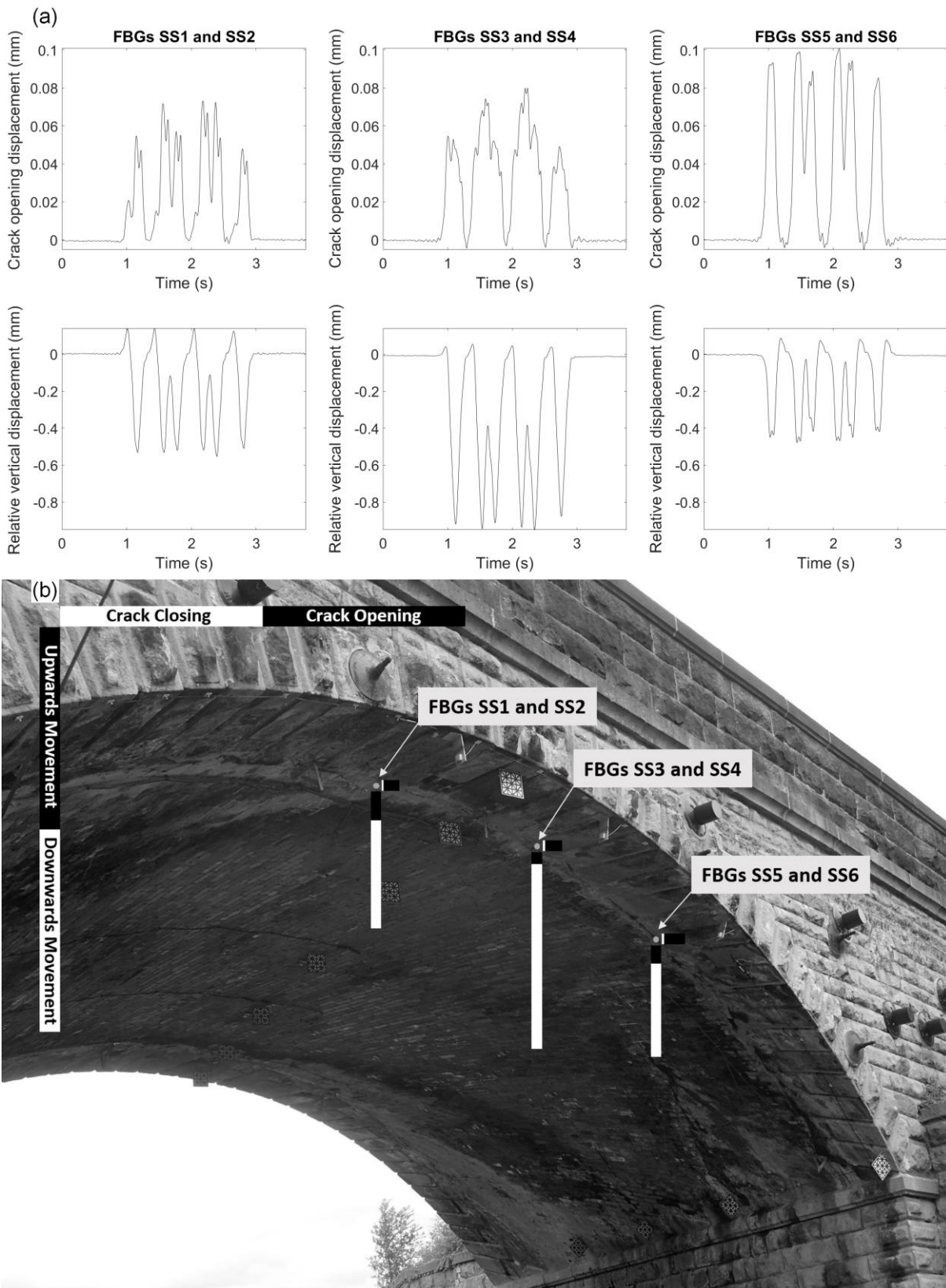


Figure 5.7: (a) Typical time histories of the crack opening and pumping displacements at the southern spandrel separation crack, for a Class 185 train passing on the southern track, and (b) schematic showing the distribution of these peak-to-peak displacements

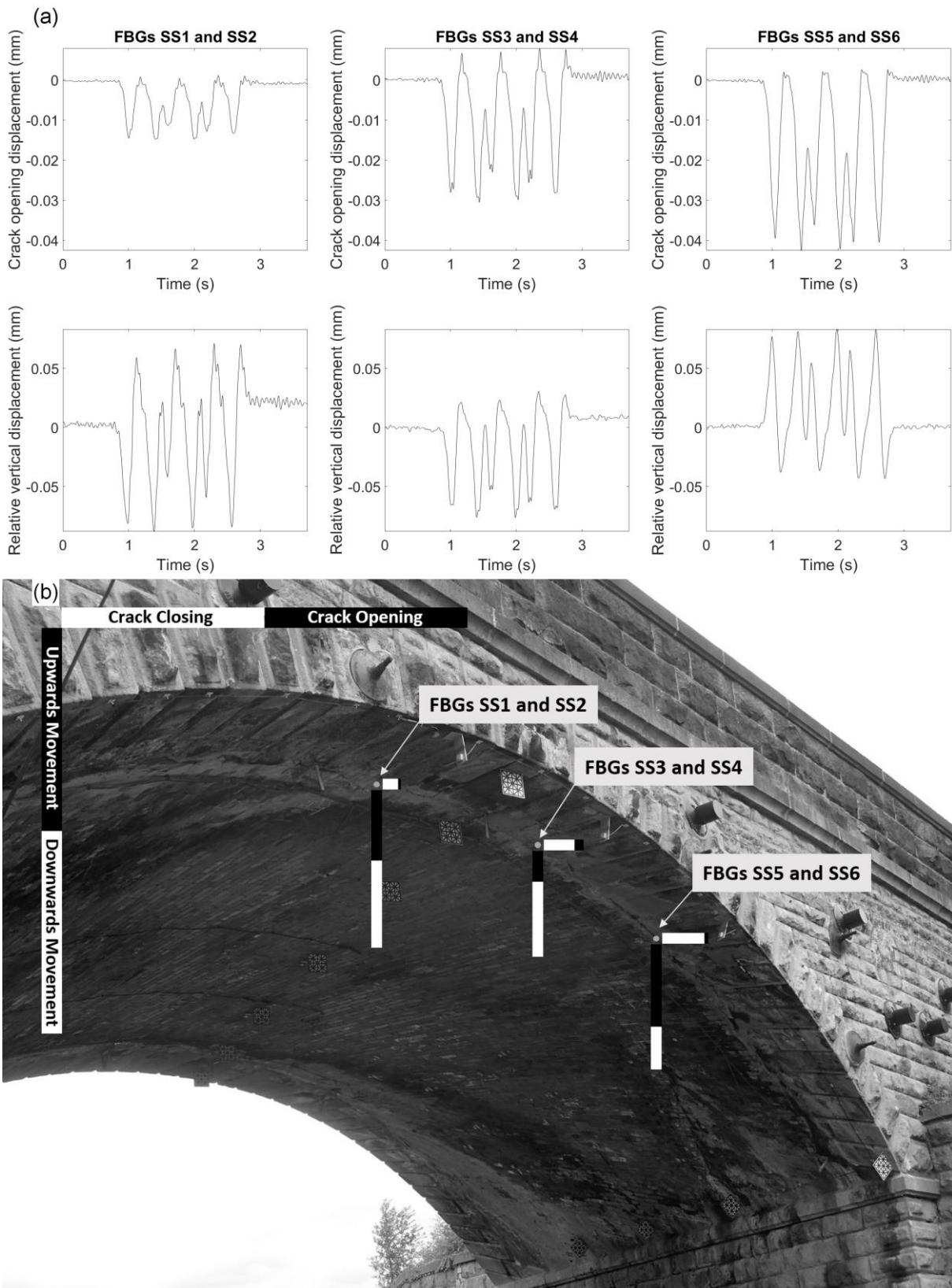


Figure 5.8: (a) Typical time histories of the crack opening and pumping displacements at the southern spandrel separation crack, for a Class 185 train passing on the northern track, and (b) schematic showing the distribution of these peak-to-peak displacements

Table 5.3: Vertical movements at the south spandrel separation crack for key load locations

<b>Train passing on the south track</b>			
Axle location:	Vertical deflections at FBG		
	SS2 (west of crown):	SS4 (east of crown):	SS6 (eastern quarter point):
East quarter point	+0.13 mm	-0.23 mm	-0.45 mm
East of crown	-0.43 mm	-0.92 mm	-0.15 mm
West of crown	-0.53 mm	-0.69 mm	+0.045 mm
<b>Train passing on the north track</b>			
Axle location:	Vertical deflections at FBG		
	SS2 (west of crown):	SS4 (east of crown):	SS6 (eastern quarter point):
East quarter point	+0.059 mm	+0.020 mm	-0.038 mm
East of crown	-0.060 mm	-0.066 mm	+0.073 mm
West of crown	-0.081 mm	-0.059 mm	+0.074 mm

In Figure 5.9, the left-hand plots show the statistical distribution of peak compressive strains, in black, and peak tensile strains, in light grey. The right-hand plots show the statistical distribution of peak-to-peak strains. Peak tensile strains reach their maximum values close to the arch crown, while peak compressive strains reach theirs close to the two  $1/3$  points of the arch. These observations match those made earlier, during discussion of Figure 5.4, regarding the two critical loading cases for concentrated loads applied to an arch. Peak-to-peak strains, dominated by the higher magnitudes of the peak compressive strains, also reach their maximum values close to the arch  $1/3$  points.

In most cases in Figure 5.9, the median strains are close to the centres of their respective boxes. This indicates that these data sets have low sample skewness and that the median and mean strains are likely to coincide. There is also a general trend that the amount of dispersion increases as the strain magnitude rises. At most, the magnitude of the interquartile range reaches approximately 4% of the median strain magnitude, with an absolute value of roughly  $5 \mu\epsilon$ .

In Figure 5.10, the statistical distributions of the instantaneous strain responses also show reasonable agreement between different train events, for most FBGs. Here, strain responses are considered at times when the leading axle of a Class 185 train is positioned above the western and eastern third points of the arch, as well as either side of the arch crown. In each case, these plots maintain the pattern observed for typical instantaneous strains in Figure 5.4(a). Again, the spread in the strain data is typically low in absolute terms, although this can be up to 15% of the median strain magnitude in some cases.

Sorting the FBG data into groups, corresponding to fast or slow trains travelling during commuter or off-peak times, does not substantially affect the distribution of median strains, or the spread in these data. This is the case for both peak-to-peak and instantaneous strain responses. For brevity, plots showing the statistical distributions of subgroups of data are not included here.

Each strain response summarised in Figure 5.10 corresponds to a distinct thrust line, adopted by the arch under instantaneous loading, and therefore the median strain distribution represents a typical thrust line for the arch under this load. Variation in the adopted thrust line gives rise to dispersion in the statistical strain distribution.

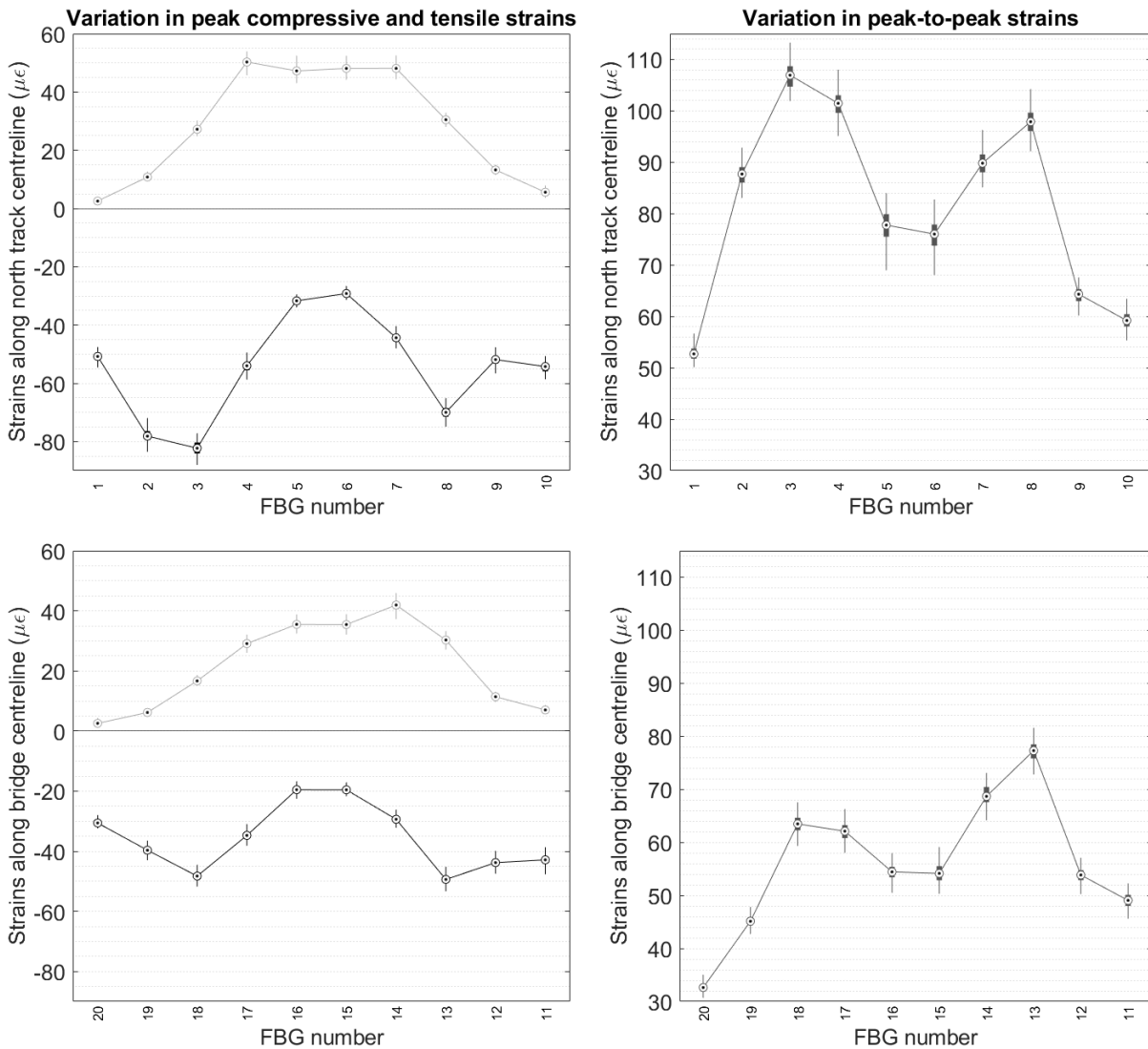


*Figure 5.9: (Left) Boxplots showing the longitudinal distributions of peak compressive (negative) and tensile (positive) strains, in black and grey respectively, and (Right) Boxplots showing the longitudinal distributions of peak-to-peak strains, for all Class 185 trains passing on the northern track*

There is often considerable skew in this dispersion, which is evident in Figure 5.10 in those boxplots for which the median is clearly not centred in its interquartile range. A consequence of this skew is that the mean strain cannot be presumed to give an accurate measure of typical, instantaneous behaviour. The median, conversely, is more resistant to the influence of outliers, which are themselves also useful since they represent the largest deviations from typical behaviour over the sample period.

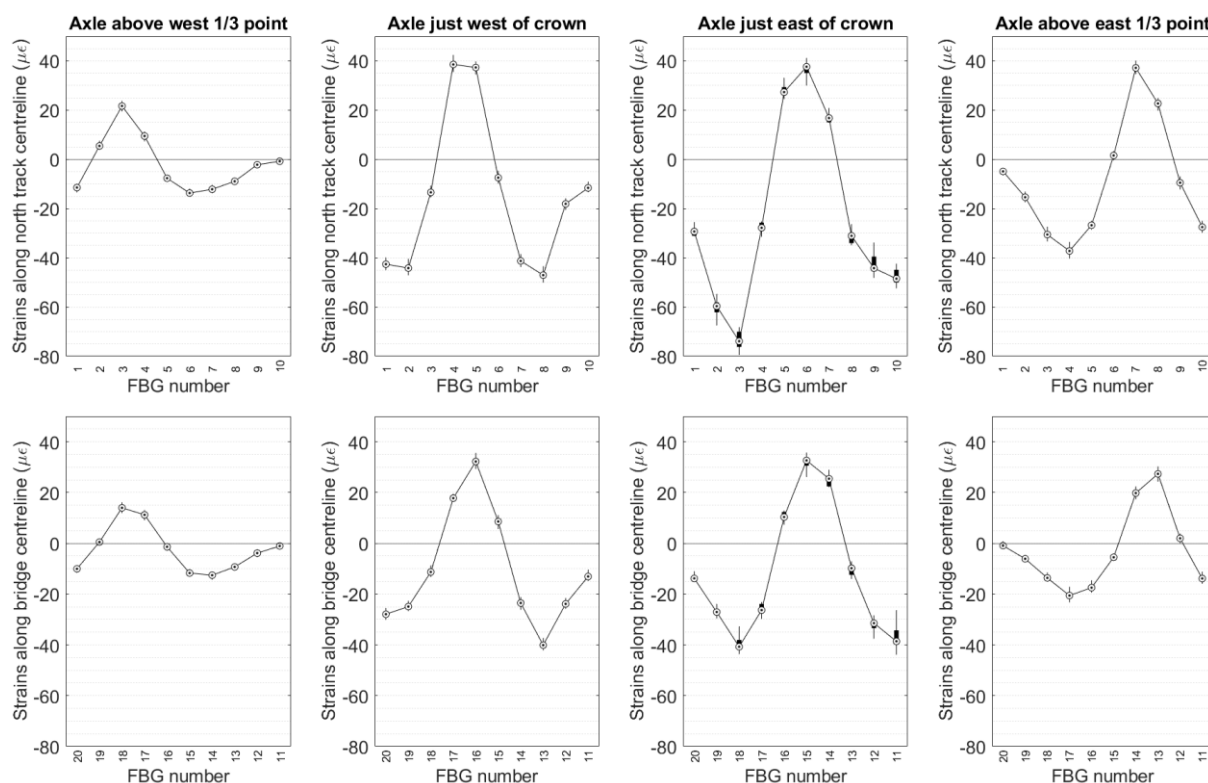


*Figure 5.10: Boxplots showing the statistical distributions of the instantaneous longitudinal strains which arise when the leading axles of all Class 185 trains passing on the northern track reach key locations along the arch span*

Therefore, when comparing arch behaviour over time, in order to search for any long-term changes in this behaviour, one potential approach is to track the median and extreme outliers of the instantaneous strain response for various positions of applied loading. For the monitoring data considered here, covering the period of September 2018 to February 2019, the remarkable consistency of the strain responses, as visualised by the low statistical spread in these data, suggests that there is very little variation in the load path being adopted by the arch when it is subjected to train loading. This is despite the variation in passenger loading, which is discussed in the next section. Over time, however, damage or deterioration of the arch may cause the load path to change; such changes could be detected using this statistical approach.

Statistical representations of monitoring data therefore have useful asset management applications, in the form of identifying changes in behaviour which could indicate damage or deterioration of the structure. The ability of FBGs to measure statistical changes in the strain response, when these strains are themselves very small in magnitude, offers considerable practical benefits. Although there have not been significant changes in the bridge response over

the 6-month monitoring period presented here, these results nevertheless demonstrate that FBGs are capable of identifying such changes.

## 5.4 Variability of the longitudinal strain distributions

Figures 5.11 and 5.12 plot peak-to-peak strains for a subset of the longitudinal FBGs against time of day and train speed, for which trends have been observed. The data that are plotted correspond to all Class 185 trains passing on the northern train, and a subset of FBGs underneath the north track and along the bridge centreline. These include FBGs L3 and L18, underneath the western  $\frac{1}{3}$  point; FBGs L5, L6, L15, and L16, close to the arch crown; and FBGs L8 and L13 underneath the eastern  $\frac{1}{3}$  point.

In both Figures 5.11 and 5.12, data are plotted for all recorded trains, including trains travelling at any speed. The entire 6-month monitoring period is included in these, and in the remaining plots in this chapter. Data are coloured in clusters based on train speed, as can be seen clearly in Figure 5.12. Fast trains with speeds above 82 mph are plotted as red dots with black borders; slow trains below 72 mph are plotted as green dots with black borders; and trains with intermediate speeds (i.e., 72–82 mph) are coloured blue with black borders.

In Figure 5.11, time of day is used as a proxy for passenger loading. The actual axle loads applied to the bridge are not known a priori; although the train weights are known, the overall axle loads can vary significantly depending on passenger levels. Information from Network Rail, the asset managers, suggests that the axle loads applied by a Class 185 train may increase by as much as 10–16% between typical and maximum, termed ‘crush,’ passenger loading scenarios. Furthermore, ‘crush’ loadings can be 27% higher than those applied by an empty train. These increases are not uniform across all axles.

Despite the spread in the data, a clear increase in the peak strain responses of the longitudinal FBGs can be seen in Figure 5.11 around the evening commute, between 5pm and 7pm, before decreasing later in the evening to a lower level than is observed during the day. Qualitatively, this trend matches well with anticipated passenger behaviour. Although the precise increases between off-peak and peak conditions are obscured by the remaining scatter in the data, especially for off-peak trains, the changes observed are broadly consistent with those anticipated. Furthermore, the amount of scatter is generally observed to decrease during peak times of travel, suggesting more consistent levels of passenger loading at these times.

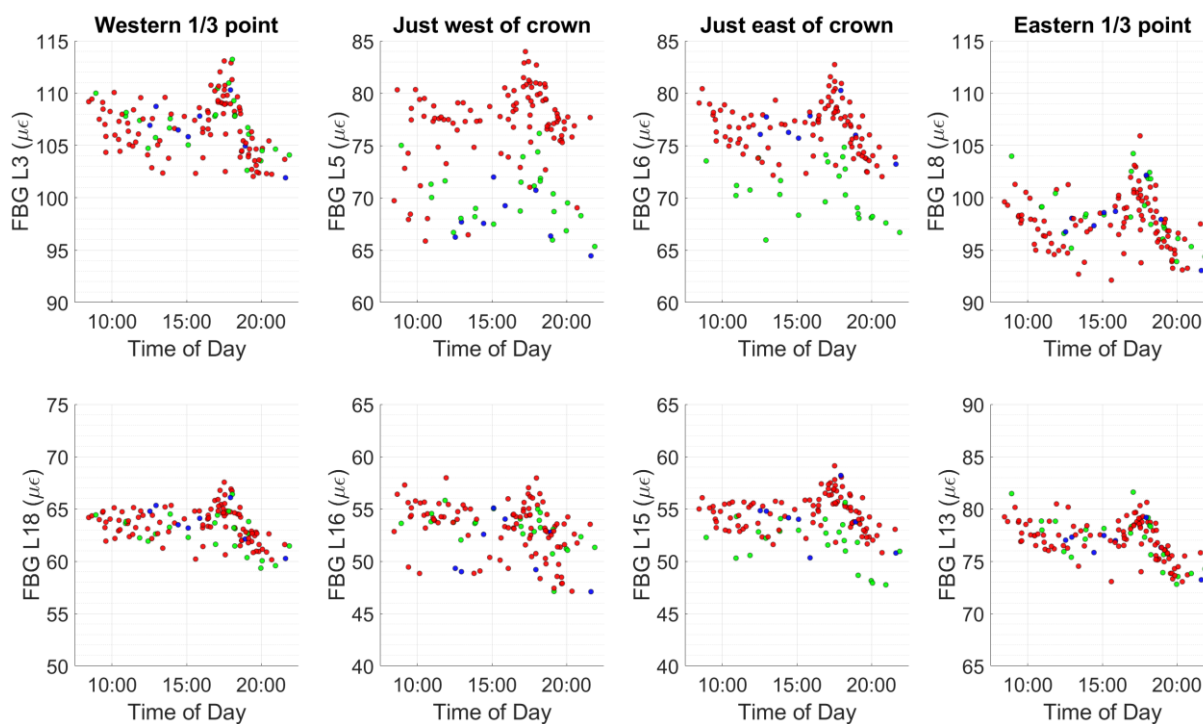


Figure 5.11: Variation of peak-to-peak longitudinal strains with time of day, for all Class 185 trains passing on the northern track (data coloured by train speed)

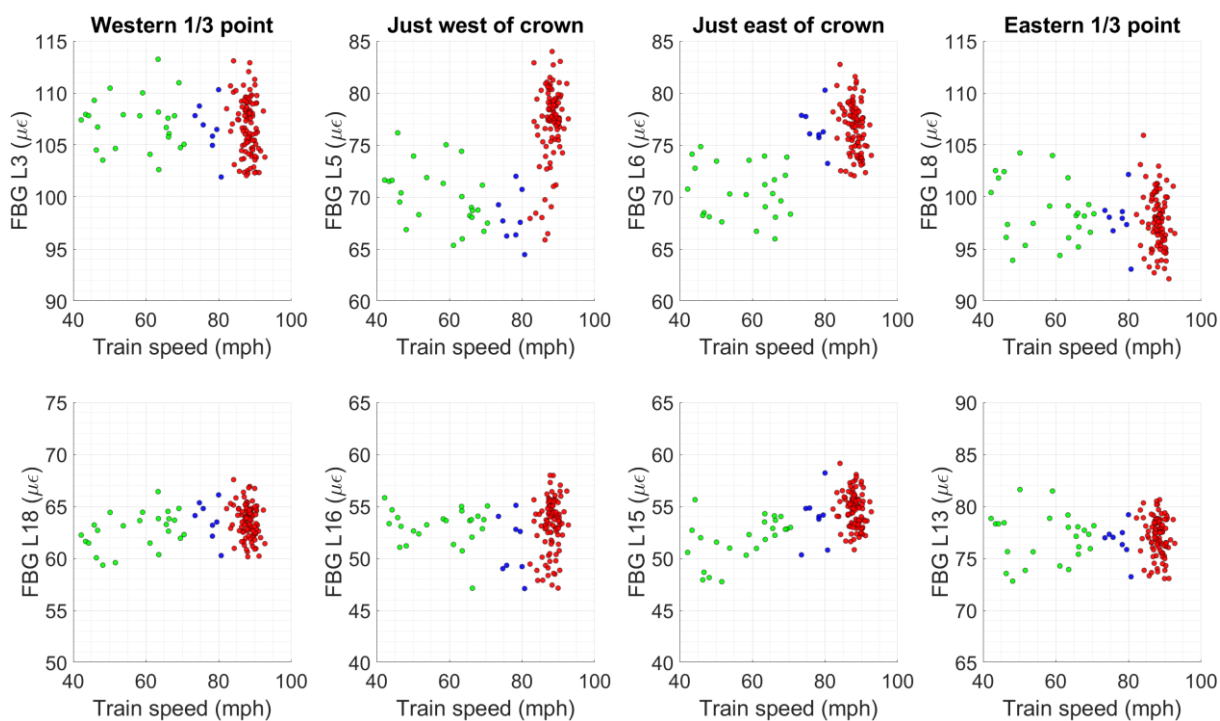


Figure 5.12: Variation of peak-to-peak longitudinal strains with train speed, for all Class 185 trains passing on the northern track (data coloured by train speed)

Considering only the fast trains plotted in Figure 5.11, Table 5.4 presents bounds on the increase in strain magnitude that is observed during peak travel times. These are calculated by comparing the largest strains recorded during peak travel times with the largest and smallest strains recorded during off-peak times, excluding extreme outliers. The upper limits of these bounds generally agree well with the 10–16% estimate stated above: the loading increase due to full passenger capacity, relative to typical passenger levels. The lower limits of these bounds may be explained by the large variation in strain measurements for trains recorded during off-peak times; passenger levels are expected to vary significantly during these times, and it is not unreasonable to expect some of these trains to approach full capacity.

The upper limits on the strain increases for FBGs L5 and L16, close to the arch crown, exceed this estimated load increase for full capacity trains relative to typical passenger levels. Although the bounds in Table 5.4 have been calculated only considering fast trains travelling at over 82 mph, the strain increase at these FBGs could be due in part to a residual impact of train speed. As is seen in Figure 5.12, strain amplification due to high train speed is only observed close to the arch crown. Further sub-dividing the FBG data by train speed may help to fully decouple this effect. However, in order to do this, more data will be required to reliably characterise each group.

Nonetheless, the findings in Table 5.4 suggest that uncertainty regarding precise train and passenger loading can be mitigated if repeat measurements are taken at the same time of day over a long period of time. In particular, data recorded during weekday commuter times are likely to give the best repeatability. Loading at this time can be assumed to correspond to well-defined ‘crush’ scenarios, while the precise loading during other times of day is more uncertain. Using this approach, time of day could be employed as a simple framework to classify railway traffic loading, instead of bridge weigh-in-motion techniques.

For FBGs L5, L6, L15, and L16, close to the arch crown, variation of the strain response based on train speed can be observed, with an increase in measured strains for the fast trains. In Figure 5.11, the subplots for these FBGs contain bands of red and green dots corresponding to the separate time-of-day variation for both fast and slow trains, respectively. The increase in strain response for fast trains can be seen in Figure 5.12 for FBGs close to the arch crown, most clearly for FBGs L5, L6, and L15. Here, there is a marked increase in peak-to-peak strains for fast trains relative to slow trains.

*Table 5.4: Increases in longitudinal strain magnitude observed during peak travel times*

	<b>Location:</b>	<b>FBG:</b>	<b>Strain increase:</b>
North track	Western third point	L3	3 – 11%
	Just west of arch crown	L5	6 – 27%
	Just east of arch crown	L6	6 – 15%
	Eastern third point	L8	5 – 15%
Bridge centreline	Western third point	L18	3 – 14%
	Just west of arch crown	L16	5 – 23%
	Just east of arch crown	L15	6 – 16%
	Eastern third point	L13	3 – 12%

It is important to note that variation of the strain response with train speed is not observed at FBGs further away from the arch crown. The variation is also more pronounced for FBGs L5 and L6 underneath the northern track, on which the trains are passing, than it is for FBGs L15 and L16 along the bridge centreline. This suggests that the impact of train speed is localised, primarily affecting regions of the bridge with relatively little backfill, and which are also close to the point of application of the load.

In Figure 5.12, the crown FBGs under the north track centreline show an increase of up to 15% in the magnitude of the strain response for fast (>82 mph) trains relative to slow (<72 mph) trains. The corresponding value for crown FBGs at the bridge centreline is 10%. For FBGs further away from the crown, no variation of the peak-to-peak strains with train speed can be observed, although more data for slow trains are needed to confirm these observations and identify the precise nature of any trends with speed below 72 mph, which are currently obscured by scatter. Nevertheless, from the available data, the pronounced increase in strain response and reduction in scatter for trains travelling above 82 mph is clear.

Note that these findings agree with the transient FE analyses performed by Gibbons (2014), who found that typical dynamic enhancement did not exceed 10% for train speeds up to 125 mph. Furthermore, for simulated train speeds up to 250 mph, dynamic enhancement was not observed to exceed 30%.

The current guidance from Network Rail (2006) prescribes a dynamic factor of 1.8, to be applied to the critical axle loading; this is significantly higher than the strain amplification

measured at this bridge and reported above. The guidance states that this factor may be reduced where the depth of ballast and fill, between the sleeper and arch crown extrados, exceeds 600 mm, but gives no suggestions on how to calculate this reduction and does not allow for the increase in fill at locations other than the arch crown. The average depth of ballast and fill at the crown, for this bridge, is 352 mm according to record drawings. The findings here suggest that continued monitoring of multiple bridges could enable revisions to the current dynamic amplification factor used by Network Rail for assessment of masonry arch rail bridges.

Separate guidance on dynamic amplification factors for traffic loading, such as rail, is given in Eurocode EN 1991-2 (CEN, 2003). This guidance is founded on the use of simplified beam models, resulting in expressions for dynamic amplification factors that depend on a determinant length for the structure, its first natural frequency, and the vehicle speed. These expressions were not derived with masonry arches specifically in mind, and it has been demonstrated that they produce results which are too conservative for masonry rail bridges (Gibbons, 2014). Attempts to improve this guidance are an active area of research (see, for example, Smith and Acikgoz, 2019).

Variation of longitudinal strains with ambient temperature and date was also studied, to investigate any seasonal and long-term trends, respectively. However, no discernible trends could be identified for the data available over this 6-month monitoring period.

## 5.5 Variability of crack opening displacements

Figures 5.13(a) and 5.13(b) show the variation of peak-to-peak crack opening displacements at the south-eastern longitudinal crack with time of day and temperature, respectively. The data that are plotted correspond to Class 185 trains travelling on the south track. In Figure 5.13(a), all fast Class 185 trains travelling above 82 mph are plotted, while in Figure 5.13(b) only fast Class 185 trains travelling between 5pm and 7pm (i.e., at evening commute times) are plotted. All data in Figure 5.13 are coloured by temperature, as can be seen more clearly in Figure 5.13(b). Data for which the ambient temperature was between 0 and 5°C are plotted as blue dots with black borders; data for ambient temperatures between 5 and 10°C are plotted as yellow dots with black borders; and data for higher temperatures are plotted as red dots with black borders. ‘Red’ data were recorded in September and October 2018, ‘yellow’ data were recorded in November 2018 and February 2019, and ‘blue’ data were recorded in December 2018 and January 2019.

In Figure 5.13(a), the increase in response magnitude around the evening commute can be observed but it is less notable than it was for the longitudinal strains in the previous section. In

the subplots for FBGs SE5 to SE8, over the upper half of the crack, the peaks for evening commuter trains appear to be larger and more pronounced for data recorded during cold ambient conditions than they are for the subplots corresponding to FBGs SE1 to SE4 over the lower half of the crack. For these FBGs, there is no clear relationship with temperature over the evening commuter period. Additionally, the time-of-day plots are now dominated by a significant decrease in the magnitudes of peak-to-peak crack opening displacements between approximately 08:30 and 13:30. This corresponds to a steady, approximately linear increase in the recorded ambient temperature, which also occurred between these times.

In Figure 5.13(b), a notable decrease in the magnitudes of peak-to-peak displacements as the ambient temperature rises is observed for FBGs SE5 to SE8, located over the upper half of the crack where the response is primarily tensile (i.e., crack opening). However, this is not observed for FBGs SE1 to SE4 over the lower half of the crack, where the response is primarily compressive (i.e., crack closing). For FBGs SE5 to SE8, the decrease in peak-to-peak displacements is approximately 10% over a rise in temperature of 15.5°C.

No clear relationships between crack opening displacements and either temperature or time of day were observed for data corresponding to trains passing on the northern track. Note that in this case the crack opening displacements are always primarily compressive, while in Figure 5.13 the only significant observed relationships are for crack opening displacements that are primarily tensile.

In summary, for the south-eastern longitudinal crack, there is some sensitivity to temperature observed when crack movements are tensile. The peak-to-peak crack opening magnitudes decreased as the ambient temperature rose. However, when crack movements were compressive, no relationship with temperature was observed. This could be explained by thermal expansion causing cracks to partially close. In other words, crack widths are larger when the bridge is cold, so dynamic tensile strains across these open cracks are also larger.

Furthermore, this sensitivity to temperature appears to match the anticipated increase in response for evening commuter trains, when these peak-to-peak displacements are plotted against time of day. Therefore, it could be that a lower ambient temperature, and corresponding thermal contraction of the masonry, simply leads to tensile movements of this crack becoming more sensitive to the precise magnitude of the applied loading, while compressive movements remain less sensitive to this.

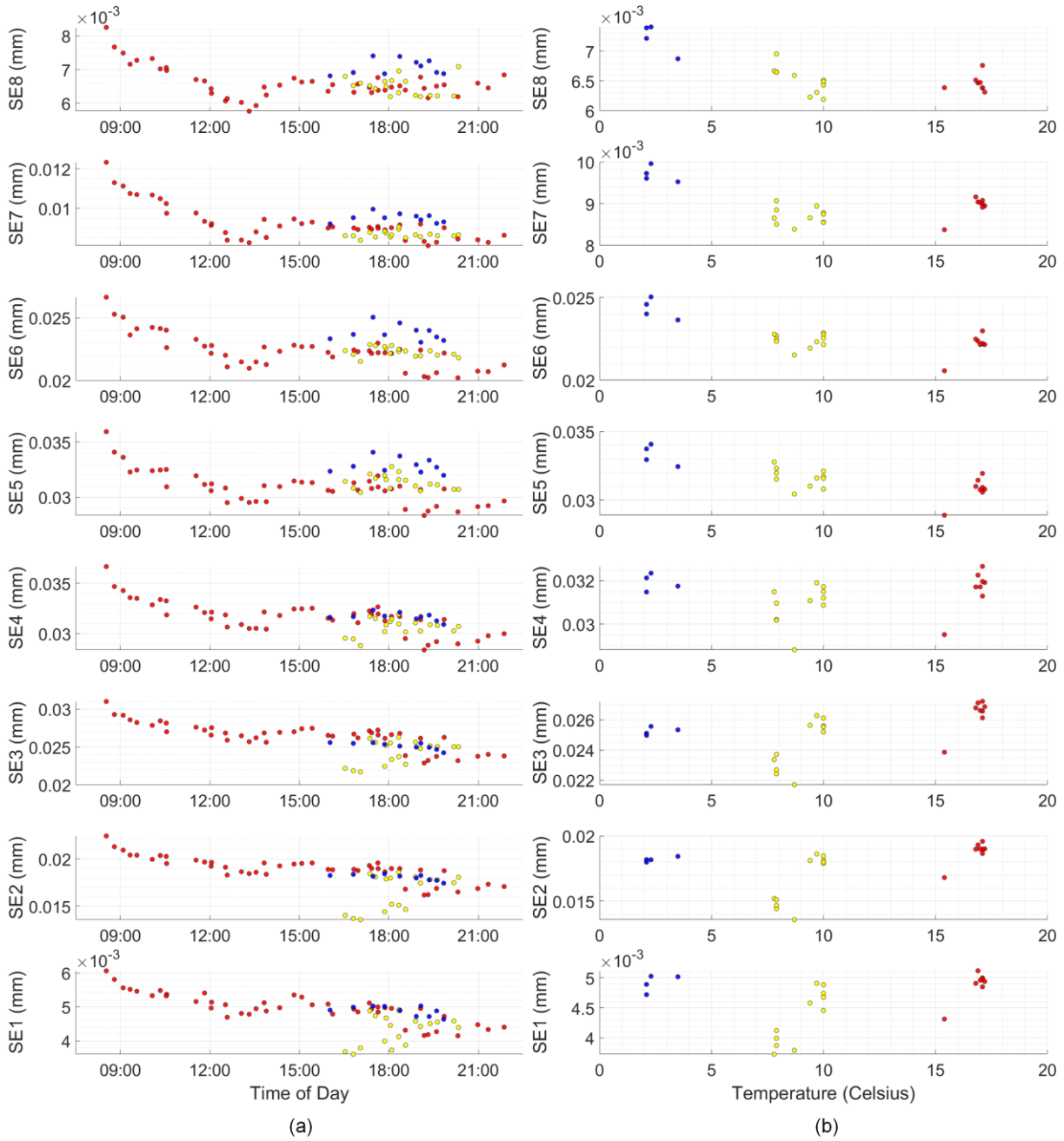


Figure 5.13: Variation of peak-to-peak crack opening displacements at the south-east longitudinal crack with (a) time of day, only plotting data for fast Class 185 trains passing on the southern track, and (b) temperature, only plotting data for fast, evening commuter Class 185 trains passing on the southern track (data coloured by temperature)

It is worth noting that the general observation of an inverse relationship between the magnitude of dynamic deformation and ambient temperature, in certain circumstances, agrees with the findings of a recent study into a masonry viaduct of similar construction, reported by Alexakis et al. (2019b) and Alexakis, Lau, and DeJong (2021). In that study, a clear inverse relationship was identified. However, it is likely that the large number of arch spans at that viaduct affects its sensitivity to temperature, in contrast to the single-span bridge studied here which has different boundary conditions at the arch abutments. In Chapter 8, long-term data, gathered over a greater range of temperatures, allow the thermal effects at CFM-5 to be characterised in greater detail.

No relationship between crack movements and train speed was observed, in keeping with the earlier observation that the impact of train speed on the strain response is highly localised to the regions in which loading is applied to the arch, and to places where little backfill is present. For brevity, plots of the crack movements against train speed are not included here. However, these are plotted for the long-term FBG data in Chapter 8.

Variation of crack opening and pumping displacements was also investigated for the south spandrel separation crack. However, no relationships were identified for the 2018–2019 data. The spread in the magnitudes of peak-to-peak crack displacements was significantly higher for this crack, and it is possible that this obscured any underlying trends in the data.

## 5.6 Conclusions

In this study, high sensitivity FBGs have been utilised to monitor a damaged, skewed masonry arch railway bridge in unprecedented levels of detail, at a wide range of points across its extent. Data for Class 185 trains, the most common SLS train loading for this bridge, have been analysed, and a comprehensive overview of the typical structural response of this bridge has been presented. This has covered the longitudinal strain distributions over the undamaged northern half of the arch, and the behaviour across cracked interfaces of interest. At the southern spandrel separation crack, a novel implementation of FBGs has been deployed to allow this technology to measure both in-plane crack opening and out-of-plane relative vertical displacements across the crack, for the first time.

By capturing the structural response in these regions in detail and visualising the monitoring data in a range of ways, it has been possible to relate the measured bridge movements to expectations of its structural behaviour. In the case of the longitudinal strain distributions, accurate measurements allowed meaningful statistical representations to be created – even when peak strains only reached tens of microstrain, and the interquartile range of measurements

was at most  $6 \mu\epsilon$  and frequently much lower. The simple statistical approach described in this chapter has the potential to be of benefit to asset managers who wish to identify the early onset of changes in the behaviour of similar masonry structures, potentially before these changes become visible to coarser monitoring techniques or visual inspections.

The ability of FBGs to accurately measure microstrain-scale movements has also been leveraged to study the sensitivity of the structural response of this bridge to various parameters of interest. Trends in the longitudinal strain distributions were identified with time of day, which was observed to be an approximate indicator of passenger loading, and with train speed. In the first instance, this opens up the potential for time of day to be used as a proxy for the magnitude of train loading, instead of complex bridge weigh-in motion systems.

Secondly, the results regarding train speed suggest that, pending further data for slow trains, it may be appropriate for current Network Rail guidance on the impact of train speed on the structural response of masonry bridges to be revisited. It was found that the sensitivity of the arch's longitudinal strain response to train speed is localised – only being observed in regions of the arch with low cover of backfill and ballast above the arch extrados – and is most notable close to the point at which train loads are applied. A dynamic amplification factor of approximately 1.15 was observed in the FBGs directly underneath the active track on which the train was passing, with the corresponding factor for FBGs 1.5 m to the side of these, at the bridge's longitudinal centreline, being approximately 1.10. These factors describe a relative increase in strain response for trains travelling above 82 mph, compared to those travelling below 72 mph. More data will be gathered to refine these factors, based on a more precise understanding of the response for slower trains. The current Network Rail recommendation for this dynamic factor is significantly higher, at 1.8 (Network Rail, 2006).

At the south-eastern longitudinal crack, tensile crack openings were similarly found to be sensitive to a combination of temperature and time of day. However, it may simply be that thermal contraction of the masonry, in cold conditions, allowed these displacements to become more sensitive to the precise applied loading on the bridge, in the manner described above for the longitudinal strains.

The sensitivity of the bridge response to ambient temperature and date, representing, respectively, seasonal variation and potential deterioration over time, was also investigated. However, no other clear trends in the response were identified for these variables, in the 2018–2019 monitoring data.

# Chapter 6

## The flow of force in the skewed arch

This chapter examines the three-dimensional nature of the response of the CFM-5 bridge in more detail. A novel structural-scale FBG strain rosette is introduced and used to monitor the full strain state along two longitudinal lines: directly underneath the north track and following the bridge centreline (in the skewed span direction). From these data, assumptions of symmetry in the bridge response are investigated. Principal strains are then plotted, which visualise the flow of force through the arch barrel. Strain states aligned with the skewed span and square span directions are also studied.

Following this, videogrammetry data are used to investigate a possible transverse bending component of the bridge response. A simplified beam model is constructed which is consistent with the videogrammetry data. This model is then compared with the corresponding intrados strains in this transverse direction, found using the FBG rosettes.

### 6.1 Measurement and visualisation of force flow in the arch

#### 6.1.1 The FBG strain rosettes

Two longitudinal lines of FBGs were installed on the arch intrados at CFM-5 in the skewed span direction, underneath the north track centreline and the overall bridge centreline. In Chapter 5, these were referred to as FBGs L1 to L20 (see Figure 5.1). Strain distributions across these FBGs were analysed in depth, in that chapter.

Adjacent to each of these lines, 20 further FBGs were installed in a ‘sawtooth’ configuration using the new clamp design presented in section 4.3.2 of Chapter 4. Together, these resulted in two lines of triangular FBG rosettes, as shown in Figure 6.1. Note that the numbering

convention for these rosettes is different from the convention used for FBGs L1 to L20; rosettes are numbered progressively from west to east, along each longitudinal line.

By assuming rotational symmetry in the arch behaviour, the responses of rosettes R1 to R10 when trains pass on the south track can be used to predict the behaviour of an imagined row of rosettes, R21\* to R30\* along the centreline of the south track, when trains pass on the north track. Additionally, owing to a fibre breakage during the installation process, it was not possible to complete rosette R20 on the eastern end of the bridge centreline. Therefore, applying the same assumption of rotational symmetry, the response at rosette R11 is used here to infer the response of imaginary rosette R20\*. In Figure 6.1, imaginary rosettes are drawn with dashed lines and shaded grey, to differentiate them from the real, installed FBG rosettes. The assumption of rotational symmetry is investigated in section 6.1.1.2.

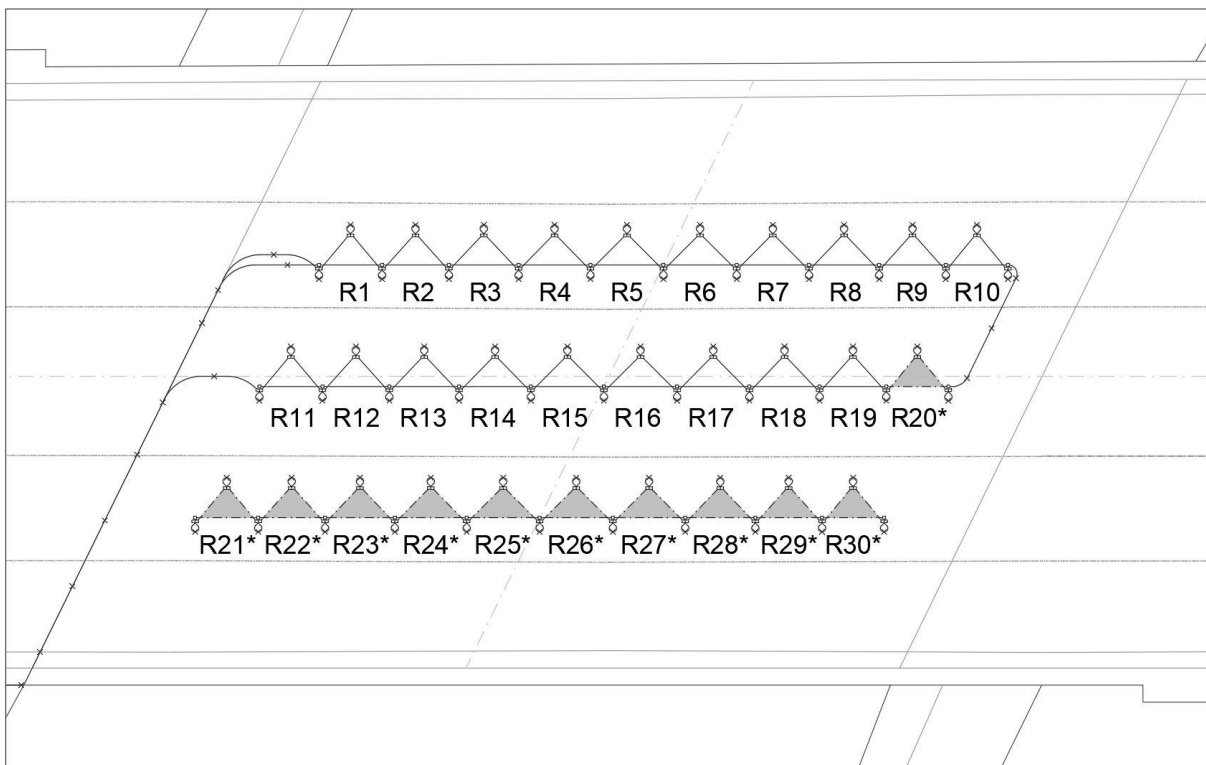


*Figure 6.1: Plan view of the arch soffit at CFM-5, showing the installed FBG rosettes R1 to R19, and the locations of imagined rosettes R20\* to R30\*, for which results are inferred*

The fibre breakage occurred in the loop at one of the sawtooth clamps (see Figures 4.7 and 6.2), because the fibre had been twisted as the loop was installed. It was noted earlier, in section 4.3.2, that the loop at each sawtooth clamp has been designed so that the induced bending

stresses are admissible. However, the combination of bending and twisting stresses in this instance was enough to cause failure.

### 6.1.1.1 Calculating the general strain state in an FBG rosette

A typical FBG rosette is shown in Figure 6.2. The three FBG strains  $\epsilon_{a,b,c}$  represent an average of the strain state, over the  $0.25 \text{ m}^2$  area of the rosette, and can be related to the strains in a local  $x, y$  coordinate system using equation (6.1).

$$\epsilon_{a,b,c} = \frac{\epsilon_x + \epsilon_y}{2} + \frac{\epsilon_x - \epsilon_y}{2} \cos(2\theta_{a,b,c}) + \frac{\epsilon_{xy}}{2} \sin(2\theta_{a,b,c}) \quad (6.1)$$

Here,  $\theta$  represents the angle between the local  $x$  axis and the orientation of the FBG in question. A convenient starting orientation aligns the local  $y$  axis with the eastward skewed span direction. Hence,  $\theta_a = 90^\circ$ ,  $\theta_b = 135^\circ$ , and  $\theta_c = 225^\circ$ , and this local strain state is given by:

$$\epsilon_x = \epsilon_b + \epsilon_c - \epsilon_a, \epsilon_y = \epsilon_a, \epsilon_{xy} = \epsilon_c - \epsilon_b \quad (6.2)$$

Having defined the strains in this  $x, y$  coordinate system, strains in other orientations can easily be found by applying Equation (6.1). The Mohr's circle of strain for this rosette, shown schematically in Figure 6.2, can also be obtained. This has radius  $R = \sqrt{\left(\frac{\epsilon_y - \epsilon_x}{2}\right)^2 + \left(\frac{\epsilon_{xy}}{2}\right)^2}$  and centre  $C = \frac{\epsilon_x + \epsilon_y}{2}$ .

The principal strains are found by identifying the local 1,2 coordinate system for which the shear strain in the rosette is  $\epsilon_{12} = 0$ , at each instance in the time history. The orientations of the 1,2 axes can be found relative to the  $x$  axis defined above, using the Mohr's circle of strain, as half of the respective angles subtended between the point  $\left(\epsilon_x, \frac{-\epsilon_{xy}}{2}\right)$  and the points  $(\epsilon_{1,2}, 0)$ . The magnitudes of the principal strains are found simply as  $\epsilon_{1,2} = C \pm R$ .

The sign convention used here is that  $\epsilon_1 < \epsilon_2$ . Since tensile strains are defined as positive,  $\epsilon_2$  is typically tensile while  $\epsilon_1$  tends to be compressive. Principal strain orientation  $\phi$  is defined to be zero along the eastward skewed span direction, and positive for right-hand rotations when the bridge is viewed in plan from above.

Time histories of the principal strains for the 19 installed FBG rosettes, under the passage of a typical Class 185 passenger train on the north track, are given in Figure 6.3. In this figure, the orientation of the tensile principal strain  $\epsilon_2$ ,  $\phi_2$ , is plotted simply as  $\phi$ . By definition, the two principal strains are always orthogonal to each other. It can be seen from Figure 6.3 that, when

they reach their maximum values,  $\epsilon_1$  and  $\epsilon_2$  tend to be approximately aligned with the skewed span direction (i.e.,  $\phi_{1,2} = 0$ ).

The principal strains at CFM-5 are studied in greater depth in section 6.1.2. Strain states in coordinate systems aligned with the skewed span and square span directions are also investigated, in section 6.1.3.

This is believed to be the first application of dynamic monitoring with FBG strain rosettes, as well as the first use of FBG monitoring of any kind at a skewed masonry arch. A larger scale fibre-optic rosette, using Brillouin sensing, has previously been developed for monitoring geotechnical earth structures. This was reported by Brückl et al. (2013) and Lienhart (2015). Brillouin sensing permitted only static strain monitoring, with measurements taken every 15 minutes. While this was appropriate for the geotechnical structures considered in that study, the smaller scale and significantly higher sampling frequencies of the FBG rosettes presented here make these applicable for monitoring a far broader range of civil engineering structures.

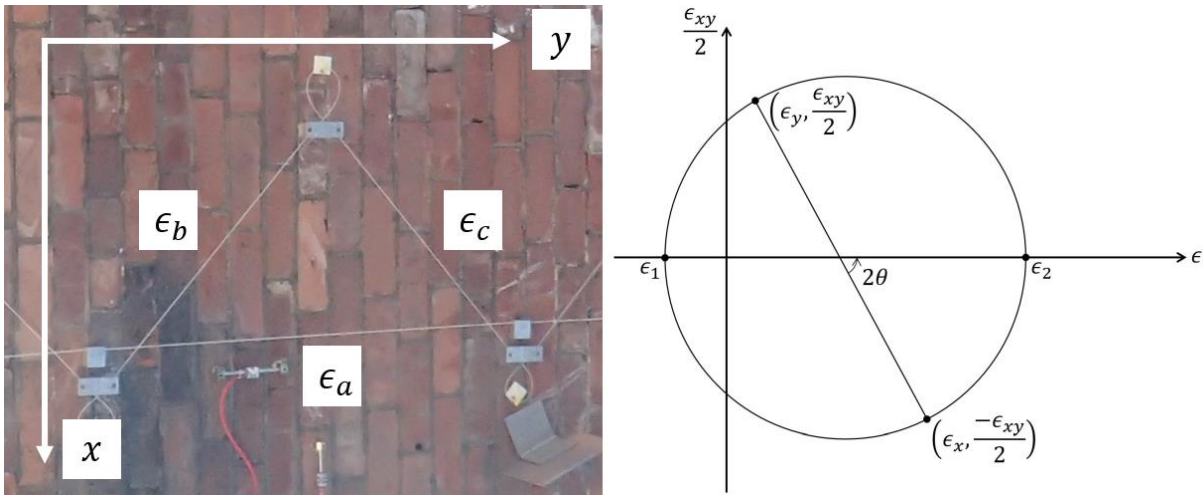


*Figure 6.2: (Left) view of a typical FBG rosette, highlighting the three measured strains  $\epsilon_{a,b,c}$  and local  $x, y$  coordinate system, and (right) the Mohr's circle of strain, showing the rosette's locally-defined strain state  $\epsilon_{x,y,xy}$  in relation to its principal strains  $\epsilon_{1,2}$  which are oriented by an angle  $\theta$  relative to this local  $x, y$  coordinate system*

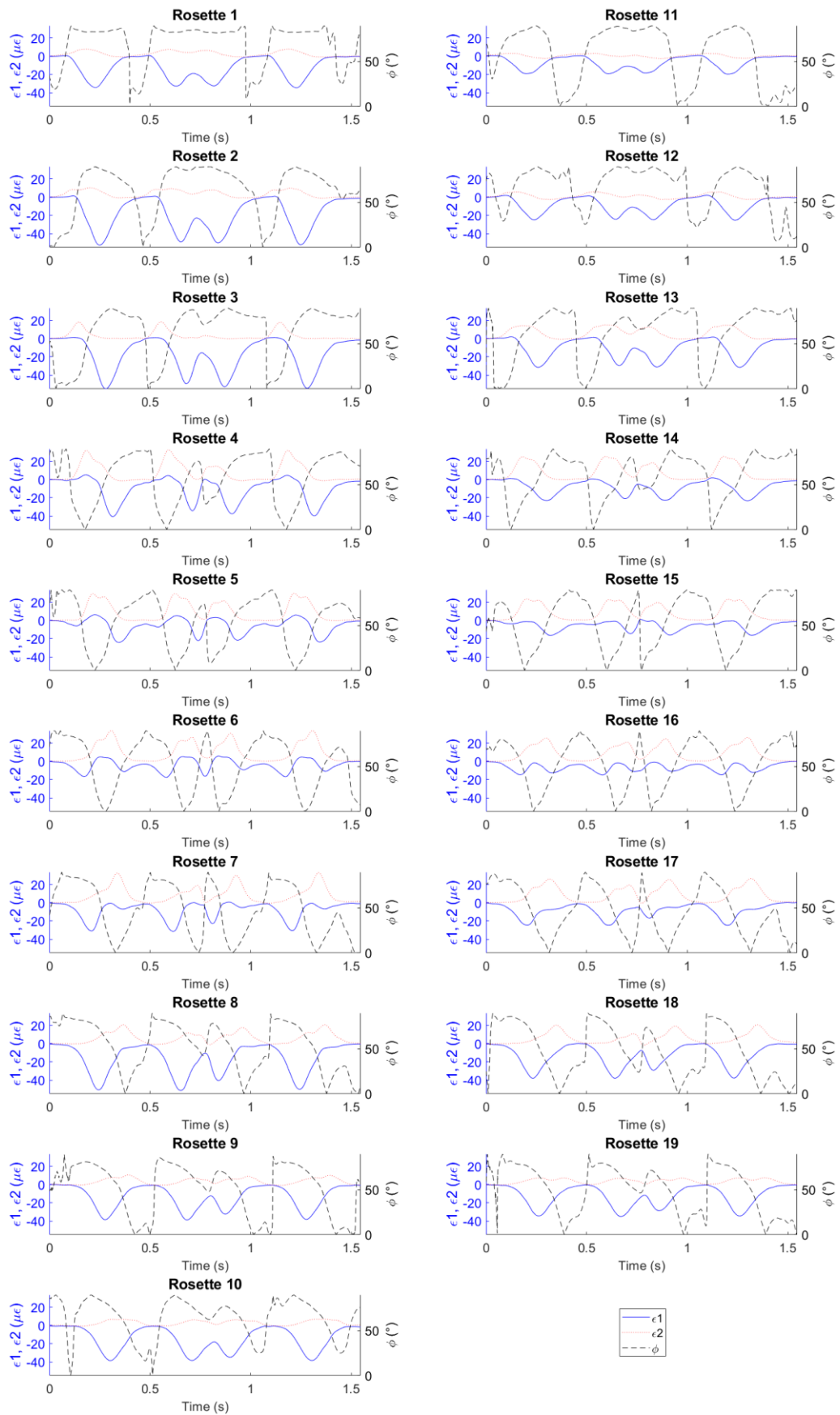


Figure 6.3: Time histories of the principal strains  $\epsilon_{1,2}$  and orientation  $\phi$  of principal strain  $\epsilon_2$  for rosettes R1 to R19, during the passage of a typical Class 185 passenger train

### 6.1.1.2 Symmetry in the bridge response

It can be seen – for instance, in Figure 6.1 – that there is rotational symmetry of order two in the geometry and loading (i.e., track locations) of the arch barrel. Intuitively, then, it seems reasonable that when trains pass on the south track, the response measured at rosettes R1 to R10, underneath the north track, could be used to infer the response at an imagined set of rosettes R21\* to R30\*, underneath the south track, to trains passing on the north track.

This assumption can be investigated by comparing the response at rosettes R12 to R19 for trains passing on both the north and south track. Figures 6.4(a) to 6.7(a) plot the statistical distributions of the principal strains at rosettes R12 to R19 for all recorded Class 185 passenger trains, considering key moments in the time history response. Plan views of the arch in Figures 6.4(b) to 6.7(b) have been highlighted to show the locations of applied loads at these instances in time, at which the responses plotted above in boxplots were recorded. Figure 6.4 shows the responses for peak axle loads applied directly above the western third point of the north track. Figures 6.5, 6.6, and 6.7 correspond, respectively, to peak axle loads on the north track applied just west of the arch crown, just east of the arch crown, and at the eastern third point.

In these plots, distributions of the responses to trains passing on the north and south track are shown in red and blue boxplots, respectively. For the boxplots corresponding to trains passing on the south track, the load locations and rosette strains have been rotated to match each case that has been plotted for trains passing on the north track. For clarity, Figures 6.4(b) to 6.7(b) label the rosettes, load locations, and directions of train travel, in red and blue for trains on the north and south tracks, respectively. In Figure 6.4, for example, data recorded at rosette R12 for loads applied at the south-eastern third point are plotted alongside the response at rosette R19 under loads applied at the north-western third point. Thus, for south track trains, this rosette is labelled as R19' in Figure 6.4(b). A consequence of plotting the data in this way is that, if the bridge exhibits perfect rotational symmetry, then the red and blue data points would coincide exactly.

Figures 6.4(a) to 6.7(a) show that the two sets of principal strain distributions share broadly good agreement in their patterns, across the arch span, but typically some disagreement in the strain magnitudes. It is important to view this disagreement within the context of the known bridge damage. To provide this context, Figures 6.4(b) to 6.7(b) also show the most notable cracking damage to the arch barrel as red, dashed lines.

In these figures, the tensile principal strains  $\epsilon_2$  typically reach their peak values at the rosettes whose locations along the skewed arch span match those of the applied loads. In other words,

planes containing both the applied vertical load and the point along the longitudinal centreline where peak tensile strain is observed will typically be aligned with the skewed transverse direction. Compressive principal strains  $\epsilon_1$  reach their peak values on the opposite side of the arch to the applied loads. Both principal strains are seen to have an orientation that, at their peak magnitudes, approaches the skewed span direction,  $\phi = 0^\circ$ . These observations are in line with the earlier discussion on the arching response in the longitudinal direction, in section 5.2.1.

In Figure 6.4, the peak values of  $\epsilon_1$  and  $\epsilon_2$  are seen to reach larger magnitudes and exhibit greater variability in response to loads at the south track – i.e., the blue boxplots show larger median values and increased statistical spread for the peak strains. One possible explanation for this could be increased damage over the southern half of the arch – in particular, the south-eastern longitudinal crack. This can be seen in Figure 6.4(b) to be directly below the point of application of the load, on the south track, and could potentially lead to a larger magnitude of response when loads are applied in this region.

It can also be seen in Figure 6.4 that, for the case of loading on the south track, the peak tensile strain  $\epsilon_2$  occurs closer to the arch crown than is the case for loading on the north track. It is likely that this is also influenced by the south-eastern crack. If the peak tensile strain were to occur in line with the loading point, in accordance with the trend described above, then the peak strain would also be in line with this crack. However, transverse load transfer will be more feasible within the uncracked portion of the arch barrel, and so it makes sense for the peak tensile strains to occur ahead of the crack tip. It is possible that this mechanism of transverse load transfer could contribute to growth of the south-eastern crack over time, although this has not yet been observed in long-term monitoring (see section 8.4).

In Figure 6.4, the orientations of principal strains agree very well for rosettes R13 to R16, a region that includes the peak tensile strains  $\epsilon_2$ . However, there is less agreement over the region of peak compressive strains  $\epsilon_1$  (i.e., rosettes R17 to R19). Here, the response to trains on the north track is more closely aligned with the skewed span direction than is the case when trains are on the south track;  $\phi = 3.64^\circ$  to  $11.41^\circ$  compared to  $\phi = 14.17^\circ$  to  $23.54^\circ$ . In the latter case, these obliquely oriented strains suggest a tendency for thrusts to develop into the acute corner of the skewed arch, towards the south-western end of the abutment. However, this trend is less prominent towards the north-eastern acute corner.

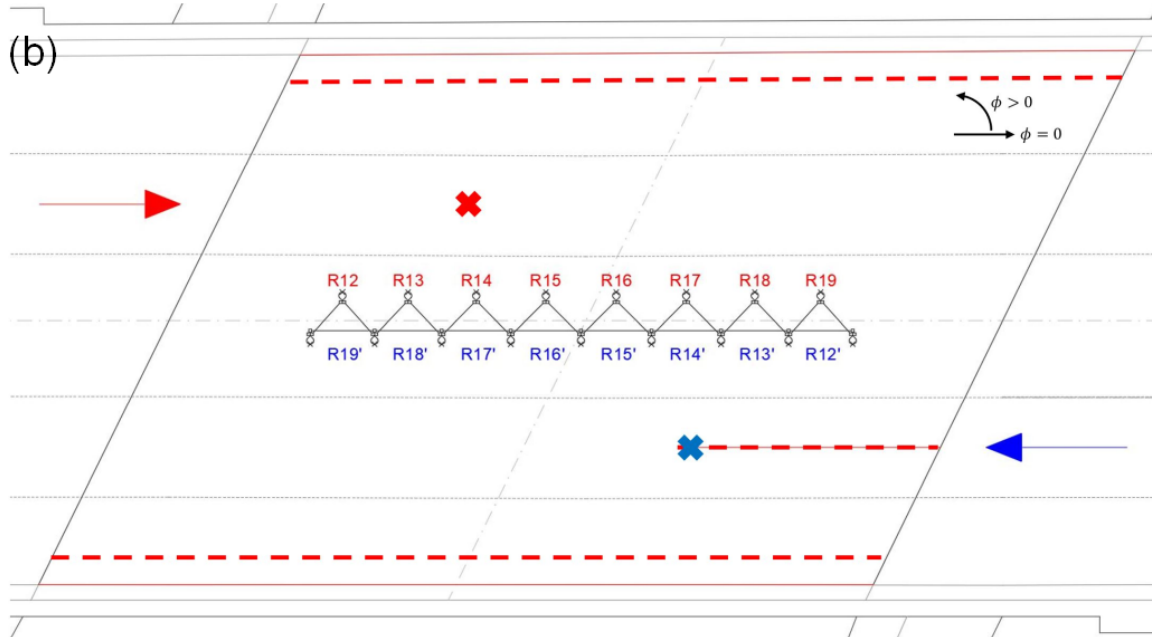
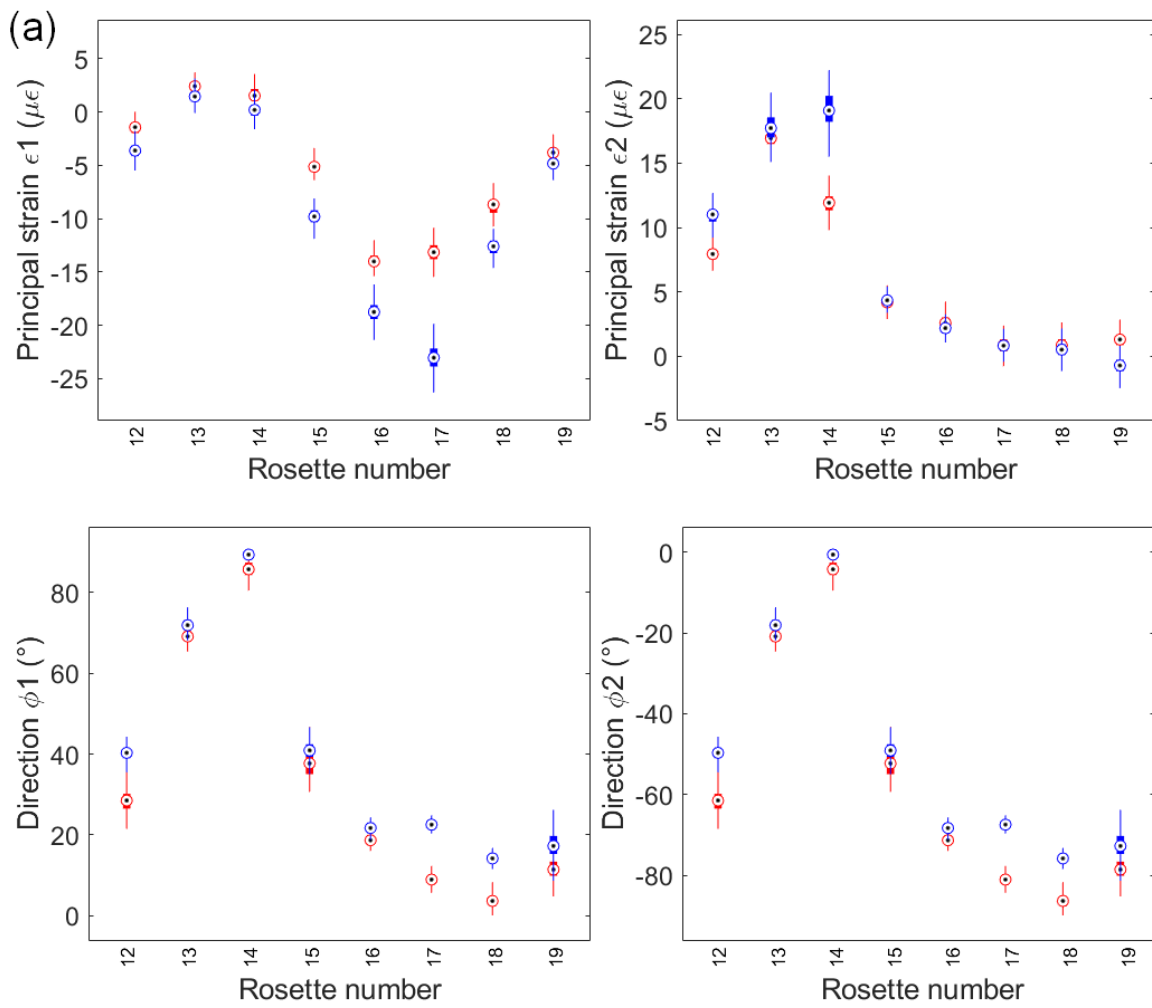


Figure 6.4: (a) Statistical distributions of instantaneous principal strains along the bridge centreline, for peak axles of all recorded Class 185 passenger trains applied to the western third point of the north track (in red), and the eastern third point of the south track (in blue, response rotated to match north track); (b) schematic showing load and rosette locations, and key arch damage

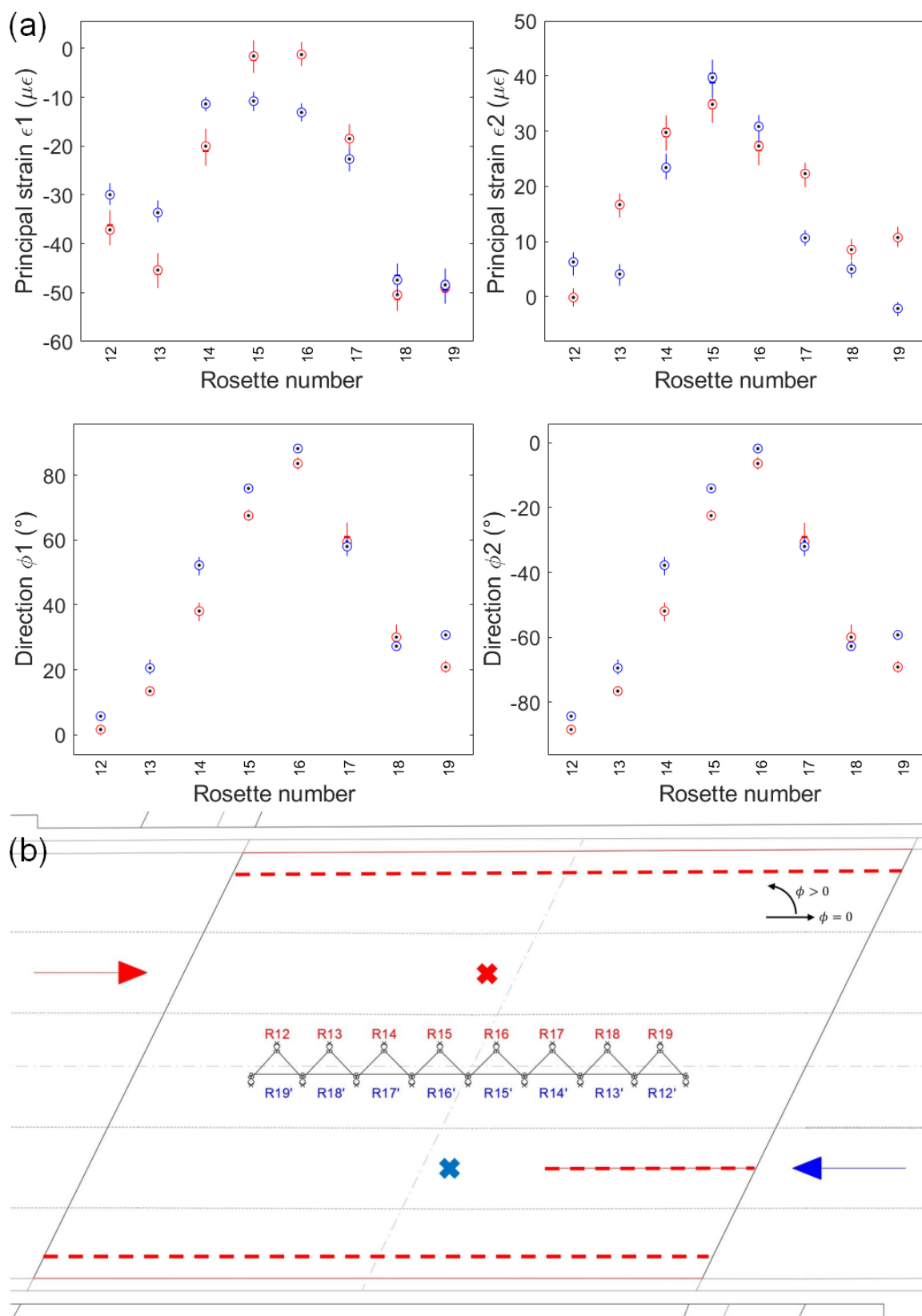


Figure 6.5: (a) Statistical distributions of instantaneous principal strains along the bridge centreline, for peak axes of all recorded Class 185 passenger trains applied just west of the arch crown on the north track (in red), and just east of the arch crown on the south track (in blue, response rotated to match north track); (b) schematic showing load and rosette locations, and key arch damage

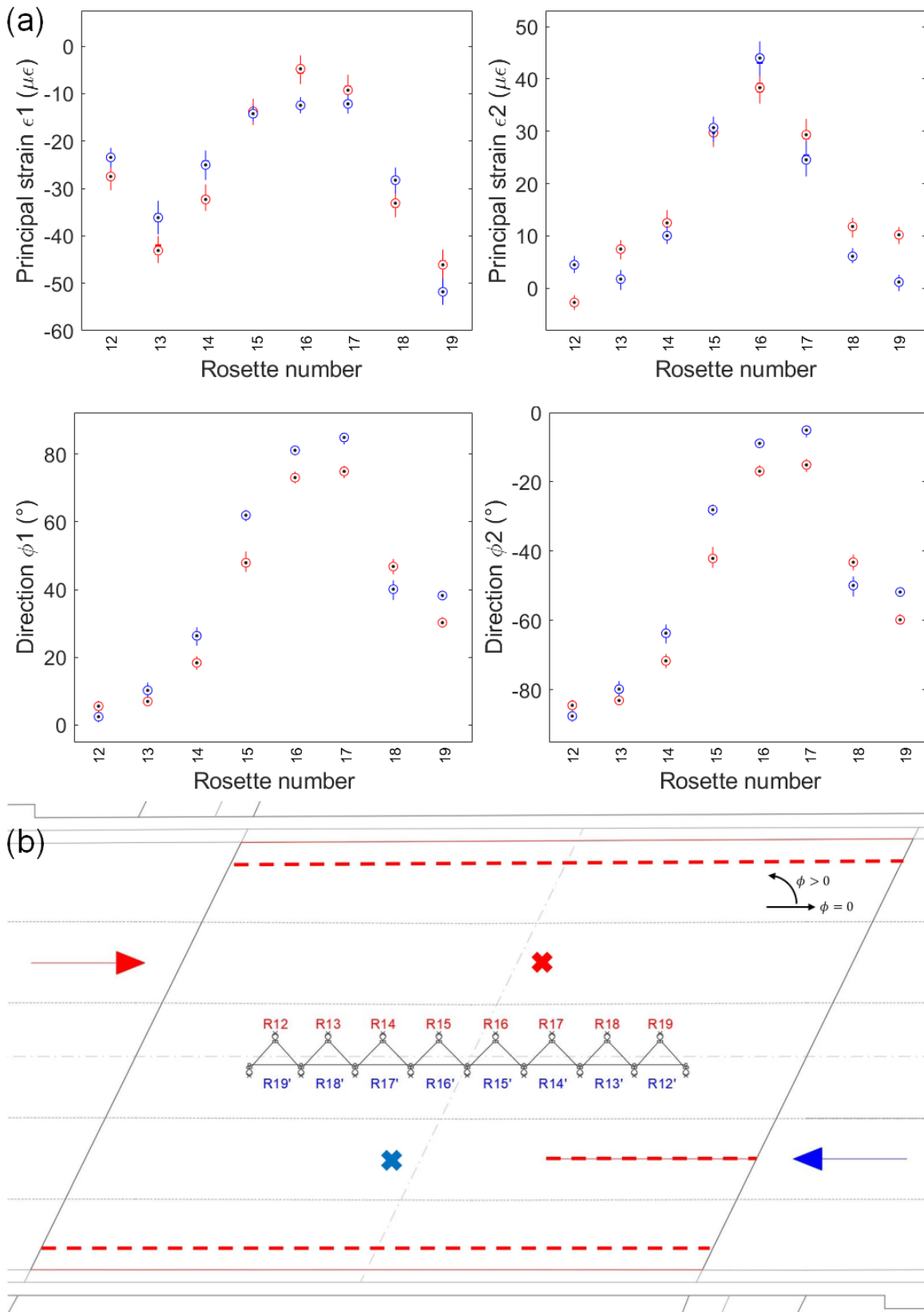


Figure 6.6: (a) Statistical distributions of instantaneous principal strains along the bridge centreline, for peak axes of all recorded Class 185 passenger trains applied just east of the arch crown on the north track (in red), and just west of the arch crown on the south track (in blue, response rotated to match north track); (b) schematic showing load and rosette locations, and key arch damage

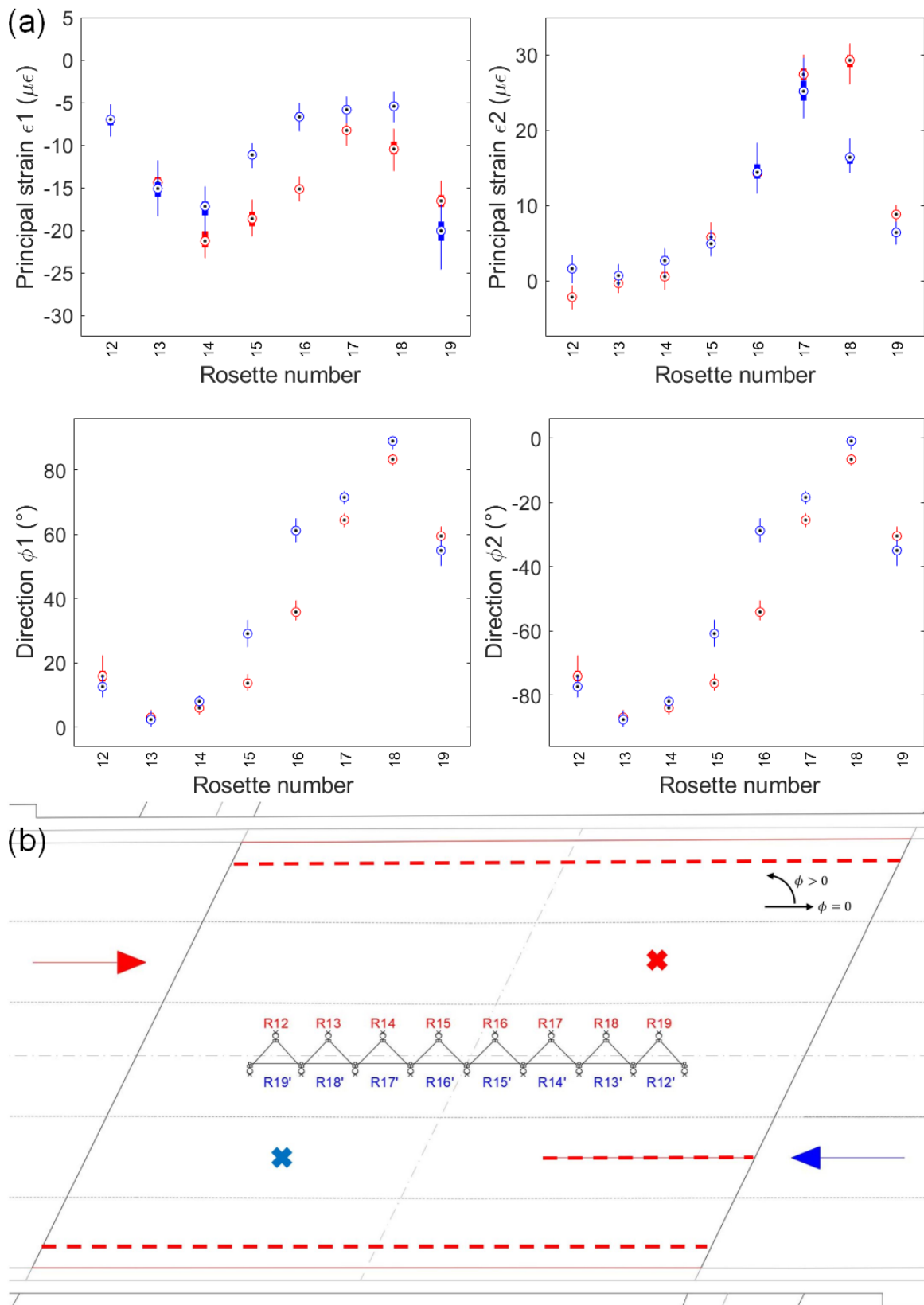


Figure 6.7: (a) Statistical distributions of instantaneous principal strains along the bridge centreline, for peak axes of all recorded Class 185 passenger trains applied to the eastern third point of the north track (in red), and the western third point of the south track (in blue, response rotated to match north track); (b) schematic showing load and rosette locations, and key arch damage

Note that, for the case of trains on the north track, these compressive strains occur in the vicinity of the south-eastern crack, while the response to trains on the south track occurs in the undamaged western half of the barrel. This damage may limit the extent to which compressive thrusts can develop towards the north-eastern acute corner. Furthermore, the detailed distributions of damage along the two spandrel separation cracks are unknown and these cracks may therefore have an uneven influence on the behaviour of the adjacent edges of the arch barrel.

Figures 6.5 and 6.6 show the responses along the bridge centreline when axle loads are applied either side of the arch crown. In both cases, peak compressive strains  $\epsilon_1$  tend to reach higher magnitudes in response to trains passing on the north track, with the opposite being true of peak tensile strains  $\epsilon_2$ . Furthermore, when  $\epsilon_2$  reaches peak values in response to trains on the north track, the smaller principal strain,  $\epsilon_1$ , approaches zero. However, when loads are applied to the south track, the magnitudes of compressive strains do not drop below  $10 \mu\epsilon$  even at points where tensile strains reach their peak values (see the results plotted for rosettes R14 to R16 in Figure 6.5(a), and R15 to R17 in Figure 6.6(a)). This suggests that, when trains pass on the south track, the transverse component of the arch response plays a more significant role in resisting the applied loads.

In response to trains on the south track, the orientations of  $\epsilon_1$  tend to be slightly higher (although both loading cases result in thrusting towards the acute corners) and the orientations of  $\epsilon_2$  tend to be slightly closer to  $0^\circ$  – i.e., the skewed span direction. This is particularly the case when  $\epsilon_1$  and  $\epsilon_2$  reach peak values.

Figure 6.7 shows the bridge centreline responses to train loads applied at the eastern third point of the north track and western third point of the south track. Although the patterns of strain response agree well, higher peak tensile strains  $\epsilon_2$  and generally higher compressive strains  $\epsilon_1$  are observed in response to trains passing on the north track.

Strain orientations agree well on the unloaded half of the arch span while there is some disagreement on the loaded half, over which the response to trains on the south track tends to have an orientation that is aligned slightly closer towards the skewed span direction. The response to trains on the north track, however, is more inclined. Furthermore, for trains on the north track, the magnitudes of compressive strain remain more appreciable – at approximately  $8\text{-}10 \mu\epsilon$  – at locations where tensile strains reach their highest values. In the response to trains on the south track, the corresponding compressive strains are smaller, at around  $5 \mu\epsilon$ .

These results highlight the impact of the asymmetric distribution of damage, particularly the south-eastern crack, on the bridge response to applied loading. However, while the high sensitivity of the FBG measurements allows for these trends to be clearly observed, it is important to note that the strain magnitudes – and the observed differences in strain – are often very small; the effects of the damage may therefore also be small. In particular, the underlying similarities in the responses to trains passing on the north and south tracks suggest that, in the absence of this damage, the bridge would be likely to display rotational symmetry in its structural behaviour.

In the following sections, strain states across the bridge are visualised through quiver plots of the rosette strain data. The assumption of rotational symmetry has been used to extrapolate responses for the imagined rosette locations shown in Figure 6.1, although it is recognised that, due to the findings in this section, such predictions will be imperfect. The south-eastern crack will influence the measured response at the rosettes on the north side of the bridge, to some extent, but will have a more significant impact on the behaviour of its south side, which cannot be properly accounted for in these predictions.

Likewise, since this crack does have some impact on the behaviour of the north side of the bridge, where strains are measured, the flow of force that is visualised in the quiver plots will not be fully representative of the behaviour of an equivalent but undamaged bridge. However, these deviations are expected to be minor.

The statistical spread of the rosette strain data is generally very low, as can be seen in the boxplots of Figure 6.4(a) to 6.7(b). Given this high consistency of response, the following sections will consider the spatial distribution of median strain responses over the bridge.

## **6.1.2 Mapping principal strains in the arch**

### **6.1.2.1 The principal strain response for Class 185 trains**

Averaged across all recorded Class 185 passenger trains, the median principal strain responses in the arch, to loads applied on the north track at key points along the arch span, are shown in Figure 6.8. At each rosette, quiver plots show tensile and compressive principal strains as red and blue vectors, respectively. Consistent scaling is used throughout the quiver plots. These strains have been calculated at times in the train loading events corresponding to peak responses (a) at the western third point (above rosette R3 in Figure 6.1), (b) just west of the arch crown (above rosette R5), (c) just east of the arch crown (above rosette R6), and (d) at the eastern third point (above rosette R8). In each of these four cases, the location of applied axle loads is highlighted by a green circle.

These quiver plots clearly visualise several of the key findings identified previously. In the region of the arch beneath the applied axle load, a band of tensile strains is observed which, at least directly underneath the loading point, is roughly aligned with the skewed span direction. Outside of the tensile region, compressive principal strains dominate the response; these are more likely to be inclined towards the acute corners of the arch. The pattern of tensile and compressive strains matches the expectations for arching action in the longitudinal direction, whereby the thrust lines will pass closest to the extrados underneath the point of loading – and hence give rise to tensile intrados strains – while thrust lines approach the arch extrados either side of this loaded region – hence giving rise to compressive intrados strains in these areas. This arching action approximately follows the skewed span direction.

Although the relatively large size of the vectors that are roughly aligned with the skewed span direction suggests that longitudinal arching action is the primary load path within the arch barrel, rosettes often exhibit appreciable secondary principal strains that suggest the existence of another load path in the transverse direction of the bridge. The transverse response is studied later in section 6.2, utilising vertical deflection data measured with videogrammetry.

Note that the directions of peak shear strain will be at  $\pm 45^\circ$  to the principal strains in Figure 6.8. Either side of the bands of tensile principal strain, which occur directly underneath the applied axle loading, there is a general tendency for principal strains to be aligned at roughly  $\pm 45^\circ$  to the skewed span direction, meaning that the peak shear strains at these locations will be approximately aligned with the transverse direction of the bridge. Distributions of shear strain are discussed further in section 6.1.3, in which strain distributions in key orientations are presented.

#### **6.1.2.2 Variability of this response to different train loads**

Statistical spread in the rosette principal strains is low, suggesting a consistent arch response to applied train loads over many loading cycles. Additionally, this response is found to be similar between different train classes, and very similar between different categories within the same train class – for instance, between groups of data that have been classified by train speed or time of day/predicted passenger levels, as in the analysis in Chapter 5. In particular, the orientations of the principal strains are consistent between these different data groups. Variation of the principal strain magnitudes is in line with the observations made in the strain sensitivity study in Chapter 5. Quiver plots for these different train categories are not presented here, as the differences are small enough to often be visually indistinguishable.

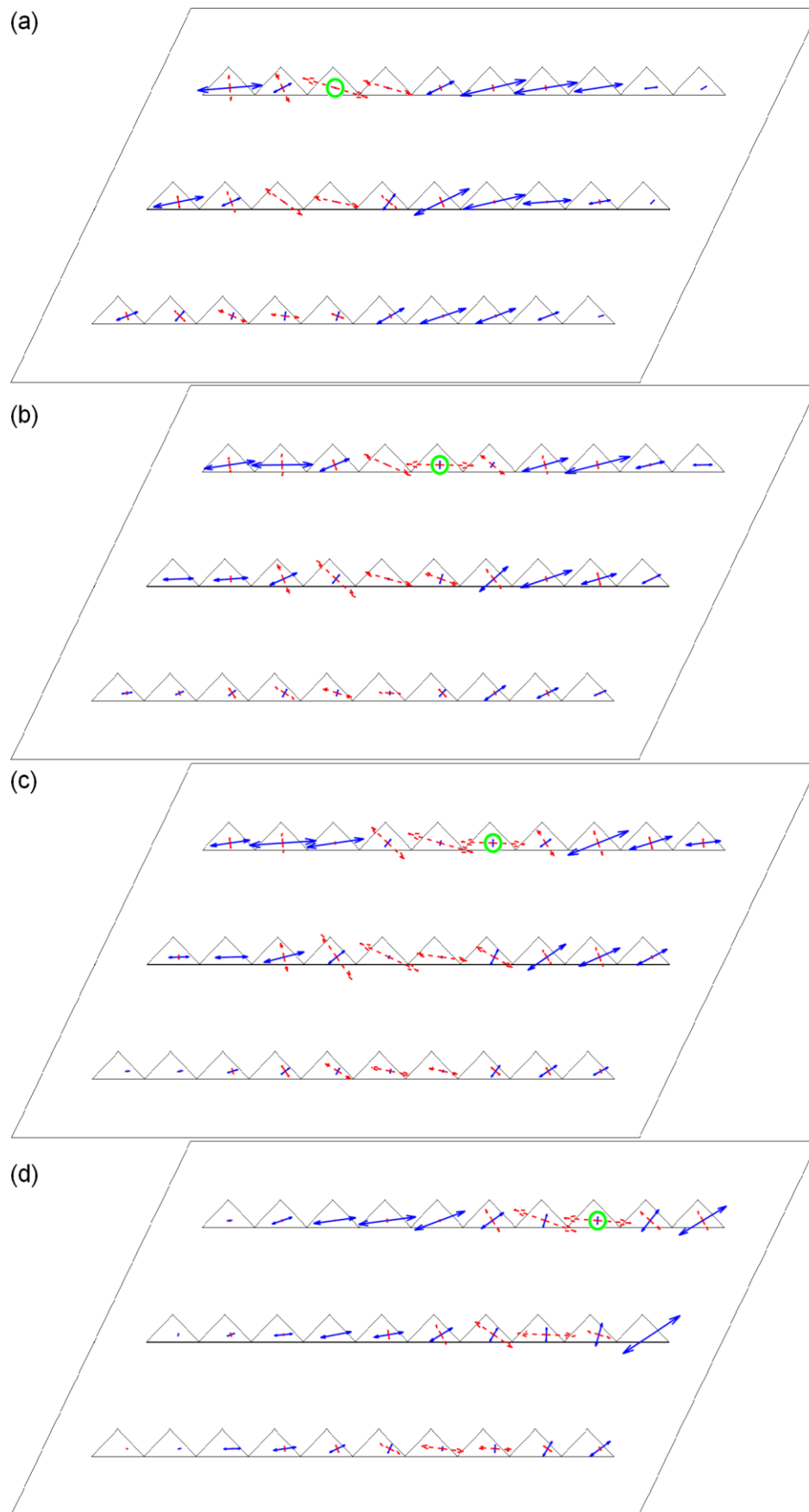


Figure 6.8: Quiver plots showing the median principal strain response in the arch to Class 185 trains, with axle loads applied to the (a) western third point, (b) western side of the arch crown, (c) eastern side of the arch crown, and (d) eastern third point (tensile principal strains in red; compressive principal strains in blue)

Instead, the rosette strain data for the different train classes have been tabulated for comparison. Tables 6.1 to 6.3 compare the median principal strain responses for Class 185 trains against those of Class 150 and Class 222 trains: magnitudes of the principal strains,  $\epsilon_1$  and  $\epsilon_2$ , and the orientation of the the first principal strain,  $\phi_1$ . Variation of the second principal strain orientation,  $\phi_2 = \phi_1 + 90^\circ$ , is not tabulated since this will be identical to the variation of  $\phi_1$ .

These tables include data for each rosette, R1 to R30\* in Figure 6.1; borders are used to distinguish between the three lines of rosettes, and the imaginary rosettes – for which results have been inferred using symmetry – are shaded grey. Results are presented for each of the four axle load locations plotted in Figure 6.8.

In Tables 6.1 and 6.2, the relative strain changes are given as percentage changes compared to the Class 185 response. The colour scheme in these tables is a graphic representation of a boxplot. For each column, values within the inter-quartile range are not shaded; values within the whiskers – defined to extend by 1.5 times the inter-quartile range beyond the upper and lower quartiles – are shaded in yellow; and values beyond the whiskers are outliers and are shaded in orange. Therefore, in each of these columns, the half of the data that is furthest from the median will be coloured either yellow or orange.

Often, the highest percentage changes in principal strain magnitude occur for strains whose absolute values are very low – for instance, the minor principal strains  $\epsilon_1$  occurring at points where  $\epsilon_2$  reaches peak values of tension. Small changes in their strain magnitudes can therefore result in high percentage variations, and importance should not be attached to these outliers.

It is also worth noting that there is little pattern in the median values of strain magnitude variation, between Class 185, Class 150, and Class 222 trains. The critical applied axle loads for Class 185 trains are approximately 2% higher than those of Class 150 trains and 19% higher than those of Class 222 trains, in conditions of maximum passenger loading. However, at CFM-5 the median decrease in the strain response under Class 150 trains, relative to Class 185 trains, is 29%, and the corresponding relative increase for Class 222 trains is 6% – these variations bear no resemblance to the anticipated differences in applied axle loading.

It is possible that spread in the passenger levels between trains could explain this. The majority of recorded Class 185 trains are known to have been heavily loaded commuter trains, but corresponding passenger levels are not known for the Class 150 and Class 222 trains. Furthermore, a significantly higher number of Class 185 trains were recorded (see Table 4.1), while the lower numbers of Class 150 and Class 222 trains could mean that, statistically speaking, the responses to these train types are more poorly defined.

The orientations of the principal strains, shown in Table 6.3, are broadly consistent for the responses to the three train classes. In this table, relative changes from the Class 185 response are given as angles (in degrees) rather than percentage changes. A simplified colour scheme has been used to highlight significant deviations from the Class 185 response. Changes in angle of more than  $5^\circ$  are highlighted in light blue, while changes greater than  $10^\circ$  are highlighted in dark blue.

It is clear from Table 6.3 that, in most cases, the orientations of principal strains are remarkably consistent in the three responses to Class 185, Class 150, and Class 222 trains. One clear exception is the response to Class 222 trains, when axle loads are applied above rosette R6 – or, more precisely speaking, when loads are applied such that they produce the peak response at R6. For this load case, outliers are also observed in the relative changes in strain magnitudes, particularly for strain  $\epsilon_1$ . While the majority of the orange-coloured outliers in Tables 6.1 and 6.2 often correspond to low-magnitude strains, for which even small variations in their value will result in high percentage changes, this is not always the case when Class 222 axles are above rosette R6.

*Table 6.1: Variation of arch principal strains  $\epsilon_1$  between different classes of passenger train (percentage changes shown relative to Class 185; results inferred from symmetry are highlighted in grey)*

Rosette:	Response to C185 trains; axle above:				Axle above rosette 3				Axle above rosette 5				Axle above rosette 6				Axle above rosette 8			
	Rosette 3	Rosette 5	Rosette 6	Rosette 8	C150		C222													
	Strain ( $\mu\epsilon$ ):	Strain ( $\mu\epsilon$ ):	Strain ( $\mu\epsilon$ ):	Strain ( $\mu\epsilon$ ):	Strain ( $\mu\epsilon$ ):	Relative to C185 (%):	Strain ( $\mu\epsilon$ ):	Relative to C185 (%):	Strain ( $\mu\epsilon$ ):	Relative to C185 (%):	Strain ( $\mu\epsilon$ ):	Relative to C185 (%):	Strain ( $\mu\epsilon$ ):	Relative to C185 (%):	Strain ( $\mu\epsilon$ ):	Relative to C185 (%):	Strain ( $\mu\epsilon$ ):	Relative to C185 (%):	Strain ( $\mu\epsilon$ ):	Relative to C185 (%):
1	-17.69	-47.29	-43.02	-2.71	-12.48	29.48	-19.51	-10.28	-32.48	31.32	-48.96	-3.53	-28.78	33.10	-25.01	41.85	-1.99	26.65	-2.96	-9.26
2	-5.38	-56.52	-72.27	-10.89	-3.84	28.54	-6.48	-20.48	-40.17	28.93	-66.49	-17.64	-48.97	32.23	-55.42	23.32	-7.79	28.42	-10.95	-0.59
3	0.41	-29.04	-62.11	-21.99	0.29	-28.27	0.32	-20.05	-21.20	27.02	-33.67	-15.95	-46.39	25.31	-71.36	-14.88	-15.62	28.96	-22.68	-3.14
4	0.46	-0.76	-10.22	-29.82	0.55	19.46	0.50	8.78	-0.12	84.82	-0.43	43.60	-8.03	21.46	-50.51	-394.20	-21.03	29.49	-31.60	-5.95
5	-8.20	6.71	5.12	-27.69	-5.84	28.82	-8.63	-5.25	5.46	-18.71	7.03	4.69	3.94	-23.06	-9.54	-286.47	-19.67	28.96	-29.16	-5.31
6	-18.31	-5.62	7.44	-14.03	-12.59	31.25	-19.53	-6.65	-3.89	30.82	-5.91	-5.02	5.88	-21.04	6.27	-15.76	-10.48	25.30	-15.01	-6.97
7	-17.53	-43.70	-14.03	-6.59	-11.95	31.83	-18.78	-7.15	-30.99	29.08	-44.61	-2.08	-10.01	28.67	-0.12	99.12	-5.40	18.07	-7.09	-7.61
8	-13.32	-61.48	-70.08	-3.80	-9.47	28.94	-14.17	-6.37	-42.90	30.23	-66.13	-7.57	-49.19	29.81	-44.74	36.16	-3.49	8.10	-4.91	-29.29
9	-3.54	-26.93	-48.36	-13.86	-2.78	21.59	-3.85	-8.64	-18.62	30.84	-31.37	-16.52	-33.26	31.23	-52.79	-9.17	-10.79	22.18	-15.82	-14.12
10	-1.80	-17.56	-37.90	-28.27	-1.48	17.78	-2.11	-17.46	-12.61	28.21	-20.58	-17.16	-27.18	28.29	-53.46	-41.06	-20.88	26.15	-30.89	-9.25
11	-13.91	-27.85	-22.04	-1.46	-9.88	28.94	-15.87	-14.13	-18.67	32.94	-28.53	-2.45	-14.02	36.38	-10.96	50.26	-1.02	30.14	-1.59	-8.91
12	-5.42	-31.34	-35.15	-4.17	-3.80	29.84	-5.78	-6.64	-22.01	29.76	-34.53	-10.18	-22.92	34.80	-23.85	32.15	-2.86	31.51	-4.11	1.41
13	0.37	-27.09	-44.89	-9.48	0.38	3.83	0.09	-76.32	-19.59	27.69	-34.07	-25.78	-30.14	32.87	-41.96	6.54	-6.39	32.58	-9.70	-2.35
14	0.32	-10.13	-21.80	-16.26	0.14	-54.94	0.17	-45.69	-7.90	21.94	-11.46	-13.19	-16.31	25.15	-32.17	-47.57	-11.29	30.56	-17.09	-5.11
15	-5.32	-1.84	-3.43	-15.55	-3.79	28.68	-5.86	-10.15	-1.82	1.05	-2.33	-26.50	-3.33	3.04	-19.35	-463.37	-11.01	29.22	-16.29	-4.73
16	-16.52	-8.63	-2.47	-13.46	-11.50	30.37	-17.63	-6.73	-6.14	28.82	-8.42	2.52	-2.59	-4.94	-11.64	-372.04	-9.45	29.77	-13.92	-3.39
17	-17.27	-33.86	-17.93	-7.56	-11.93	30.91	-18.54	-7.37	-23.92	29.36	-34.78	-2.70	-13.04	27.26	-11.41	36.37	-5.38	28.87	-8.21	-8.51
18	-13.16	-49.65	-48.79	-6.89	-9.40	28.54	-14.21	-8.01	-35.17	29.16	-52.43	-5.60	-34.10	30.10	-32.35	33.70	-5.03	26.97	-7.35	-6.68
19	-5.95	-33.47	-47.96	-11.72	-4.51	24.31	-6.61	-11.00	-23.23	30.59	-37.15	-10.99	-32.92	31.36	-46.58	2.86	-8.87	24.27	-12.57	-7.29
20*	-1.48	-18.72	-36.50	-34.73	-1.14	23.23	-1.52	-2.84	-14.56	22.21	-18.24	2.58	-24.08	34.03	-34.07	6.64	-23.70	31.75	-36.94	-6.35
21*	-6.26	-9.69	-4.96	-0.62	-4.07	35.05	-6.72	-7.40	-6.51	32.82	-10.36	-6.90	-4.27	13.86	-5.74	-15.70	-0.66	-7.04	-0.58	5.49
22*	-3.53	-8.08	-5.99	-1.76	-2.39	32.24	-3.88	-9.85	-5.77	28.56	-8.78	-8.62	-4.57	23.70	-6.66	-11.30	-1.78	-0.95	-2.00	-13.64
23*	-1.88	-8.11	-11.66	-8.81	-1.28	32.10	-1.92	-2.28	-6.49	19.94	-8.66	-6.76	-8.04	31.03	-12.25	-5.06	-5.96	32.42	-8.87	-0.58
24*	-2.25	-8.00	-11.24	-11.90	-1.45	35.70	-2.42	-7.63	-6.23	22.03	-8.68	-8.56	-7.93	29.49	-11.42	-1.59	-7.44	37.49	-11.46	3.68
25*	-2.44	-5.70	-7.58	-8.86	-1.75	28.39	-2.72	-11.43	-4.41	22.67	-5.92	-3.81	-5.60	26.05	-7.88	-3.96	-5.66	36.12	-8.94	-0.86
26*	-8.52	-3.43	-4.64	-4.91	-5.54	34.99	-8.79	-3.14	-2.39	30.29	-3.38	1.56	-3.29	29.14	-4.62	0.45	-3.64	25.78	-5.15	-4.96
27*	-13.15	-8.50	-2.60	-2.23	-8.18	37.76	-13.81	-5.04	-5.64	33.73	-9.21	-8.30	-2.31	11.12	-2.77	-6.35	-1.74	22.26	-2.57	-15.38
28*	-11.57	-23.36	-15.32	-3.93	-7.20	37.76	-12.23	-5.71	-16.49	29.38	-25.16	-7.72	-12.60	17.76	-16.98	-10.82	-3.14	20.24	-3.98	-1.28
29*	-6.05	-21.49	-22.15	-8.59	-3.68	39.20	-6.27	-3.59	-15.46	28.05	-22.34	-3.99	-16.61	25.03	-23.77	-7.30	-6.89	19.79	-9.11	-5.98
30*	-1.55	-11.91	-17.93	-12.87	-1.13	26.89	-1.59	-2.67	-8.75	26.52	-12.37	-3.87	-12.33	31.26	-18.34	-2.28	-9.31	27.69	-13.60	-5.63

Table 6.2: Variation of arch principal strains  $\epsilon_2$  between different classes of passenger train (percentage changes shown relative to Class 185; results inferred from symmetry are highlighted in grey)

Rosette:	Response to C185 trains; axle above:				Axle above rosette 3				Axle above rosette 5				Axle above rosette 6				Axle above rosette 8			
	Rosette 3		Rosette 5		Rosette 6		Rosette 8		C150:		C222:		C150:		C222:		C150:		C222:	
	Strain ( $\mu\epsilon$ ):	Strain ( $\mu\epsilon$ ):	Strain ( $\mu\epsilon$ ):	Strain ( $\mu\epsilon$ ):	Strain ( $\mu\epsilon$ ):	Relative to C185 (%):	Strain ( $\mu\epsilon$ ):	Relative to C185 (%):	Strain ( $\mu\epsilon$ ):	Relative to C185 (%):	Strain ( $\mu\epsilon$ ):	Relative to C185 (%):	Strain ( $\mu\epsilon$ ):	Relative to C185 (%):	Strain ( $\mu\epsilon$ ):	Relative to C185 (%):	Strain ( $\mu\epsilon$ ):	Relative to C185 (%):	Strain ( $\mu\epsilon$ ):	Relative to C185 (%):
1	9.24	9.23	5.37	-0.94	6.28	-32.00	10.00	8.25	6.41	-30.53	10.09	9.27	3.36	-37.52	1.33	-75.26	-0.67	28.64	-0.79	16.31
2	12.51	13.14	9.59	-1.01	8.49	-32.13	13.12	4.87	9.20	-29.97	14.02	6.67	6.38	-33.48	2.92	-69.53	-0.89	12.12	-0.99	1.90
3	26.08	6.66	1.52	0.64	18.07	-30.72	27.35	4.87	4.80	-27.95	6.88	3.25	1.26	-17.38	0.95	-37.45	0.50	-22.37	0.83	29.31
4	19.95	32.92	23.81	-1.50	13.56	-32.01	21.51	7.84	23.68	-28.06	36.16	9.85	17.24	-27.62	5.91	-75.18	-1.12	25.58	-1.80	-19.71
5	2.11	43.24	35.57	1.02	1.36	-35.52	2.43	15.41	29.61	-31.52	45.69	5.67	24.26	-31.80	29.13	-18.10	0.80	-22.00	0.88	-14.13
6	2.41	20.72	33.78	10.66	1.57	-34.66	2.70	12.18	15.08	-27.22	23.34	12.64	24.55	-27.31	49.27	45.88	7.52	-29.49	11.51	7.97
7	1.82	11.42	16.89	27.45	1.22	-33.24	2.18	19.47	8.04	-29.59	12.62	10.50	12.37	-26.73	28.55	69.04	18.62	-32.15	29.14	6.16
8	-0.08	4.98	13.00	28.14	-0.02	74.87	-0.13	-60.79	3.53	-29.13	5.62	12.83	8.95	-31.17	18.44	41.84	18.78	-33.25	30.00	6.62
9	-0.26	1.78	6.31	10.98	-0.39	-51.95	-0.52	-101.93	1.01	-43.39	2.16	21.35	4.41	-30.00	10.05	59.31	7.98	-27.32	12.20	11.17
10	-0.12	0.53	4.41	8.47	-0.30	-143.08	-0.25	-107.50	0.47	-11.98	0.73	38.06	3.07	-30.28	8.03	82.14	6.10	-27.99	9.11	7.60
11	4.53	-0.41	-2.45	0.10	3.24	-28.56	4.86	7.35	-0.24	40.57	-0.49	-21.30	-1.65	32.91	-2.21	9.69	0.26	162.53	0.31	213.93
12	8.13	3.87	-0.39	-1.72	5.50	-32.41	8.61	5.93	2.68	-30.73	4.08	5.49	-0.39	1.08	-2.47	-533.27	-1.13	34.17	-1.56	9.25
13	17.28	20.47	15.13	-0.93	12.42	-28.16	18.15	5.05	14.56	-28.88	20.82	1.73	10.30	-31.91	4.86	-67.87	-0.55	41.13	-0.97	-3.61
14	18.19	33.25	27.48	0.10	12.43	-31.65	19.61	7.82	23.15	-30.37	35.21	5.90	18.57	-32.42	7.72	-71.91	-0.01	-109.95	-0.05	-151.98
15	7.47	32.18	33.85	3.65	5.17	-30.72	8.06	7.89	22.08	-31.36	35.71	10.99	21.88	-35.37	24.67	-27.13	2.40	-34.41	3.81	4.33
16	3.88	23.24	27.17	8.72	2.79	-28.02	4.22	8.91	15.96	-31.31	25.18	8.35	19.78	-27.21	39.69	46.08	5.94	-31.91	9.17	5.12
17	1.13	15.05	21.81	18.73	0.79	-29.71	1.34	18.93	11.37	-24.46	16.80	11.58	16.71	-23.37	36.07	65.39	12.90	-31.15	19.68	5.05
18	0.86	3.39	8.32	24.34	0.63	-26.56	0.92	6.72	2.76	-18.78	3.89	14.57	6.48	-22.07	15.21	82.82	16.29	-33.06	25.68	5.52
19	1.74	7.81	10.11	9.83	1.28	-26.67	2.25	29.09	5.68	-27.32	8.69	11.24	7.09	-29.89	9.94	-1.69	6.57	-33.16	10.43	6.13
20*	0.15	-1.06	-1.79	-0.42	0.13	-15.93	0.17	11.64	-0.78	25.88	-1.15	-9.18	-1.11	38.37	-1.67	6.67	-0.31	26.90	-0.47	-12.07
21*	2.96	2.21	0.97	0.74	1.98	-33.05	3.16	6.73	1.24	-43.92	2.34	5.96	0.73	-25.20	1.20	23.72	0.29	-60.52	0.33	-55.98
22*	5.64	3.00	1.16	-0.02	3.76	-33.26	5.85	3.84	2.00	-33.27	3.26	8.72	0.75	-35.49	1.27	9.21	0.13	620.83	0.08	438.75
23*	12.50	7.51	3.11	0.66	7.91	-36.75	13.13	5.04	4.83	-35.72	8.07	7.47	2.27	-27.06	3.37	8.24	0.30	-55.00	0.81	24.18
24*	11.26	14.29	6.84	2.15	6.79	-39.71	11.88	5.48	9.63	-32.62	15.36	7.50	5.11	-25.29	7.46	9.04	1.33	-38.46	2.06	-4.60
25*	5.02	20.49	16.37	3.29	3.08	-38.65	5.53	10.10	14.65	-28.51	22.22	8.45	12.52	-23.51	18.09	10.47	2.55	-22.53	3.46	5.04
26*	1.83	13.85	20.69	9.19	1.15	-37.14	2.07	12.93	10.37	-25.13	14.71	6.15	14.72	-28.85	21.98	6.22	7.19	-21.76	9.34	1.60
27*	0.99	6.86	15.94	17.82	0.62	-37.91	0.97	-2.03	5.36	-21.83	7.07	3.06	10.51	-34.06	15.87	-0.45	12.15	-31.82	18.33	2.89
28*	1.05	2.90	6.14	14.74	0.55	-47.26	1.20	14.41	2.43	-16.13	2.98	2.81	4.02	-34.44	5.77	-5.99	8.55	-41.98	15.05	2.09
29*	0.57	3.74	4.30	4.23	0.33	-42.12	0.43	-23.87	2.71	-27.53	3.84	2.62	3.23	-24.95	4.49	4.55	2.75	-35.03	4.40	4.14
30*	-0.06	1.35	2.29	1.84	-0.04	26.00	0.01	121.82	0.85	-37.50	1.32	-2.51	1.51	-33.95	2.31	0.70	1.27	-30.85	2.04	10.94

Table 6.3: Variation of arch principal strain directions  $\phi_1$  between different classes of passenger train (changes shown relative to Class 185; results inferred from symmetry are highlighted in grey)

Rosette:	Response to C185 trains; axle above:				Axle above rosette 3				Axle above rosette 5				Axle above rosette 6				Axle above rosette 8			
	Rosette 3		Rosette 5		Rosette 6		Rosette 8		C150:		C222:		C150:		C222:		C150:		C222:	
	Angle $\phi$ (°)	Angle $\phi$ (°)	Angle $\phi$ (°)	Angle $\phi$ (°)	Angle $\phi$ (°)	Relative to C185 (°):	Angle $\phi$ (°)	Relative to C185 (°):	Angle $\phi$ (°)	Relative to C185 (°):	Angle $\phi$ (°)	Relative to C185 (°):	Angle $\phi$ (°)	Relative to C185 (°):	Angle $\phi$ (°)	Relative to C185 (°):	Angle $\phi$ (°)	Relative to C185 (°):	Angle $\phi$ (°)	Relative to C185 (°):
1	4.27	7.79	7.67	5.74	4.32	0.05	4.43	0.16	7.49	-0.30	7.49	-0.30	7.43	-0.25	7.12	-0.55	7.35	1.60	5.55	-0.20
2	25.48	0.60	3.59	17.41	24.76	-0.72	24.82	-0.66	1.08	0.49	1.00	0.41	3.74	0.16	6.63	3.04	17.43	0.02	17.04	-0.37
3	74.36	21.32	7.63	7.24	74.70	0.35	74.12	-0.23	21.38	0.06	21.63	0.31	7.67	0.05	0.84	-6.78	6.38	-0.86	7.30	0.06
4	75.44	67.75	48.48	6.90	74.60	-0.84	76.11	0.66	68.38	0.62	68.46	0.71	48.67	0.20	22.20	-26.28	7.76	0.86	7.14	0.24
5	24.24	88.88	74.78	18.97	21.50	-2.74	25.03	0.79	87.45	-1.43	88.71	-0.17	76.15	1.37	51.80	-22.98	19.50	0.53	19.39	0.42
6	12.43	51.82	87.98	33.51	11.86	-0.57	12.39	-0.03	50.36	-1.46	51.59	-0.23	84.10	-3.88	79.15	-8.83	34.01	0.50	33.55	0.04
7	8.68	15.12	33.76	71.83	8.83	0.14	8.58	-0.10	14.63	-0.49	15.82	0.70	32.52	-1.24	78.01	44.25	72.17	0.34	72.10	0.27
8	8.15	13.20	20.31	85.96	8.84	0.69	8.12	-0.03	13.10	-0.10	13.52	0.32	20.01	-0.30	32.95	12.64	84.99	-0.97	85.10	-0.85
9	6.20	12.17	16.04	49.47	9.28	3.08	5.80	-0.40	12.34	0.17	12.35	0.18	16.21	0.17	22.30	6.26	51.08	1.61	49.75	0.28
10	28.35	0.85	6.37	29.43	18.35	-10.00	31.93	3.58	1.10	0.26	1.30	0.45	6.18	-0.18	11.75	5.38	30.11	0.68	29.18	-0.25
11	10.62	2.04	1.66	77.52	10.10	-0.52	10.35	-0.27	2.58	0.54	1.91	-0.13	1.96	0.31	8.65	7.00	72.88	-4.63	68.64	-8.88
12	21.91	3.88	1.44	19.18	21.52	-0.39	21.37	-0.54	4.12	0.24	3.79	-0.09	1.32	-0.12	6.81	5.37	15.47	-3.71	20.21	1.03
13	56.51	22.47	13.29	5.29	56.35	-0.16	56.67	0.16	22.72	0.25	22.42	-0.05	13.48	0.19	5.35	-7.94	3.69	-1.60	5.49	0.21
14	78.89	49.14	36.79	9.86	78.26	-0.62	78.40	-0.49	49.01	-0.12	48.89	-0.25	35.85	-0.94	12.77	-24.02	8.97	-0.89	9.77	-0.09
15	50.63	75.72	66.40	8.98	49.44	-1.19	51.35	0.73	76.79	1.07	76.29	0.57	66.55	0.15	40.07	-26.33	9.10	0.12	8.88	-0.10
16	24.03	71.33	82.89	29.09	23.44	-0.59	24.31	0.28	71.21	-0.12	71.40	0.07	82.44	-0.45	64.94	-17.95	29.18	0.09	29.11	0.02
17	12.02	39.24	62.29	57.60	12.17	0.15	12.25	0.23	39.56	0.32	39.62	0.38	62.25	-0.03	81.67	-19.38	58.10	0.50	57.73	0.13
18	3.97	17.17	32.41	87.95	4.61	0.64	4.23	0.26	16.83	-0.33	17.50	0.33	32.24	-0.17	52.22	19.81	88.46	0.50	88.37	0.42
19	9.24	15.14	22.27	73.05	10.36	1.12	9.49	0.25	15.19	0.05	15.14	0.00	22.61	0.34	33.10	10.84	73.49	0.44	73.36	0.32
20*	43.89	23.95	25.96	31.47	43.99	0.09	41.89	-2.00	23.74	-0.21	23.32	-0.63	25.60	-0.36	24.99	-0.97	31.54	0.07	31.45	-0.02
21*	20.09	7.26	5.78	71.59	21.09	1.00	19.51	-0.57	6.98	-0.28	6.68	-0.58	3.28	-2.50	4.78	-1.00	50.86	-20.72	67.74	-3.84
22*	46.09	21.46	10.85	12.40	45.47	-0.62	44.68	-1.40	20.34	-1.12	20.51	-0.95	9.75	-1.10	10.84	-0.02	10.17	-2.23	13.53	1.13
23*	67.69	35.83	16.10	1.44	68.37	0.68	66.44	-1.24	33.56	-2.27	35.58	-0.25	16.73	0.63	16.45	0.35	1.68	0.24	1.47	0.04
24*	82.84	58.30	35.92	7.36	85.05	2.21	82.53	-0.32	55.66	-2.64	58.26	-0.04	38.70	2.78	38.14	2.21	8.70	1.34	8.03	0.67
25*	70.95	73.46	59.79	24.23	65.43	-5.51	71.63	0.68												

For this peak response to loads above rosette R6, changes in the principal strain orientations  $\phi_1$  under Class 222 trains are most notable for rosettes R3 to R19. A general trend may be observed in Table 6.3 that these changes in angle are negative to the west of the load application point and positive to the east of it. However, the changes are more clearly observed graphically.

In Figure 6.9, median quiver plots are presented for Class 185 and Class 222 trains, both for the loading case that produces the peak response at rosette R6. It can be seen that the band of longitudinal tensile strains, which is anticipated to occur directly underneath the location of the peak axle load, is shifted to the east – i.e., the direction of train travel – for Class 222 trains (Figure 6.9(b)), relative to Class 185 trains (Figure 6.9(a)). This suggests that the peak arch response may occur later in the passage of a Class 222 train than is the case for a Class 185 train. The tensile band also appears to be slightly larger for Class 185 trains than it is for Class 222 trains, although this is difficult to judge precisely given the 1 metre gauge lengths of the rosettes, in the longitudinal direction. These observations can be explored further by considering the differences in the precise loading that is applied by the two trains.

Each ‘axle load’ – as discussed here – is applied by a bogie that has two wheels. Therefore, concentrated loads enter the rail track in two discrete locations. For Class 185 and 222 trains, the bogie wheelbases are, respectively, 2.6 m and 2.25 m. Loads are assumed to pass from the track into the sleepers before entering the ballast and fill material – with half of each wheel load being carried by the nearest sleeper and one quarter going to each of the two adjacent sleepers (Network Rail, 2006). In the same guidance, it is assumed that the average and maximum separation of sleepers is 0.65 m and 0.8 m, respectively, and so the difference in bogie wheelbase may mean that Class 185 loads are spread over one additional sleeper than is the case for Class 222 trains.

Having been distributed through the ballast and fill material, forces are then applied, as a patch load, to the arch extrados. Such patch loads are typically assumed to have either a uniform load intensity or a quasi-normal distribution with the peak intensity located in the centre of the patch, which is, in turn, presumed to be vertically in line with the centroid of the applied loads at track level. Where significant differences arise in the magnitudes of the wheel loads, or minimal load distribution can occur in the fill – for instance, close to the arch crown – the patch may be more accurately approximated by two overlapping quasi-normal distributions, each with a peak value corresponding to a wheel load.

Wheel loads at the heaviest bogie are more variable for Class 222 trains – a difference between the wheel loads of 3.5% compared to only 1.1% for Class 185 trains. In both cases the leading

wheels of these bogies are slightly lighter and the applied patch load intensities, at the arch extrados, may be expected to have their peak values skewed towards the rear of the patch. If the extent of this skew is proportional to the difference in wheel load magnitudes, then this would be more pronounced for Class 222 trains than for Class 185 trains and, consequently, the peak response would be observed in the arch at a point in time when the Class 222 axles had progressed correspondingly further across the bridge span.

The increase in skew in the load distributions applied by Class 222 trains, as well as the potentially reduced width of their patch loads relative to Class 185 trains – owing to their shorter bogie wheelbase – may both contribute to the differences in arch strain response observed in Figure 6.9.

However, it is also important to note that the detailed distribution of damage along the north spandrel separation crack, adjacent to the loaded region of the bridge, is not known. If a nonlinear mechanism is occurring here, then the higher loads of Class 185 trains – 19% greater than the loads of Class 222 trains – could be more heavily distributed. This could be another factor that contributes towards the differences observed in Figure 6.9.

### **6.1.3 Mapping other strain states in the arch**

It was remarked in section 6.1.2.1 that, either side of the band of longitudinal tensile strains, the orientations of principal strains suggest a shear strain response that is approximately aligned with the transverse direction of the bridge. This can be explored further by plotting the rosette strain distributions for given orientations, aligned with directions of interest. Taking the four load cases – for which principal strains were plotted in Figure 6.8 – Figures 6.10 and 6.11 plot the median distributions of strain states aligned, respectively, with the skewed span and square span directions.

In these figures, tensile and compressive normal strains are plotted in each rosette using red and blue vectors, respectively. Once again, tensile strains are defined as positive and compressive strains as negative. Shear strains are plotted at  $45^\circ$  to the local  $x$  axis, which in these plots is oriented along the bridge span directions, facing east. Positive and negative shear strains are plotted, at each rosette, as magenta and cyan vectors.

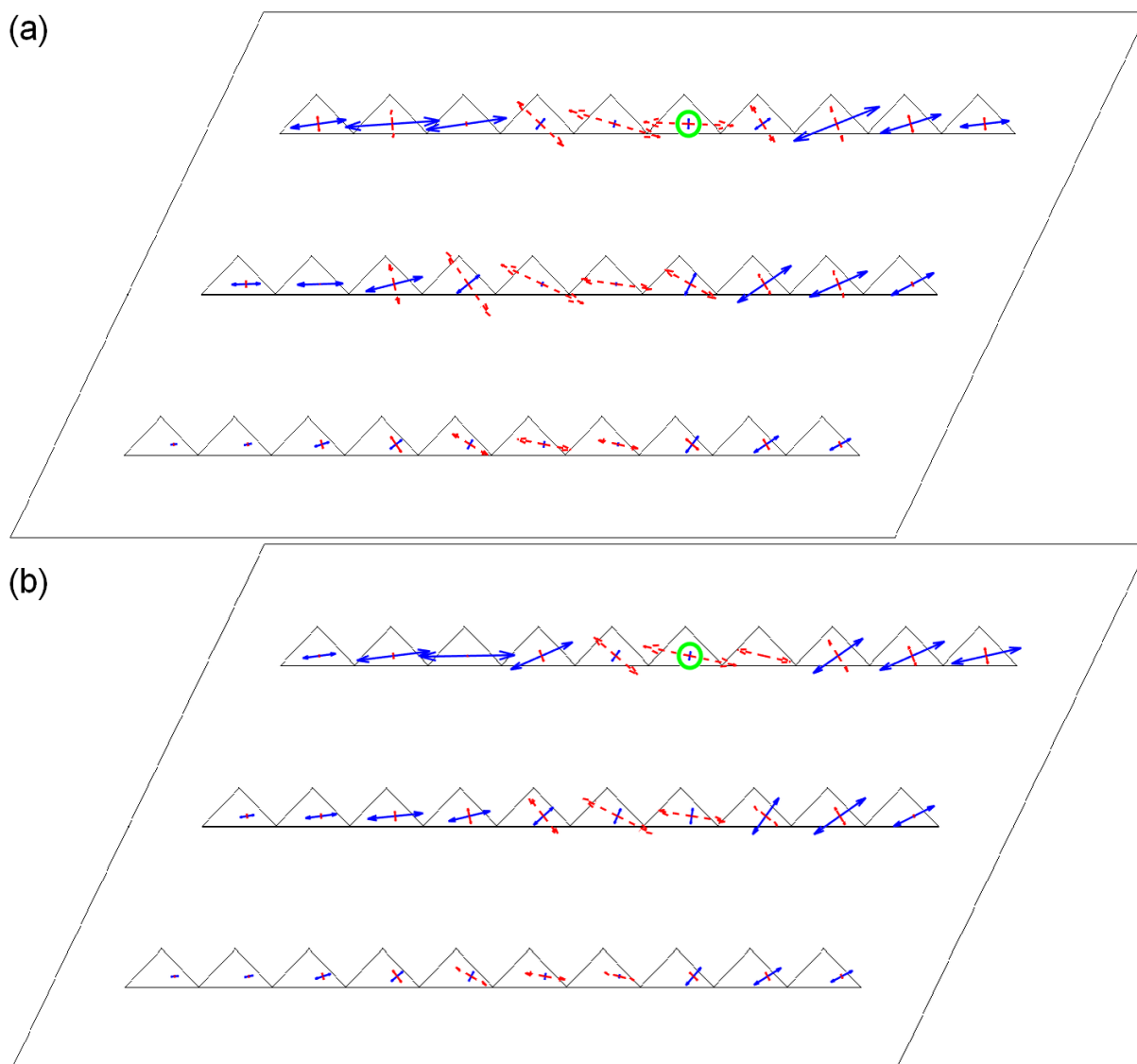


Figure 6.9: Quiver plots showing the median principal strain responses for (a) Class 185 and (b) Class 222 passenger trains, when peak axle loads are applied above rosette R6, just east of the arch crown (tensile principal strains in red; compressive principal strains in blue)

The statistical spread of these strain states is, once again, found to be very low, as is the variation between strain state distributions corresponding to different groups of data that have been classified by train class, train speed, and expected passenger levels (based on the time of day when the train has been recorded). Because of this, only median strain states calculated for all recorded Class 185 passenger trains are presented and discussed here.

### 6.1.3.1 Strains aligned with the skewed span direction

In Figure 6.10 – which plots the distribution of strains aligned with the skewed span direction of the bridge – the bands of longitudinal tensile strains underneath the applied loading can again

be seen, with compressive strains either side of these bands. Transverse strains reach their peak values on either side of these bands of tensile longitudinal strain. These transverse strains are tensile to the west of the applied loading and compressive to the east of it.

Shear strains are seen to be positive to the east of the applied loading and negative to the west of it. Either side of the loaded region, the shear strains rise in magnitude to peak values, which occur a short distance either side of the loading point, before decaying further away towards the arch haunches. This pattern is typically more pronounced along the bridge centreline. The change in sign of the shear strains suggests that, in the region of the vertically applied axle loading, there is also a transverse in-plane reaction applied to the arch barrel by the spandrel walls. This could be another indication of a transverse load path, in addition to the previously discussed longitudinal response through arching action. Note that these shear strains are approximately aligned with the direction of peak shear strain that was observed on either side of the band of longitudinal tensile strains, in the discussion of Figure 6.8.

#### **6.1.3.2 Strains aligned with the square span direction**

Figure 6.11 plots the distribution of strains oriented with the square span direction of the bridge. Longitudinal strains are dominated by arching action; these strains are again observed to be tensile in the region of applied axle loads and compressive on either side of this. However, there are differences in the distributions of shear and transverse normal strains in this coordinate system.

In each loading case represented in Figure 6.11, shear strains are predominantly positive over the region in which the longitudinal normal strains are tensile, and axle loading is being applied overhead. Outside of this region, shear strains are negative and follow a similar pattern to the one described for shear strains oriented in the skewed span direction – rising in magnitude to peak values a short distance ahead of and behind the loaded region, before decaying further towards the arch haunches. Within the loaded region of the arch, where longitudinal strains are tensile, the positive shear strains rise to a maximum value – occurring close to the point at which peak loading is applied – and die away, on either side, towards the edges of this loaded region.

Transverse strains also display a different pattern to that observed for the corresponding strains oriented in the skewed span direction. Now, the transverse strains are observed to be tensile in the region of applied axle loading. Behind (west of) the applied train loads, a wave of significant compressive transverse strains is observed, similar in pattern to that previously described for shear strains. Ahead (east) of the applied train loads, transverse strains are often small in magnitude and vary in sign. The south-eastern longitudinal crack may well have some influence

on this behaviour. In this region, strains will be concentrated in crack opening or closing and, since this crack approximately follows the skewed span direction, these movements may well be oriented with the transverse of the skewed span direction.

Note, in addition, that when axle loads are applied at the western third point of the arch (see Figure 6.11(a)), significant compressive strains are observed in the south-west, acute corner of the arch. These results have been inferred for the south-west corner – based on the response at the north-east corner of the bridge when axle loads are applied to the eastern third point of the south track – and may correspond to compressive thrusting into the acute corners of the arch. It was noted in section 6.1.2.1 that compressive principal strains in these regions are inclined towards the acute corners.

## **6.2 Out-of-plane behaviour of the arch**

The results in the previous sections of this chapter suggest that, in addition to the expected longitudinal arching action, a component of the bridge response occurs in its transverse direction. Here, this response is explored further using videogrammetry monitoring data of the out-of-plane vertical deformations along the arch crown line. These measurements are used to fit a relationship to describe the potential transverse bending response. This relationship is then compared against the intrados strains in the transverse direction, which were measured by FBGs and presented above.

### **6.2.1 Visualising vertical dynamic displacements of the arch crown line**

As discussed in section 4.4, the videogrammetry data have been processed to minimise noise resulting from adverse environmental effects. Data recorded during January and February 2019 have been determined to be of higher quality and are used here for further analysis. Maximum peak-to-peak vertical displacements have been calculated for each target, across all of the 64 recorded trains (see Table 4.2).

In Figure 6.12, boxplots show the statistical distribution of these peak-to-peak target displacements. Different plots show the measurements captured for Class 185, 150, and 222 trains, travelling on the two tracks. The median displacements at each target are joined by solid lines, to better highlight the deflection mode shapes along the crown line. Note that only one Class 222 train was recorded on the south track in January 2019 (see Table 4.2), and therefore boxplots cannot be generated in this instance. In general, the low number of Class 222 trains that have been recorded means that the statistical distribution of displacements for these trains is poorly defined.

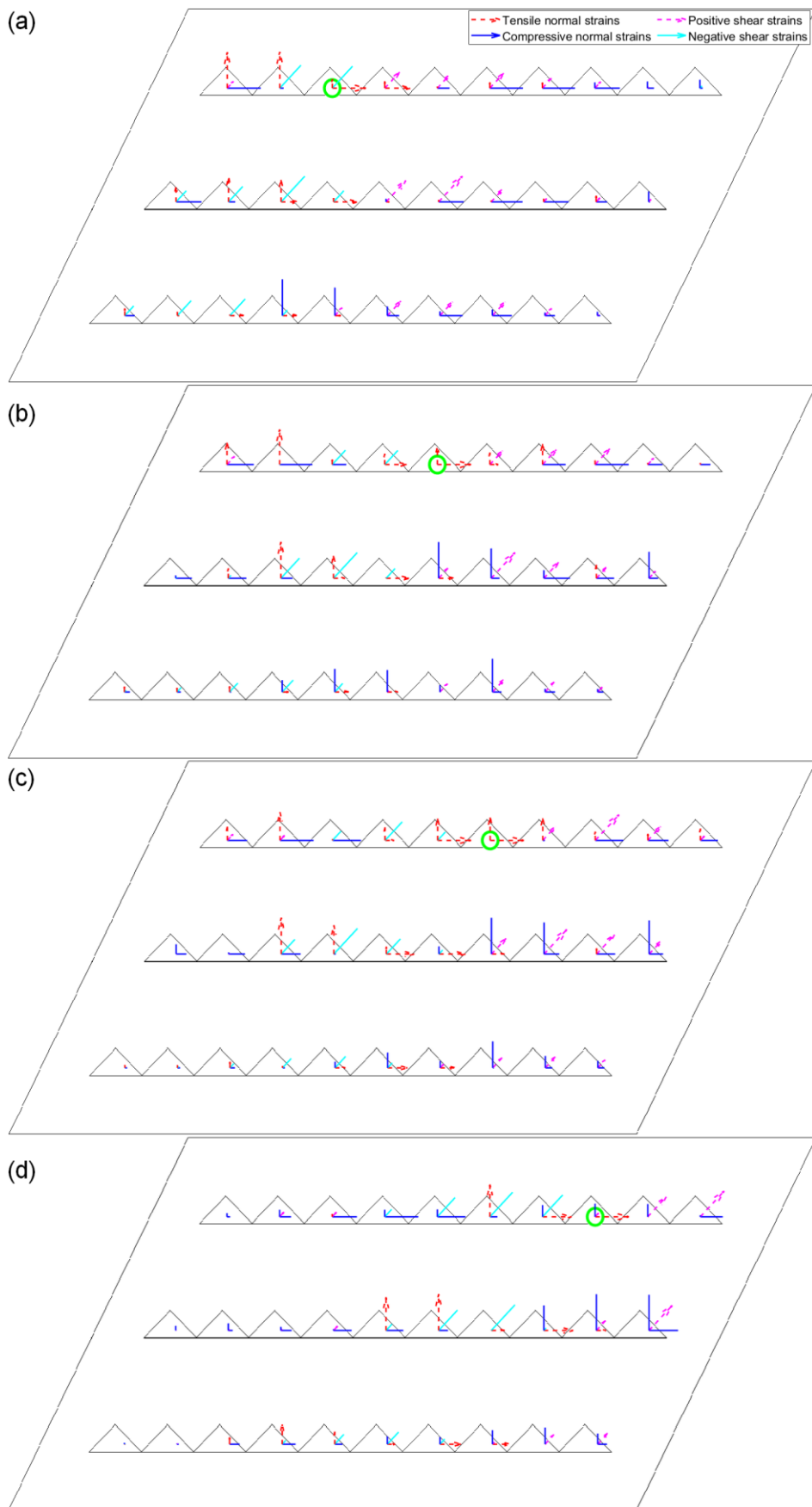


Figure 6.10: Quiver plots showing the median strain states aligned with the skewed span direction that arise in response to axle loads of Class 185 passenger trains applied at the (a) western third point, (b) western side of the arch crown, (c) eastern side of the arch crown, and (d) eastern third point

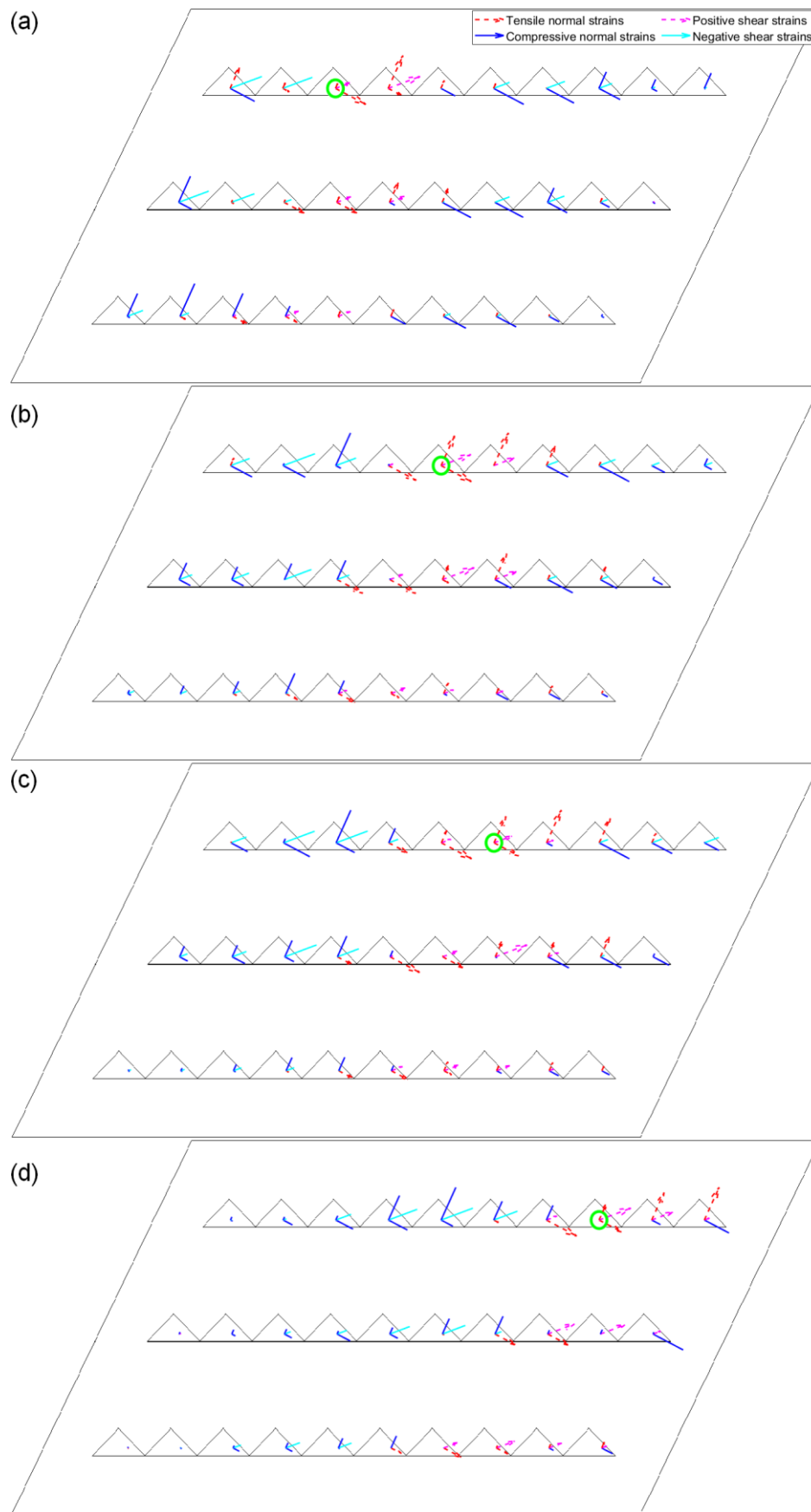


Figure 6.11: Quiver plots showing the median strain states aligned with the square span direction that arise in response to axle loads of Class 185 passenger trains applied at the (a) western third point, (b) western side of the arch crown, (c) eastern side of the arch crown, and (d) eastern third point

Data recorded during February 2019 are plotted in black; these displacements were calculated in reference frames defined at each of the crown line targets. A different approach had been used in January 2019. Here, reference frames were defined at the north and south spandrel walls and the resulting displacements were later corrected to account for the fact that the targets had a different depth (along the crown line of the bridge) to the reference frame. The methodology for doing this was presented in section 4.4.2.3. In Figure 6.12, boxplots corresponding to data measured in the south and north spandrel reference frames are plotted in red and blue, respectively.

January data calculated for the south spandrel reference frame are in good agreement with the February data, but the north spandrel reference frame consistently produces measurements of larger magnitude. This is likely caused by the increased difficulty of calibrating the north reference frame, since this was on the far side of the bridge from the monitoring location (see Figure 4.10). Not only was calibrating this reference frame more challenging, but its increased distance from the camera meant that each pixel corresponded to larger metric distances, and so the consequences of a poor calibration were more severe. As a result, only January displacement data calculated in the south spandrel reference frame are used from this point.

Figure 6.13 shows overall boxplots for combined January and February data, with the former generated using the south spandrel reference frame. Displacements due to trains passing on the north track are shown in red while those resulting from trains on the south track are shown in blue. These are plotted on top of each other so that the magnitudes of response can be compared for trains on the two tracks. It is seen that peak displacements are consistently larger under trains travelling on the south track. Note that the low overlap of boxplots at adjacent videogrammetry targets means that the deformed shape of the arch intrados is clear in the data.

## 6.2.2 Derivation of displacement and strain profiles along the crown line

In this section, the median vertical deflections in Figure 6.13 are used to fit a simplified beam model to an effective strip of the arch along its crown line. Figure 6.14(a) shows the model that is used: a linear elastic beam with rotational and translational support springs  $k_r$  and  $k_v$ . Train loads applied on one track are modelled at the extrados as the uniformly distributed force  $f$ , which extends from the support on the loaded side of the beam ( $x = 0$ ) up to a distance  $x = a$ . The extent of the loaded region has been found using guidance issued by Network Rail (2006). Geometric parameters needed to specify the simplified beam model are presented in Table 6.4.

The beam is assumed to have its left-hand support at the south spandrel separation crack. Therefore, Figure 6.14(a) shows the case for train loads applied on the south track. When trains

are passing on the north track (not shown in Figure 6.14(a)), the patch load is instead on the right side of the beam. In this instance, the edges of the patch load are at  $x = b$  and  $x = L$ .

The orientation of this beam can be assumed to be perpendicular to either the skewed or square span direction. Figure 6.14(b) is a plan view of the bridge showing the edges of the beams modelled in these two orientations with red and blue dashed lines, respectively. Grey patches show the regions at the extrados over which patch loads are applied, based on assumptions of load distribution through the fill used by Network Rail (2006). Videogrammetry targets are also shown in Figure 6.14(b); the central five targets are used to fit displacements to the beam model, which are calculated relative to the outer targets at the two spandrel walls.

Note that the spandrel separation cracks (shown, with red dotted lines, in Figure 6.14(b)) are adjacent to the outer edges of the two grey patch loads. Therefore, it is assumed that the load  $f$  extends to the crack at the support on the loaded side of the beam (the left-hand support in Figure 6.14(a)).

*Table 6.4: Geometric parameters used to specify the simplified beam model*

Parameter:	Value for	
	Square-oriented beam:	Skew-oriented beam:
$L$ (m)	7.110	6.418
$a$ , for trains on the south track (m)	3.270	2.937
$b$ , for trains on the north track (m)	3.840	3.481
Beam width, $w$ (m)	1.977	3.890
Beam depth, $d$ (m)	0.457	0.457
Second moment of area, $I$ (m <sup>4</sup> )	0.01572	0.03094

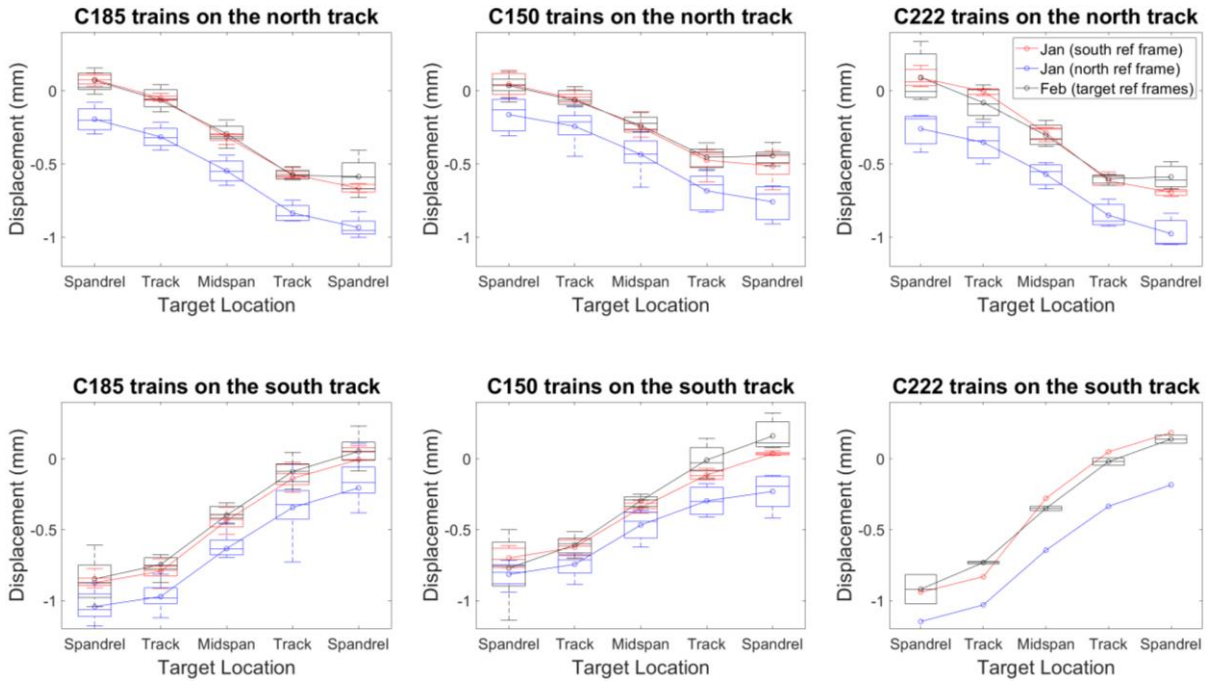


Figure 6.12: Statistical distributions of all recorded videogrammetry measurements, grouped by train class and direction, showing the impact of the two references frames used in January 2019, relative to individual target reference frames used in February 2019

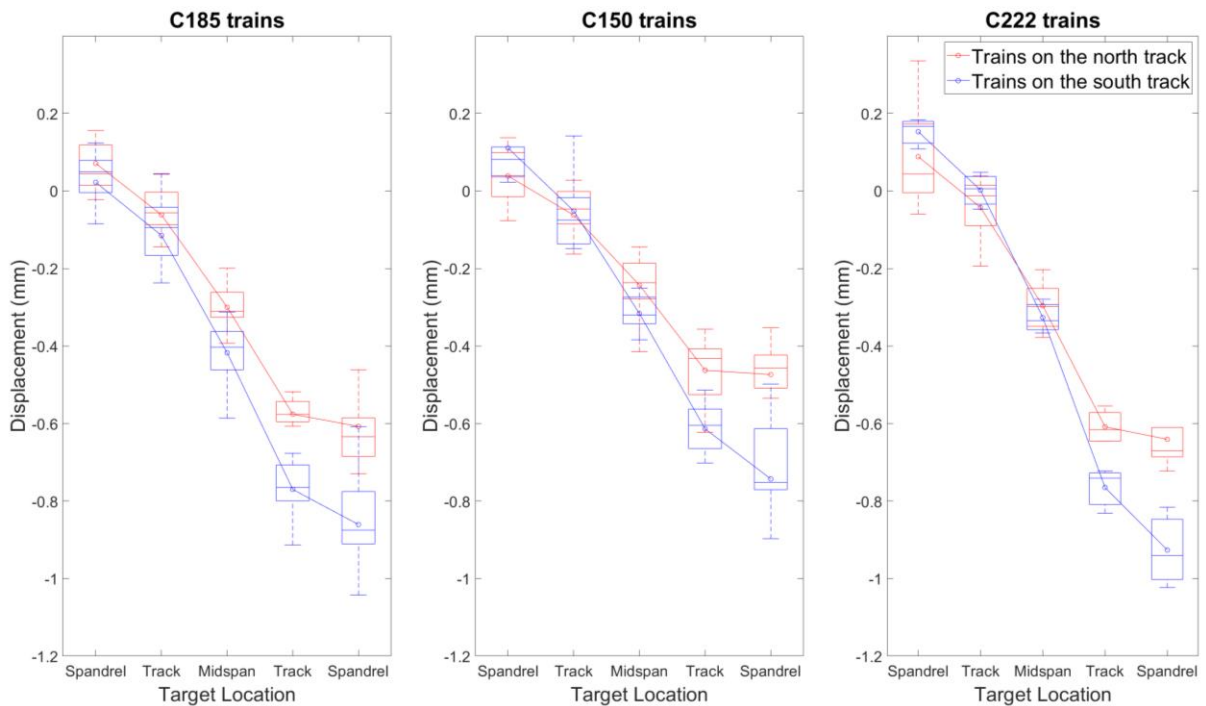


Figure 6.13: Statistical distributions of the combined videogrammetry measurements for January and February 2019, with data grouped by train class and direction

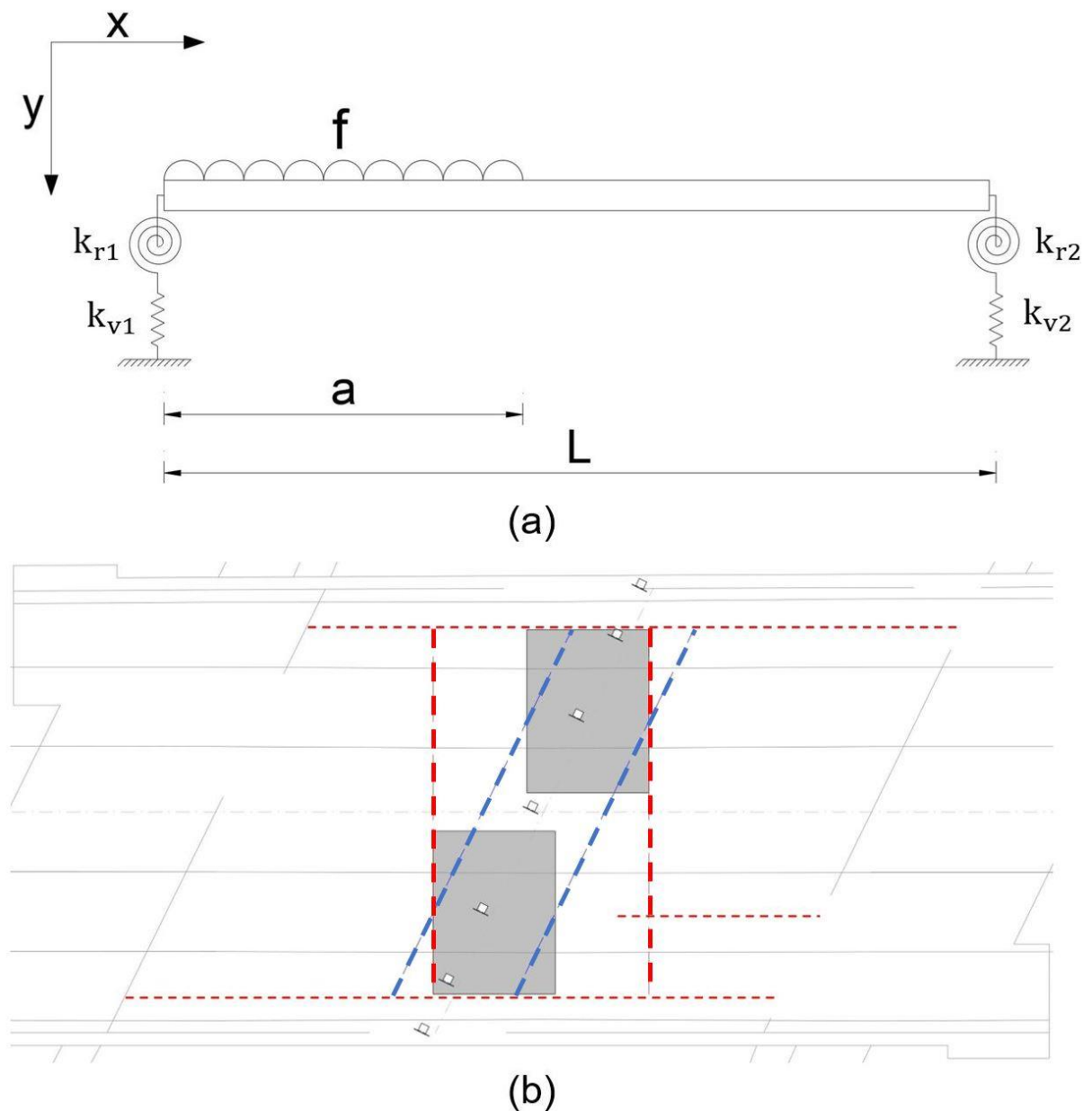


Figure 6.14: (a) Schematic of the simplified beam model for transverse bending at CFM-5, and (b) plan view of the CFM-5 bridge showing the patch loads applied to the beam model (shaded grey), the edges of the beam as defined in the skewed and square transverse orientations (in red and blue dashed lines, respectively), and the key cracks in the arch (in red dotted lines)

Beginning with the case of train loads applied to the south track, the force distribution along the beam can be expressed as:

$$f_S(x) = f x - f \{x - a\} \quad (6.3)$$

Here,  $\{ \}$  are Macaulay brackets; bracketed terms may only take values above zero. These are used to capture the discontinuous nature of the patch load, which is only active between  $x = 0$  and  $x = a$  in this instance. The subscript  $S$ , used here and in the following equations, denotes that these expressions correspond to train loading applied on the south track.

In order to relate this force distribution to the internal shear forces over the length of the beam, the shear at the left-hand support  $x = 0$  can be equated with the reaction force, which causes displacement  $y_S(0)$  of the linear spring  $k_{v1}$  at this support. Hence the shear distribution is:

$$S_S(x) = -f(x - \{x - a\}) + k_{v1}y_S(0) \quad (6.4)$$

Integrating shears to obtain the moment distribution, and expressing the constant of integration similarly as the moment at the left-hand support, yields Equation (6.5):

$$M_S(x) = \int S_S(x) dx = -f \left( \frac{x^2 - \{x - a\}^2}{2} \right) + k_{v1}y_S(0)x + k_{r1}\theta_S(0) \quad (6.5)$$

From here, an expression for rotations,  $\theta$ , along the beam is obtained from basic statics, with the assumption that rotations are small and hence  $M = EI \frac{d^2y}{dx^2} = EI \frac{d\theta}{dx}$ . This yields Equation (6.6), in which the constant of integration has been equated with the rotation at  $x = 0$ .

$$\theta_S(x) = \frac{1}{EI} \int M_S(x) dx = \frac{-f}{EI} \left( \frac{x^3 - \{x - a\}^3}{6} \right) + \frac{k_{v1}y_S(0)}{EI} \left( \frac{x^2}{2} \right) + \frac{k_{r1}\theta_S(0)}{EI} (x) + \theta_S(0) \quad (6.6)$$

Lastly, this can be integrated once more to yield Equation (6.7), an expression for the vertical displacements along the length of the beam:

$$y_S(x) = \int \theta_S(x) dx = \frac{-f}{EI} \left( \frac{x^4 - \{x - a\}^4}{24} \right) + \frac{k_{v1}y_S(0)}{EI} \left( \frac{x^3}{6} \right) + \frac{k_{r1}\theta_S(0)}{EI} \left( \frac{x^2}{2} \right) + \theta_S(0)x + y_S(0) \quad (6.7)$$

When loads are applied at the north track (the right half of the beam), the expression for applied forces is different as the patch load is now applied to the right side of the beam between the points  $x = b$  and  $x = L$ . This may be expressed as follows, using the subscript  $N$  to denote that trains are now passing on the north track:

$$f_N(x) = f \{x - b\} \quad (6.8)$$

Following the procedure outlined above, the expression for vertical displacements – when trains are travelling on the north track – is found to be:

$$y_N(x) = \frac{-f}{EI} \left( \frac{\{x-b\}^4}{24} \right) + \frac{k_{v1}y_N(0)}{EI} \left( \frac{x^3}{6} \right) + \frac{k_{r1}\theta_N(0)}{EI} \left( \frac{x^2}{2} \right) + \theta_N(0)x + y_N(0) \quad (6.9)$$

Expressions can also be obtained for the intrados strains, by assuming that the centroidal axis is always at the mid-depth of the overall section (i.e., that no damage has locally reduced the effective thickness of the arch at any point along the crown line that is modelled here).

Therefore, strains are given by  $\epsilon = \frac{Md}{2EI}$ , where  $d = 0.457$  m is the thickness of the arch barrel.

For trains passing on the south and north track, respectively, intrados strains are given by Equations (6.10) and (6.11) as follows:

$$\epsilon_S = \frac{d}{2EI} \left[ -f \left( \frac{x^2 - \{x-a\}^2}{2} \right) + k_{v1}y_S(0)x + k_{r1}\theta_S(0) \right] \quad (6.10)$$

$$\epsilon_N = \frac{d}{2EI} \left[ -f \left( \frac{\{x-b\}^2}{2} \right) + k_{v1}y_N(0)x + k_{r1}\theta_N(0) \right] \quad (6.11)$$

Equations (6.7) and (6.9) can be set equal to the measured videogrammetry displacements, and the known locations of these targets plugged in as  $x$  coordinates. Table 6.5 shows the measurements used to do this. Specifically, these are the median displacements observed for each train group in Figure 6.13. Once the displacement profiles have been fitted based on videogrammetry data, their coefficients are used to obtain predictions of the intrados strain profiles in Equations (6.10) and (6.11). Note that the sign convention used here (and shown earlier in Figure 6.14) is that downwards displacements are positive.

These predicted strain profiles can be compared with the median measurements of transverse strain – also given in Table 6.5 – which have been recorded independently by the FBG rosettes. Since the rosettes are in fact situated either side of the arch crown, the strains in Table 6.5 have been obtained by averaging the median peak strains at Rosettes 5 and 6, and Rosettes 15 and 16 (see Figure 6.1), at the points in the train data which produce peak responses at these rosettes. These points are taken to correspond approximately to the instances when axle loads are applied above the crown, although it is recognised that there may be some uncertainty in specifying this instance (see the discussion in section 6.1.2.2). As in previous sections, tensile strains are taken to be positive while compressive strains are negative.

The displacements at the five videogrammetry targets (in Table 6.5) can be plugged into Equations (6.7) and (6.9) to yield sets of simultaneous equations. Since each equation has five unknown coefficients, this is sufficient information for each coefficient to be evaluated. The

simultaneous equations have been solved in MATLAB to give the coefficients listed in Table 6.6, for each train group. Note that using these coefficients in Equations (6.7) and (6.9) will yield displacements  $y(x)$  in units of metres.

The coefficients for the quadratic, cubic, and quartic terms include the second moment of area  $I$  and the support movements  $y(0)$  and  $\theta(0)$ , which are known (see Tables 6.4 and 6.6). Therefore, these can be converted to express the ratios of the applied force and support springs in terms of the Young's Modulus:  $f/E$ ,  $k_{v1}/E$ , and  $k_{r1}/E$ . These ratios are given in Table 6.7.

Furthermore, in Table 6.7, support springs at the north support are also calculated in terms of the Young's Modulus – i.e.,  $k_{v2}/E$ , and  $k_{r2}/E$ . This is done by using the coefficients from Table 6.6 and Equations (6.4) to (6.9) to evaluate  $y(L)$ ,  $\theta(L)$ ,  $\frac{M}{EI}(L)$ , and  $\frac{S}{EI}(L)$ , and then calculating the spring stiffness as:

$$\frac{k_{v2}}{E} = I \frac{\frac{S}{EI}(L)}{y(L)}, \quad \frac{k_{r2}}{E} = I \frac{\frac{M}{EI}(L)}{\theta(L)} \quad (6.12)$$

Interesting patterns emerge in the coefficients listed in Table 6.6, and the ratios of  $f/E$  and  $k/E$  in Table 6.7. In general, the magnitudes of each coefficient and ratio agree reasonably well between the different train data sets for which they have been calculated. As expected from the sign convention used in deriving the displacement and strain profiles along the arch crown line,  $f$  is always positive. However, in certain circumstances, the signs of the spring stiffnesses predicted at the supports vary.

Inspecting Table 6.7, the translational springs are always positive at the south spandrel ( $k_{v1}$ ) but negative at the north spandrel ( $k_{v2}$ ). This is the case regardless of which track the trains pass on. The pattern is more complex for the rotational springs. At the north spandrel,  $k_{r2}$  is positive when trains pass on the north track and negative when trains are on the south track. However,  $k_{r1}$  at the south spandrel is generally positive, with some exceptions for individual sets of train data – namely, Class 185 trains on the south track and Class 222 trains on the north track. Compare this with the coefficients  $\frac{k_{r1}\theta(0)}{EI}$  and  $\theta(0)$  listed in Table 6.6, which generally agree in sign except for these train groups. Recall from earlier that only a small number of Class 222 trains were recorded, and so coefficients for this data group may be poorly defined. However, a large number of Class 185 trains was measured (see Table 4.2).

Table 6.5: Displacement data used to fit the simplified beam models, and strain data compared against the modelled predictions

Parameter:	Measurements taken at the				
	South spandrel:	South track:	Bridge centreline:	North track:	North spandrel:
$x$ coordinate (square-oriented beam)	0.114 m	1.531 m	3.576 m	5.429 m	7.038 m
$x$ coordinate (skew-oriented beam)	0.201 m	1.473 m	3.309 m	4.973 m	6.418 m
Displacements, $y$ (C185 trains on south track)	0.88 mm	0.76 mm	0.40 mm	0.09 mm	-0.05 mm
Displacements, $y$ (C150 trains on south track)	0.75 mm	0.60 mm	0.32 mm	0.08 mm	-0.08 mm
Displacements, $y$ (C222 trains on south track)	0.94 mm	0.74 mm	0.33 mm	-0.01 mm	-0.17 mm
Displacements, $y$ (C185 trains on north track)	-0.04 mm	0.06 mm	0.31 mm	0.58 mm	0.63 mm
Displacements, $y$ (C150 trains on north track)	-0.04 mm	0.05 mm	0.24 mm	0.43 mm	0.46 mm
Displacements, $y$ (C222 trains on north track)	-0.04 mm	0.01 mm	0.30 mm	0.62 mm	0.67 mm
Strains, $\epsilon$ (C185 trains on south track)	Square-oriented strains:		-6.0	-3.6	$\mu\epsilon$
	Skew-oriented strains:		-10.4	-3.0	
Strains, $\epsilon$ (C150 trains on south track)	Square-oriented strains:		-4.5	-2.8	$\mu\epsilon$
	Skew-oriented strains:		-8.0	-2.3	
Strains, $\epsilon$ (C222 trains on south track)	Square-oriented strains:		-5.4	-3.5	$\mu\epsilon$
	Skew-oriented strains:		-10.8	-3.2	
Strains, $\epsilon$ (C185 trains on north track)	Square-oriented strains:		1.0	12.4	$\mu\epsilon$
	Skew-oriented strains:		-1.2	6.5	
Strains, $\epsilon$ (C150 trains on north track)	Square-oriented strains:		0.3	9.7	$\mu\epsilon$
	Skew-oriented strains:		-1.2	5.2	
Strains, $\epsilon$ (C222 trains on north track)	Square-oriented strains:		-4.2	8.4	$\mu\epsilon$
	Skew-oriented strains:		-1.0	6.1	

Table 6.6: Coefficients of the fitted displacement relationships

Train group:	Beam orientation:	Coefficients:				
		$\frac{f}{EI}$ (m <sup>-3</sup> )	$\frac{k_{v1}y(0)}{EI}$ (m <sup>-2</sup> )	$\frac{k_{r1}\theta(0)}{EI}$ (m <sup>-1</sup> )	$\theta(0)$ (-)	$y(0)$ (m)
C185 trains on the south track	Square transverse	$1.990 \times 10^{-5}$	$8.540 \times 10^{-5}$	$-1.706 \times 10^{-4}$	$2.970 \times 10^{-5}$	$8.727 \times 10^{-4}$
	Skewed transverse	$3.390 \times 10^{-5}$	$1.279 \times 10^{-4}$	$-2.297 \times 10^{-4}$	$5.730 \times 10^{-5}$	$8.680 \times 10^{-4}$
C150 trains on the south track	Square transverse	$6.300 \times 10^{-6}$	$2.930 \times 10^{-5}$	$-5.990 \times 10^{-5}$	$-6.650 \times 10^{-5}$	$7.604 \times 10^{-4}$
	Skewed transverse	$1.080 \times 10^{-5}$	$4.360 \times 10^{-5}$	$-8.030 \times 10^{-5}$	$-6.570 \times 10^{-5}$	$7.672 \times 10^{-4}$
C222 trains on the south track	Square transverse	$1.800 \times 10^{-6}$	$2.790 \times 10^{-5}$	$-7.880 \times 10^{-5}$	$-8.750 \times 10^{-5}$	$9.509 \times 10^{-4}$
	Skewed transverse	$3.200 \times 10^{-6}$	$3.960 \times 10^{-5}$	$-1.024 \times 10^{-4}$	$-8.730 \times 10^{-5}$	$9.600 \times 10^{-4}$
C185 trains on the north track	Square transverse	$4.079 \times 10^{-5}$	$-1.006 \times 10^{-5}$	$4.809 \times 10^{-5}$	$3.613 \times 10^{-5}$	$-4.932 \times 10^{-5}$
	Skewed transverse	$5.875 \times 10^{-5}$	$-1.363 \times 10^{-5}$	$6.058 \times 10^{-5}$	$3.457 \times 10^{-5}$	$-5.305 \times 10^{-5}$
C150 trains on the north track	Square transverse	$3.657 \times 10^{-5}$	$-5.600 \times 10^{-6}$	$2.865 \times 10^{-5}$	$3.920 \times 10^{-5}$	$-4.386 \times 10^{-5}$
	Skewed transverse	$5.268 \times 10^{-5}$	$-7.490 \times 10^{-6}$	$3.589 \times 10^{-5}$	$4.037 \times 10^{-5}$	$-4.804 \times 10^{-5}$
C222 trains on the north track	Square transverse	$4.442 \times 10^{-5}$	$-2.099 \times 10^{-5}$	$9.389 \times 10^{-5}$	$-2.853 \times 10^{-5}$	$-4.087 \times 10^{-5}$
	Skewed transverse	$6.390 \times 10^{-5}$	$-2.870 \times 10^{-5}$	$1.189 \times 10^{-4}$	$-4.310 \times 10^{-5}$	$-3.720 \times 10^{-5}$

Table 6.7: Ratios of the applied force and support spring stiffnesses to the Young's Modulus, as predicted by the simplified beam models

Train group:	Beam orientation:	$f/E$ (m)	$k_{v1}/E$ (m)	$k_{r1}/E$ (m <sup>3</sup> )	$k_{v2}/E$ (m)	$k_{r2}/E$ (m <sup>3</sup> )
C185 trains on the south track	Square transverse	$3.129 \times 10^{-7}$	$1.539 \times 10^{-3}$	$-9.032 \times 10^{-2}$	$-6.259 \times 10^{-3}$	$-4.357 \times 10^{-2}$
	Skewed transverse	$1.049 \times 10^{-6}$	$4.559 \times 10^{-3}$	$-1.240 \times 10^{-1}$	$-1.795 \times 10^{-2}$	$-7.990 \times 10^{-2}$
C150 trains on the south track	Square transverse	$9.906 \times 10^{-8}$	$6.059 \times 10^{-4}$	$1.416 \times 10^{-2}$	$-1.609 \times 10^{-3}$	$-8.034 \times 10^{-3}$
	Skewed transverse	$3.341 \times 10^{-7}$	$1.758 \times 10^{-3}$	$3.782 \times 10^{-2}$	$-4.341 \times 10^{-3}$	$-1.585 \times 10^{-2}$
C222 trains on the south track	Square transverse	$2.830 \times 10^{-8}$	$4.614 \times 10^{-4}$	$1.416 \times 10^{-2}$	$-2.073 \times 10^{-3}$	$-4.111 \times 10^{-2}$
	Skewed transverse	$9.901 \times 10^{-8}$	$1.276 \times 10^{-3}$	$3.629 \times 10^{-2}$	$-5.461 \times 10^{-3}$	$-6.866 \times 10^{-2}$
C185 trains on the north track	Square transverse	$6.414 \times 10^{-7}$	$3.207 \times 10^{-3}$	$2.093 \times 10^{-2}$	$-3.602 \times 10^{-3}$	$3.333 \times 10^{-2}$
	Skewed transverse	$1.818 \times 10^{-6}$	$7.949 \times 10^{-3}$	$5.422 \times 10^{-2}$	$-9.089 \times 10^{-3}$	$8.227 \times 10^{-2}$
C150 trains on the north track	Square transverse	$5.750 \times 10^{-7}$	$2.008 \times 10^{-3}$	$1.149 \times 10^{-2}$	$-4.381 \times 10^{-3}$	$2.908 \times 10^{-2}$
	Skewed transverse	$1.630 \times 10^{-6}$	$4.824 \times 10^{-3}$	$2.751 \times 10^{-2}$	$-1.098 \times 10^{-2}$	$6.988 \times 10^{-2}$
C222 trains on the north track	Square transverse	$6.985 \times 10^{-7}$	$8.076 \times 10^{-3}$	$-5.175 \times 10^{-2}$	$-3.958 \times 10^{-3}$	$3.062 \times 10^{-2}$
	Skewed transverse	$1.977 \times 10^{-6}$	$2.387 \times 10^{-2}$	$-8.535 \times 10^{-2}$	$-9.957 \times 10^{-3}$	$7.486 \times 10^{-2}$

### 6.2.3 Evaluation of the fitted displacement and intrados strain profiles

In Figures 6.15 to 6.20, the displacement and strain profiles that are predicted for each train group by the simplified beam models are plotted as solid red lines. On top of these, the median measurements of displacement and strain, obtained from videogrammetry and FBGs, are plotted as black circles. Plots on the left and right of each figure correspond, respectively, to the square- and skew-oriented beam models. The top row of each figure plots displacements along the crown line, while the bottom row plots intrados strain. Class 185, 150, and 222 trains on the south and north tracks are plotted in separate figures. Note that, in these figures, downwards vertical displacement is shown as negative, to better visualise the deformed profile of the crown line.

Since the number of videogrammetry measurements, along the span, matched the number of coefficients that they were used to fit in the displacement relationships, these measurements and predictions match well in Figure 6.15 to 6.20. Notable features in the fitted displacement relationships include the increased curvature over the loaded region of the beam when trains are passing on the northern track, compared to when trains are on the south track, suggesting an increased amount of transverse bending in the response to these trains. This is most noticeable for Class 150 trains (Figure 6.18 compared to Figure 6.17) and Class 222 trains (Figure 6.20 relative to Figure 6.19). In these cases, the relationships for train loading on the south track (Figures 6.17 and 6.19) show very little curvature. Note that this does not agree with earlier observations based on the FBG strains, in section 6.1.1.2.

Predicted strain relationships, plotted as solid red lines on the bottom rows of Figures 6.15 to 6.20, exhibit some agreement with the FBG measurements when trains are on the north track (Figures 6.16, 6.18, and 6.20). They are generally in better agreement when these relationships are defined for a square-oriented beam. However, there is little or no agreement when trains are on the south track (Figures 6.15, 6.17, and 6.19). This is particularly true of Class 222 trains (Figure 6.19), where the predicted strain distribution along the crown line is almost linear, although these predictions are the most uncertain because considerably fewer Class 222 trains were recorded, compared to any of the other train groups (see Table 4.2).

One possible contributing factor towards the poorer agreement of the model, when trains pass on the south track in particular, is that the south-eastern longitudinal crack has not been accounted for. Although this crack does not extend as far as the arch crown (see, for example, in Figure 6.14(b) earlier), it may have a local impact on the effective  $EI$  of the transverse beams that are modelled here – particularly for the wider skew-oriented beam. This could explain why

the deflection profiles generally indicate less curvature when trains are passing on the south track. Furthermore, strains will be concentrated at this crack, and so the strains predicted by the model for the south end of the beam will be higher than those exhibited by the real bridge. This cannot be verified, as FBGs have not been installed in this region. However, it could help to explain why the predicted compressive strains on the north side of the beam are higher than those observed by FBGs (at the bridge centreline and underneath the north track) and, furthermore, why these predictions and measurements seem to exhibit different trends.

As for the different levels of agreement for predictions based on orienting the beam with the transverse of either the skewed or square span, it is important to note that the models do not account for the variable depth of the arch, due to its curvature. This has a significantly higher impact on the skew-oriented beam. This beam is wider, and its axis is not aligned with the locus of centre of curvature of the arch, meaning that the depth of this beam varies along its length. A combination of bending and axial response, in this strip of the arch, will complicate behaviour. Therefore, it is not necessarily surprising that the square-oriented beam provides a better fit to the measured strains.

Modifications of the beam models, which increase the level of agreement between predicted and measured strains, are discussed in the following section 6.2.3.1.

Since median peak-to-peak displacements from the videogrammetry data have been used to fit the expressions for crown line displacements, and hence to predict the strain distributions, it is worth considering whether statistical spread in these data could significantly affect the fitted coefficients and predicted ratios of  $f/E$  and  $k/E$ . Tables 6.6 and 6.7 show some agreement in the ranges of magnitudes, between values calculated for each train group. Note that this agreement is better in Table 6.6 than it is in Table 6.7. In order to obtain the values in Table 6.7, the effective width of the beams was estimated and used to obtain their second moments of area,  $I$ . Approximate widths have been based on the sizes of the applied patch loads in Figure 6.14(b), meaning that  $I$  for the skew-oriented beam is significantly larger than for the square-oriented beam (see Table 6.4).

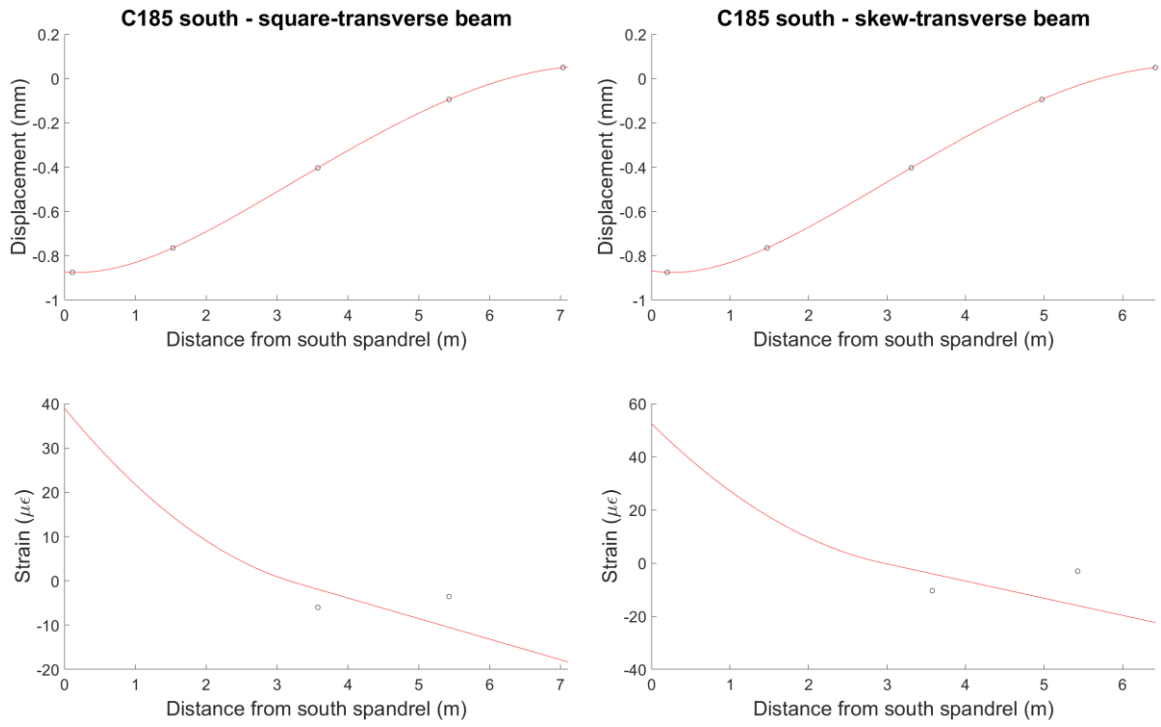


Figure 6.15: Profiles of vertical displacements and intrados strains based on simplified transverse beams oriented along the transverse of the (left) square and (right) skewed span directions, under Class 185 trains passing on the south track, compared with videogrammetry and FBG measurements of these displacements and strains

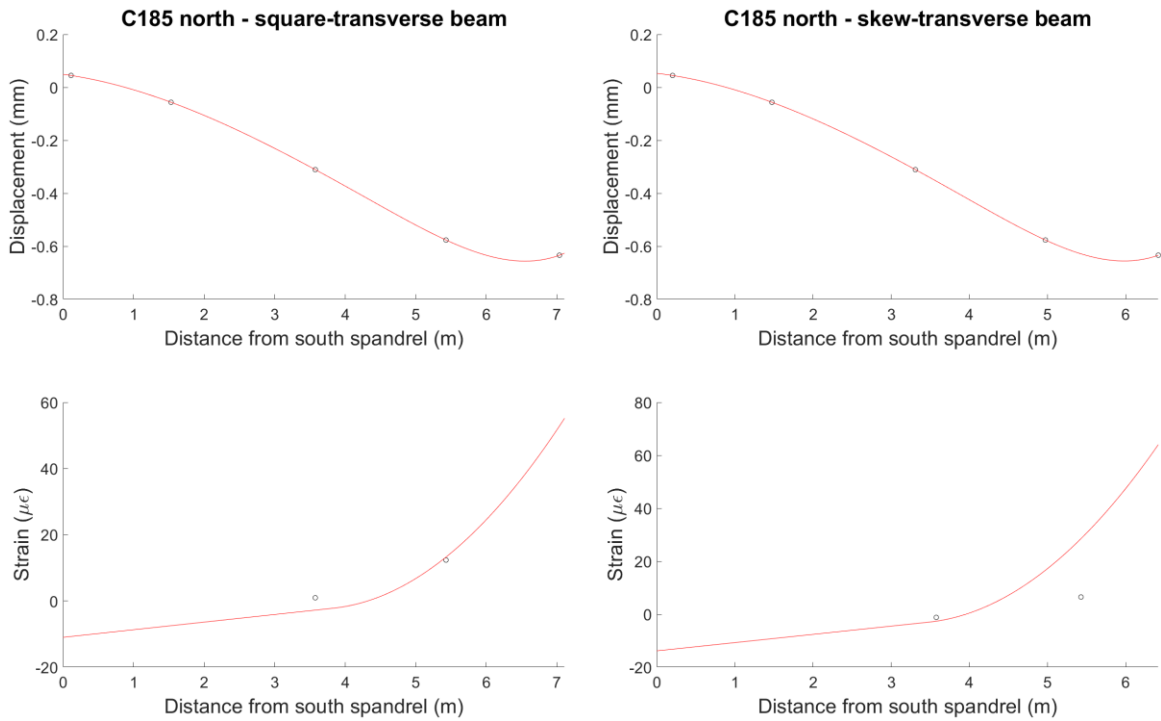


Figure 6.16: Profiles of vertical displacements and intrados strains based on simplified transverse beams oriented along the transverse of the (left) square and (right) skewed span directions, under Class 185 trains passing on the north track, compared with videogrammetry and FBG measurements of these displacements and strains

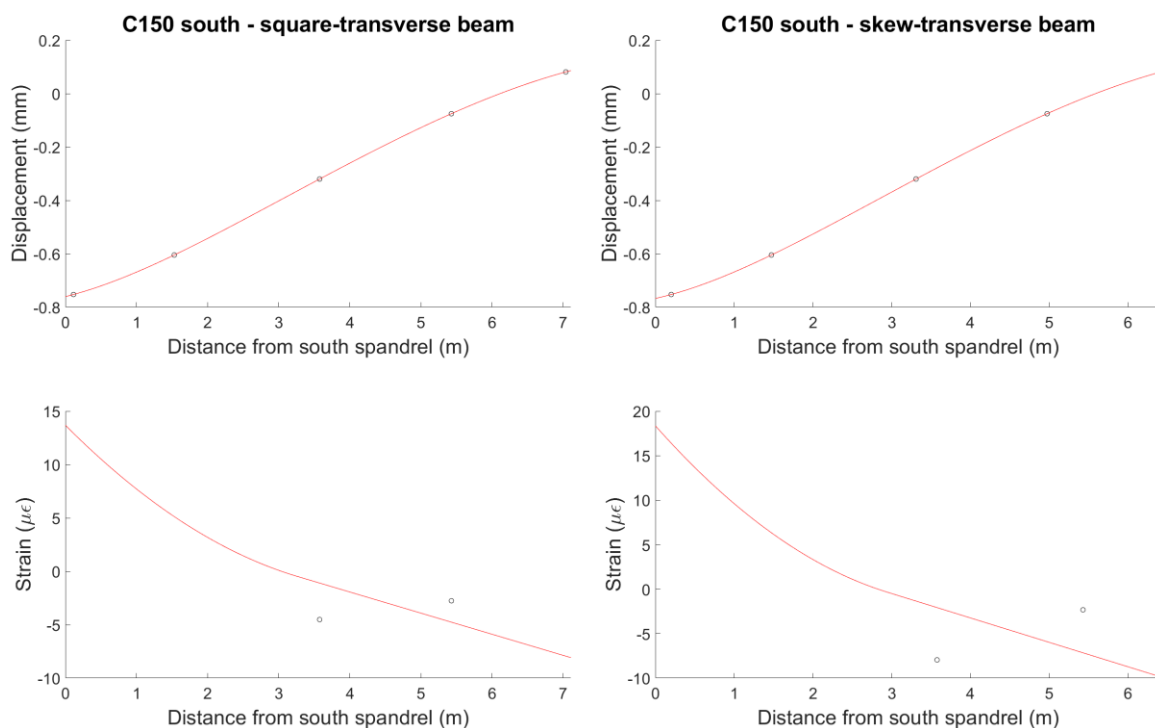


Figure 6.17: Profiles of vertical displacements and intrados strains based on simplified transverse beams oriented along the transverse of the (left) square and (right) skewed span directions, under Class 150 trains passing on the south track, compared with videogrammetry and FBG measurements of these displacements and strains

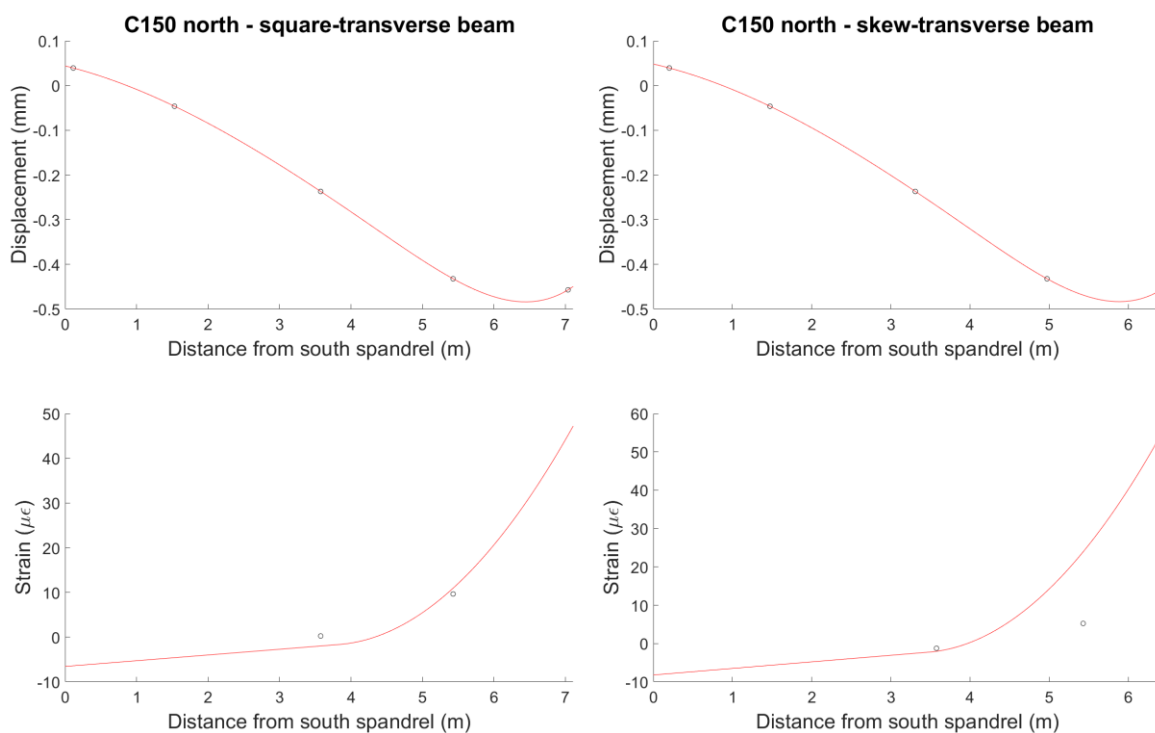


Figure 6.18: Profiles of vertical displacements and intrados strains based on simplified transverse beams oriented along the transverse of the (left) square and (right) skewed span directions, under Class 150 trains passing on the north track, compared with videogrammetry and FBG measurements of these displacements and strains

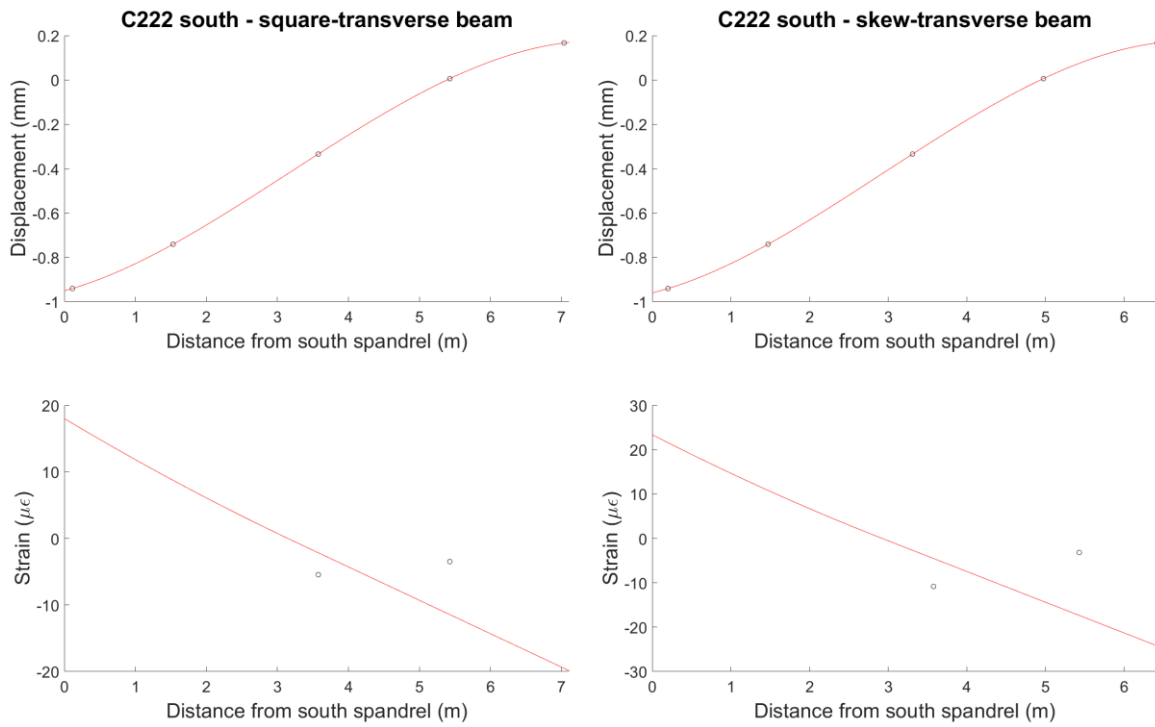


Figure 6.19: Profiles of vertical displacements and intrados strains based on simplified transverse beams oriented along the transverse of the (left) square and (right) skewed span directions, under Class 222 trains passing on the south track, compared with videogrammetry and FBG measurements of these displacements and strains

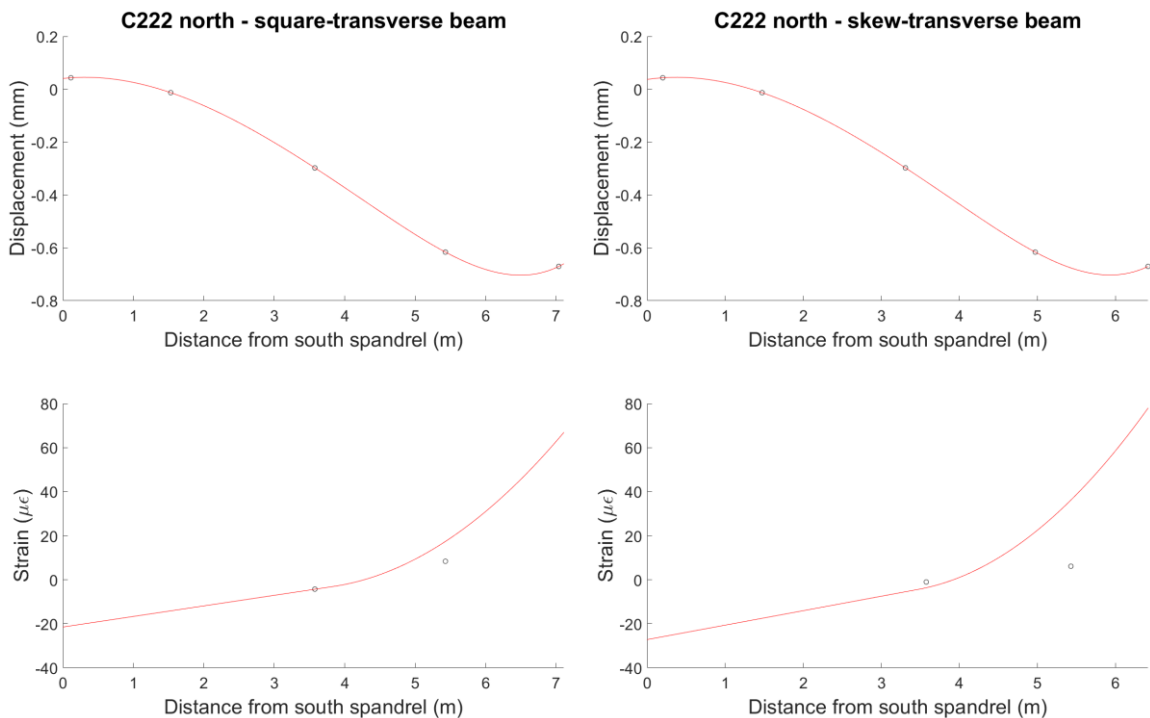


Figure 6.20: Profiles of vertical displacements and intrados strains based on simplified transverse beams oriented along the transverse of the (left) square and (right) skewed span directions, under Class 222 trains passing on the north track, compared with videogrammetry and FBG measurements of these displacements and strains

Nevertheless, this level of agreement – especially in Table 6.6 – suggests a certain amount of consistency in the out-of-plane response under different types of train loading, implying that it is not unreasonable to have based the earlier beam calculations on observations of the average response in each case.

Furthermore, inspection of the boxplots in Figure 6.13 shows low overlap between the statistical spread of displacements recorded at adjacent targets along the arch crown line. This means that the general deformed shape of the arch crown line – to which the displacement expression is fitted – is consistent across data recorded for different train events. Likewise, the FBG rosette strains have low statistical variation, of the order of several microstrain, which would not be enough to appreciably change the quality of their agreement with the generated strain profiles.

The fact that the deformed profile of the crown line is so consistent in the videogrammetry data is impressive, given the initially low quality of these data before they had been corrected for adverse environmental effects. This demonstrates that useful results can still be obtained through videogrammetry in the field, as long as an appropriate experimental setup and post-processing strategies are used.

#### **6.2.3.1 Modifications of the fitted beam model**

In the previous section, disagreement between the FBG strain data and the strain profiles predicted by the fitted beam model was noted. Furthermore, in the fitted displacement relationships, a high amount of curvature is present over the loaded ends of the beams. This may not be realistic, given the small magnitudes of the FBG strain measurements, although the low number of locations along the crown line at which strain is monitored makes it difficult to draw firm conclusions.

By manually reducing the support spring stiffnesses, where these appear as coefficients in the modelled beam profiles, it is possible to decrease the curvature that is predicted for the loaded ends of the beams. This can also lead to improved agreement with the measured strain data, at the cost of lower agreement with the displacement data.

Figure 6.21 plots the median displacements and strains for Class 185 trains against a set of square-oriented beam profiles, which are obtained by progressively lowering the stiffness of the support springs. It can be seen that reducing these stiffnesses quickly gives rise to a worse fit of the displacement data; the fit remains best close to the left-hand support, but this is simply because  $y(0)$  features explicitly in the displacement expressions (Equations (6.7) and (6.9)). However, this process also leads to a progressively improved fit of the strain data.

The final profile in Figure 6.21, corresponding to a 30% reduction in  $k_v$  and a 64% reduction in  $k_r$ , offers the best agreement with the strain data and a particular improvement for the response to trains travelling on the south track. However, it also predicts very little variation of displacement along the crown line, which is inconsistent with the videogrammetry data. This suggests that the observed displacements may not be wholly explained by transverse bending. Although it is difficult to be conclusive, since strain data are only available at two points along the crown line, it is certainly possible that axial deformations of the arch in its longitudinal spanning direction could also contribute to the measured distortion of the crown line.

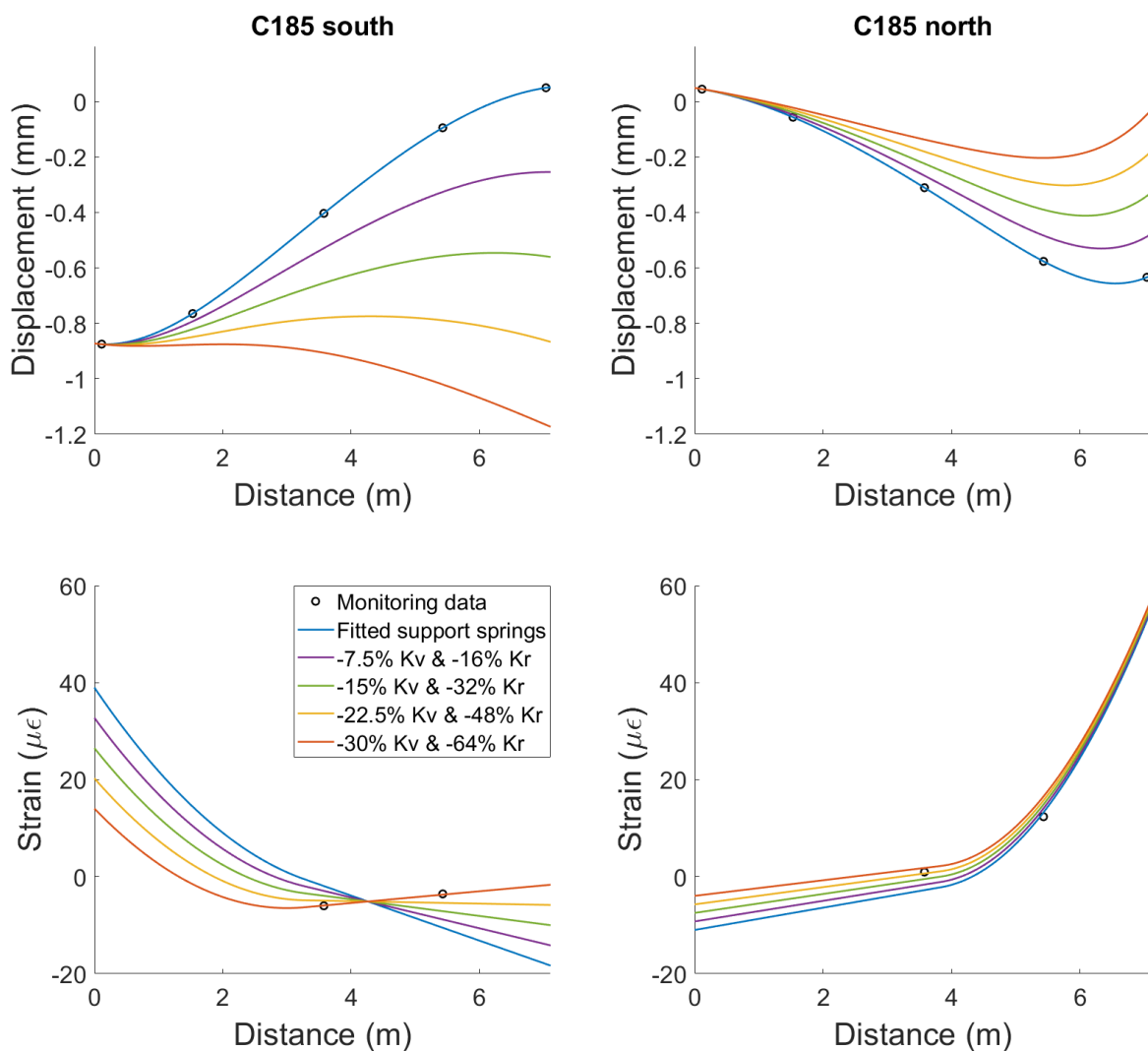


Figure 6.21: Comparison of the median videogrammetry and FBG measurements, for Class 185 trains, with a range of crown line displacement and strain profiles, found by varying the support spring stiffnesses of the square-oriented beam model from the original, fitted coefficients

---

The effective beam model used in this chapter can be further refined to include this stiffness of the arch in its longitudinal direction – for instance, by modelling this as a Winkler foundation. This will be explored in future work.

Separately, modelling of the overall arch in future work will allow the range of support spring stiffnesses along its transverse edges – both those predicted by the original beam models and the modified values considered in this section – to be studied, and bounds placed on their acceptable limits.

### 6.3 Conclusions

In this chapter, the novel FBG strain rosette design has been introduced and used to obtain distributed principal strain data which visualised, for the first time, the in-plane flow of force through the skewed arch barrel. It has also been shown that these rosettes allow for strain states to be visualised in other useful orientations – here, in directions aligned with the skewed and square spans. Symmetry in the arch response was confirmed and used to extend the usefulness of rosette data captured over the northern half of the arch barrel, so that strain states for the full extent of the arch could be visualised.

The flow of force through the arch was observed to be multi-dimensional, with notable transverse strains at certain points, in addition to the significant longitudinal strains related to arching action. Other interesting features of the response, such as the inclined strains oriented towards the acute corners of the arch, were identified through this principal strain analysis.

As in Chapter 5, a highly consistent response was observed in the FBG data, across a large number of monitored trains. Potential explanations for the one clear case of a dissimilar response, namely when Class 222 trains apply their critical axle loads close to the arch crown, were explored.

The out-of-plane behaviour of the arch was then investigated, using videogrammetry measurements of vertical displacements along the arch crown line. These measurements clearly showed the deformed profile adopted by the bridge under peak applied loads, which was consistent across different train events. Similar patterns were observed for different train classes, and there was significant symmetry in the response to trains travelling on the south and north tracks.

The videogrammetry data were used to fit a simplified beam model to transverse strips of the arch barrel, oriented with the skewed and square span directions of the bridge. These models yielded expressions for the vertical displacements and intrados strains along the crown line.

Videogrammetry data could be well matched by these models since there were sufficient data to perform an exact fitting. However, this sometimes led to significant predicted curvature over the loaded ends of these strips, and there was often low agreement between the modelled strain profiles and the available FBG data. Relaxing the stiffnesses of support springs resulted in a poorer fit of the vertical displacements but also led to significantly improved fit of the transverse strains. This suggests that transverse bending may only be responsible for a component of the observed vertical deflections of the crown line. Possible contributions to these deflections from axial deformation of the arch, spanning in its longitudinal direction, will be explored in future work.

Both the fitted and modified beam relationships also yielded useful predictions about the support conditions for the beams – in other words, the interfaces between the arch barrel and spandrel walls. Recent repair work at this bridge focussed on re-establishing connectivity across these interfaces, and so, pending their validation through future modelling, these findings may well have practical relevance in potentially quantifying the effectiveness of these repairs.





## **Part 3**

# **Long-term monitoring of the skewed masonry bridge**



# Chapter 7

## An autonomous FBG sensing system

Following the initial 2018–2019 monitoring period, the FBG system was upgraded to enable autonomous, remote monitoring of the CFM-5 bridge. Installed in summer 2020, the new system was powered by solar panels and programmed to record data at set times every day. Using a 4G router, these data were then uploaded to servers in Cambridge for processing and analysis.

This chapter details the changes that were made to the FBG system to bring about this upgrade, both in terms of the on-site equipment and the resultant modifications of the data processing methodology. Initially, problems related to setting up a reliable and stable power supply for the FBG monitoring equipment meant that the system did not log data as frequently as planned. However, further refinements to the power supply resolved this by late February 2021; these modifications are described in this chapter.

Lastly, a summary of the trains recorded to date by this new FBG system is presented. This includes an outline of changes in the rolling stock used by one of the main route operators, relative to the period considered in Part 2 of this thesis.

### 7.1 On-site changes for long-term, autonomous FBG sensing

In contrast to the earlier monitoring described in Part 2 of this thesis, in which an FBG interrogator was brought to site for monthly data acquisition and was powered by a petrol generator, remote FBG sensing required a dedicated interrogator to be left on site with its own power source, PC, and internet connection. In keeping with the on-site monitoring, a Micron Optics sm130 FBG interrogator was used. This was installed in July 2020, alongside a Shuttle

mini-PC and TP-Link 4G router. The equipment was housed in a temperature-controlled cabinet.

The power supply consisted of solar panels and batteries – an expansion of a previous system installed by AECOM in 2018, originally used to power their point sensor network. This supplied a ~12 V DC signal; a pure sine wave inverter was used to convert this to a 230 V AC input for the FBG system. AECOM carried out these changes to the power supply.

It was desired to log data at set times of day – specifically, during morning and evening commute times, as these were identified in Chapter 5 to correspond to times of consistent passenger loading. Initially, a PowerUSB smart timer switch was used to regulate the FBG monitoring times, as this allowed for the timer settings to be changed remotely, without visiting the bridge. Ahead of the timer switch, an Uninterrupted Power Supply (UPS) was installed as a buffer, to protect the sensitive timer and data acquisition system from any potential power surges from the inverter.

Although this approach initially worked, the AC inverter was found to exert a disproportionate drain on the power supply outside of the FBG monitoring times. To remove this issue, a further DC timer switch was installed ahead of the inverter and programmed to match the FBG monitoring times. It was not possible to install the PowerUSB smart timer in this location.

This DC timer had to be programmed manually, on site. Consequently, this defeated the purpose of the smart timer, as reprogramming this remotely would be ineffective until the DC timer was also updated, in person. The new DC timer also led to a secondary issue with the UPS, as its internal battery now tended to fully drain while the inverter was switched off between monitoring times and, when the power supply was next restored, the UPS was not able to simultaneously recharge its battery and power the FBG equipment.

These issues with the power supply led to the FBG system initially failing to log data over a significant proportion of the planned monitoring shifts. To resolve this, the UPS and smart timer were ultimately replaced with a simpler AC timer, similar to the DC timer. This was installed after the inverter and was programmed to turn on several minutes after the DC timer and turn off several minutes before it; in this way, transient fluctuations in the power supply as the inverter switched on and off would not pass through to the sensitive FBG equipment.

These refinements to the installation were carried out over a number of site visits and completed in late February 2021. Unfortunately, there were appreciable delays in arranging the necessary site work, due to the ongoing effects of the COVID-19 pandemic.

Since this time, however, the FBG system has successfully logged data for a much higher proportion of the planned monitoring periods. The residual times when the system has not come online may have been due to poor light conditions leading to an insufficient solar supply, in which case the performance should improve towards summer. As part of future work, further improvements to the efficiency of the power supply system will be explored.

A schematic overview of this equipment is given in Figure 7.1, while Figure 7.2 shows the FBG equipment installed in its site cabinet.

## **7.2 Data-processing strategies for long-term FBG data**

During the 2018–2019 monitoring, which was carried out on site, detailed observations of the trains were made, which allowed the recorded data to be manually matched to timetabled train events. However, since such notes would not be available for remote monitoring, it was necessary to automate this train classification procedure. Scripts to perform this task were developed in collaboration with Austin Chen, an undergraduate researcher at the University of California, Berkeley, and have been based on an approach used by AECOM for the classification of their point sensor data at CFM-5.

This approach, developed by Matthew Audley at AECOM, involves two key steps:

1. Publicly available train timetable information is scraped from an online source and assembled into a spreadsheet. Specifically, this comprises the historic dates and times at which known, timetabled trains passed through the two stations either side of CFM-5 – Micklefield and Church Fenton – as well as other train data, such as the route operators. AECOM have shared this train timetable spreadsheet, to enable classification of the FBG data.
2. An SQL script then compares the timestamps of measured data with the available windows in the timetable, during which it is possible for a given train to have passed over CFM-5. Data that can be linked to unique timetabled events are duly matched, and used in further analysis, while other data are discarded.

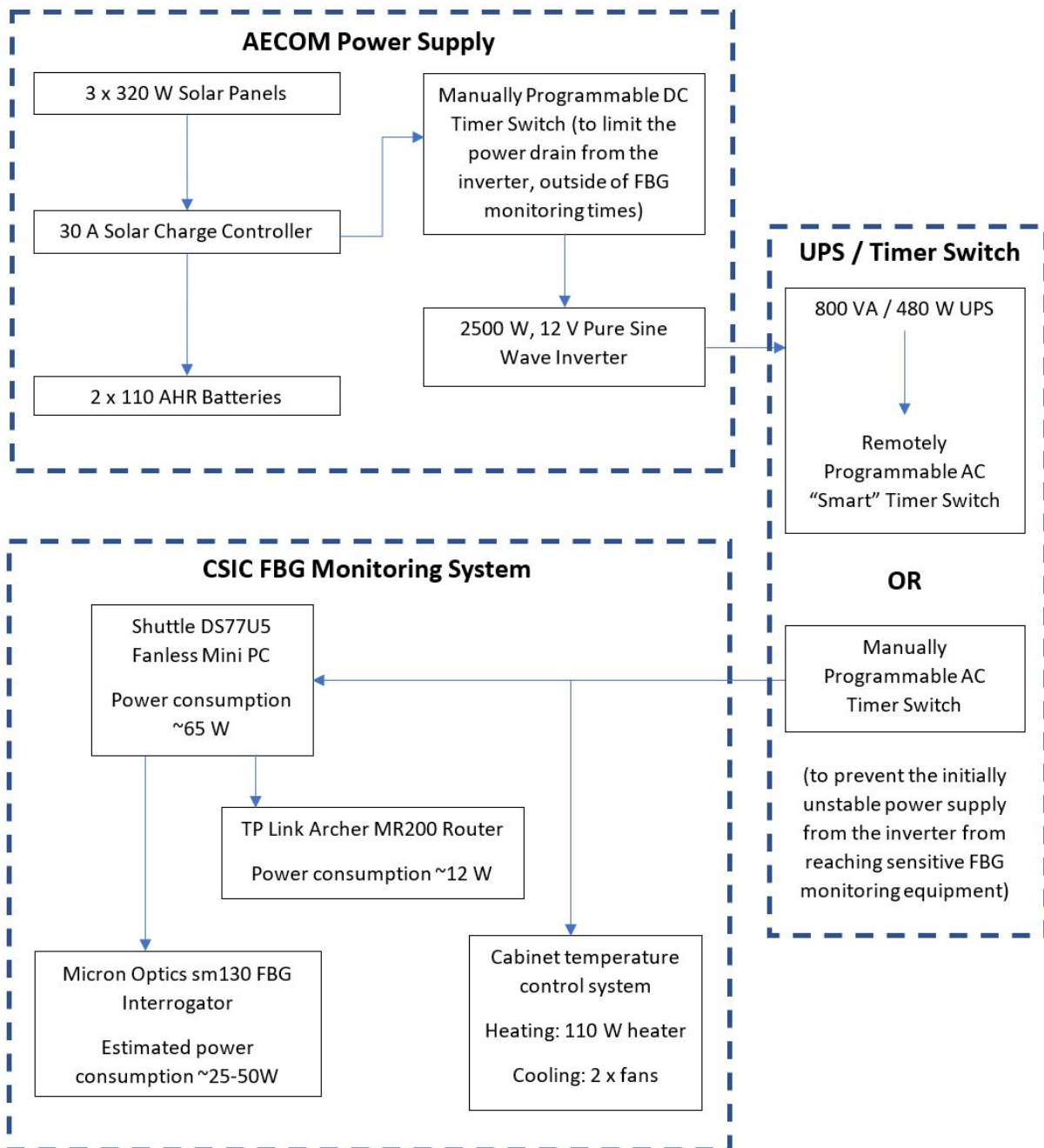
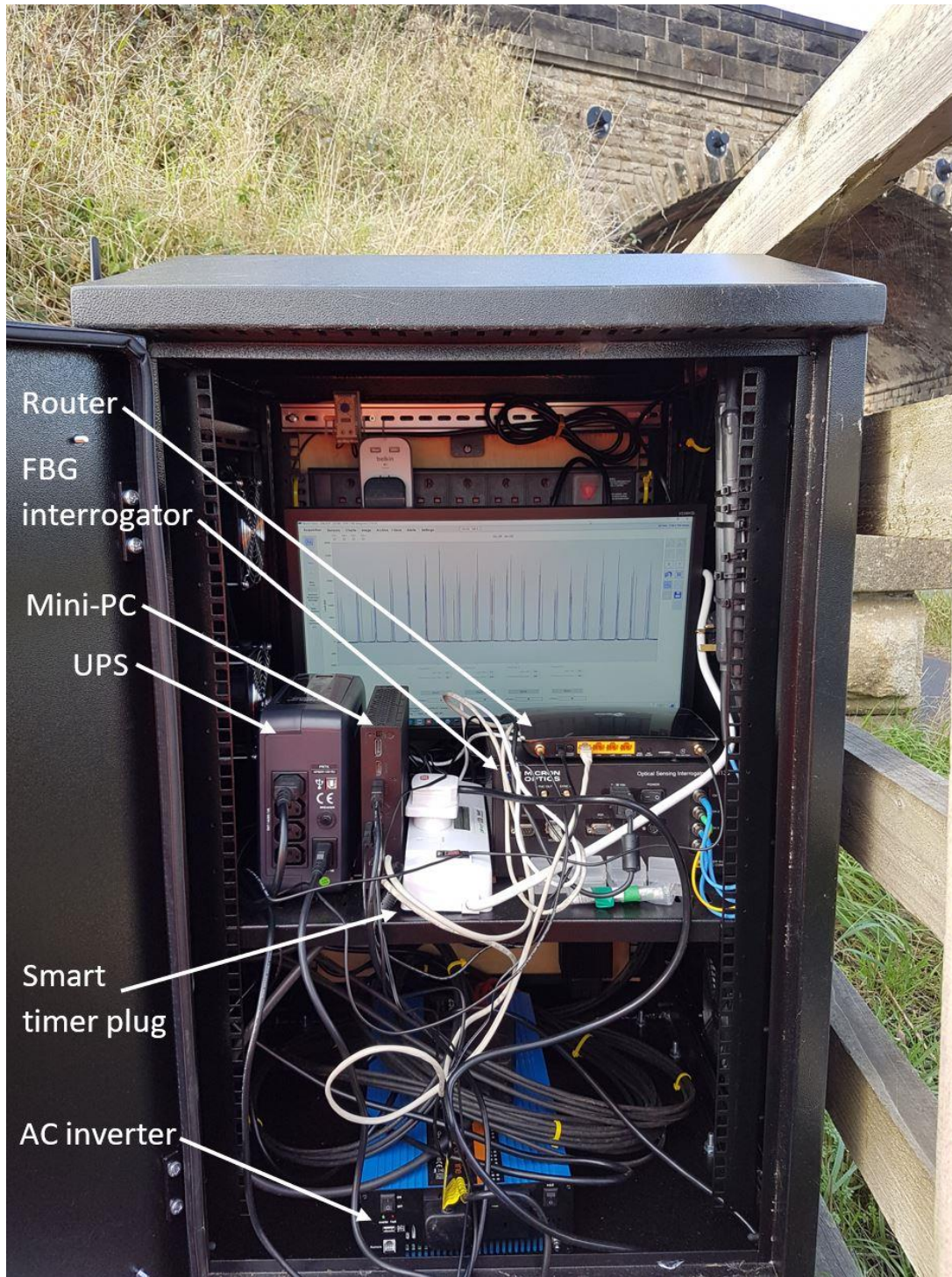


Figure 7.1: Schematic overview of the FBG system and power supply, used for long-term monitoring at CFM-5



*Figure 7.2: View of the FBG equipment cabinet installed at CFM-5, before the replacement of the UPS and smart timer plug with a simpler AC timer switch*

Note that it is possible to ascertain train directions before performing this classification procedure. This is established for the timetable and sensor data, respectively, by considering the order in which a train travels through the two adjacent stations and the track on which it passes over CFM-5, which can be identified by comparing peak measurements from sensors on the two sides of the bridge. Using this information, the algorithm only allows data to be matched to timetabled events when the train directions are consistent. This significantly increases the likelihood that data can be matched to unique timetabled events. Furthermore, since AECOM's point sensor network theoretically logs all trains passing over the bridge, a very large data set is gathered. The impact on the quality of the overall analysis, which results from discarding data that cannot be uniquely matched, is correspondingly low.

In contrast to this, FBG data are only gathered during morning and evening commute times. While this still results in an appreciable number of recorded trains, as shown later in section 7.3, it is more important to match a high proportion of these data to the timetabled events now that the starting size of the data set is smaller. This is especially the case for time periods when the system did not log data as frequently as planned, due to the issues discussed in section 7.1.

To increase the success rate of the train classification algorithm, refinements have been made to the approach during its adaptation for FBG data. These have been implemented in collaboration with Austin Chen, as previously noted. In the latest version of the algorithm, work has focussed on improving the calculation of train direction, by comparing readings between sensors at an increased number of locations over the bridge. This has reduced the number of files which could not be matched to any available timetabled trains, leading to a suitably high success rate overall. This is the version of the algorithm that has been applied in this thesis and has classified the trains presented in section 7.3 (see Table 7.1).

However, the algorithm still fails to successfully match some other files, in cases where there are multiple potential timetabled trains to choose between. To address these cases, further refinements to the algorithm are being investigated, as follows:

1. After an initial pass of the algorithm, successfully matched timetabled trains will be removed from the timetable array and the algorithm run again. This will remove some failure cases, in which overlapping windows in the timetable mean that a file cannot be uniquely matched to a timetable entry.
2. The number of train carriages can be calculated for a data file, using a peak-finding algorithm, and utilized to further reduce the potential matches in the timetable. Note that the carriage count is already performed during analysis and used to calculate the train

speed. This approach would leverage the fact that Train Operating Companies use a standard fleet of rolling stock to run their passenger services, and trains typically conform to a limited set of carriage configurations. For instance, some CrossCountry trains run with a larger number of carriages than First TransPennine and Northern Rail services. However, since there is a wide range of potential train configurations, and companies occasionally run services with non-standard configurations, this approach may be challenging to implement robustly.

Other characteristics, such as train speed and ambient temperature, are assigned in a similar manner to that discussed previously in Chapter 4. Train speed is calculated based on the number of carriages, identified by a peak-finding algorithm, and the known carriage dimensions of trains operated on each route, which are assigned based on the results of the train classification algorithm described above. Temperature data are logged every hour by separate point sensors, distributed across the bridge, and averaged to give a single hourly temperature value for the bridge. Based on the timestamp of a given FBG file, these temperature readings are linearly interpolated to estimate the ambient temperature at the time of the corresponding train event.

### 7.3 Trains recorded during long-term FBG monitoring

Table 7.1 gives a breakdown of the FBG data recorded between July 2020 and April 2021. Note that this only shows data which have been successfully matched to specific timetabled trains – using the procedure outlined in section 7.2 – and which corresponds to one of the three main passenger routes operating over CFM-5: First TransPennine, Northern Rail, and CrossCountry.

*Table 7.1: Summary of the trains recorded to date, during remote FBG monitoring at CFM-5*

<b>Train Class (&amp; Route):</b>	<b>Passing on track:</b>	<b>July 20:</b>	<b>Aug 20:</b>	<b>Sep 20:</b>	<b>Oct 20:</b>	<b>Nov 20:</b>	<b>Dec 20:</b>	<b>Jan 21:</b>	<b>Feb 21:</b>	<b>Mar 21</b>	<b>Apr 21:</b>	<b>Σ:</b>
Nova (First Trans Pennine)	North	208	61	0	96	0	5	1	12	131	174	688
	South	229	64	0	86	1	5	1	11	125	174	696
Class 150 (Northern Rail)	North	82	25	0	93	0	7	2	6	74	108	397
	South	83	22	0	80	0	6	1	6	65	81	344
Class 222 (Cross Country)	North	77	23	0	41	0	3	0	6	51	73	274
	South	81	28	0	33	0	3	0	4	51	78	278
Overall total:												2677

However, this was a high proportion of the overall recorded data. During this time period, data were logged for a total of 3105 trains. 2713 of these files (87%) were matched to timetabled events, of which 2677 (99%) belonged to one of the three main routes. Only these 2677 data files, presented in Table 7.1, are analysed further in this thesis; the very high percentage justifies the focus on these three passenger routes.

It is important to note that, between the 2018–2019 monitoring period and the start of long-term monitoring in summer 2020, the rolling stock used on the First TransPennine route has changed. Originally, services on this route used either 3-carriage or 6-carriage Class 185 trains. These have been replaced with a new ‘Nova’ fleet, of which two types pass over CFM-5:

1. ‘Nova 1’ – Class 802 trains, typically running with either 5 or 9 carriages.
2. ‘Nova 3’ – Class 68 locomotives, hauling a set of 5 Mark 5A coaches; this produces a time history in which 6 carriages are effectively counted, of which either the leading or rear vehicle (the Class 68 locomotive) produces a higher magnitude strain response.

Figure 7.3 shows typical time histories of the rolling stock used on the First TransPennine route. It can be seen that the Class 185 and Nova 1 trains yield a very similar pattern of response, while the response for Nova 3 trains is notably different due to the two vehicle types these trains are composed of. The highest magnitude response is caused by the Class 68 locomotives of the new Nova 3 trains, although their Mark 5A carriages produce significantly smaller strains. For Nova 1 trains, the response appears to be slightly smaller in magnitude than was previously observed for Class 185 trains.

Note that the critical bogie loads of Class 185, Nova 1, and Nova 3 trains are 36.4 t, 32.8 t, and 43.1 t, respectively. The ratios between these peak bogie loads roughly align with the ratios between the peak strains, for the trains shown in Figure 7.3.

## 7.4 Summary

In this Chapter, long-term FBG monitoring at the CFM-5 bridge has been introduced. The necessary changes to both the on-site equipment, for data acquisition and transfer, and the data processing strategies have been discussed. In particular, the procedure for classifying data files by train type has had to be significantly changed now that monitoring is performed remotely.

An overview of the trains measured to date was then presented, and the change in rolling stock used by the most common passenger route operating at CFM-5 – the First TransPennine Express – was discussed.

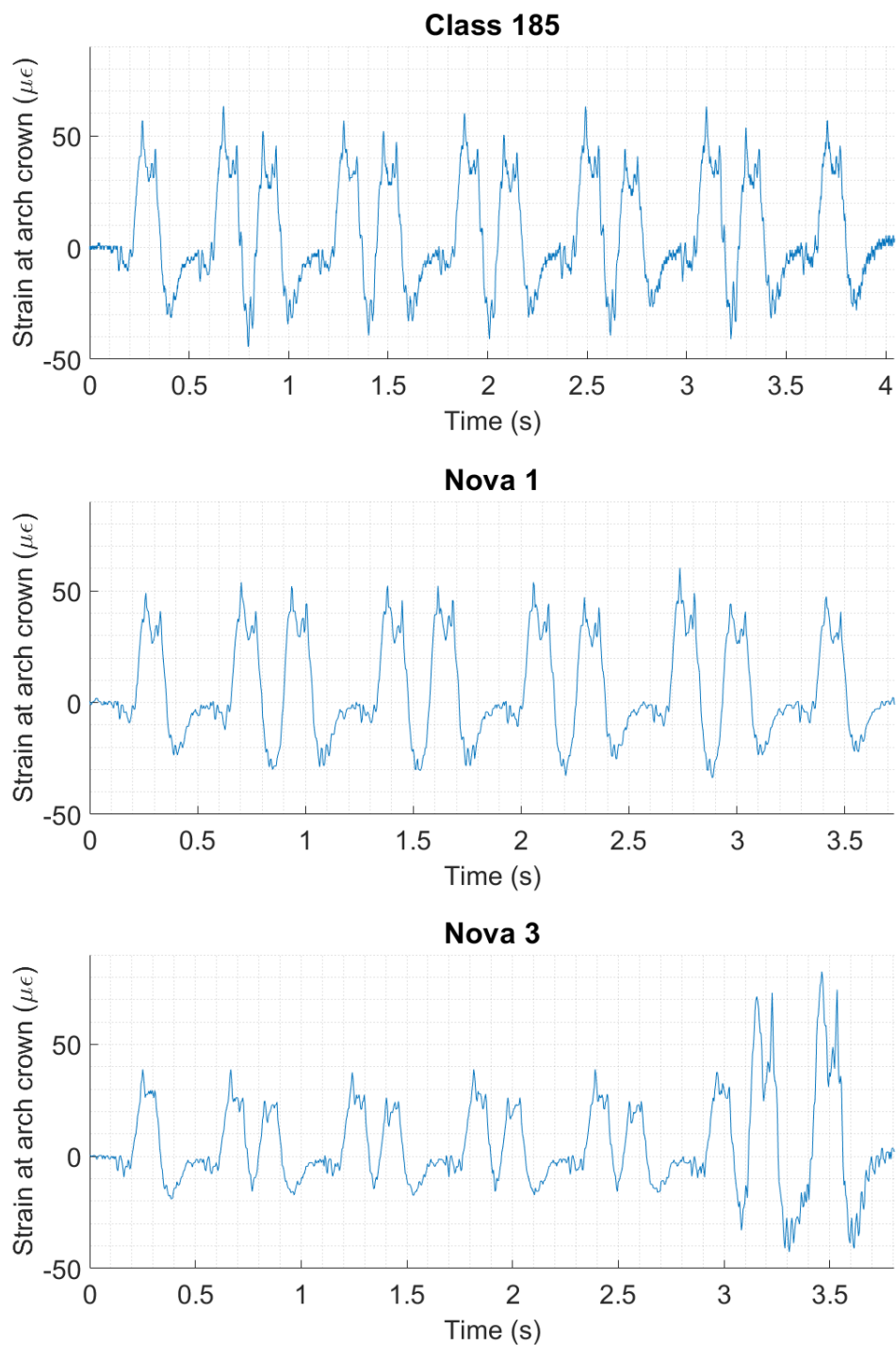


*Figure 7.3: Comparison of typical strain time histories for the various rolling stock used on the First TransPennine route, measured at the arch crown underneath the track centreline*



# Chapter 8

## Analysis of the long-term FBG data

### 8.1 Introduction

This chapter presents an analysis of all FBG monitoring data gathered to date, from September 2018 up to the end of April 2021. The data have first been categorised by route operator – in order to minimise the range of possible rolling stock represented in each plot – and train direction – i.e., the side of the bridge on which the trains are travelling. In this chapter, data are presented for trains operated by First TransPennine Express. Full sets of plots for trains run by Northern Rail and CrossCountry are given in Appendices A and B, respectively. Note that trains passing on both tracks are used to generate quiver plots of the principal strains, following the procedure outlined in Chapter 6.

Plots of the peak-to-peak strains and peak crack movements show the sensitivity of these responses to several variables: date, time of day, train speed, and ambient temperature. In these scatter plots, each point corresponds to the peak response for a particular train event. An overview of the plotted trains was given in the last chapter, in Table 7.1.

### 8.2 The instantaneous dynamic strain response in the arch

Figures 8.1 and 8.2 show, for trains on the north and south tracks, respectively, the statistical distributions of the instantaneous longitudinal strain profiles in the arch, along both the bridge centreline and underneath the north track centreline, at times when critical axle loads are applied at the arch third points and either side of the crown. The numbering of the FBGs follows the same convention used in Chapter 5 (see Figure 5.1) to plot the statistical distributions of longitudinal strains in Figure 5.10. In keeping with the earlier Figure 5.10, distributions of strains are plotted as boxplots, with median values at adjacent FBGs joined using solid lines.

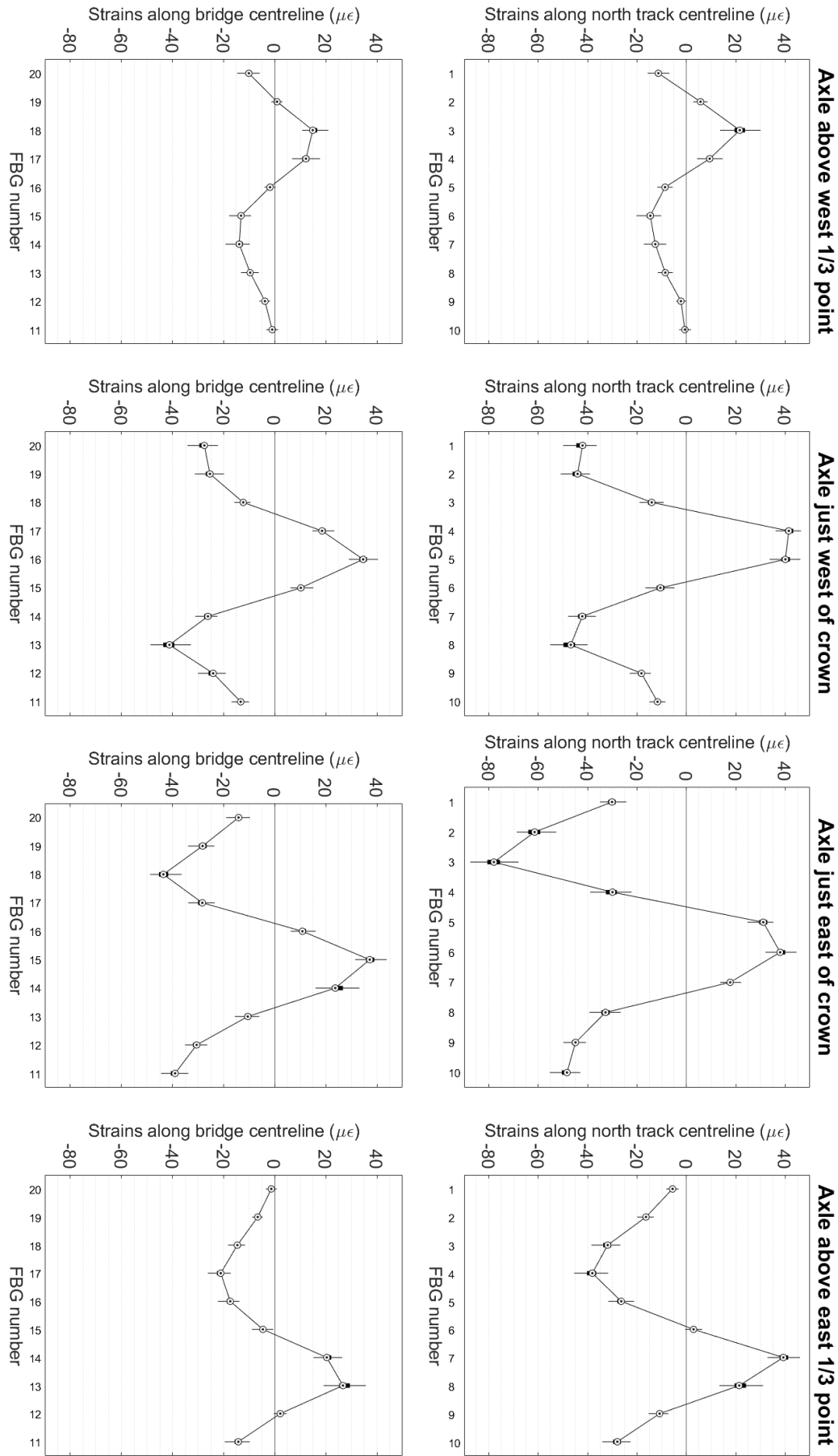


Figure 8.1: Statistical variation of the instantaneous longitudinal strains over the northern half of the arch, when the critical axle loads are applied at key locations along the arch span, across all First TransPennine trains passing on the north track

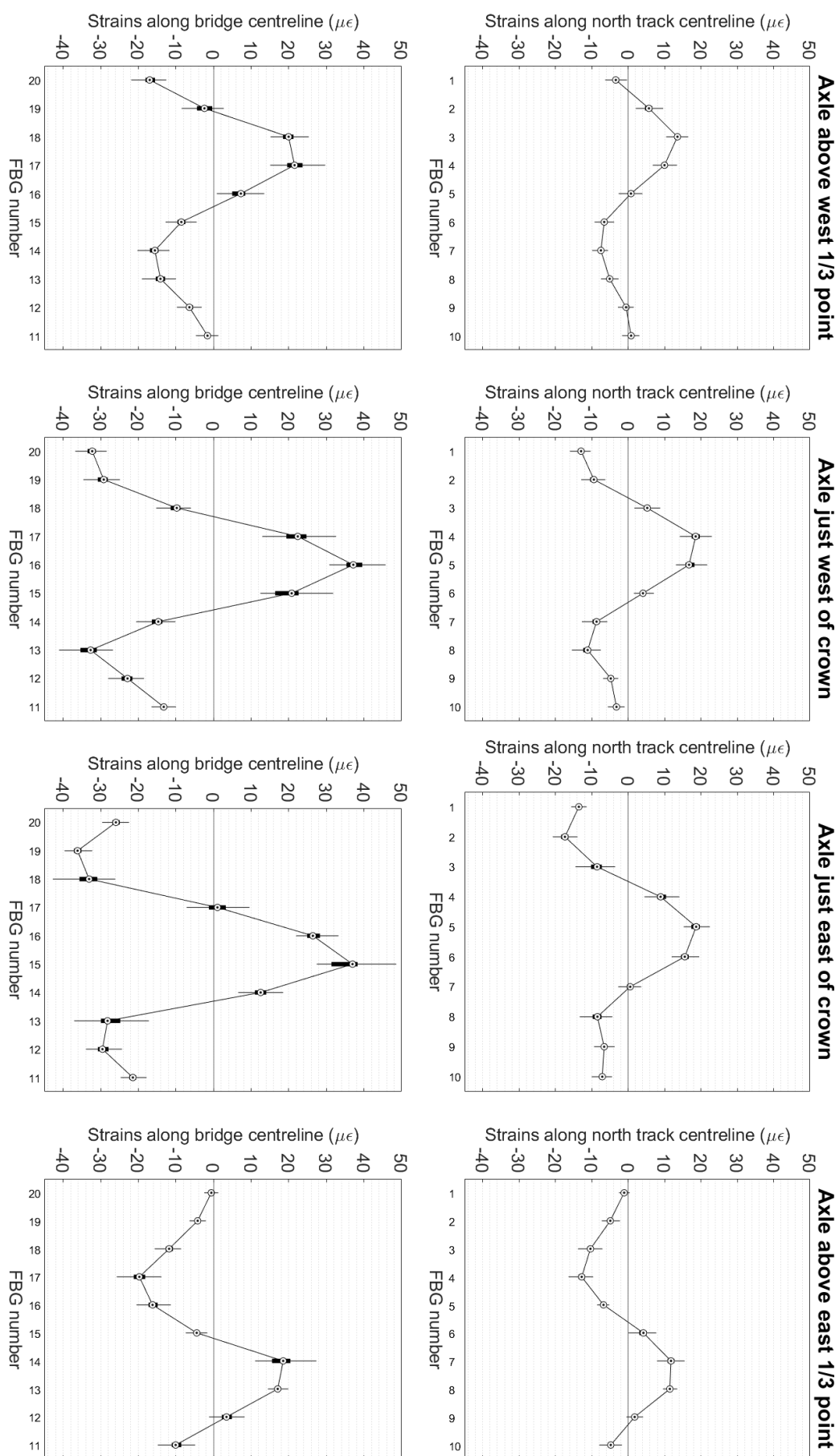


Figure 8.2: Statistical variation of the instantaneous longitudinal strains over the northern half of the arch, when the critical axle loads are applied at key locations along the arch span, across all First TransPennine trains passing on the south track

Comparing Figure 8.1 with the earlier Figure 5.10 gives an indication of the changes in longitudinal strain profiles, over the two years since the data shown in Figure 5.10 were originally gathered. Small increases in the magnitudes of median longitudinal strains are observed in many cases. Larger increases in the interquartile ranges of most boxplots are also seen although, in both cases, these changes are only of the order of several microstrain.

It is likely that a major contributing factor, behind this increase in the instantaneous strain magnitudes, is the presence of heavier Nova 3 trains in the new data set. This change in loading cannot easily be decoupled from the effects of any potential bridge deterioration which, if present, would also be likely to cause local changes in the strain magnitudes. Having said this, however, it is interesting to note that, when trains are passing on the south track as in Figure 8.2, the interquartile ranges of instantaneous strains are significantly larger along the bridge centreline – i.e., towards the south side of the bridge – especially when loads are applied close to the arch crown and are therefore more concentrated when they enter the arch extrados. Since the southern half of the arch is known to be in worse condition, due to the presence of the south-eastern longitudinal crack, this suggests that an increased damage state leads to greater variability of the instantaneous strain profile in the arch. As was discussed previously, in section 5.3, the consistency of this intrados longitudinal strain profile is linked to the consistency of the thrust line adopted by the arch as its primary load path.

It can also be seen, in Figures 8.1 and 8.2, that, when train axles reach the arch third points, a higher magnitude strain response occurs if these loads are applied in the acute corners, as opposed to the obtuse corners, of the skewed arch. This corresponds to the eastern third point for trains travelling on the north track, and the western third point for trains travelling on the south track. This is consistent with the observations, made earlier in Chapter 6 and seen again later in Figure 8.19, that principal strains, and hence the flow of force, are oriented towards the acute corners of the skewed arch.

### **8.3 The peak-to-peak dynamic strain response in the arch**

The following Figures 8.3 to 8.6 consider the peak-to-peak dynamic longitudinal strain responses occurring at both third points and either side of the arch crown, underneath the north track centreline and the bridge longitudinal centreline. These plots take the same form as Figures 5.11 and 5.12 earlier, although a different convention is now used to colour the scatter points.

Data are now coloured by the time period of the train events. This is most clearly seen in the plots showing peak response against date (see, for instance, Figure 8.3(a)). Data corresponding

to trains recorded in the initial monitoring period, between September 2018 and February 2019, are coloured green. Data recorded between July and August 2020 are cyan, while September to October 2020 are blue, November 2020 to February 2021 are magenta, and March to April 2021 are red. Note that the same colouring convention is also used in section 8.4, for plots of the peak crack movements, and in Appendices A and B.

Variation of peak-to-peak strains with date, time of day, train speed, and temperature are plotted separately, in this section, for trains travelling on the north and south tracks.

### 8.3.1 Trains on the north track

Figures 8.3(a) and 8.3(b) show the variation of peak-to-peak longitudinal strains with date and time of day, respectively, for trains travelling on the north track. In Figure 8.3(a), the two new Nova train types, used on the First TransPennine route since summer 2020, can be clearly distinguished. As observed in the discussion of Figure 7.3 earlier, Nova 1 trains produce a slightly reduced peak-to-peak response, relative to the original Class 185 trains, while the heavy Class 68 locomotives of the Nova 3 trains cause a notably higher peak-to-peak response.

In Figure 8.3(b), the time-of-day variation discussed in Chapter 5 cannot be seen in the new data set, because the remote FBG monitoring system is only configured to record data during morning and evening commute times. A small amount of data has been recorded outside of these times, because the initial power issues, described in section 7.1, occasionally caused the monitoring system to log data at unexpected times. However, this is insufficient for the time-of-day trend to be visualised. Furthermore, the impact of COVID-19 lockdowns on commuter behaviour is likely to have significantly changed this trend, for the 2020–2021 data.

Figures 8.4(a) and 8.4(b) show the variation of peak-to-peak strains with train speed and ambient temperature, respectively, for trains travelling on the north track. In Figure 8.4(a), the clearest trend with train speed remains within the green data set recorded during the 2018–2019 monitoring (see also Figure 5.12). Corresponding trends for the 2020–2021 data cannot be discerned. This is likely due, at least in part, to a significant lack of data for slow trains; note that this is also the case among the data recorded for Northern Rail and CrossCountry trains, which is plotted in Appendices A and B, respectively.

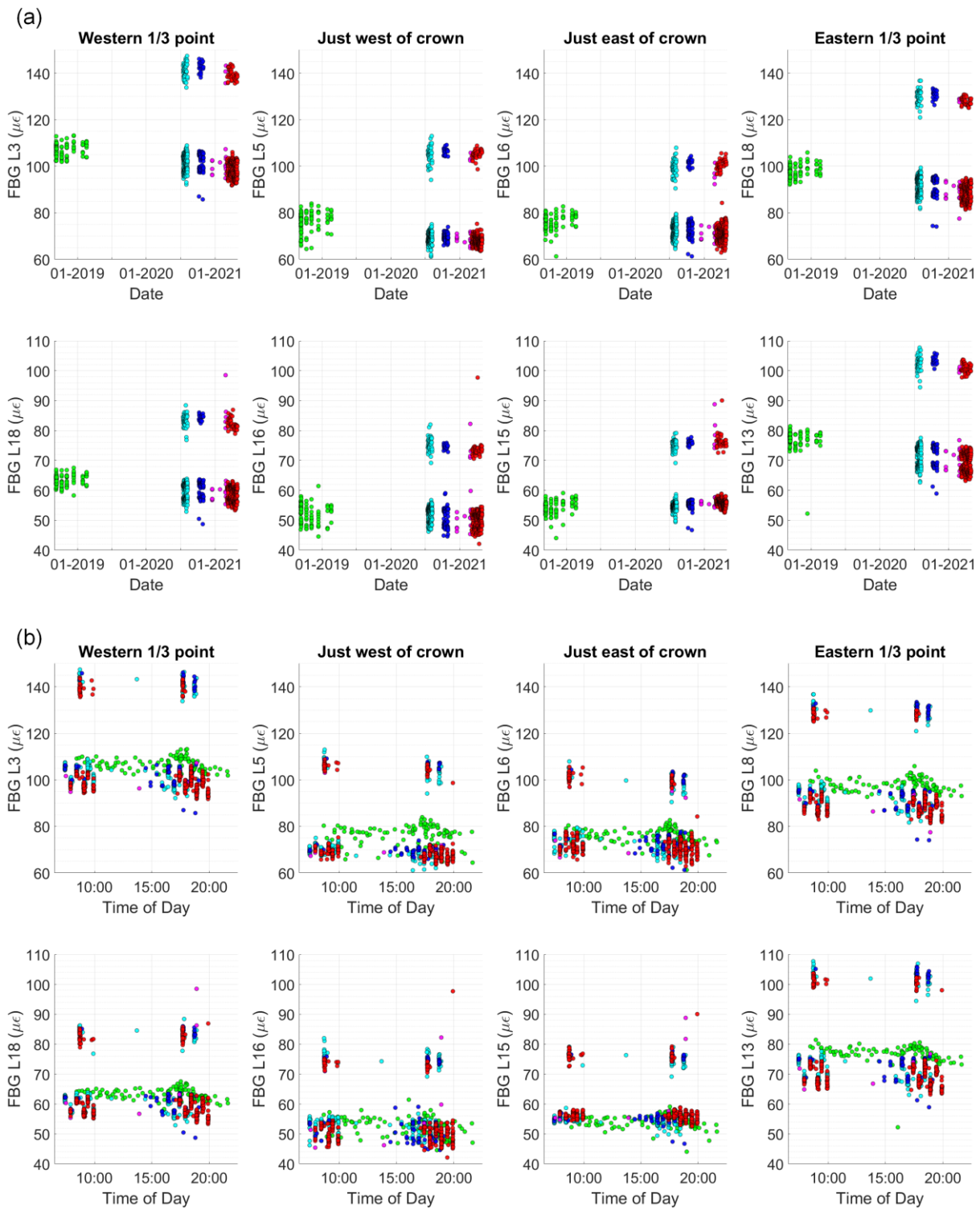


Figure 8.3: Variation of peak-to-peak longitudinal strains over the northern half of the arch with (a) date and (b) time of day, for all recorded First TransPennine trains passing on the north track

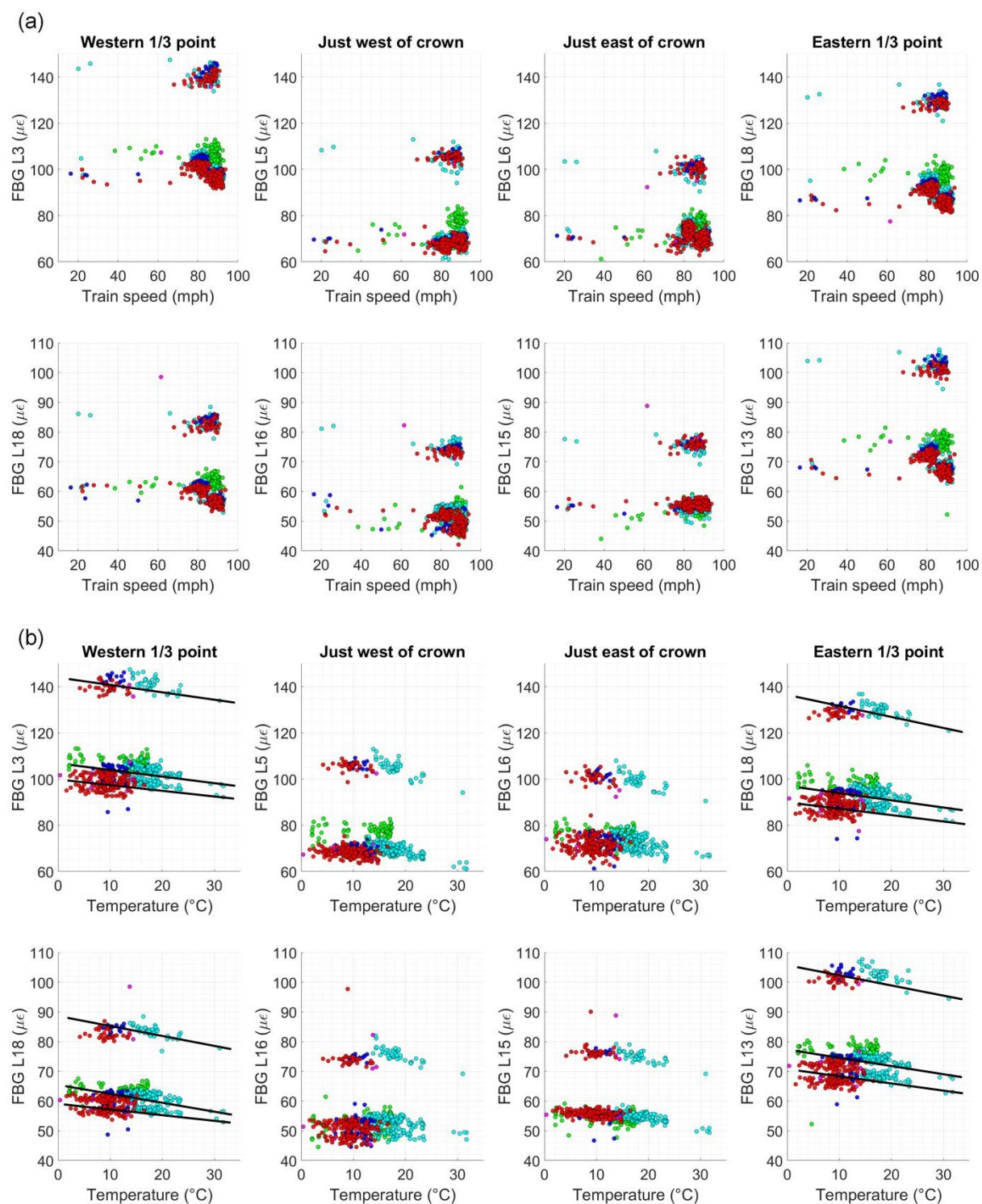


Figure 8.4: Variation of peak-to-peak longitudinal strains over the northern half of the arch with (a) train speed and (b) temperature, for all recorded First TransPennine trains passing on the north track

Conversely, trends with temperature in Figure 8.4(b) are now easier to identify. Ignoring the ‘green’ data for Class 185 trains, plotting peak-to-peak strains against temperature reveals bands in the data – most clearly distinguishable for the Nova 1 and Nova 3 trains, as commented on above, although the lower group of Nova 1 trains in most subplots is now observed to split into two bands, particularly when loads are applied at the arch third points.

Each band appears to show a clear linear relationship between peak-to-peak strain and ambient temperature, with higher temperature leading to a slightly reduced strain magnitude. However, more data are needed for higher ambient temperatures before these relationships can be accurately quantified with fitted trend lines. In Figure 8.4(b), lines have been added manually to demarcate the behaviour of the various bands, for the responses at both arch third points, but these are purely illustrative.

This relationship between peak-to-peak strain and temperature makes intuitive sense, as thermal contraction at lower temperature would tend to open any cracks in the masonry and lead to greater potential for movements in the bridge. In this sense, the thermal relationship agrees with the findings regarding the behaviour at the south-eastern longitudinal crack – discussed previously in section 5.5 and later in section 8.4 – and with relationships identified in other studies (see, for example, Alexakis et al., 2019b; Alexakis, Lau, and DeJong, 2021).

### 8.3.2 Trains on the south track

Figures 8.5(a), 8.5(b), 8.6(a), and 8.6(b) present the variation of peak-to-peak strains with date, time of day, train speed, and ambient temperature, for the response to trains travelling on the south track. Observations made above for Figures 8.3 and 8.4 broadly apply to these data as well, with the added observation that, in Figure 8.6(b), the thermal variation for ‘cyan’ (July to August 2020) and ‘red’ (March to April 2021) data is more clearly distinct than in Figure 8.4(b), especially for FBGs along the bridge centreline. Similar to the discussion in section 8.2, this could suggest that the behaviour of the more heavily damaged southern half of the bridge is more variable, when loads are also applied in this region.

This more pronounced trend, linking peak-to-peak strain magnitude to the date of recording, can also be seen in Figure 8.5(a) (relative to Figure 8.3(a)). The trend is most evident close to the arch crown and the eastern third point, and for FBGs along the bridge centreline, and appears to show a decrease in strain magnitude over time that could be linear. However, the precise nature of the trend is obscured by gaps in the data, for dates when the monitoring system was unexpectedly offline, and more continuous data will need to be collected over a substantial period of time in order for these trends to be properly quantified.

## 8.4 The peak dynamic crack movements

Figures 8.7 to 8.14 plot the variation of peak crack movements, at the south-eastern longitudinal crack and south spandrel separation crack. Data for trains travelling on the south and north tracks are plotted separately, and the same convention for colouring data by date is used (see section 8.3).

### 8.4.1 Trains on the south track

Figures 8.7 and 8.8 show the variation of peak movements at the south-eastern longitudinal crack, with date, time of day, train speed, and ambient temperature, for trains travelling on the south track. Figures 8.9 and 8.10 plot the sensitivity of peak movements at the south spandrel separation crack to the same variables.

At some locations along the length of the south-eastern crack, peak movements appear to have some sensitivity to the date of recording. For instance, measurements at FBGs SE2 and SE3, close to the crack root, show a slight decrease in magnitude with date, in Figure 8.7. However, this is not observed at other FBGs, especially those located towards the crack tip. At SE2 and SE3, this distinction between ‘cyan’ and ‘red’ data is also seen in Figure 8.8 for the variation with ambient temperature; the trend here matches the observations made in section 8.3.2 for the longitudinal strain response, although note that this is also a feature of the crack response when trains are travelling on the north track (see Figure 8.12).

In most cases, it is difficult to distinguish bands in the data that could correspond to a difference in response for Nova 1 and Nova 3 trains. Some banding of the data can be seen in Figure 8.8, for FBGs SE2 to SE6, although the difference in response magnitude between the bands is minor. Furthermore, and in keeping with the observations made in section 8.3 for the longitudinal strain response, there are no clear trends with time of day or train speed.

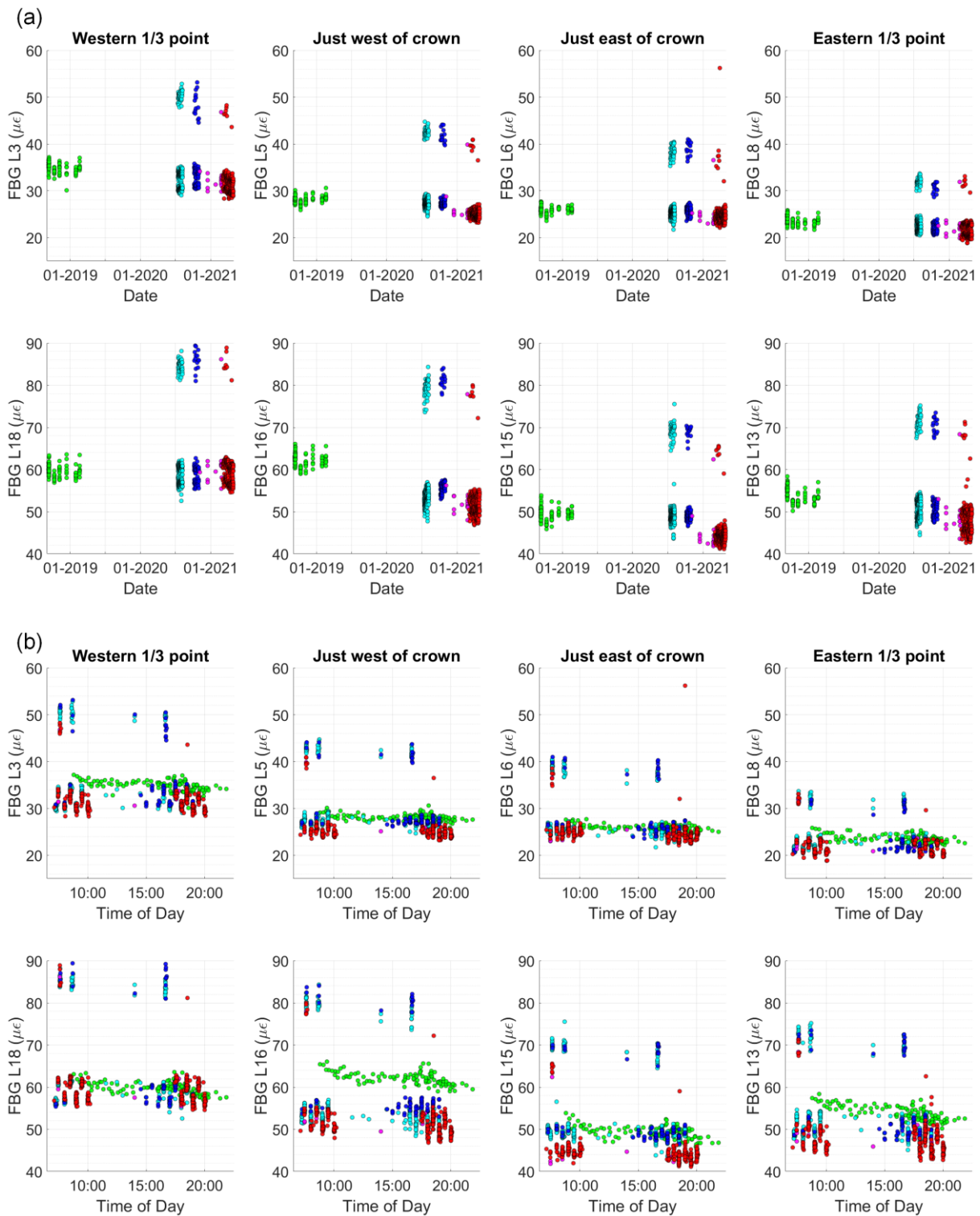


Figure 8.5: Variation of peak-to-peak longitudinal strains over the northern half of the arch with (a) date and (b) time of day, for all recorded First TransPennine trains passing on the south track

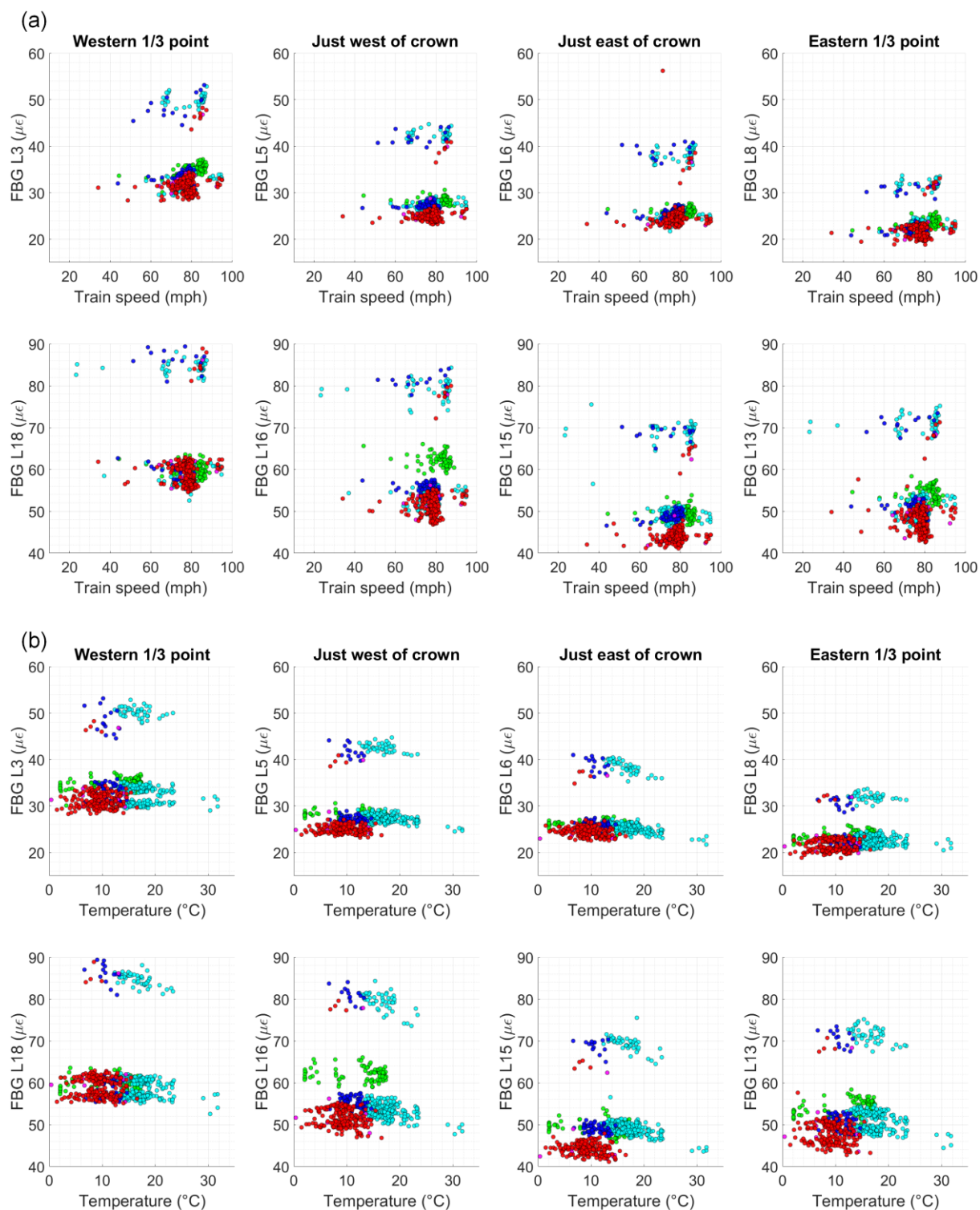


Figure 8.6: Variation of peak-to-peak longitudinal strains over the northern half of the arch with (a) train speed and (b) temperature, for all recorded First TransPennine trains passing on the south track

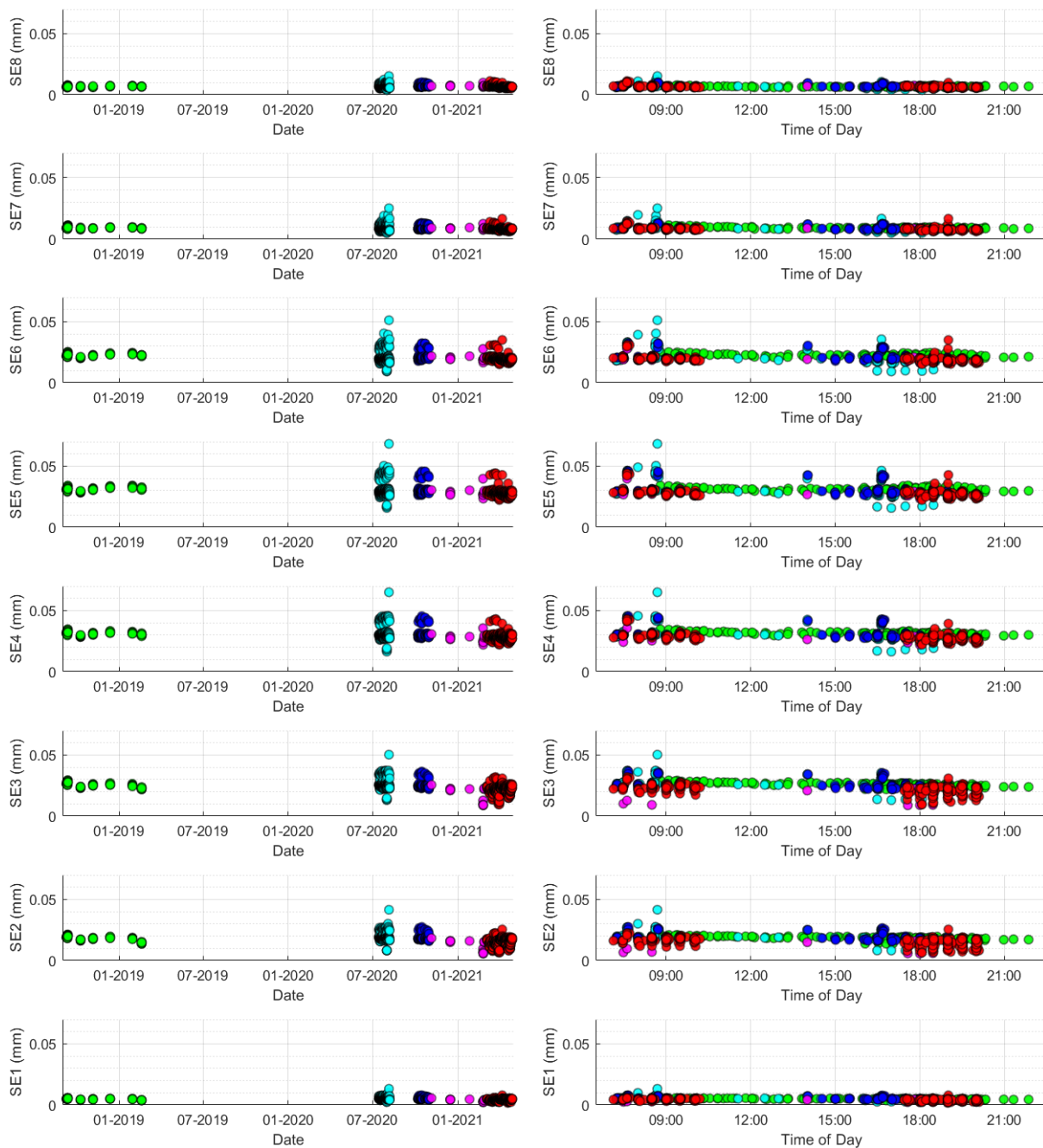
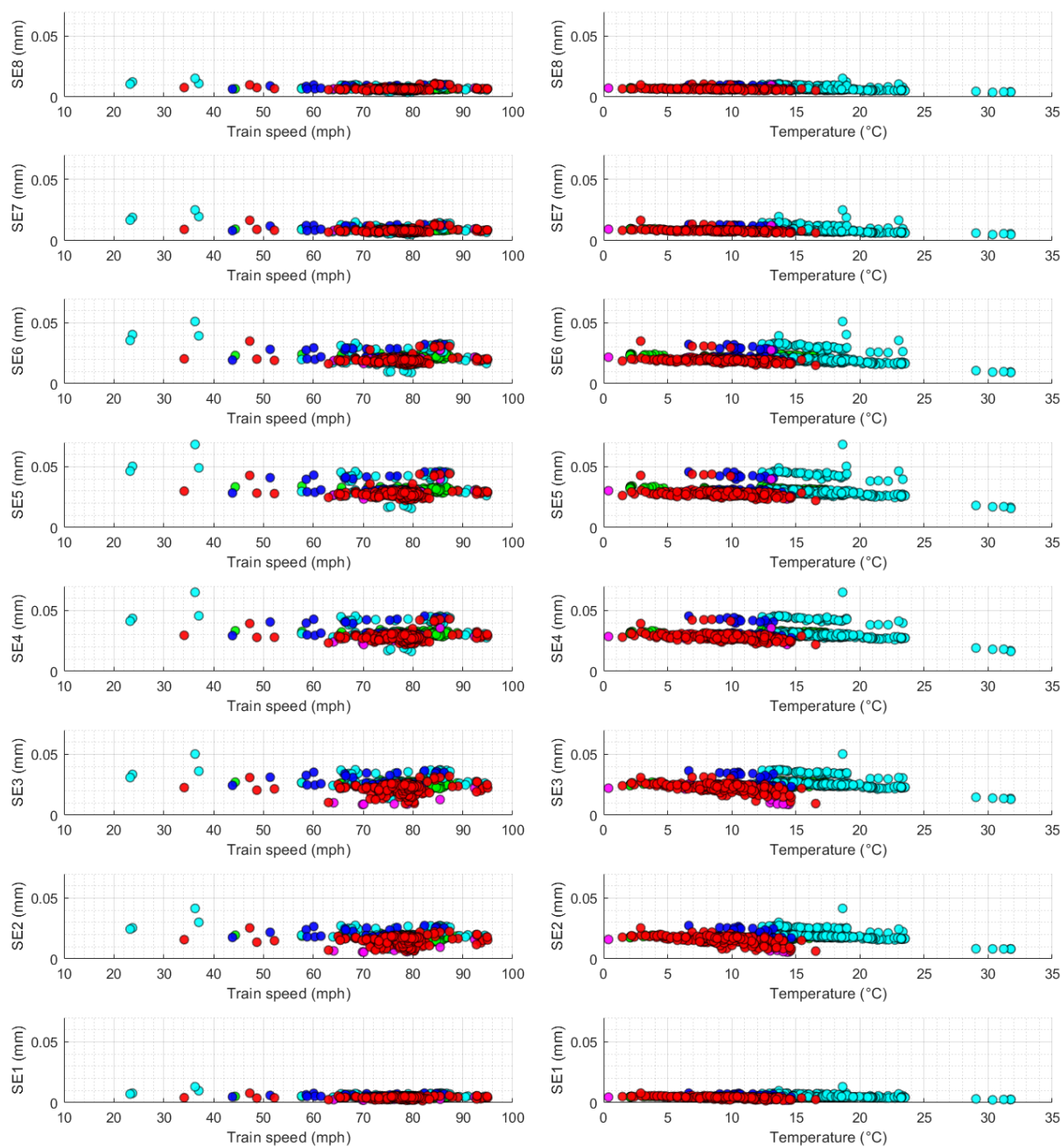


Figure 8.7: Variation of peak dynamic movements at the south-eastern longitudinal crack with (left) date and (right) time of day, for all recorded First TransPennine trains passing on the south track



*Figure 8.8: Variation of peak dynamic movements at the south-eastern longitudinal crack with (left) train speed and (right) temperature, for all recorded First TransPennine trains passing on the south track*

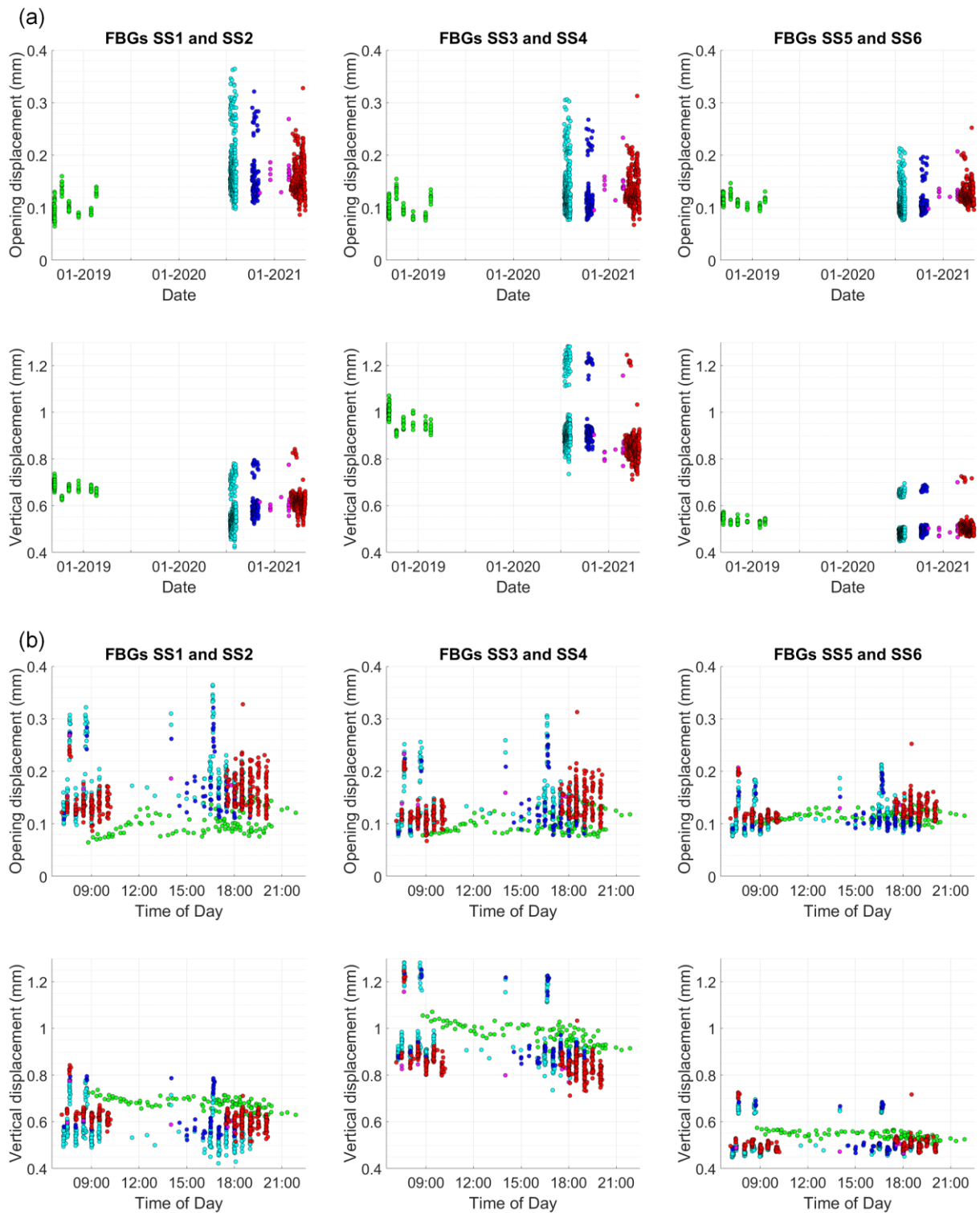
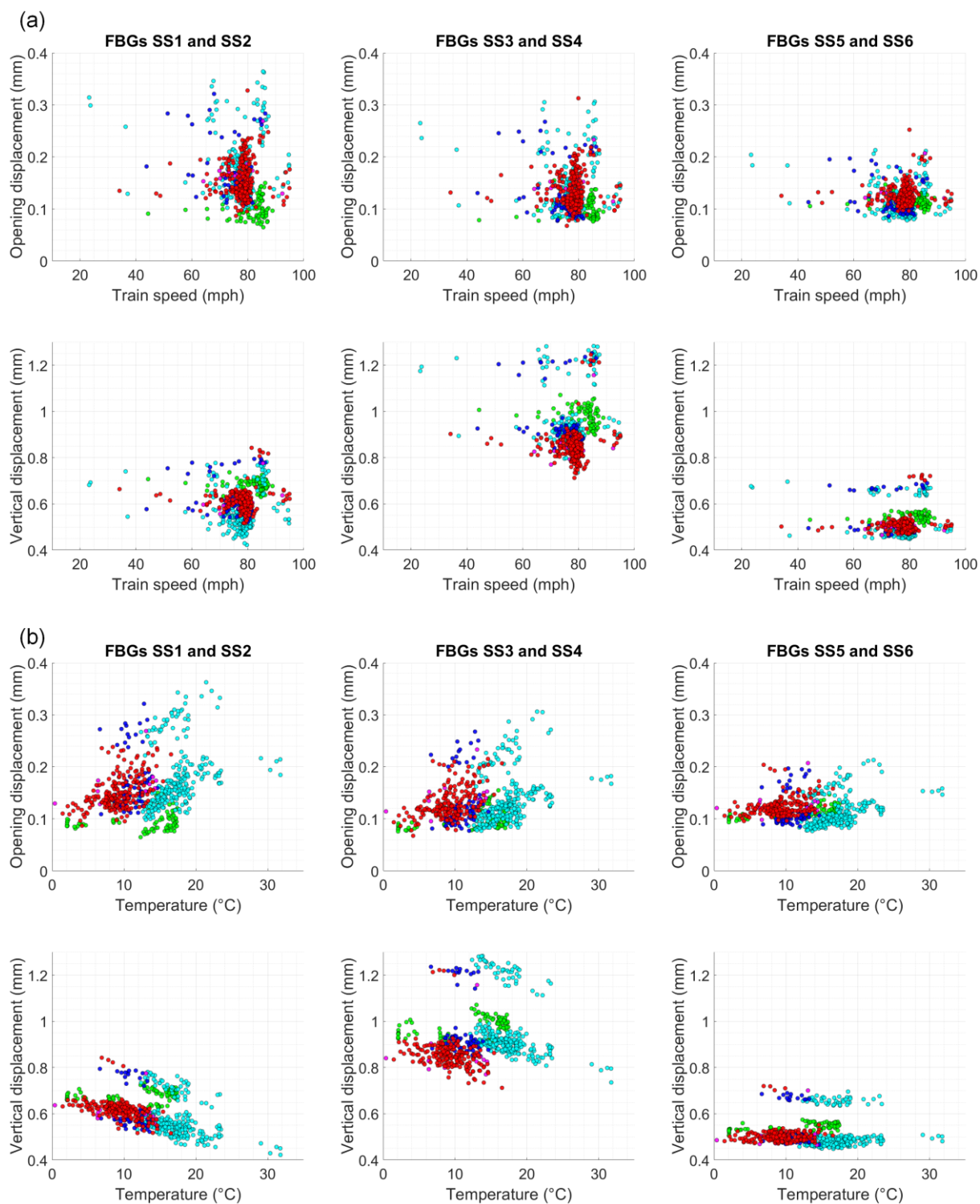


Figure 8.9: Variation of peak dynamic movements at the south spandrel separation crack with (a) date and (b) time of day, for all recorded First TransPennine trains passing on the south track



*Figure 8.10: Variation of peak dynamic movements at the south spandrel separation crack with (a) train speed and (b) temperature, for all recorded First TransPennine trains passing on the south track*

Figures 8.9 and 8.10 plot peak movements at the south spandrel separation crack, separated into crack opening (in-plane) and vertical (out-of-plane) displacements. These are calculated following the approach outlined in Chapter 5. The average magnitudes of peak crack opening displacements are broadly similar in the three measurement locations, although increased spread and higher maximum values are observed towards the western side of the crack – especially at FBGs SS1/SS2. Vertical displacements reach their maximum values on the eastern side of the arch crown (at FBGs SS3/SS4), with the response at the eastern quarter point only slightly smaller than that observed at the western side of the crown. This is all in keeping with earlier descriptions of the typical crack movements during the 2018–2019 monitoring period, presented in section 5.2.3, which suggests that this pattern of response has not notably changed.

Figure 8.9(a) indicates that the peak crack movements display some sensitivity to the date of recording. These trends are not uniform in all measurement locations, and gaps in the measurement data sometimes obscure their pattern (e.g., for FBGs SS3/SS4). Logging data more continuously, over a significant period of time, will help to specify these trends more precisely.

The movements at the south spandrel crack do not show clear sensitivity to the time of day and train speed, plotted in Figures 8.9(b) and 8.10(a), respectively.

In Figure 8.10(b), which presents the sensitivity of crack movements to ambient temperature, there is appreciable scatter in some subplots – particularly those which plot the crack opening displacements. This scatter obscures the precise nature of these trends. The thermal relationship for vertical displacements is more clearly linear and, although this is very flat for the response at the eastern quarter point (FBGs SS5/SS6), a clear inverse relationship is observed at the other monitoring locations on either side of the crown. Since, close to the crown, the spandrel wall is least supported by the abutments, and hence the crack may be most open, it is reasonable that thermal effects may be most pronounced over this region.

In all cases, separate trends can be seen for the two distinguishable bands of data in each subplot.

## **8.4.2 Trains on the north track**

For trains travelling on the north track, variation of peak movements with date, time of day, train speed, and ambient temperature, at the south-eastern longitudinal crack, are shown in Figures 8.11 and 8.12. The corresponding movements of the south spandrel separation crack are plotted in Figures 8.13 and 8.14.

These plots for the south-eastern crack demonstrate very similar behaviour to Figures 8.7 and 8.8 earlier, showing little difference in the absolute values of peak crack responses regardless of whether trains travel on the south or north tracks. This is in keeping with the earlier findings in Chapter 5, where it was noted that the magnitudes of peak movements at this crack were very similar, regardless of which track a train passed on, although the patterns of the displacement time histories were markedly different.

The magnitudes of peak movements at the south spandrel separation crack are, however, substantially lower when trains pass on the north track. The distributions of crack movements also follow different patterns, depending on which track a train is passing. In Figure 8.13(a), variation with date once again shows two clear bands of displacements, potentially differentiating the response to Nova 1 and Nova 3 trains. Variation of response magnitude with date is also observed in the peak vertical displacements, although not as clearly for peak crack opening displacements. In Figures 8.13(b) and 8.14(a), there are no clear trends with time of day and train speed.

Some variation with ambient temperature is observed in Figure 8.14(b) although, in contrast to earlier findings, an increase in temperature now appears to lead to larger vertical displacements. The thermal relationship at these cracks may be further complicated by the presence of the steel tie bars, which were installed as part of the 2016 repair works. Although the material properties at CFM-5 are unknown, it is likely that these steel bars may have a notably different thermal expansion coefficient to the surrounding masonry. However, since this response is to loads applied on the far side of the bridge, the magnitudes of movements are small, and the apparent change in response magnitude with temperature is very small, it may not necessarily be significant that the trends here are less clear.

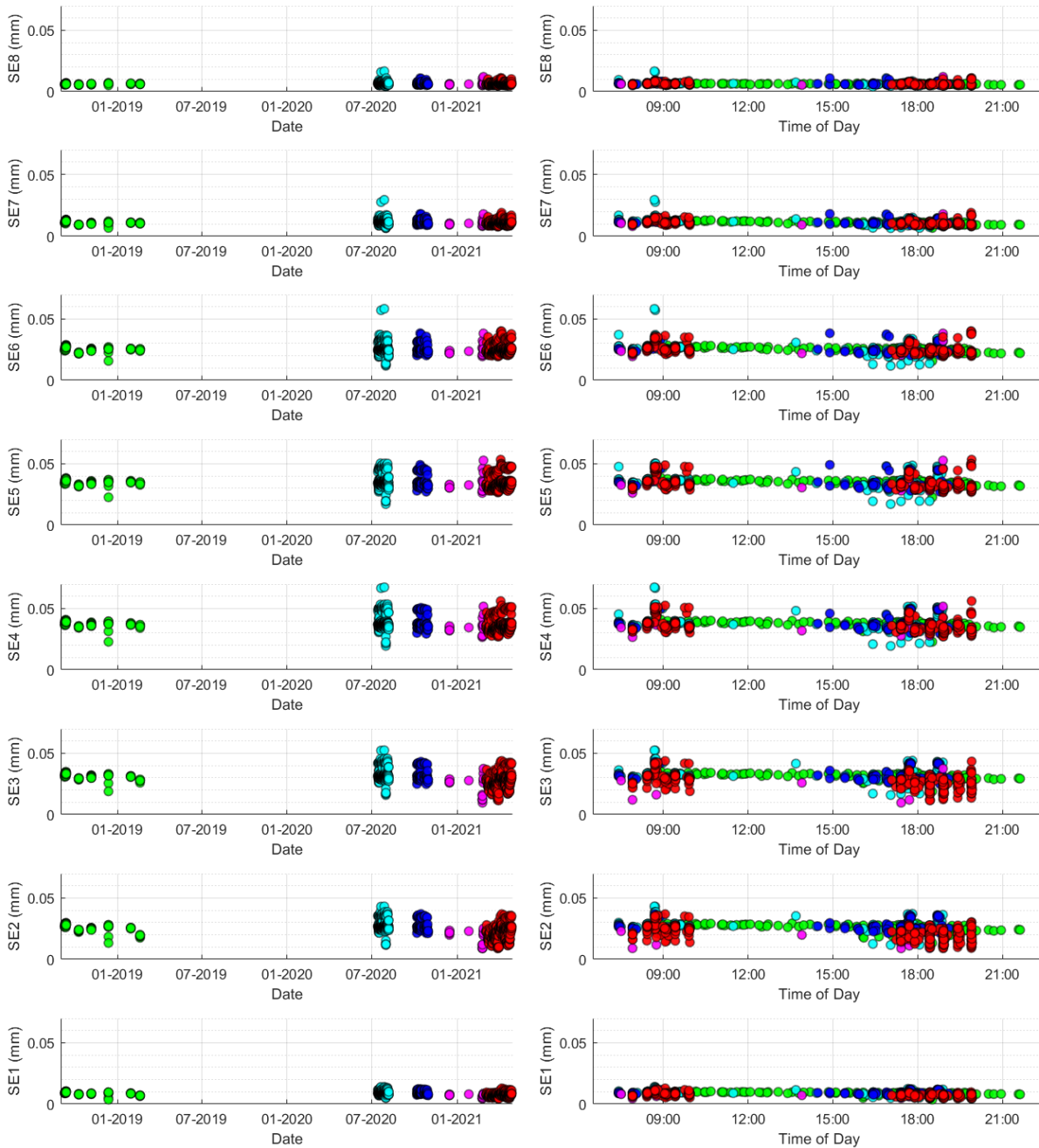


*Figure 8.11: Variation of peak dynamic movements at the south-eastern longitudinal crack with (left) date and (right) time of day, for all recorded First TransPennine trains passing on the north track*

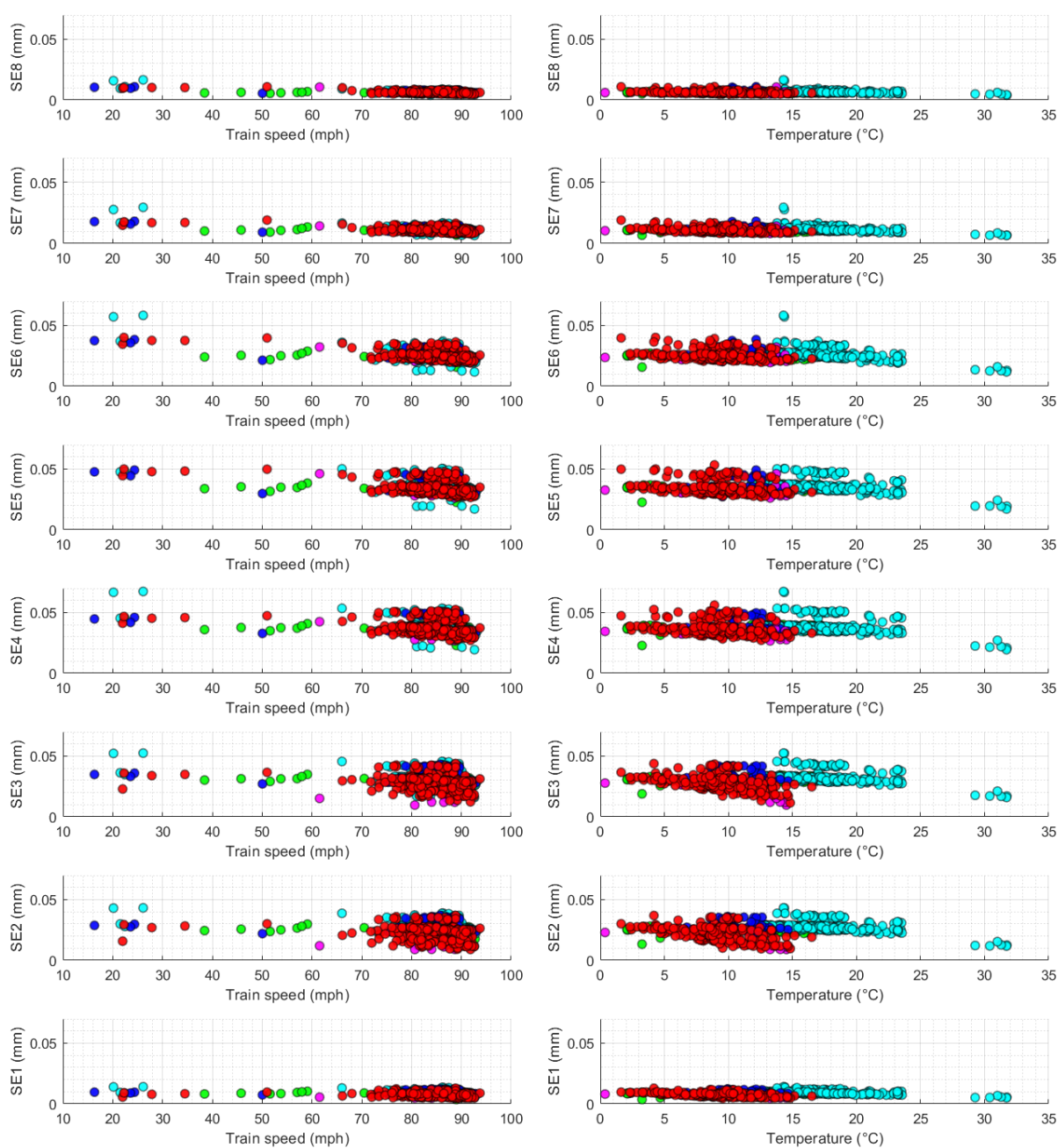


*Figure 8.12: Variation of peak dynamic movements at the south-eastern longitudinal crack with (left) train speed and (right) temperature, for all recorded First TransPennine trains passing on the north track*

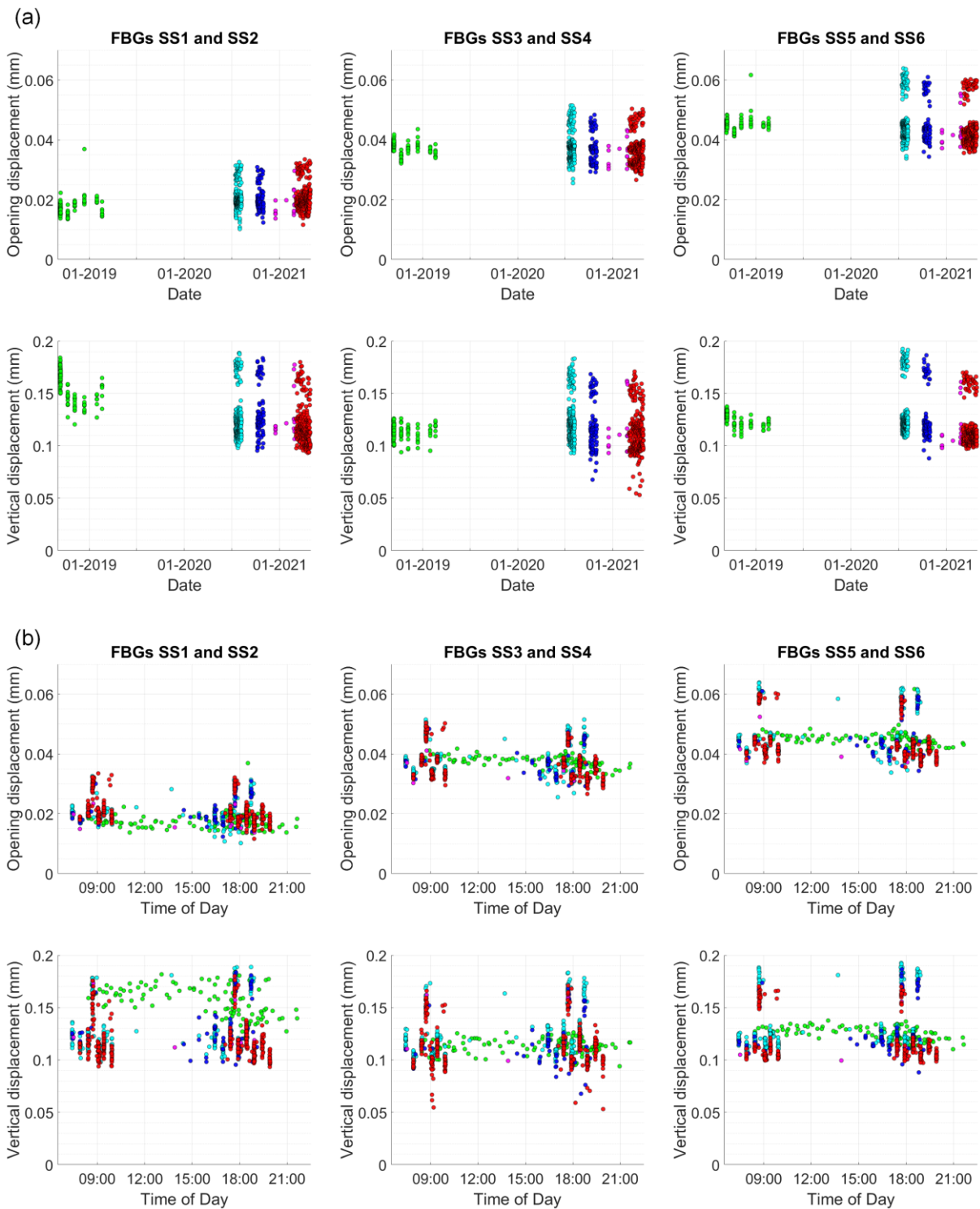
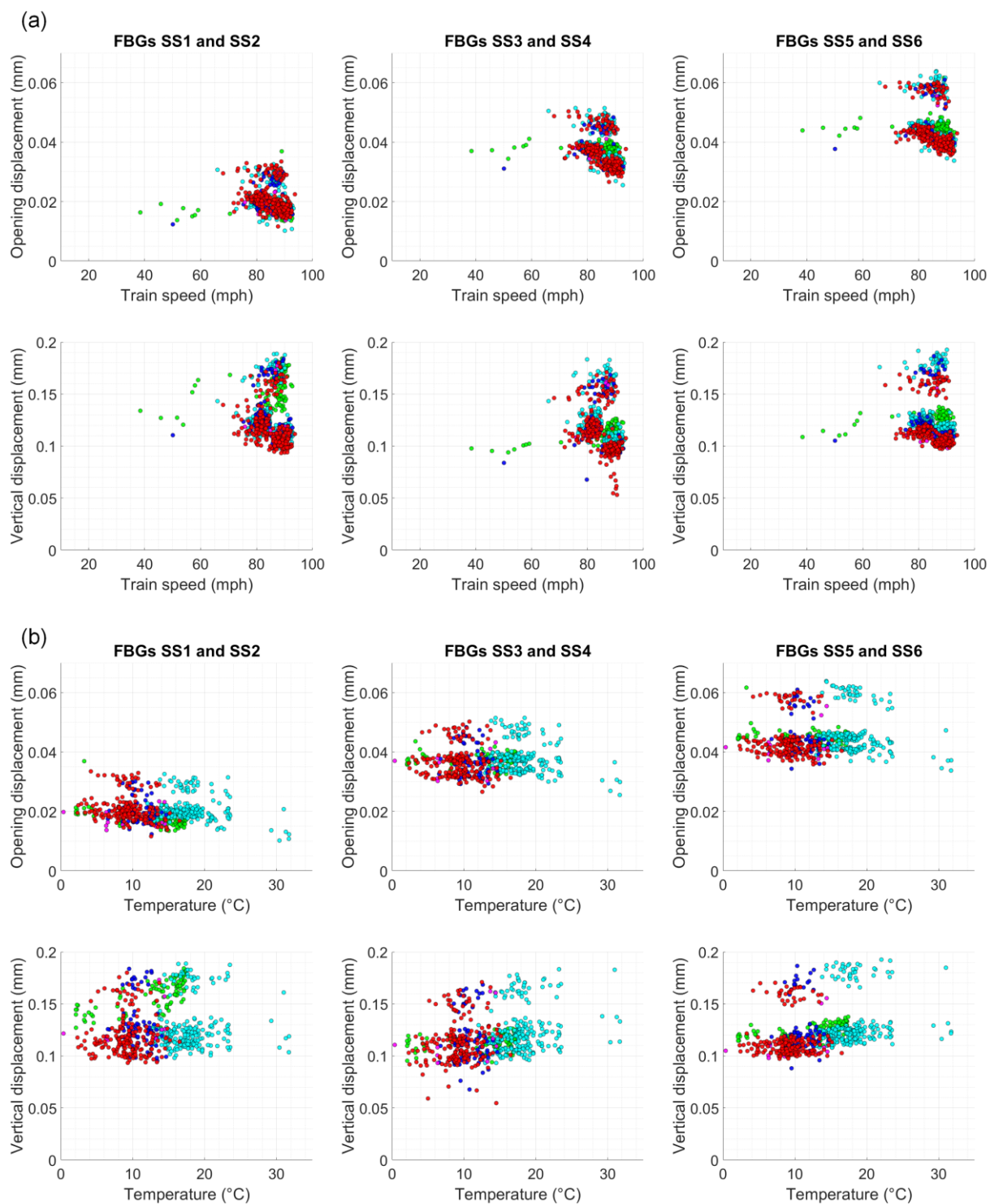


Figure 8.13: Variation of peak dynamic movements at the south spandrel separation crack with (a) date and (b) time of day, for all recorded First TransPennine trains passing on the north track



*Figure 8.14: Variation of peak dynamic movements at the south spandrel separation crack with (a) train speed and (b) temperature, for all recorded First TransPennine trains passing on the north track*

Throughout Figures 8.13 and 8.14, the distribution of crack opening displacements along the arch span is seen to be asymmetric, with higher displacements occurring towards the eastern side of the bridge – especially for FBGs SS5/SS6, at the eastern quarter point. This asymmetry could potentially be a sign of differences in behaviour between the obtuse and acute corners of the skewed arch, although it is important to note that the detailed distribution of damage along this crack is unclear. Conversely, the distribution of peak vertical displacements shows a similar magnitude of response at all three measurement locations.

## 8.5 The principal strain response in the arch

Figures 8.15 to 8.18 show the statistical distribution of the arch principal strains – measured at each FBG rosette, following the procedure outlined in Chapter 6 – when critical axle loads of all First TransPennine trains are applied, respectively, at the western third point, the western side of the arch crown, the eastern side of the crown, and the eastern third point. In each of these plots, the left and right columns of subplots show the distributions of principal strains measured for trains travelling on the north and south tracks, respectively. These are used to plot the principal strains over the full extent of the arch, by applying the symmetry assumptions put forward in Chapter 6. See Figure 6.1 for the locations of these rosettes on the arch.

These plots demonstrate that there is significant variability in the principal strain magnitudes. This was not found previously, in the analysis of Class 185 trains in Chapter 6, and the corresponding variability of all measured trains on the Northern Rail and CrossCountry routes is also notably lower (see Appendices A and B, specifically Figures A-15 to A-18 and B-15 to B-18). Because, for these other routes, train loading is consistent throughout the time periods being considered, it is very likely that the spread in principal strain magnitudes seen in Figures 8.15 to 8.18 is due to the changes in rolling stock used on the First TransPennine route. Note also that this spread is largest when axle loads are applied to the east of the arch crown (Figure 8.17); it was discussed previously, in section 6.1.2.2, that axle loads of different trains applied in this location led to the most disagreement in the generated principal strain maps.

Despite the appreciable spread in principal strain magnitudes, these figures also show that the spread of principal strain orientations is less variable, in most cases. This suggests that, despite variable strain magnitudes in response to different train types, the pattern of the flow of force through the arch remains highly similar. However, the spread increases significantly when the magnitudes of the corresponding principal strains are negligible. In these instances, the orientations carry less significance. Furthermore, the FBG measurements used to calculate these principal strains will themselves be very small, meaning that the calculation results are more

---

likely to be influenced by measurement noise. This may explain the increased spread in these principal strain orientations.

In Figure 8.19, quiver plots map the median principal strains across the arch, for each of the four load locations considered in Figures 8.15 to 8.18. These principal strain distributions are almost identical to the median principal strain distributions presented earlier, in Figure 6.8, for the 2018–2019 monitoring data alone. The only notable differences are observed when axle loads are applied to the east of the arch crown (Figure 8.19(c), c.f. Figure 6.8(c)). As already discussed, this is the load location which results in the most spread in the principal strain response. It was also noted in section 6.1.2.2 that, since the detailed distribution of damage along the north spandrel separation crack is unknown, it is possible that damage close to this location is increasing the nonlinearity of the local load distribution, and hence the variability of the response under different types of applied train loading.

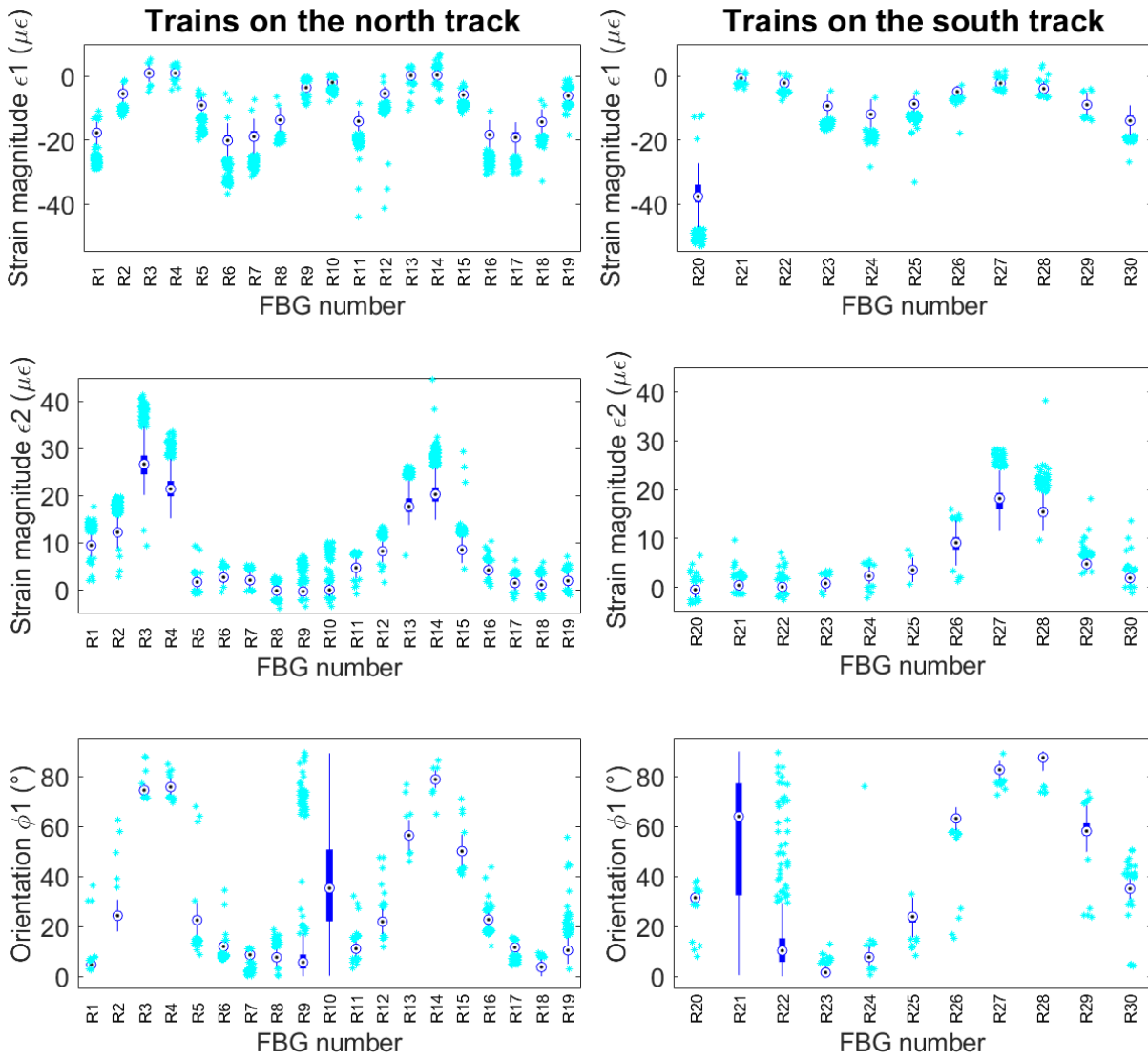


Figure 8.15: Statistical variation of the principal strain measurements for each FBG rosette location, across all First TransPennine trains, when critical axle loads are applied at the western third point

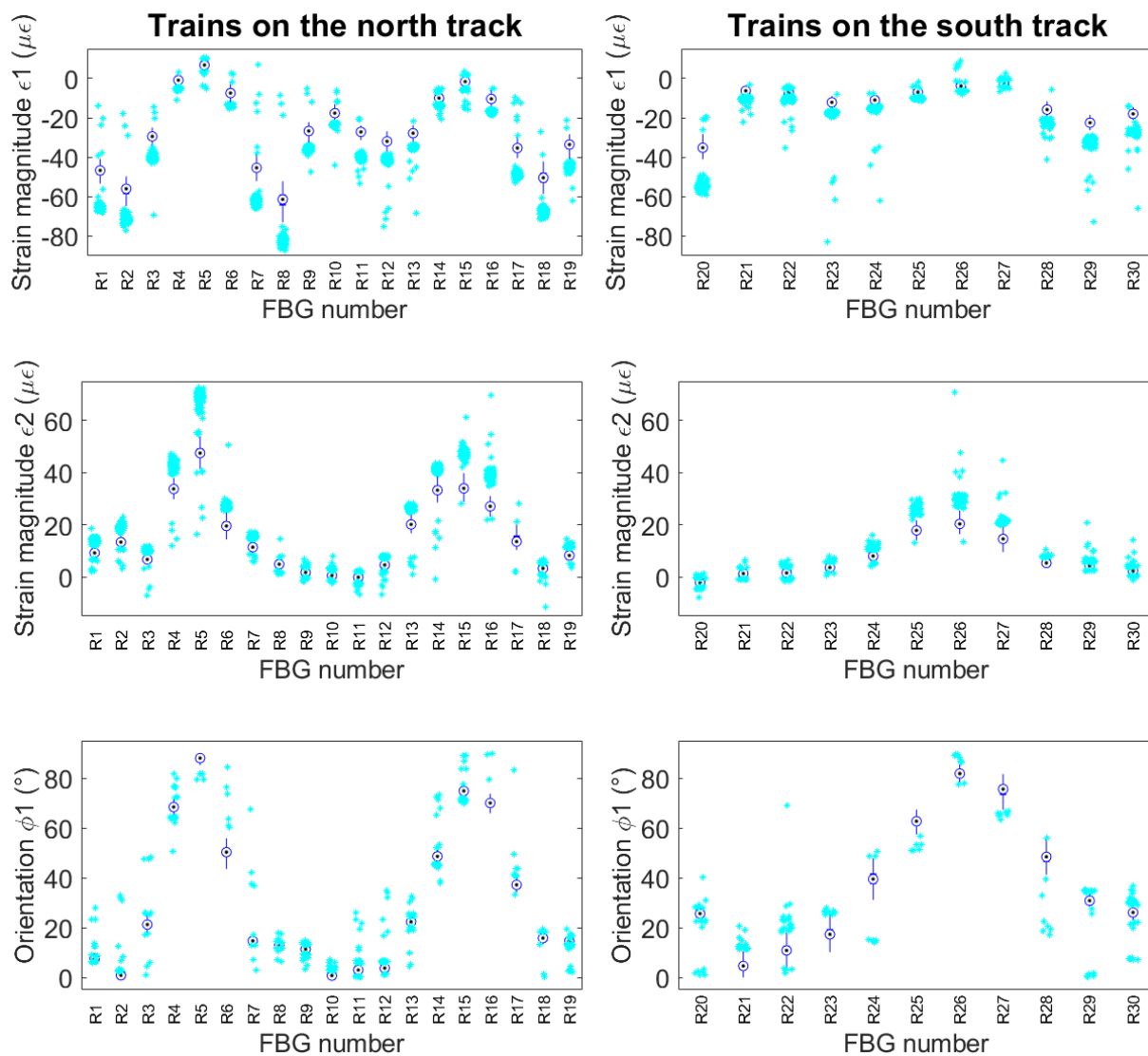


Figure 8.16: Statistical variation of the principal strain measurements for each FBG rosette location, across all First TransPennine trains, when critical axle loads are applied just west of the arch crown

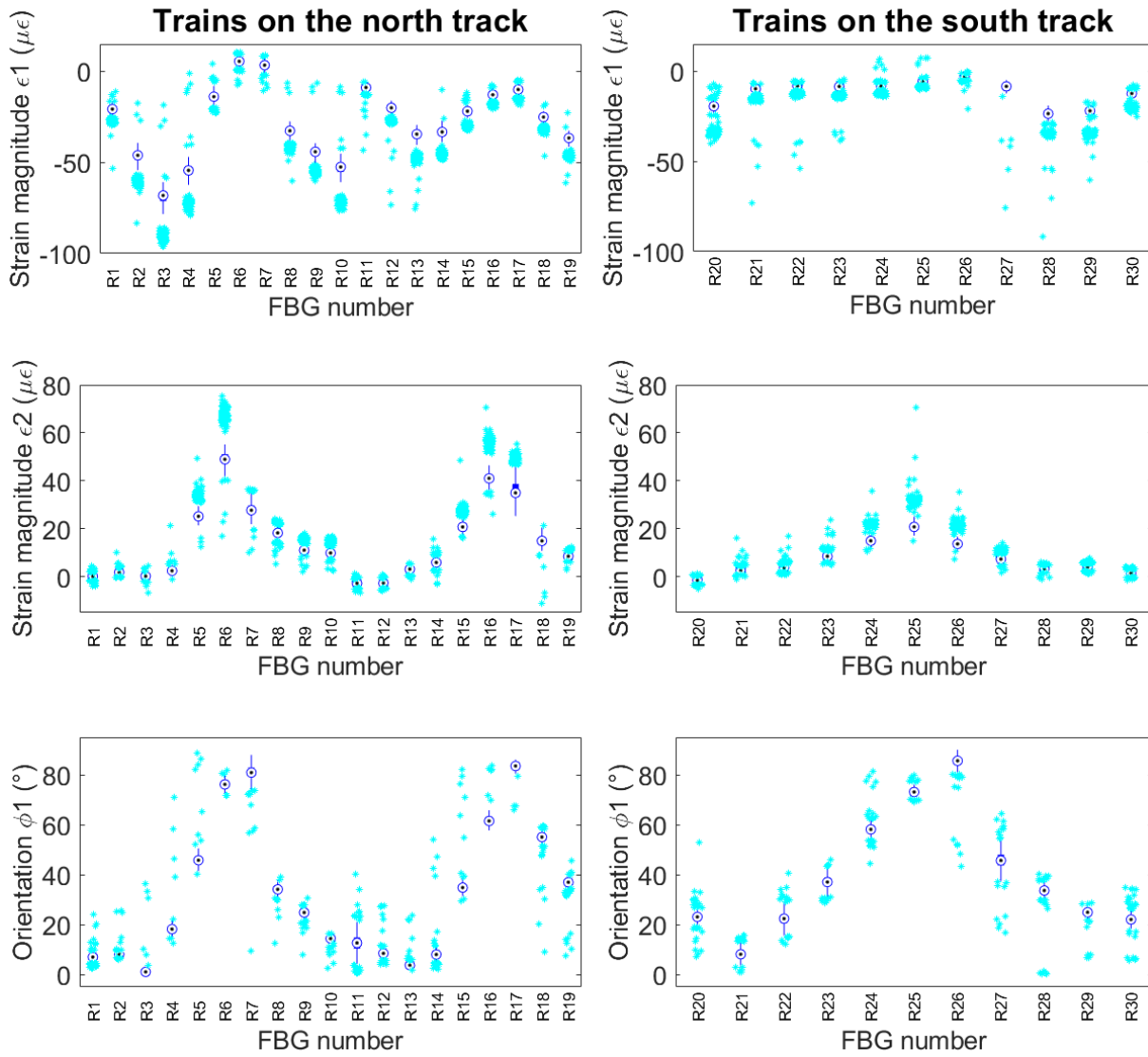


Figure 8.17: Statistical variation of the principal strain measurements for each FBG rosette location, across all First TransPennine trains, when critical axle loads are applied just east of the arch crown

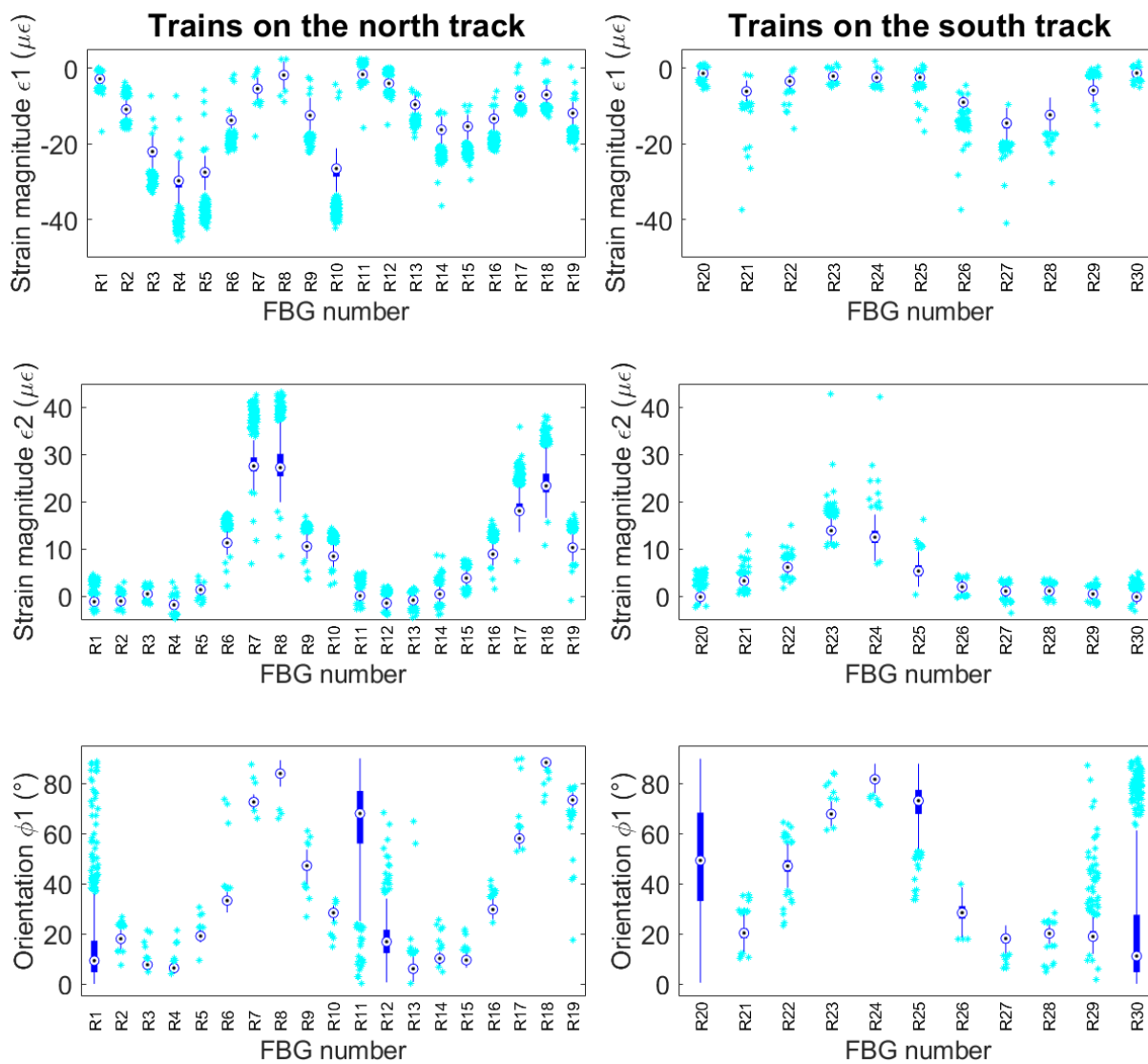


Figure 8.18: Statistical variation of the principal strain measurements for each FBG rosette location, across all First TransPennine trains, when critical axle loads are applied at the eastern third point

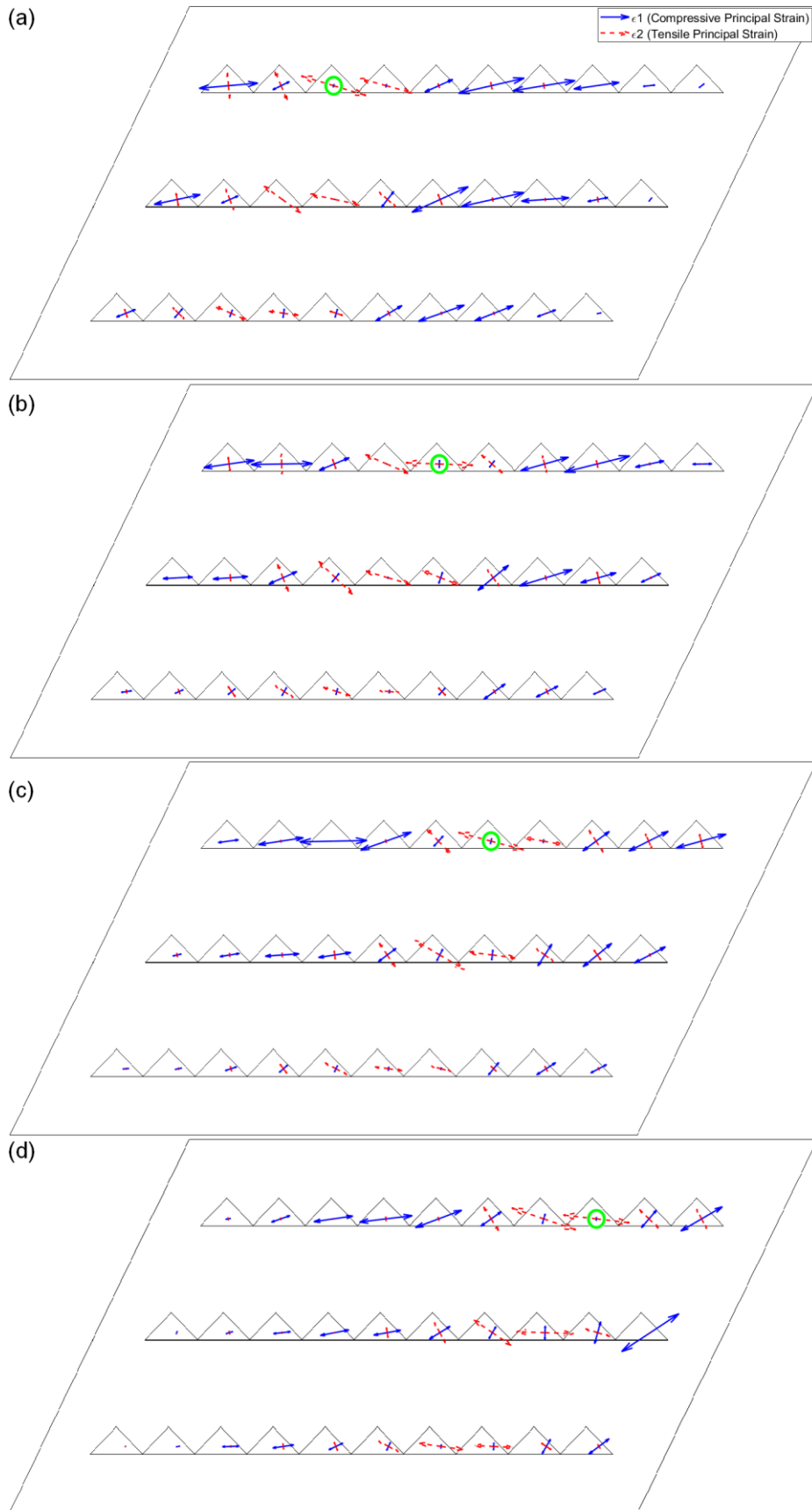


Figure 8.19: Quiver plots showing the median principal strain response in the arch, across all First TransPennine trains, when critical axle loads are applied (a) at the western third point, (b) just west of the crown, (c) just east of the crown, and (d) at the eastern third point

## 8.6 Conclusions

In this chapter, all FBG data recorded between September 2018 and the end of April 2021, which corresponds to First TransPennine Express passenger trains, has been analysed.

It was observed that the spread of magnitudes in the strain and crack movement responses, relative to that observed in earlier chapters, was increased. In those chapters, all recorded First TransPennine services used Class 185 trains, whereas new Nova 1 and Nova 3 trains have replaced these since summer 2020. It is believed that the change in train loading is the primary factor behind this increase in the spread of the peak measurement magnitudes.

The sensitivity of the peak responses to the time of day and train speed, which was clearly observed for the 2018–2019 Class 185 trains, could not be seen in the newer data. In the former instance, this is due to the decision to only monitor new trains during peak commute times. The few trains which were accidentally recorded outside of these times are insufficient to capture the full time-of-day trend, and it is likely that this trend has been significantly altered by changes in passenger behaviour during the COVID-19 pandemic. Similarly, the sensitivity to train speed cannot be clearly discerned because the newer data contain very few slow trains.

However, new trends have been identified capturing the sensitivity of the response to ambient temperature, beyond that observed in earlier chapters. In general, these trends show an inverse correlation between response magnitude and ambient temperature, which is consistent with earlier results and the findings of other researchers. Capturing further data, particularly at higher ambient temperatures, will allow these relationships to be accurately quantified in future work.

Trends have also been observed that link the bridge response to the date of recording, among the newer data, whereas the response was previously observed to be very consistent throughout six months of monitoring between September 2018 and February 2019. These trends are obscured by occasional gaps in the new data, logged between July 2020 and April 2021, at times when power issues meant that the FBG monitoring system was unexpectedly offline. Further long-term data will be recorded, to better specify these trends in future work.

Lastly, principal strain data were analysed for this combined data set. It was observed that, although the principal strain magnitudes were variable – likely due to the range of train types within this data set – the orientations of the principal strains were generally consistent. This suggests a high degree of commonality in the behaviour of the bridge, under variable train loading.



## **Part 4**

### **Conclusions**



# Chapter 9

## Conclusions

### 9.1 Summary of main findings

The main objectives of this thesis, as presented in section 1.2, address a number of pressing concerns related to the structural performance of masonry arch bridges, under applied train loading. Overarching themes of the work have included (1) simplified modelling of the SLS behaviour of masonry arch rail bridges and viaducts, (2) detailed, distributed monitoring of dynamic SLS behaviour, and (3) the behaviour of skewed masonry arch bridges in particular. A significant proportion of this thesis has been devoted to the acquisition and analysis of monitoring data which captures the SLS response of a case study skewed masonry arch railway bridge. Throughout this work, a number of innovations have been developed which relate to the monitoring itself – particularly novel implementations for distributed fibre optic FBG sensing – and a range of techniques have been applied to process, visualise, and interpret the detailed monitoring data.

The main findings are as follows:

- *Simplified finite element modelling*: A range of linear elastic, finite element models were constructed, as estimates of the pre-damaged state of a masonry railway viaduct, and modelling output was compared with FBG monitoring data of the response of the real, damaged viaduct. Through this study, relative contributions of the various structural components towards the overall stiffness of the viaduct, in SLS conditions, were quantified. Furthermore, the minimum structural components that must be included in the model, in order for it to yield physically acceptable behaviour, were identified. Agreement, between the patterns of model output and the monitored response, was observed for common ‘global’ arch measurements – such as the vertical crown

displacements and pier-to-pier span opening displacements – but it was found that damage in the viaduct caused local differences in the strain response. This highlights the localised influence of damage on masonry arch bridge behaviour and suggests that distributed monitoring – as opposed to single point, ‘global’ monitoring – may be better able to identify the onset and progression of damage. In particular, measurements at the third or quarter points of the span may be more illuminating than measurements taken at the arch crown, as these locations tend to be close to the point of both (1) maximum peak-to-peak response, under the asymmetric loading case, and (2) a step change in local stiffness, for bridges built with internal rigid backing above the arch haunches, which may lead to damage developing in this region of the bridge.

- *Implementations of FBG monitoring:* Two novel approaches of FBG monitoring were developed over the course of this project, allowing this technology to be used to measure (1) the average generalised strain state and hence the principal strains and flow of force, through an ‘FBG strain rosette’ implementation, and (2) out-of-plane shearing behaviour across cracked interfaces, as well as in-plane crack opening, through an ‘FBG pair’ implementation. These innovations extended the range of structural behaviour that could be monitored at the case study structure using FBGs.
- *Sensitivity of the bridge response to external variables:* By monitoring over many train events, in a range of conditions, the sensitivity of the bridge response to a number of external factors has been investigated:
  - *Time of day:* Passenger levels, and hence the precise loading applied by trains, is found to vary throughout the day with two consistent peaks occurring for morning and evening commute times, in normal conditions. The spread of strain magnitudes also reduces during these peaks, suggesting that loading is most consistent at these times. Based on these findings, it is proposed that time-of-day can be used as a proxy for passenger loading, as a simplified way to normalise for train loading between different monitoring periods.
  - *Train speed:* For the monitoring data gathered between 2018 and 2019, which covered a range of train speeds, an increase in strain magnitude is observed close to the arch crown, where fill depth is lowest and there is therefore the least potential for distribution before loads are applied to the arch. This effect is localised, only affecting measurements close to the arch crown, and modest in size. The maximum ‘dynamic amplification’ is observed to be 15%, for trains travelling between approximately 80 and 90 mph. This is in contrast to the dynamic load factor of 1.8 stated in current Network Rail guidance. However,

---

more data for slower trains will be needed in order for this effect to be fully characterised. Note that, in more recent monitoring, insufficient data are available for slow trains and this effect cannot be discerned.

- *Temperature*: Long-term monitoring has captured the bridge response over a reasonable range of ambient temperatures, although more data are required in hot conditions, and suggests that, in most locations, there is an inverse linear relationship between temperature and the response magnitude. Thermal contraction contributes to the opening of cracks throughout the masonry, and hence increases the potential for movements to occur during the response to applied loads.
- *Date*: Recent monitoring data suggest the existence of long-term trends in the response. These may be related to the thermal effect noted above; however, clustering in the data from different time periods also suggests a slightly different thermal effect for each of these periods. These trends are further obscured by gaps in the data, at times when the monitoring system was unexpectedly offline. More data will be gathered on this response as part of future work.
- *Visualisation of the flow of force through a skewed masonry arch bridge*: Using the FBG strain rosette described above and assuming rotational symmetry in the arch response, which has been validated in this thesis, the distributed in-plane flow of force through a skewed masonry arch bridge, in response to applied train loading, has been mapped for the first time. A highly consistent pattern of principal strains has been found, across many monitored train events, suggesting common behaviour under different types of train loading. This response includes both an expected longitudinal arching action, aligned in the skewed span direction, as well as a secondary transverse response.
- *Videogrammetry monitoring of the vertical, out-of-plane response*: In addition to measuring the vertical shearing displacements at the south spandrel crack with FBGs, videogrammetry has been used to ascertain the distributed profile of vertical displacements along the crown line. Despite initial issues with noise in these measurements, primarily caused by environmental effects, it has been possible to process videogrammetry data to yield peak-to-peak vertical displacements at a series of measurement targets installed on the arch soffit. Statistical spread in this data does not obscure the pattern of dynamic deformation along the crown line, which has been used to fit simplified beam models of the transverse bending response.

- *Investigation of historic arch deformations:* Through collaboration to extend existing laser scan analysis methods for masonry arch bridges (Ye et al., 2018) to the special case of skewed masonry arches, point cloud geometry data for the case study bridge have been leveraged to investigate the long-term deformations of this structure. The findings suggest that historic support settlements most likely gave rise to a deformation mechanism aligned with the square span direction of the arch. This is consistent with the hypothesis, put forward by other researchers (Harvey, 2004), that, although spanning square may initially be a preferable load path for skewed masonry arches, this could give rise to significant thrusts in the obtuse corners, and that movements at these supports may only need to be small before spanning skew offers a preferable alternative response.

## 9.2 Scientific contributions

Detailed, distributed monitoring has led to a number of important conclusions regarding the behaviour of skewed masonry arch bridges. The trends identified between the dynamic strain response and time-of-day, train speed, and ambient temperature may be of particular relevance to engineers studying and working with these structures. The extension of laser scan analysis techniques to study the historic deformations of the skewed case study bridge also led to useful conclusions, regarding its possible past behaviour, and may be similarly useful in gaining insights into other skewed masonry bridges.

The significant data sets, which have been recorded over the two stages of FBG monitoring, provide a useful resource for studying the behaviour of a typical skewed masonry arch bridge. Through further long-term, autonomous FBG sensing, this data set will continue to grow in size over time, offering significant potential for future research.

The novel FBG implementations, developed in this project, have the potential to be used to monitor many other kinds of structure. In particular, this thesis contains the first known use of structural-scale FBG strain rosettes for dynamic monitoring. This approach, which allows synchronised, distributed measurements of principal strains to be obtained, at many points across a structure, could have significant future applications. It has been demonstrated that the FBGs are sensitive enough to capture very small magnitudes of response, and the repeatability offered by this technology means that trends can be accurately measured, over sufficiently large data sets, even when the resultant changes in behaviour are small. This also allows for statistically significant changes in the response to be clearly identified, which could be leveraged in the development of early-warning structural alert systems.

---

Improvements in the monitoring and processing strategies for videogrammetry field monitoring, described in this thesis, have allowed for meaningful displacement data to be gathered for the case study structure. This has been particularly useful in characterising the vertical, out-of-plane behaviour of the skewed arch and has been used to put forward simplified models describing its transverse response. Since videogrammetry is known to be particularly sensitive to environmental effects, which can easily compromise the quality of measurements, these strategies may allow this technology to be put to better use in future studies.

### **9.3 Practical applications**

Many of the motivating factors, behind the monitoring of the case study bridge in this thesis, are practical asset management concerns. The need to identify alternatives to the current Network Rail approach of deflection pole monitoring – which may be expensive and disruptive in certain settings – has led to a comparative evaluation of many different monitoring technologies at this bridge, in collaboration with AECOM. A number of the remote sensing technologies trialled in this project are likely to have applications in future monitoring work.

This project has proved the effectiveness of FBG sensing as a distributed, remote monitoring technology for masonry arch bridges. The strategies developed to facilitate autonomous data acquisition and transfer, as well as automated data categorisation, processing, analysis, and visualisation, can be readily applied in other projects. The repeatability and accuracy of FBG measurements, discussed in the previous section, make it possible to detect the early onset and progression of damage, which is of particular interest to asset managers.

In order for this potential to be realised, improvements in data visualisation will be needed, so that rich FBG data sets can be digested and interpreted by asset managers in a comparable timeframe to current, single-point monitoring data. Approaches used in this thesis, such as the statistical summaries and quiver plot maps of principal strain distributions, across the full extent of the skewed arch, demonstrate that this is possible.

Separately, the findings of the finite element modelling study are of practical relevance, as it is more likely that simplified analyses such as this will be used in industry, where more complex approaches may be prohibitively time intensive. The conclusion that, below a certain level of structural detail, the models could not produce physically permissible results is of particular importance. Furthermore, the relative contributions towards the global stiffness, that have been identified to result from each structural component in SLS conditions, highlight the potential consequences of progressive damage at these bridges and attest to the importance of sensitive

intervention work, which seeks to restore connectivity where possible, without introducing stiffness gradients which may unintentionally lead to further damage.

## 9.4 Future work

While the monitoring in this thesis has already led to useful insights, as described above, it has also opened up possible avenues for future work, as follows:

- *Further monitoring at the case study bridge:* As mentioned previously, the acquisition of further data – especially in certain conditions, such as high ambient temperatures, and slow train speeds – will allow the trends, some of which have only been identified qualitatively at this stage, to be properly quantified. Growing the data set, through further autonomous FBG sensing, will also increase its capability to be used in conjunction with more complex data analysis techniques.
- *Monitoring of additional structures:* It will be important to validate the conclusions of the monitoring work at the case study bridge, by investigating the behaviour of other masonry arch bridges and viaducts. The technological implementations and data processing strategies developed in this thesis are readily extendable to other structures. In particular, it would be illuminating to study the response of structures with varying skew angles, as well as multi-span skewed bridges and viaducts.
- *Multi-variate data analysis/machine learning:* Data analysis and interpretation in this thesis have clearly identified that the bridge response is sensitive to multiple external variables. While attempts have been made to control the effects of some variables while others are investigated, this reduces the size of the data subset available to study any one variable. Furthermore, there is a realistic possibility that residual effects of the controlled variables will persist and influence the analysis results. To address this, more advanced analytical techniques such as multi-variate statistics and machine learning will be investigated.
- *Computational modelling of the case study bridge:* Because of the focus on detailed, distributed monitoring of the case study bridge, it has not been possible to perform computational modelling of this structure as part of this thesis. Modelling can play an important role in either validating or disproving the various hypotheses discussed during interpretation of the monitoring data. This will form a key part of future work.





# References

- Acikgoz, S., Alexakis, H., Ye, C., Franza, A., and DeJong, M. (2019a). The Marsh Lane Railway Viaduct: 2 Years of Monitoring with Combined Sensing and Surveying Technologies. In *Proceedings of ARCH 2019, the 9<sup>th</sup> International Conference on Arch Bridges*, Porto, Portugal. 422-429. [https://doi.org/10.1007/978-3-030-29227-0\\_44](https://doi.org/10.1007/978-3-030-29227-0_44).
- Acikgoz, S., DeJong, M. J., Kechavarzi, C., and Soga, K. (2018a). Dynamic response of a damaged masonry rail viaduct: Measurement and interpretation. *Engineering Structures*, 168(Aug):544–558. <https://doi.org/10.1016/j.engstruct.2018.04.054>.
- Acikgoz, S., DeJong, M. J., and Soga, K. (2018b). Sensing dynamic displacements in masonry rail bridges using 2D digital image correlation. *Structural Control & Health Monitoring*, 25(8):e2187. <https://doi.org/10.1002/stc.2187>.
- Acikgoz, S., Franza, A., DeJong, M. J., and Mair, R. J. (2019b). Tunnelling Under A Heritage Structure: Distributed Sensing Data and Cracked Equivalent Beam Models. In *Proceedings of ICSIC 2019, the International Conference on Smart Infrastructure and Construction 2019*, Cambridge, UK. <https://doi.org/10.1680/icsic.64669.675>.
- Acikgoz, S., Franza, A., DeJong, M. J., and Mair, R. (2021). Cracked Equivalent Beam Models for Assessing Tunneling-Induced Damage in Masonry Buildings. *Journal of Geotechnical and Geoenvironmental Engineering*, 147(2):04020167. [https://doi.org/10.1061/\(ASCE\)GT.1943-5606.0002443](https://doi.org/10.1061/(ASCE)GT.1943-5606.0002443).
- Aita, D., Barsotti, R., and Bennati, S. (2017a). Explicit solutions for depressed masonry arches loaded until collapse—Part I: a one-dimensional nonlinear elastic model. *Meccanica*, 52:989–1001. <https://doi.org/10.1007/s11012-016-0420-4>.
- Aita, D., Barsotti, R., and Bennati, S. (2017b). Explicit solutions for depressed masonry arches loaded until collapse—Part II: a solution method for statically indeterminate systems. *Meccanica*, 52:1093–1106. <https://doi.org/10.1007/s11012-016-0440-0>.
- Alexakis, H., Franza, A., Acikgoz, S., and DeJong, M. J. (2019a). A multi-sensing monitoring system to study deterioration of a railway bridge. In *Proceedings of SHMII-9, the 9<sup>th</sup> International Conference on Structural Health Monitoring of Intelligent Infrastructure*, St. Louis, MO, USA.
- Alexakis, H., Franza, A., Acikgoz, S., and DeJong, M. J. (2019b). Monitoring bridge degradation using dynamic strain, acoustic emission and environmental data. In *Proceedings of ICSIC 2019, the International Conference on Smart Infrastructure and Construction 2019*, Cambridge, UK. <https://doi.org/10.1680/icsic.64669.523>.

- Alexakis, H., Lau, F.D.H., and DeJong, M. (2021). Fibre optic sensing of ageing railway infrastructure enhanced with statistical shape analysis. *Journal of Civil Structural Health Monitoring*, 11:49–67. <https://doi.org/10.1007/s13349-020-00437-w>.
- Alexakis, H., Liu, H., and DeJong, M. J. (2020). Damage identification of brick masonry under cyclic loading based on acoustic emissions. *Engineering Structures*, 221:110945. <https://doi.org/10.1016/j.engstruct.2020.110945>.
- Arêde, A., Costa, C., Silva, R., Gomes, A. T., and Menezes, J. E. (2016). Experimental Characterization of the Structural Behaviour of Stone Arch Railway Bridges. In *Proceedings of ARCH'16, the 8<sup>th</sup> International Conference on Arch Bridges*, Wrocław, Poland. 741–750.
- Armstrong, D. M., Sibbald, A., Fairfield, C. A., and Forde, M.C. (1995a). Modal analysis for masonry arch bridge spandrell wall separation identification. *NDT & E International*, 28(6):377–386. [https://doi.org/10.1016/0963-8695\(95\)00048-8](https://doi.org/10.1016/0963-8695(95)00048-8).
- Armstrong, D. M., Sibbald, A., and Forde, M. C. (1995b). Integrity assessment of masonry arch bridges using the dynamic stiffness technique. *NDT & E International*. 28(6):367–375. [https://doi.org/10.1016/0963-8695\(95\)00047-X](https://doi.org/10.1016/0963-8695(95)00047-X).
- Augenti, N., Acconcia, E., and Parisi. F. (2012). MADA: Masonry Database. Accessed August 1, 2017. [http://www.reluis.it/index.php?option=com\\_mada&Itemid=160](http://www.reluis.it/index.php?option=com_mada&Itemid=160).
- Augusthus-Nelson, L., Swift, G., Smith, C., Gilbert, M., and Melbourne, C. (2016). Behaviour of backfilled masonry arch bridges subjected to cyclic loading. In *Proceedings of ARCH'16, the 8<sup>th</sup> International Conference on Arch Bridges*, Wrocław, Poland. 1039–1048.
- Barsotti, R., and Bennati, S. (2017). A simple and effective nonlinear elastic one-dimensional model for the structural analysis of masonry arches. *Meccanica*, 53:1899–1915. <https://doi.org/10.1007/s11012-017-0711-4>.
- Bayraktar, A., Türker, T., and Altunisik, A. C. (2015). Experimental frequencies and damping ratios for historical masonry arch bridges. *Construction and Building Materials*, 75:234–241. <https://doi.org/10.1016/j.conbuildmat.2014.10.044>.
- Bergamo, O., Campione, G., Donadello, S., and Russo, G. (2015). In-situ NDT testing procedure as an integral part of failure analysis of historical masonry arch bridges. *Engineering Failure Analysis*, 57:31–55. <https://doi.org/10.1016/j.engfailanal.2015.07.019>.
- Boothby, T. E. (1997). Elastic plastic stability of jointed masonry arches. *Engineering Structures*, 19(5):345–351. [https://doi.org/10.1016/S0141-0296\(96\)00092-2](https://doi.org/10.1016/S0141-0296(96)00092-2).
- Boothby, T. E. (2001). Load Rating of Masonry Arch Bridges. *Journal of Bridge Engineering*, 6(2):79–86. [https://doi.org/10.1061/\(ASCE\)1084-0702\(2001\)6:2\(79\)](https://doi.org/10.1061/(ASCE)1084-0702(2001)6:2(79)).
- Boothby, T. E., Domalik, D. E., and Dalal, V. A. (1998). Service load response of masonry arch bridges. *Journal of Structural Engineering*, 124(Jan):17–23. [https://doi.org/10.1061/\(ASCE\)0733-9445\(1998\)124:1\(17\)](https://doi.org/10.1061/(ASCE)0733-9445(1998)124:1(17)).

- Boothby, T. E., and Fanning, P. J. (2004). Load Rating of Masonry Arch Bridges: Refinements. *Journal of Bridge Engineering*, 9(3):304–307. [https://doi.org/10.1061/\(ASCE\)1084-0702\(2004\)9:3\(304\)](https://doi.org/10.1061/(ASCE)1084-0702(2004)9:3(304)).
- Brencich, A., Cassini, G., and Pera, D. (2016). Load bearing structure of masonry bridges. In *Proceedings of ARCH'16, the 8<sup>th</sup> International Conference on Arch Bridges*, Wrocław, Poland. 767–774.
- Brencich, A., and De Francesco, U. (2004a). Assessment of Multispan Masonry Arch Bridges. I: Simplified Approach. *Journal of Bridge Engineering*, 9(6):582–590. [https://doi.org/10.1061/\(ASCE\)1084-0702\(2004\)9:6\(582\)](https://doi.org/10.1061/(ASCE)1084-0702(2004)9:6(582)).
- Brencich, A., and De Francesco, U. (2004b). Assessment of Multispan Masonry Arch Bridges. II: Examples and Applications. *Journal of Bridge Engineering*, 9(6):591–598. [https://doi.org/10.1061/\(ASCE\)1084-0702\(2004\)9:6\(591\)](https://doi.org/10.1061/(ASCE)1084-0702(2004)9:6(591)).
- Brencich, A., De Francesco, U., Gilbert, M., Melbourne, C., and Smith, C. (2006). Discussion of and Closure to “Assessment of Multispan Masonry Arch Bridges. I: Simplified Approach.” *Journal of Bridge Engineering*, 11(2):257–261. [https://doi.org/10.1061/\(ASCE\)1084-0702\(2006\)11:2\(259\)](https://doi.org/10.1061/(ASCE)1084-0702(2006)11:2(259)).
- Brencich, A., and Morbiducci, R. (2007). Masonry arches: Historical rules and modern mechanics. *International Journal of Architectural Heritage*, 1(2):165–189. <https://doi.org/10.1080/15583050701312926>.
- Brencich, A., and Riotto, G. (2016a). Vault-fill interaction in masonry bridges: an experimental approach - 1: statics. In *Proceedings of ARCH'16, the 8<sup>th</sup> International Conference on Arch Bridges*, Wrocław, Poland. 711–720.
- Brencich, A., and Riotto, G. (2016b). Vault-fill interaction in masonry bridges: an experimental approach - 2: dynamics. In *Proceedings of ARCH'16, the 8<sup>th</sup> International Conference on Arch Bridges*, Wrocław, Poland. 721–730.
- Brencich, A., and Sabia, D. (2008). Experimental identification of a multi-span masonry bridge: The Tanaro Bridge. *Construction and Building Materials*, 22(10):2087–2099. <https://doi.org/10.1016/j.conbuildmat.2007.07.031>.
- Brückl, E., Brunner, F. K., Lang, E., Mertl, S., Müller, M., and Sary, U. (2013). The Gradenbach Observatory – monitoring deep-seated gravitational slope deformation by geodetic, hydrological, and seismological methods. *Landslides*, 10:815–829. <https://doi.org/10.1007/s10346-013-0417-1>.
- Carr, A. J., Jáuregui, D. V., Riveiro, B., Arias, P., and Armesto, J. (2013). Structural evaluation of historic masonry arch bridges based on first hinge formation. *Construction and Building Materials*, 47:569–578. <https://doi.org/10.1016/j.conbuildmat.2013.05.084>.
- Cavicchi, A., and Gambarotta, L. (2007). Lower bound limit analysis of masonry bridges including arch-fill interaction. *Engineering Structures*, 29(11):3002–3014. <https://doi.org/10.1016/j.engstruct.2007.01.028>.
- Cazzani, A., Malagù, M., and Turco, E. (2016). Isogeometric analysis: a powerful numerical tool for the elastic analysis of historical masonry arches. *Continuum Mechanics and Thermodynamics*, 28:139–156. <https://doi.org/10.1007/s00161-014-0409-y>.

- CEN. (2003). *EN 1991-2:2003 Eurocode 1: Actions on structures – Part 2: Traffic loads on bridges*. Comité Européen de Normalisation, Brussels, Belgium.
- Chiozzi, A., Malagù, M., Tralli, A., and Cazzani, A. (2016). ArchNURBS: NURBS-Based Tool for the Structural Safety Assessment of Masonry Arches in MATLAB. *Journal of Computing in Civil Engineering*, 30:(2). [https://doi.org/10.1061/\(ASCE\)CP.1943-5487.0000481](https://doi.org/10.1061/(ASCE)CP.1943-5487.0000481).
- Clemente, P., Occhiuzzi, A., and Raithel, A. (1995). Limit Behaviour of Stone Arch Bridges. *Journal of Structural Engineering*, 121(7):1045–1050. [https://doi.org/10.1061/\(ASCE\)0733-9445\(1995\)121:7\(1045\)](https://doi.org/10.1061/(ASCE)0733-9445(1995)121:7(1045)).
- Costa, C., Arêde, A., Morais, M., and Aníbal, A. (2015). Detailed FE and DE modelling of stone masonry arch bridges for the assessment of load-carrying capacity. *Procedia Engineering*, 114:854–861. <https://doi.org/10.1016/j.proeng.2015.08.039>.
- DeJong, M. J., and Vibert, C. (2012). Seismic response of stone masonry spires: Computational and experimental modeling. *Engineering Structures*, 40(Jul):566–574. <https://doi.org/10.1016/j.engstruct.2012.03.001>.
- Dimitri, R., and Tornabene, F. (2015). A parametric investigation of the seismic capacity for masonry arches and portals of different shapes. *Engineering Failure Analysis*, 52:1–34. <https://doi.org/10.1016/j.engfailanal.2015.02.021>.
- Domede, N., Sellier, A., and Stablon, T. (2013). Structural analysis of a multi-span railway masonry bridge combining in situ observations, laboratory tests and damage modelling. *Engineering Structures*, 56(Nov):837–849. <https://doi.org/10.1016/j.engstruct.2013.05.052>.
- Eucentre. (1987). *Italian seismic design code (OPCM 3274/03 and further modifications)*. Eucentre, Pavia, Italy.
- Fanning, P. J., and Boothby, T. E. (2001). Three-dimensional modelling and full-scale testing of stone arch bridges. *Computers & Structures*, 79(29–30):2645–2662. [https://doi.org/10.1016/S0045-7949\(01\)00109-2](https://doi.org/10.1016/S0045-7949(01)00109-2).
- Fanning, P. J., Boothby, T. E., and Roberts, B. J. (2001). Longitudinal and transverse effects in masonry arch assessment. *Construction and Building Materials*, 15(1):51–60. [https://doi.org/10.1016/S0950-0618\(00\)00069-6](https://doi.org/10.1016/S0950-0618(00)00069-6).
- de Felice, G. (2009). Assessment of the load-carrying capacity of multi-span masonry arch bridges using fibre beam elements. *Engineering Structures*, 31(8):1634–1647. <https://doi.org/10.1016/j.engstruct.2009.02.022>.
- Forgács, T., Rendes, S., Adany, S., and Sarhosis, V. (2019b). Mechanical Role of Spandrel Walls on the Capacity of Masonry Arch Bridges. In *Proceedings of ARCH 2019, the 9<sup>th</sup> International Conference on Arch Bridges*, Porto, Portugal. 221–229. [https://doi.org/10.1007/978-3-030-29227-0\\_21](https://doi.org/10.1007/978-3-030-29227-0_21).

- Forgács, T., Sarhosis, V., and Adany, S. (2018a). Discrete element modeling of skew masonry arch bridges taking into account arch ring-backfill interaction. In *Proceedings of 10IMC, the 10<sup>th</sup> International Masonry Conference*, Milan, Italy. 337-346.
- Forgács, T., Sarhosis, V., and Adany, S. (2019a). Numerical Modelling of Skew Masonry Arch Bridges Taking into Account Arch Ring-Backfill Interaction. *Masonry International*, 32(1):35–42.
- Forgács, T., Sarhosis, V., and Bagi, K. (2017). Minimum thickness of semi-circular skewed masonry arches. *Engineering Structures*, 140(Jun):317–336. <https://doi.org/10.1016/j.engstruct.2017.02.036>.
- Forgács, T., Sarhosis, V., and Bagi, K. (2018b). Influence of construction method on the load bearing capacity of skew masonry arches. *Engineering Structures*, 168:612-627. <https://doi.org/10.1016/j.engstruct.2018.05.005>.
- Gibbons, N. (2014). *Modelling and assessment of masonry arch bridges*. Ph.D. thesis, University College Dublin.
- Gilbert, M. (2009). ‘Fatigue in railway bridges’, in Robinson, M., and Kapoor, A. (eds.) *Fatigue in railway infrastructure*. Cambridge, Woodhead Publishing Limited, pp. 58–95. <https://doi.org/10.1533/9781845697020>.
- Gilbert, M. (2017). LimitState: RING—Masonry arch bridge analysis software | LimitState. Accessed August 26, 2017. <http://www.limitstate.com/ring>.
- Gilbert M., and Melbourne, C. (1994). Rigid-block analysis of masonry structures. *The Structural Engineer*, 72(21):356-361.
- Gilbert, M., Melbourne, C., Smith, C. C., Augustus-Nelson, L., and Swift, G. (2016). Proposed Permissible Limit State Assessment Criteria for Masonry Arch Bridges. In *Proceedings of ARCH'16, the 8<sup>th</sup> International Conference on Arch Bridges*, Wrocław, Poland. 843–852.
- Hacıfendioğlu, K., Başağa, H. B., and Banerjee, S. (2017). Probabilistic analysis of historic masonry bridges to random ground motion by Monte Carlo Simulation using Response Surface Method. *Construction and Building Materials*, 134:199–209. <https://doi.org/10.1016/j.conbuildmat.2016.12.101>.
- Harvey, B. (2004). Skew arch behaviour. *The Structural Engineer*, 82(5):13–15.
- Harvey, B. (2005). Some problems with arch bridge assessment and potential solutions. *The Structural Engineer*, 84(3):45–50.
- Harvey, B. (2012). Stiffness and damage in masonry bridges. *Proceedings of the Institution of Civil Engineers: Bridge Engineering*, 165(3):127–134. <https://doi.org/10.1680/bren.11.00032>.
- Harvey, B. (2013). A spatial view of the flow of force in masonry bridges. *Proceedings of the Institution of Civil Engineers: Bridge Engineering*, 166(1):51-58. <https://doi.org/10.1680/bren.11.00026>.
- Harvey, B. (2017). Archie-M homepage. Accessed August 26, 2017. <http://www.obvis.com/>.

- Harvey, B., and Harvey, H. (2017). On the service behaviour of masonry viaducts. *Proceedings of the Institution of Civil Engineers: Bridge Engineering*, 170(4):248–254. <https://doi.org/10.1680/jbren.15.00031>.
- Harvey, B., Tomor, A., and Smith, F. (2005). A Three Dimensional Model for Masonry Arch Bridge Behaviour. *Structural Engineering International*, 15(2), 101–104. <https://doi.org/10.2749/101686605777963233>.
- Harvey W. J. (1988). Application of the mechanism analysis to masonry arches. *The Structural Engineer*, 66(5):77-84.
- Heyman, J. (1982). *The Masonry Arch*. Chichester, Ellis Horwood Limited.
- Highways Agency. (2001). *BD21/01: The Assessment of Highway Bridges and Structures*. Highways Agency, London, UK.
- Hughes, T. G., and Blackler, M. J. (1997). A review of the UK masonry arch assessment methods. *Proceedings of the Institution of Civil Engineers: Structures and Buildings*, 122(3):305–315. <https://doi.org/10.1680/istbu.1997.29801>.
- Imetrum (2021). Imetrum Limited homepage. Accessed April 11, 2021. <https://www.imetrum.com/video-gauge/>.
- Koltsida, S. I., Tomor, A. K., and Booth, C. A. (2014). Insights of Experimental Studies on the Load Carrying Capacity of Masonry Under Eccentric Loading. *Masonry International*, 27(3):49–54.
- Laterza, M., D'amato, M., and Casamassima, V. M. (2017). Stress-Life Curves Method for Fatigue Assessment of Ancient Brick Arch Bridges. *International Journal of Architectural Heritage*, 11(6):843–858. <https://doi.org/10.1080/15583058.2017.1315621>.
- Lemos, J. V. (2007). Discrete element modeling of masonry structures. *International Journal of Architectural Heritage*, 1(2):190–213. <https://doi.org/10.1080/15583050601176868>.
- Leon, J., and Espejo, S. R. (2007). Load test to collapse on the masonry arch bridge at Urnieta. In *Proceedings of ARCH'07, the 5<sup>th</sup> International Conference on Arch Bridges*, Madeira, Portugal. 969–977.
- Lienhart, W. (2015). Case studies of high-sensitivity monitoring of natural and engineered slopes. *Journal of Rock Mechanics and Geotechnical Engineering*, 7(4):379–384. <http://dx.doi.org/10.1016/j.jrmge.2015.04.002>.
- Majumder, M., Gangopadhyay, T. K., Chakraborty, A. K., Dasgupta, K., and Bhattacharya, D. K. (2008). Fibre Bragg gratings in structural health monitoring – Present status and applications. *Sensors and Actuators A: Physical*, 147(1):150-164. <https://doi.org/10.1016/j.sna.2008.04.008>.
- Martin-Caro, J. A., and Lopez, D. (2016). Assessment of damaged arches. In *Proceedings of ARCH'16, the 8<sup>th</sup> International Conference on Arch Bridges*, Wrocław, Poland. 1279–1290.

- McGill, R., Tukey, J. W., and Larsen, W. A. (1978). Variations of Box Plots. *The American Statistician*, 32(1):12-16. <https://doi.org/10.2307/2683468>.
- McInerney, J., and DeJong, M. J. (2014). Discrete element modeling of groin vault displacement capacity. *International Journal of Architectural Heritage*, 9(8):1037–1049. <https://doi.org/10.1080/15583058.2014.923953>.
- McKibbins, L.D., Melbourne, C., Sawar, N., and Gaillard, C.S. (2006). *Masonry arch bridges: condition appraisal and remedial treatment (CIRIA C656)*. CIRIA, London, UK.
- Melbourne, C., Cole, G., Gilbert, M., Swift, G. M., and Smith, C. C. (2013). A road-map for the assessment of masonry arch bridges. In *Proceedings of ARCH'13, the 7<sup>th</sup> International Conference on Arch Bridges*, Split, Croatia. 605–612.
- Melbourne, C., and Gilbert, M. (1995). The behaviour of multiring brickwork arch bridges. *The Structural Engineer*, 73(3):39–47.
- Melbourne, C., Gilbert, M., and Wagstaff, M. (1997). The collapse behaviour of multispan brickwork arch bridges. *The Structural Engineer*, 75(17):297–305.
- Melbourne, C., Wang, J., and Tomor, A. K. (2007). A new masonry arch bridge assessment strategy (SMART). *Proceedings of The Institution of Civil Engineers: Bridge Engineering*, 160(2):81–87. <https://doi.org/10.1680/bren.2007.160.2.81>.
- Milani, G., and Lourenço, P. B. (2012). 3D non-linear behavior of masonry arch bridges. *Computers and Structures*, 110–111(Nov):133–150. <https://doi.org/10.1016/j.compstruc.2012.07.008>.
- Moreira, V. N., Matos, J. C., and Oliveira, D. V. (2017). Probabilistic-based assessment of a masonry arch bridge considering inferential procedures. *Engineering Structures*, 134:61–73. <https://doi.org/10.1016/j.engstruct.2016.11.067>.
- Network Rail. (2006). *The structural assessment of underbridges*. Network Rail, London, UK.
- Network Rail. (2013). *Bridge detailed examination report for Marsh Lane Viaduct (HULA/48)*. Network Rail, York, UK.
- Olivieri, C., Fortunato, A., and DeJong, M. J. (*in press*). A new membrane equilibrium solution for masonry railway bridges: the case study of Marsh Lane Bridge. *International Journal of Masonry Research and Innovation*. <https://doi.org/10.1504/IJMRI.2021.10037557>.
- Pippard, A. J. S. (1948). The Approximate Estimation of Safe Loads on Masonry Bridges. *The Civil Engineer in War*, 1:365–372. <https://doi.org/10.1680/ciwv1.45170.0021>.
- Riveiro, B., DeJong, M. J., and Conde, B. (2016). Automated processing of large point clouds for structural health monitoring of masonry arch bridges. *Automation in Construction*, 72(3):258–268. <https://doi.org/10.1016/j.autcon.2016.02.009>.
- Ruddock, T. (2000) *Masonry Bridges, Viaducts and Aqueducts*. Aldershot, Ashgate Variorum.
- De Santis, S., and de Felice, G. (2014). A fibre beam-based approach for the evaluation of the seismic capacity of masonry arches. *Earthquake Engineering and Structural Dynamics*, 43(11):1661–1681. <https://doi.org/10.1002/eqe.2416>.

- De Santis, S., and Tomor, A. K. (2013). Laboratory and field studies on the use of acoustic emission for masonry bridges. *NDT & E International*, 55:64–74. <https://doi.org/10.1016/j.ndteint.2013.01.006>.
- Sarhosis, V., Forgács, T., and Lemos, J. V. (2019a). A discrete approach for modelling backfill material in masonry arch bridges. *Computers and Structures*, 224:106108. <https://doi.org/10.1016/j.compstruc.2019.106108>.
- Sarhosis, V., Forgács, T., and Lemos, J. V. (2019b). Modelling Backfill in Masonry Arch Bridges: A DEM Approach. In *Proceedings of ARCH 2019, the 9<sup>th</sup> International Conference on Arch Bridges*, Porto, Portugal. 178-184. [https://doi.org/10.1007/978-3-030-29227-0\\_16](https://doi.org/10.1007/978-3-030-29227-0_16).
- Sarhosis, V., Oliveira, D. V., Lemos, J. V., and Lourenço, P. B. (2014). The effect of skew angle on the mechanical behaviour of masonry arches. *Mechanics Research Communications*, 61:53–59. <https://doi.org/10.1016/j.mechrescom.2014.07.008>.
- Sarhosis, V., De Santis, S., and de Felice, G. (2016). A review of experimental investigations and assessment methods for masonry arch bridges. *Structure and Infrastructure Engineering*, 12(11):1439–1464. <https://doi.org/10.1080/15732479.2015.1136655>.
- Smith, J., and Acikgoz, S. (2019). Dynamic Amplification of Curved Beams Subjected to a Moving Point Load. In *Proceedings of ARCH 2019, the 9<sup>th</sup> International Conference on Arch Bridges*, Porto, Portugal. 212-220. [https://doi.org/10.1007/978-3-030-29227-0\\_20](https://doi.org/10.1007/978-3-030-29227-0_20).
- Thompson, D., Cocking, S., and DeJong, M. J. (2018). *Barkston Road Bridge (CFM-5) Monitoring Project: Stage 2 – Monitoring Specification*. AECOM and CSIC, Nottingham, UK.
- Thompson, D., Cocking, S., Mercer, A., and DeJong, M. J. (2019). *Barkston Road Bridge (CFM-5) Monitoring Project: Stage 3 – Draft Research Report*. AECOM and CSIC, Nottingham, UK.
- Tomor, A. K., De Santis, S., and Wang, J. (2013). Fatigue deterioration process of brick masonry. *Masonry International*, 26(2):41–48.
- Tomor, A., and Verstrynghe, E. (2013). A joint fatigue-creep deterioration model for masonry with acoustic emission based damage assessment. *Construction and Building Materials*, 43:575–588. <https://doi.org/10.1016/j.conbuildmat.2013.02.045>.
- Tubaldi, E., Macorini, L., and Izzuddin, B. A. (2020). Identification of critical mechanical parameters for advanced analysis of masonry arch bridges. *Structure and Infrastructure Engineering*, 16(2):328–345. <https://doi.org/10.1080/15732479.2019.1655071>.
- Tukey, J. W. (1977). *Exploratory Data Analysis*. Addison-Wesley, Reading, Massachusetts.
- UIC. (2006). *776-IR Loads to be considered in railway bridge design*. 5<sup>th</sup> Edition. International Union of Railways (UIC), Paris, France.
- Wang, J., Tomor, A. K., Melbourne, C., and Yousif, S. (2013). Critical review of research on high-cycle fatigue behaviour of brick masonry. *Construction and Building Materials*, 38:602–609. <https://doi.org/10.1016/j.conbuildmat.2012.09.010>.

- 
- Wood, C., Cocking, S., and DeJong, M. J. (2017). *Barkston Road Bridge (CFM-5) Monitoring Project: Stage 1 – Monitoring Desk Study*. AECOM and CSIC, Nottingham, UK.
- Wolf, J. P. (1994). *Foundation vibration analysis using simple physical models*. PTR Prentice Hall, Englewood Cliffs, NJ, USA.
- Ye, C., Acikgoz, S., Pendrigh, S., Riley, E., and DeJong, M. J. (2018). Mapping deformations and inferring movements of masonry arch bridges using point cloud data. *Engineering Structures*, 173(Oct):530–545. <https://doi.org/10.1016/j.engstruct.2018.06.094>.
- Zhang, Y., Macorini, L., and Izzuddin, B. A. (2016). Mesoscale partitioned analysis of brick-masonry arches. *Engineering Structures*, 124:142–166. <https://doi.org/10.1016/j.engstruct.2016.05.046>.
- Zhang, Y., Macorini, L., and Izzuddin, B. A. (2017). Numerical investigation of arches in brick-masonry bridges. *Structure and Infrastructure Engineering*, 2479 (Jul): 1–19. <https://doi.org/10.1080/15732479.2017.1324883>.
- Zhang, Y., Tubaldi, E., Macorini, L., and Izzuddin, B. A. (2018). Mesoscale partitioned modelling of masonry bridges allowing for arch-backfill interaction. *Construction and Building Materials*, 173:820–842. <https://doi.org/10.1016/j.conbuildmat.2018.03.272>.

## Related publications by the author

### 1 Peer-reviewed journal publications

Cocking, S., Alexakis, H., and DeJong, M. J. (2021). Distributed dynamic fibre-optic strain monitoring of the behaviour of a skewed masonry arch railway bridge. *Journal of Civil Structural Health Monitoring*. <https://doi.org/10.1007/s13349-021-00493-w>.

Related to: Chapter 5.

Cocking, S., Acikgoz, S., and DeJong, M. J. (2020). Interpretation of the Dynamic Response of a Masonry Arch Rail Viaduct Using Finite-Element Modeling. *Journal of Architectural Engineering*, 26(1):05019008. [http://doi.org/10.1061/\(ASCE\)AE.1943-5568.0000369](http://doi.org/10.1061/(ASCE)AE.1943-5568.0000369).

Related to: Chapter 3.

### 2 Conference proceedings

Cocking, S., Alexakis, H., and DeJong, M. J. (2019a). Measurement of the flow of force in a skewed masonry arch bridge using fibre optic sensing. In *Proceedings of SHMII-9, the 9th International Conference on Structural Health Monitoring of Intelligent Infrastructure*, St. Louis, MO, USA. <https://doi.org/10.17863/CAM.48466>.

Related to: Chapter 6.

Cocking, S., Thompson, D., and DeJong, M. (2019b). Comparative Evaluation of Monitoring Technologies for a Historic Skewed Masonry Arch Railway Bridge. In *Proceedings of ARCH 2019, the 9th International Conference on Arch Bridges*, Porto, Portugal. 439-446. [https://doi.org/10.1007/978-3-030-29227-0\\_46](https://doi.org/10.1007/978-3-030-29227-0_46).

Related to: Chapter 4.

Cocking, S. H., Ye, C., and DeJong, M. J. (2019c). Damage Assessment of a Railway Bridge using Fibre Optic Sensing and LiDAR Data. In *Proceedings of ICSIC 2019, the International Conference on Smart Infrastructure and Construction 2019*, Cambridge, UK. <https://doi.org/10.1680/icsic.64669.701>.

Related to: Chapter 4.

---

Cocking, S. H., Acikgoz, S., and DeJong, M. J. (2018). The Importance of Modelling Assumptions When Analysing the Dynamic Response of a Masonry Railway Viaduct. In *Proceedings of 10IMC, the 10th International Masonry Conference*, Milan, Italy. <https://doi.org/10.17863/CAM.48416>.

Related to: Chapter 3.

### **3 Publications in preparation**

Cocking, S., Alexakis, H., and DeJong, M. J. Fibre-Bragg Rosette and Videogrammetry Monitoring of the Three-Dimensional Flow of Force in a Damaged, Skewed Masonry Arch Railway Bridge.

Target journal: *Engineering Structures*.

Related to: Chapter 6.

Cocking, S., Mercer, A., Thompson, D., Kite, D., and DeJong, M. J. Practical Evaluation of Monitoring Strategies for Ageing Masonry Arch Bridges, Based on a Comprehensive Multi-Sensing Field Study.

Target journal: *Proceedings of the Institution of Civil Engineers: Bridge Engineering*.

Related to: Chapter 4; Chapter 7.

Cocking, S., Alexakis, H., and DeJong, M. J. Long-Term Fibre-Optic Monitoring of Structural Behaviour at an Ageing, Skewed Masonry Arch Bridge.

Target journal: *Journal of Structural Engineering*.

Related to: Chapter 8.



# Appendix A

## Long-term FBG data: Northern Rail trains

This Appendix plots the data for all trains running on the Northern Rail route, recorded to date. The majority are assumed to be Class 150 Sprinter trains, running in sets of either 2 or 3 carriages. However, some trains of other types may be present in these data; these are difficult to distinguish as they have similar characteristics. Some may be other units within the Sprinter family (Classes 153, 155, 156, and 158), while some trains recorded prior to 2020 are likely to be Class 142 or 144 Pacers.

Plots are presented in the same sequence that was used in Chapter 8, for the First TransPennine trains. In the plots of the peak response (Figures A.3 to A.14), data points are coloured according to the time period in which they were measured, using the same convention described in section 8.3. In the quiver plots of the principal strain response (Figure A.19), tensile strains are plotted in red and compressive strains are plotted in blue.

### **A1 The instantaneous dynamic strain response in the arch**

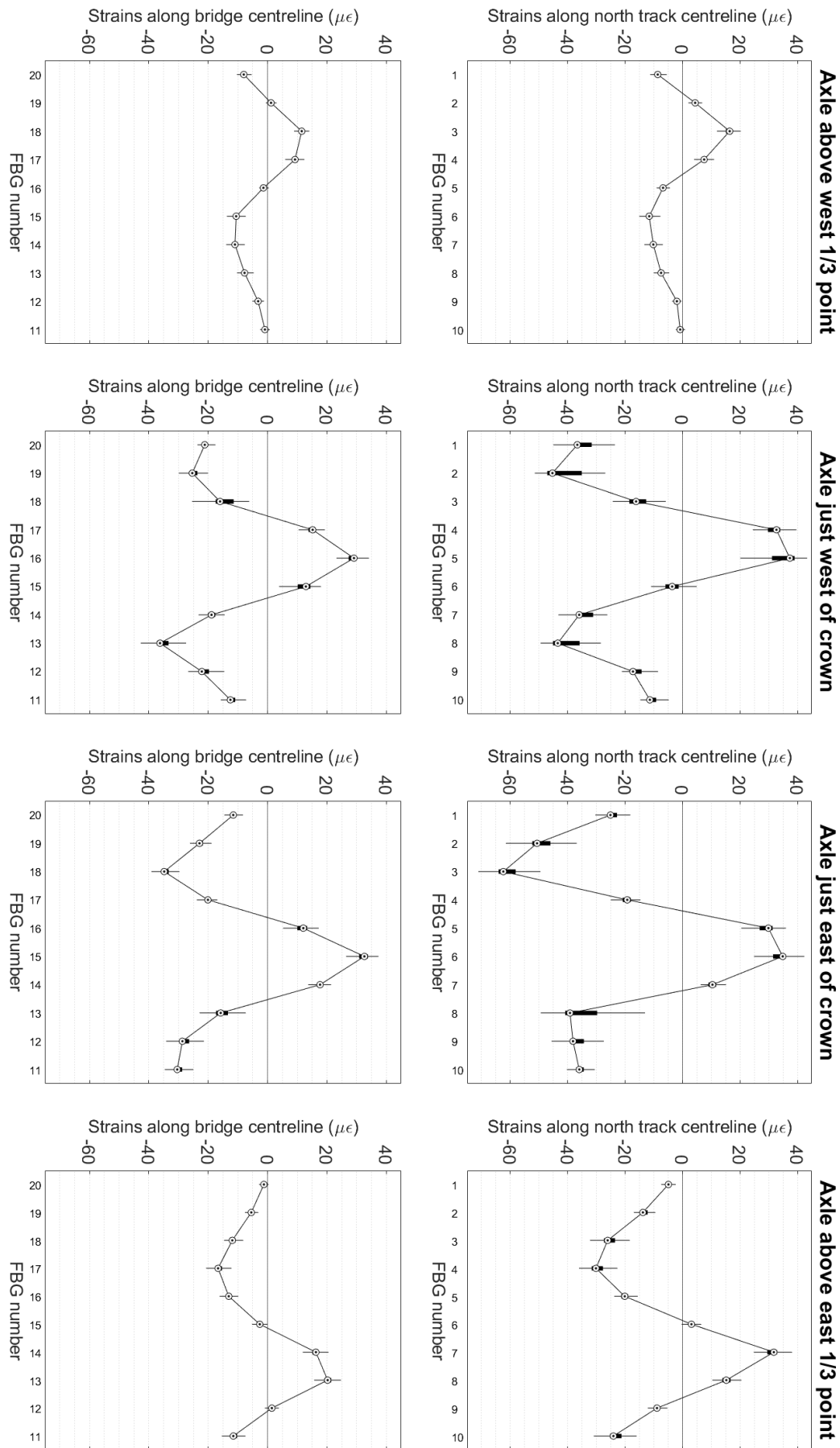


Figure A.1: Statistical variation of the instantaneous longitudinal strains over the northern half of the arch, when the critical axle loads are applied at key locations along the arch span, across all Northern Rail trains passing on the north track

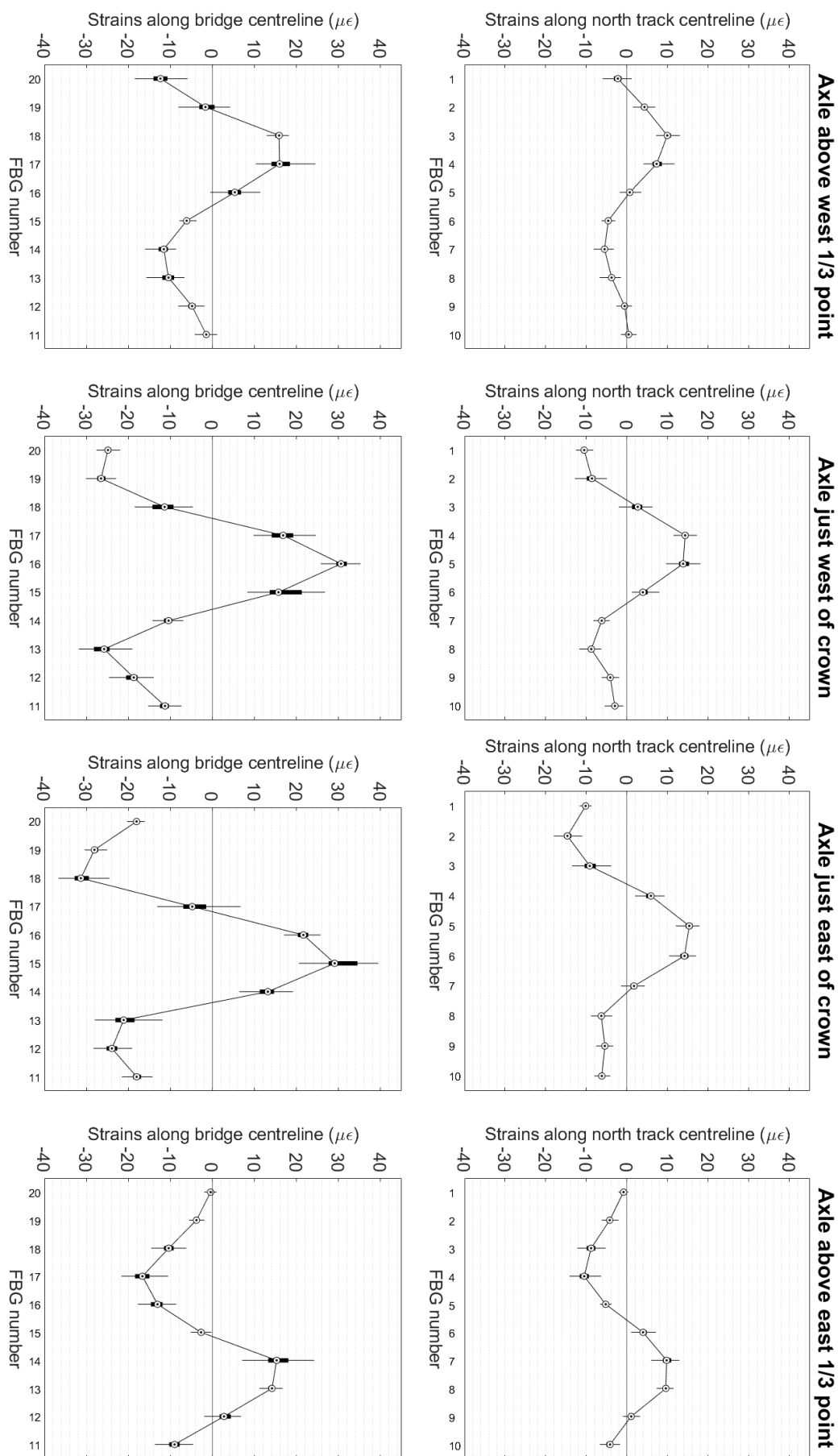


Figure A.2: Statistical variation of the instantaneous longitudinal strains over the northern half of the arch, when the critical axle loads are applied at key locations along the arch span, across all Northern Rail trains passing on the south track

## A2 The peak-to-peak dynamic strain response in the arch

### A2.1 Trains on the north track

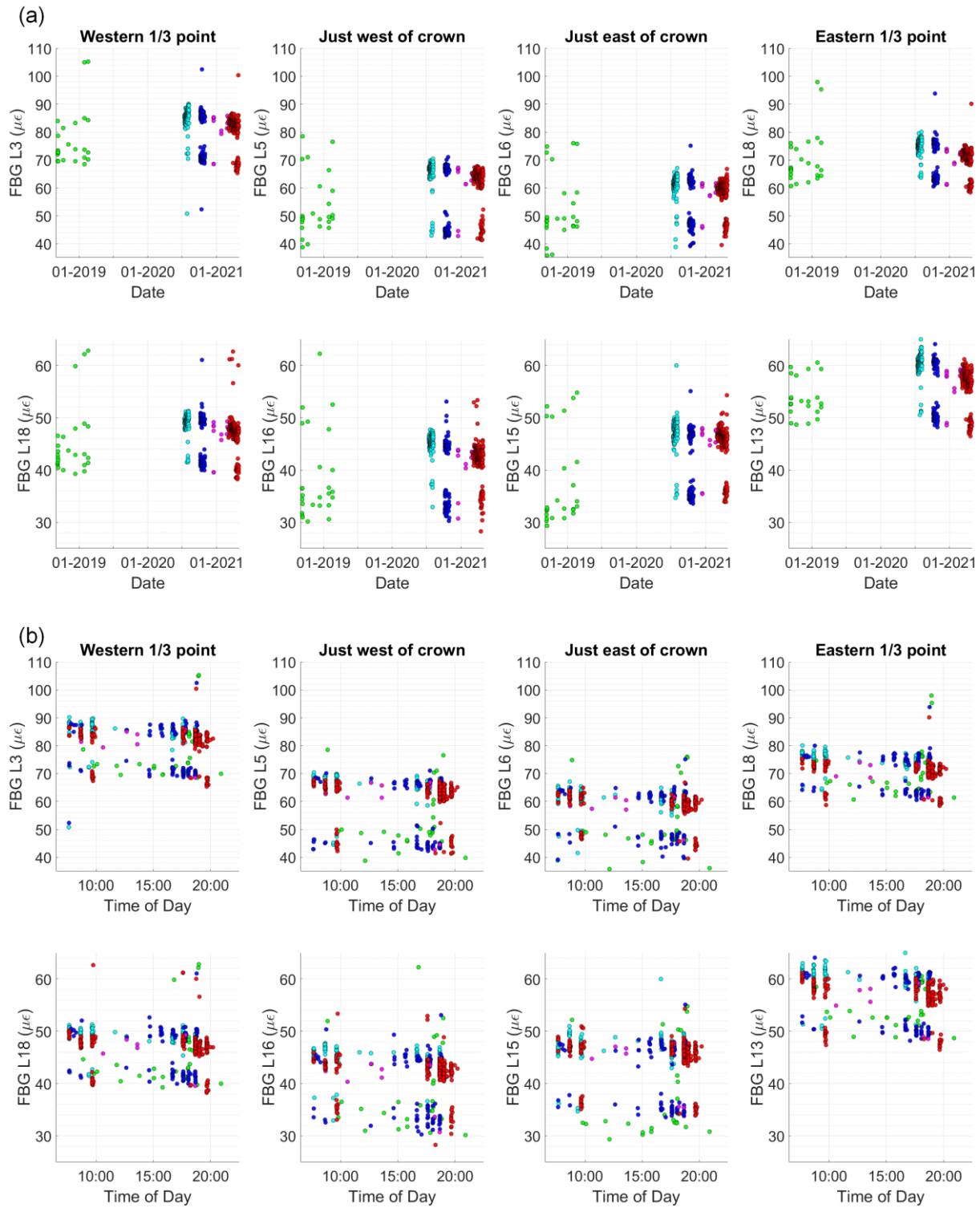


Figure A.3: Variation of peak-to-peak longitudinal strains over the northern half of the arch with (a) date and (b) time of day, for all recorded Northern Rail trains passing on the north track

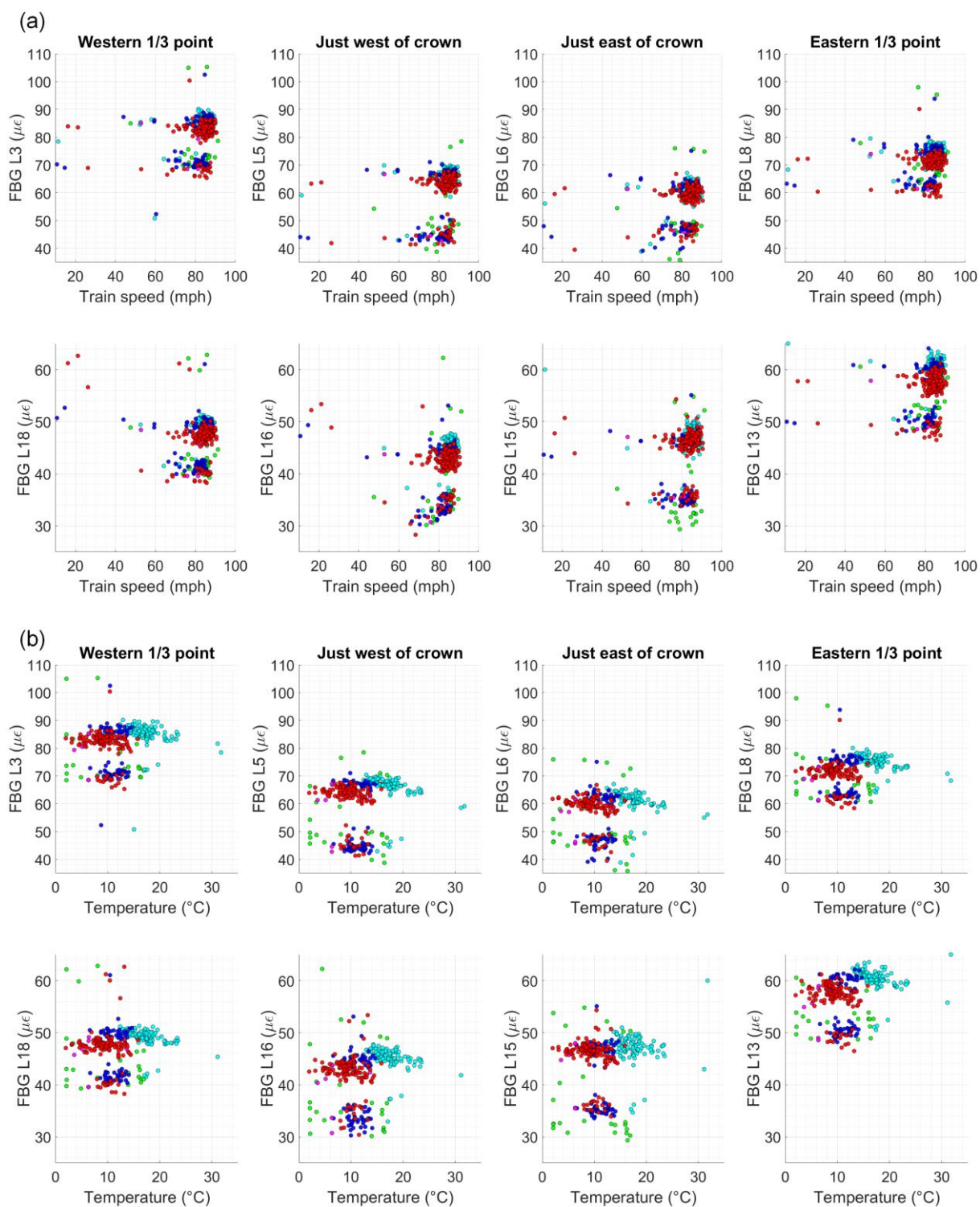


Figure A.4: Variation of peak-to-peak longitudinal strains over the northern half of the arch with (a) train speed and (b) temperature, for all recorded Northern Rail trains passing on the north track

## A2.2 Trains on the south track

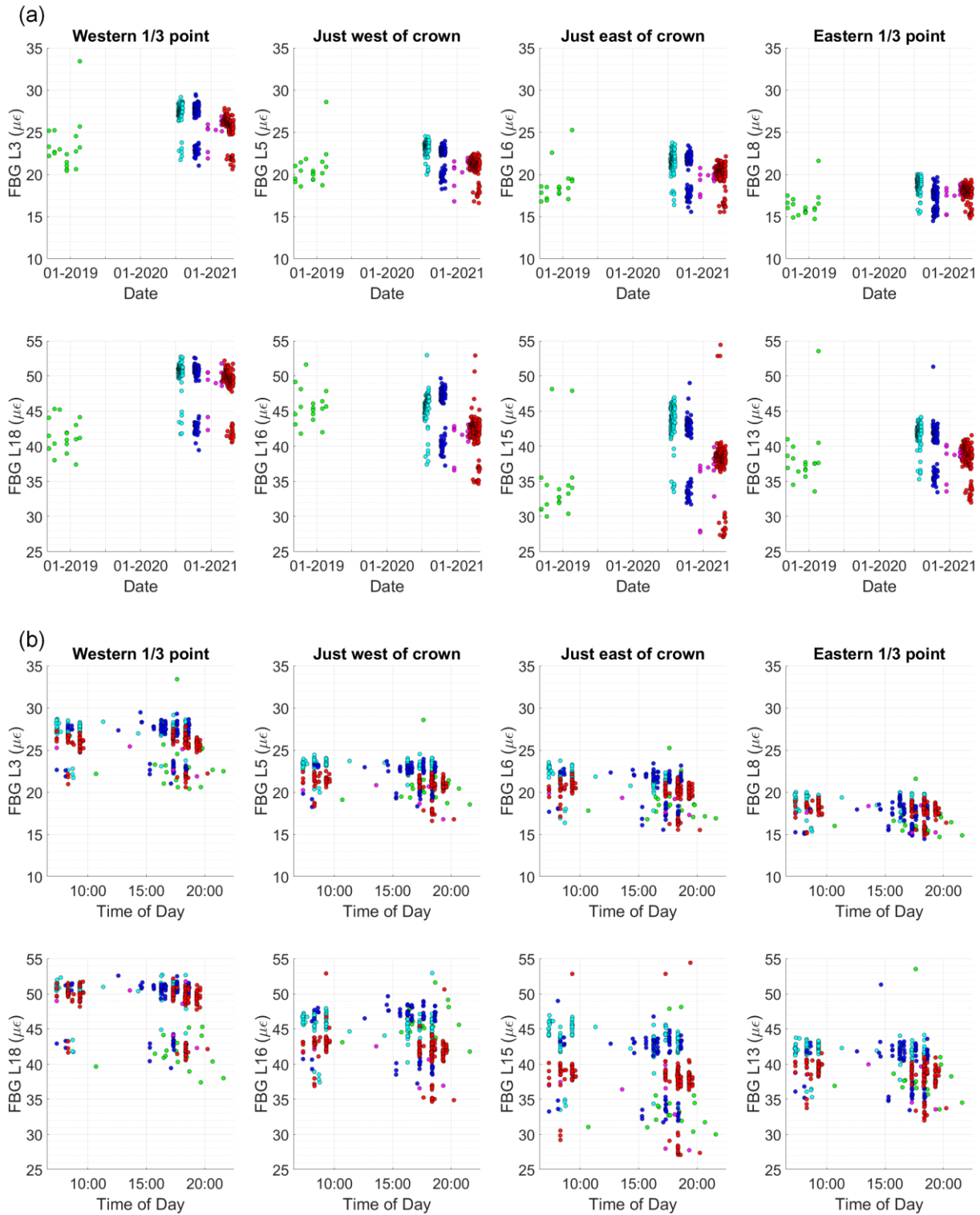


Figure A.5: Variation of peak-to-peak longitudinal strains over the northern half of the arch with (a) date and (b) time of day, for all recorded Northern Rail trains passing on the south track

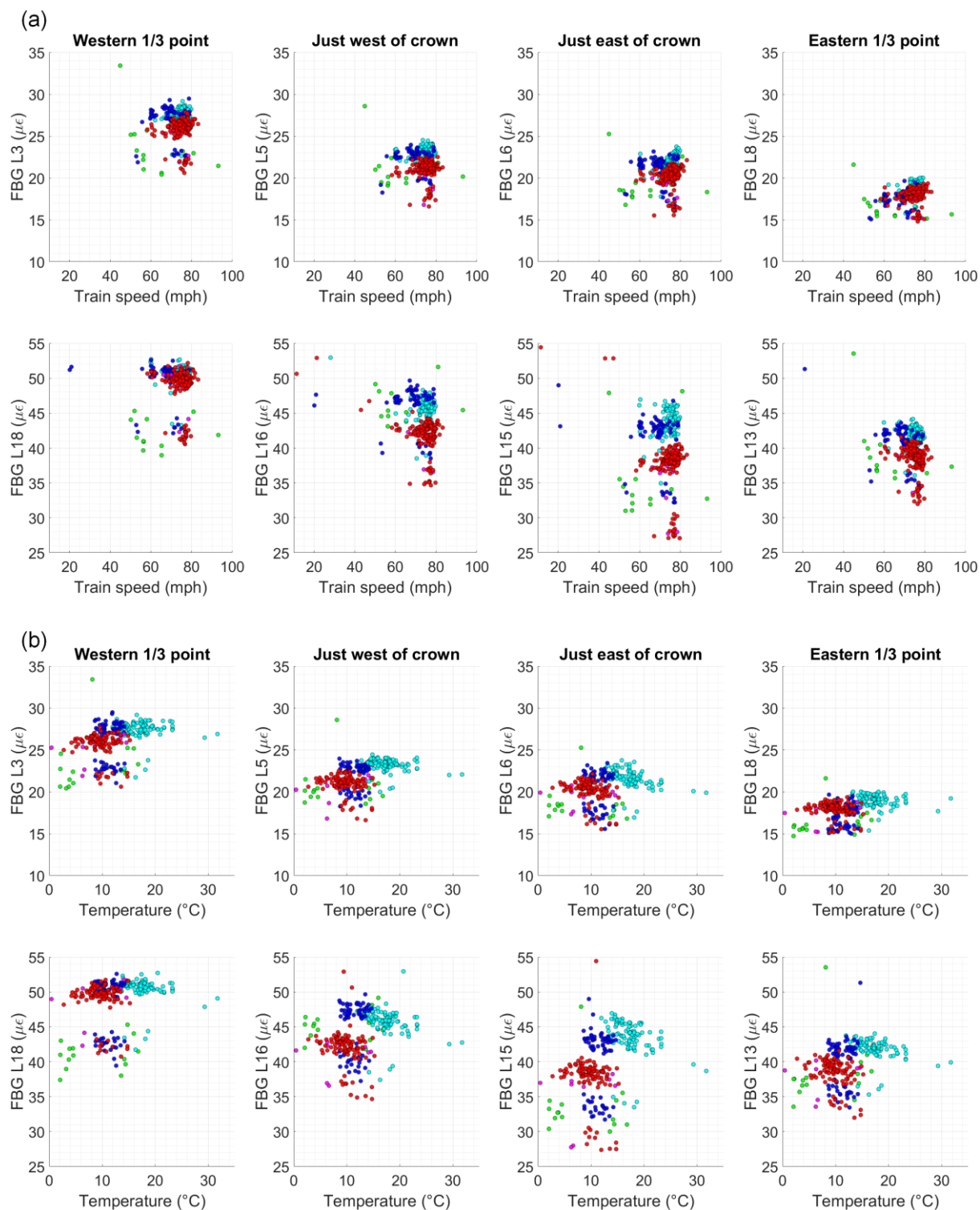


Figure A.6: Variation of peak-to-peak longitudinal strains over the northern half of the arch with (a) train speed and (b) temperature, for all recorded Northern Rail trains passing on the south track

## A3 The peak dynamic crack movements

### A3.1 Trains on the south track

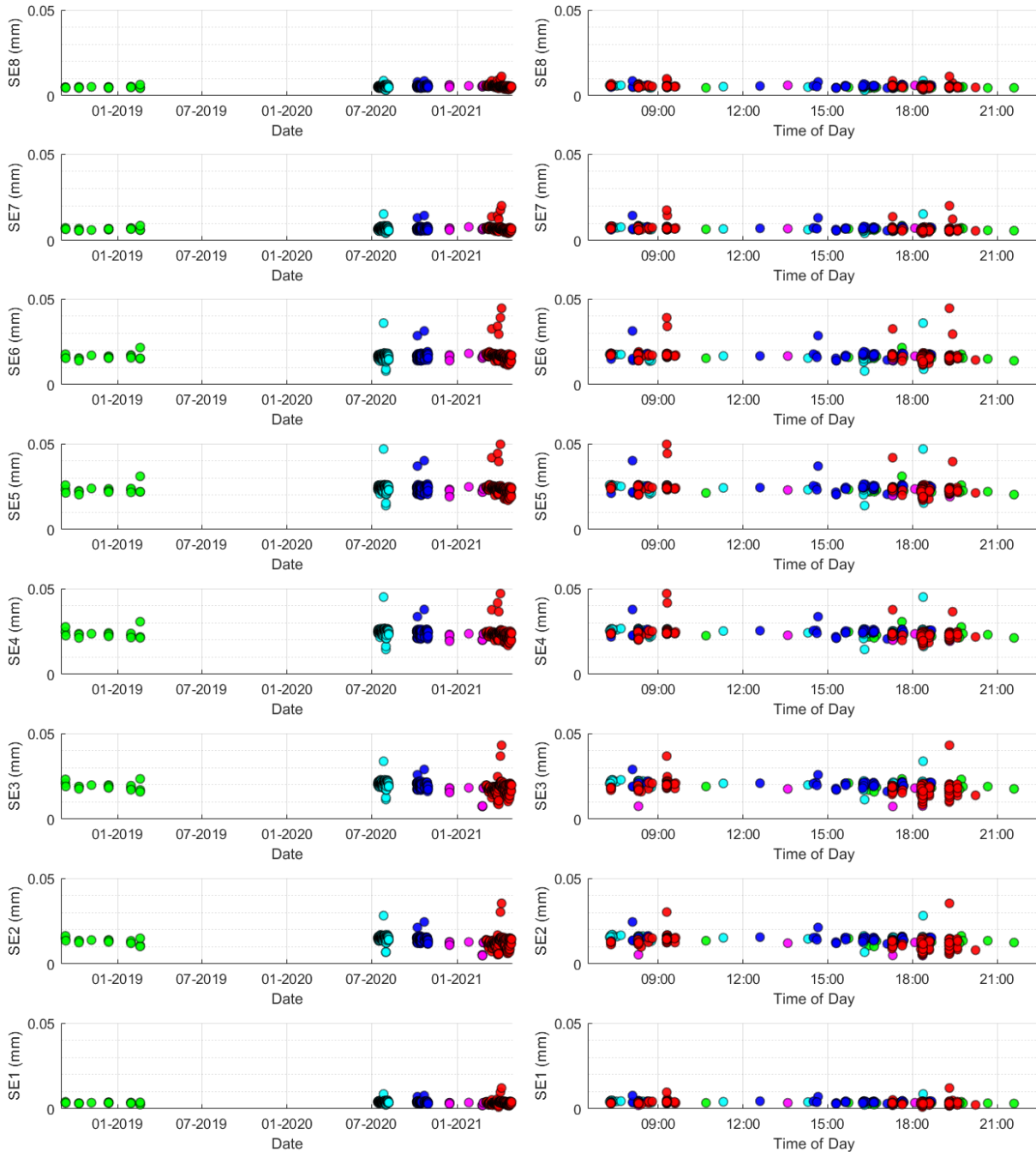


Figure A.7: Variation of peak dynamic movements at the south-eastern longitudinal crack with (left) date and (right) time of day, for all recorded Northern Rail trains passing on the south track

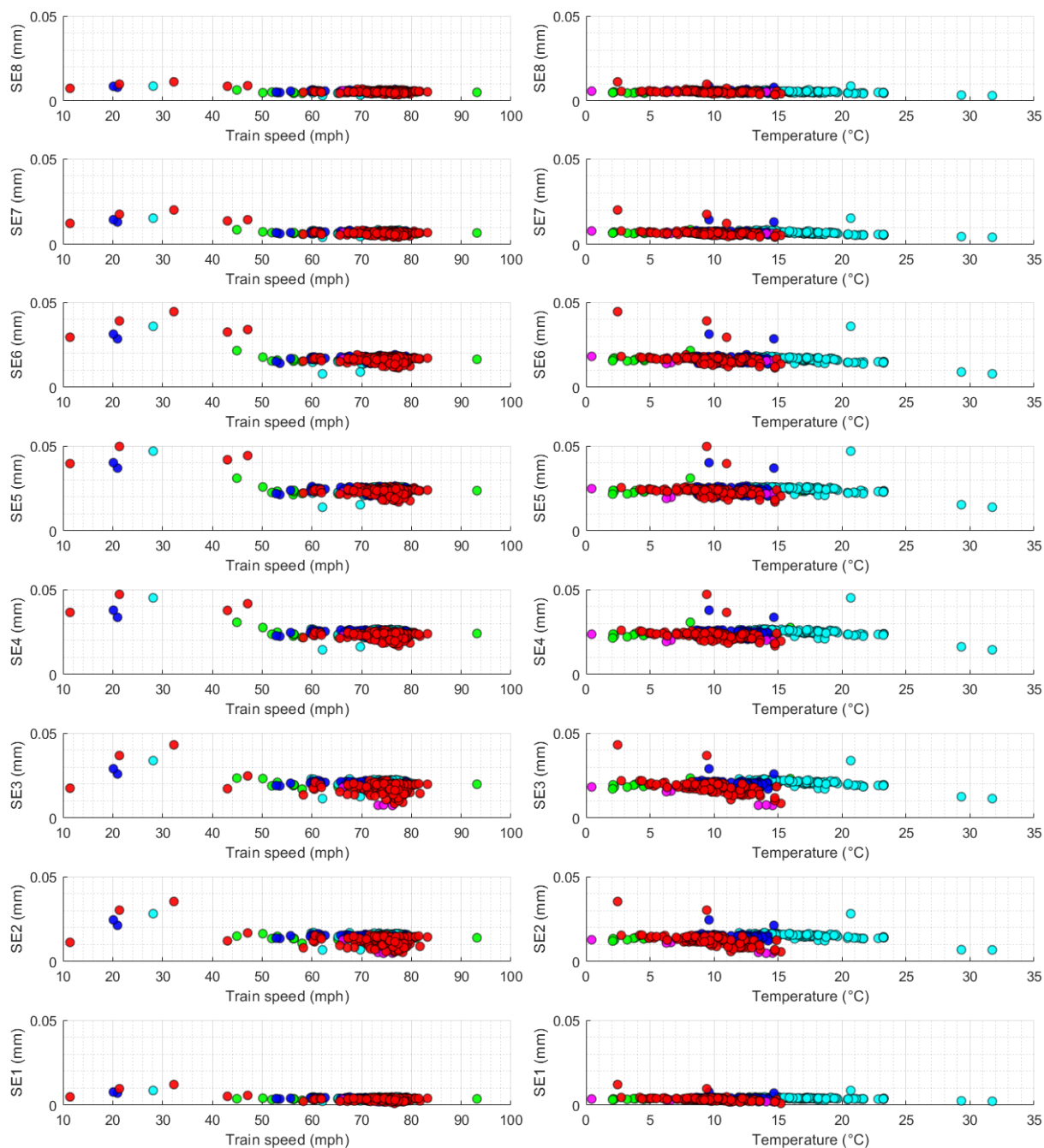


Figure A.8: Variation of peak dynamic movements at the south-eastern longitudinal crack with (left) train speed and (right) temperature, for all recorded Northern Rail trains passing on the south track

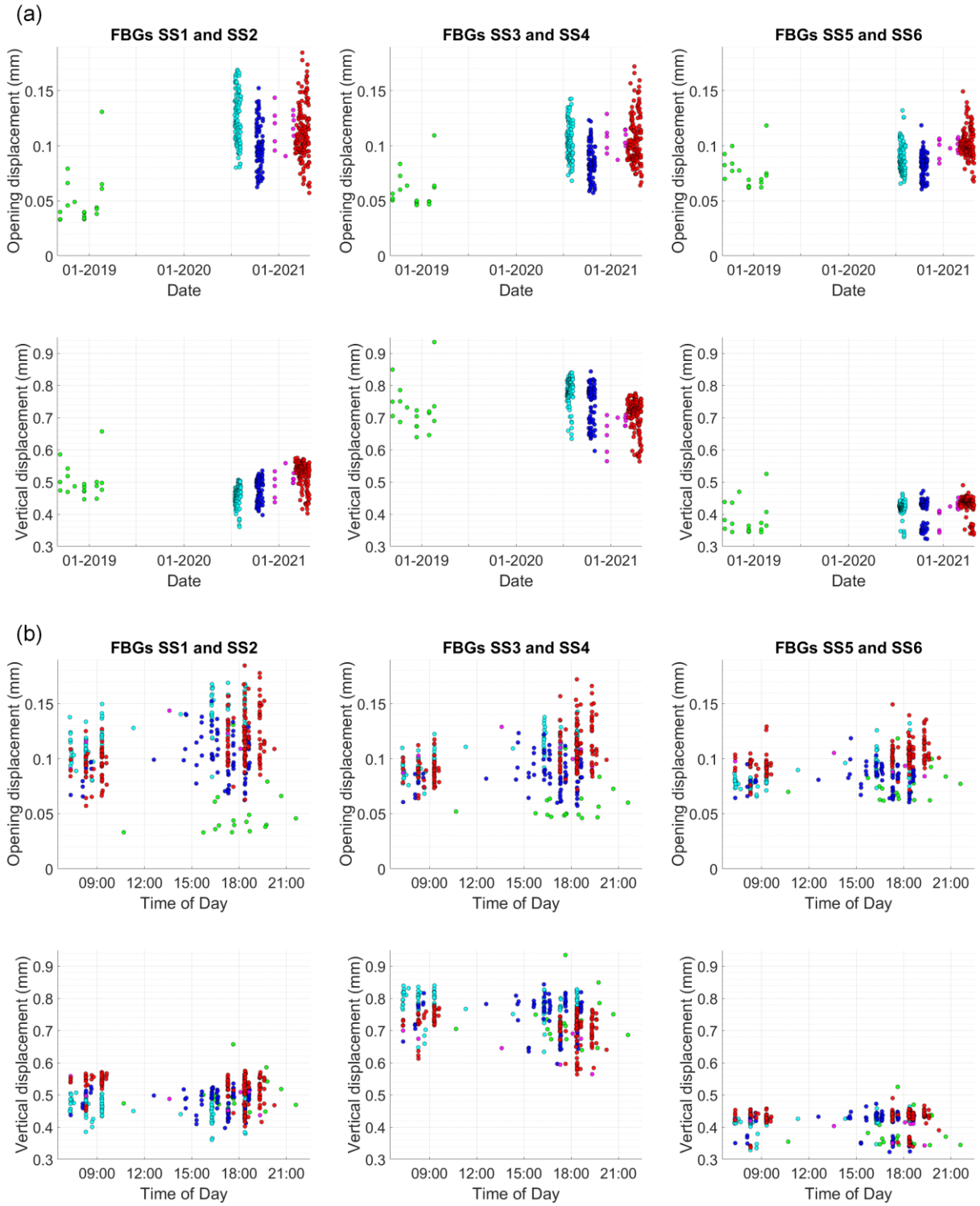
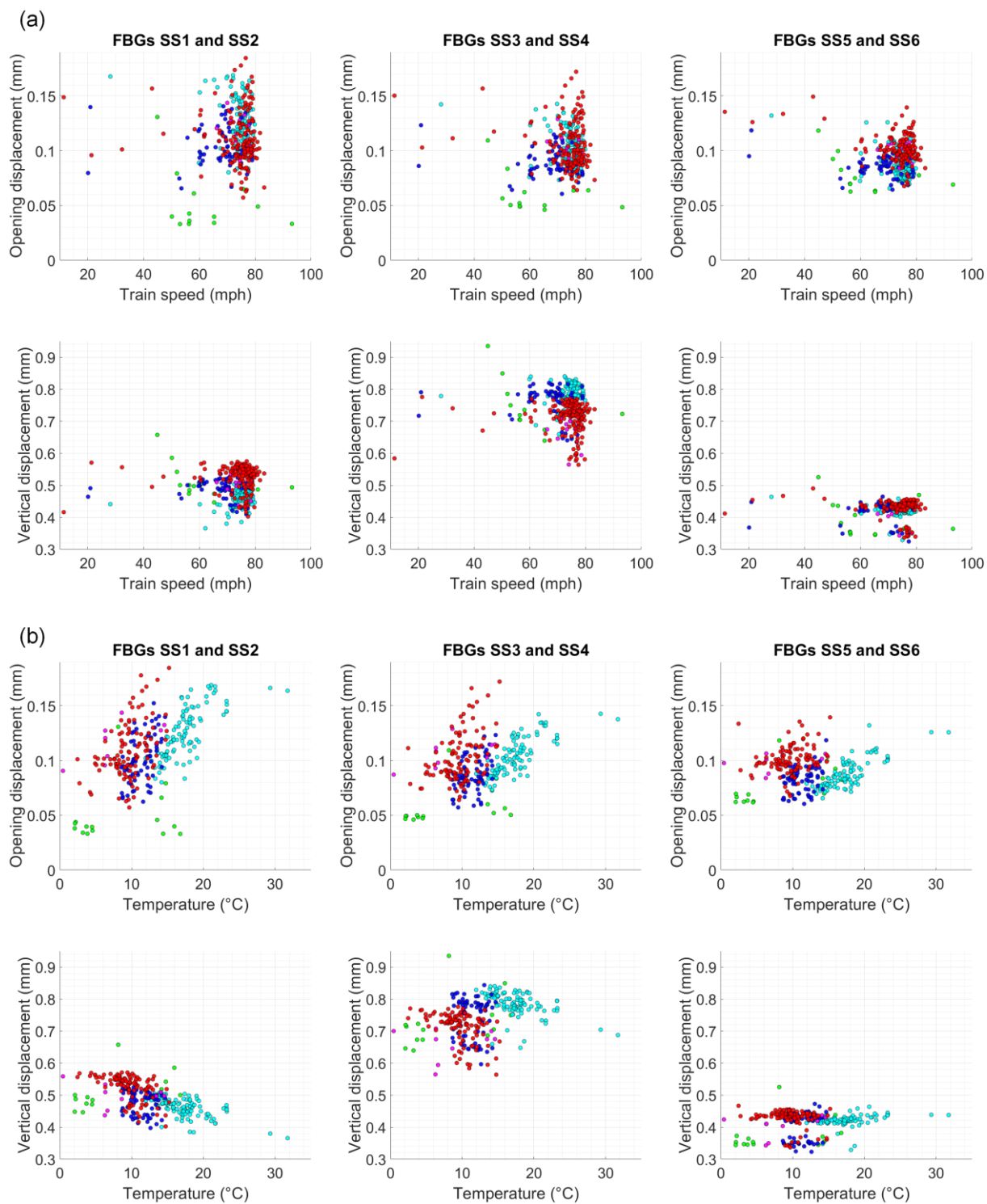
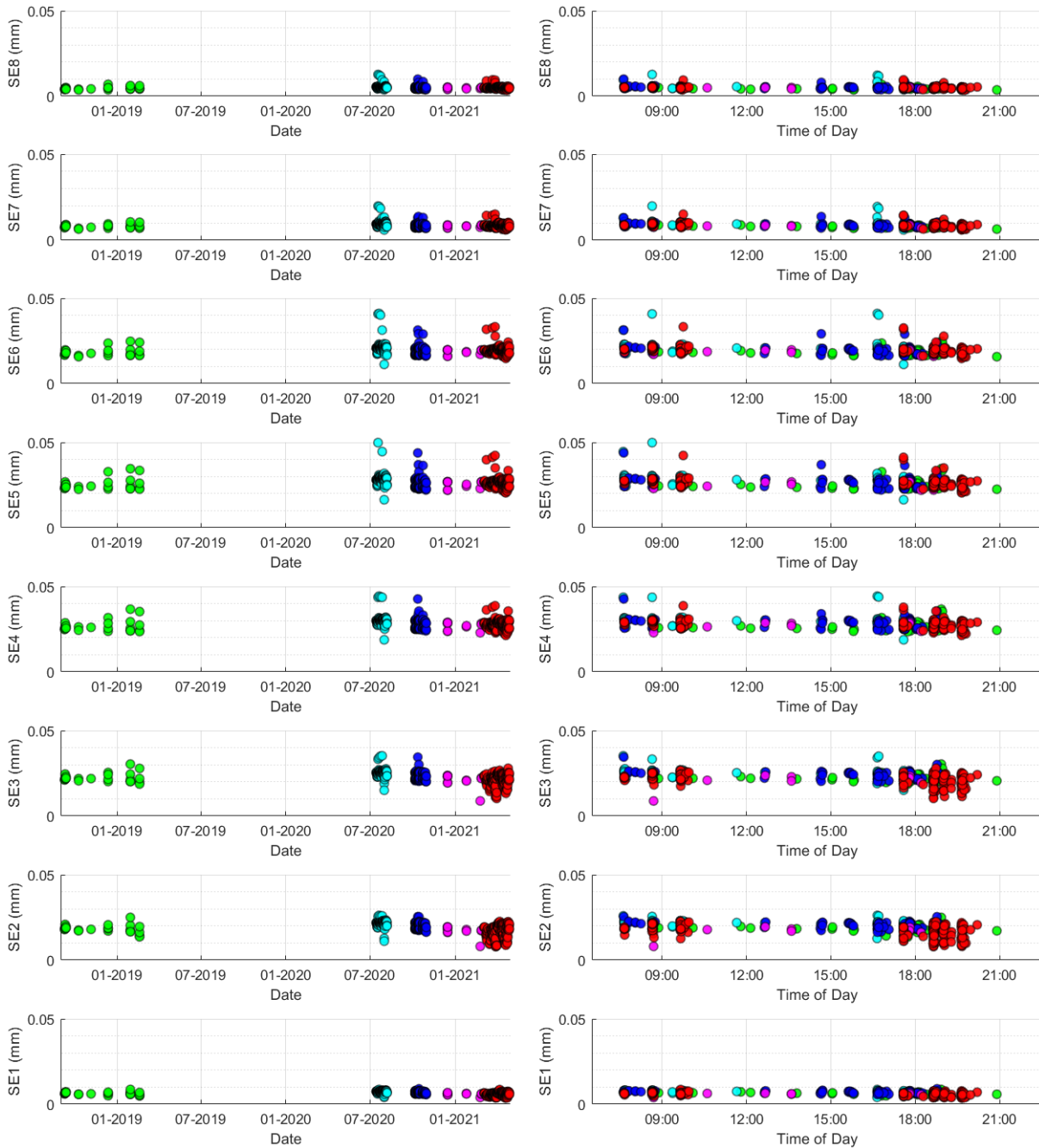


Figure A.9: Variation of peak dynamic movements at the south spandrel separation crack with (a) date and (b) time of day, for all recorded Northern Rail trains passing on the south track



*Figure A.10: Variation of peak dynamic movements at the south spandrel separation crack with (a) train speed and (b) temperature, for all recorded Northern Rail trains passing on the south track*

## A3.2 Trains on the north track



*Figure A.11: Variation of peak dynamic movements at the south-eastern longitudinal crack with (left) date and (right) time of day, for all recorded Northern Rail trains passing on the north track*

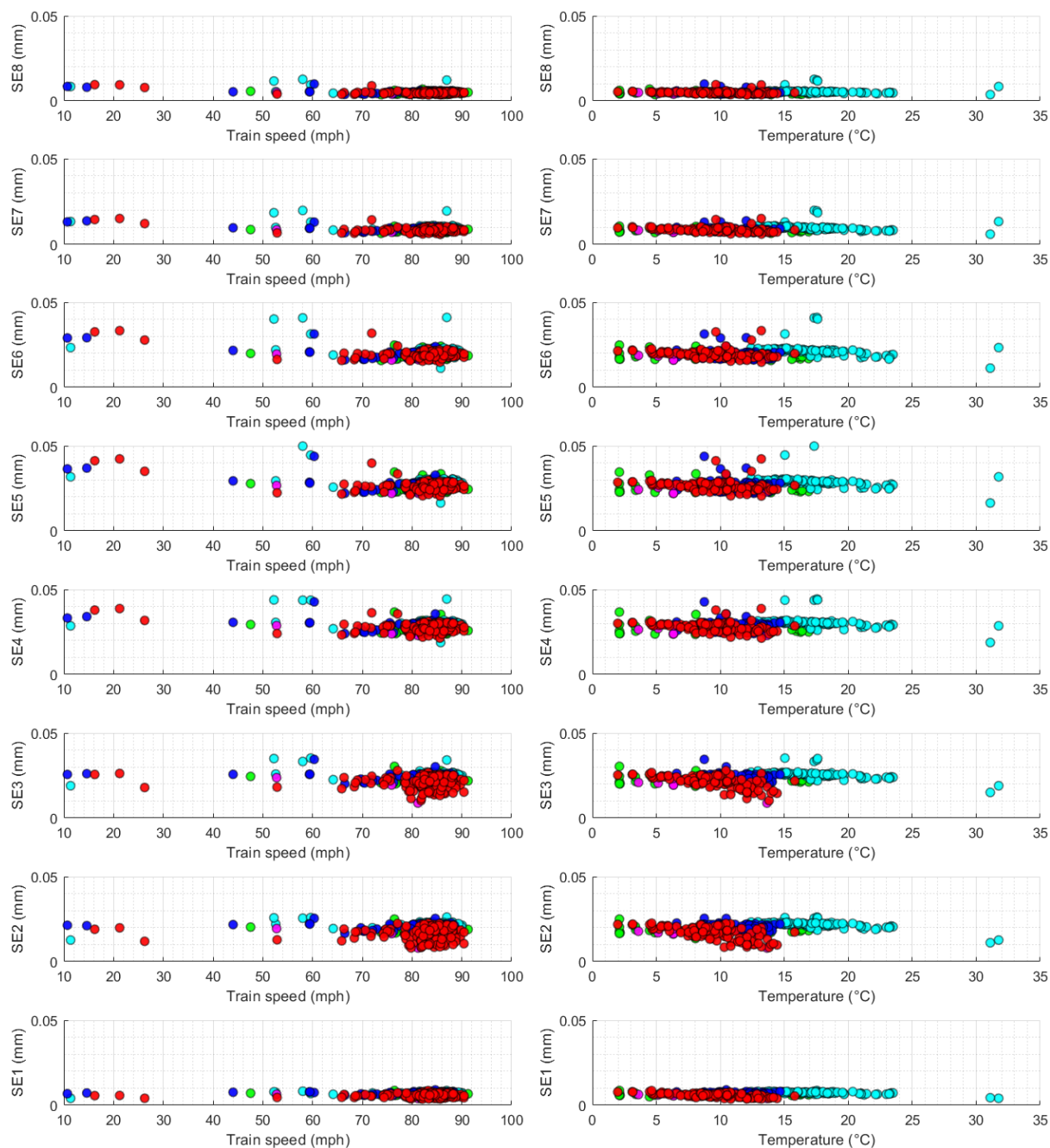


*Figure A.12: Variation of peak dynamic movements at the south-eastern longitudinal crack with (left) train speed and (right) temperature, for all recorded Northern Rail trains passing on the north track*

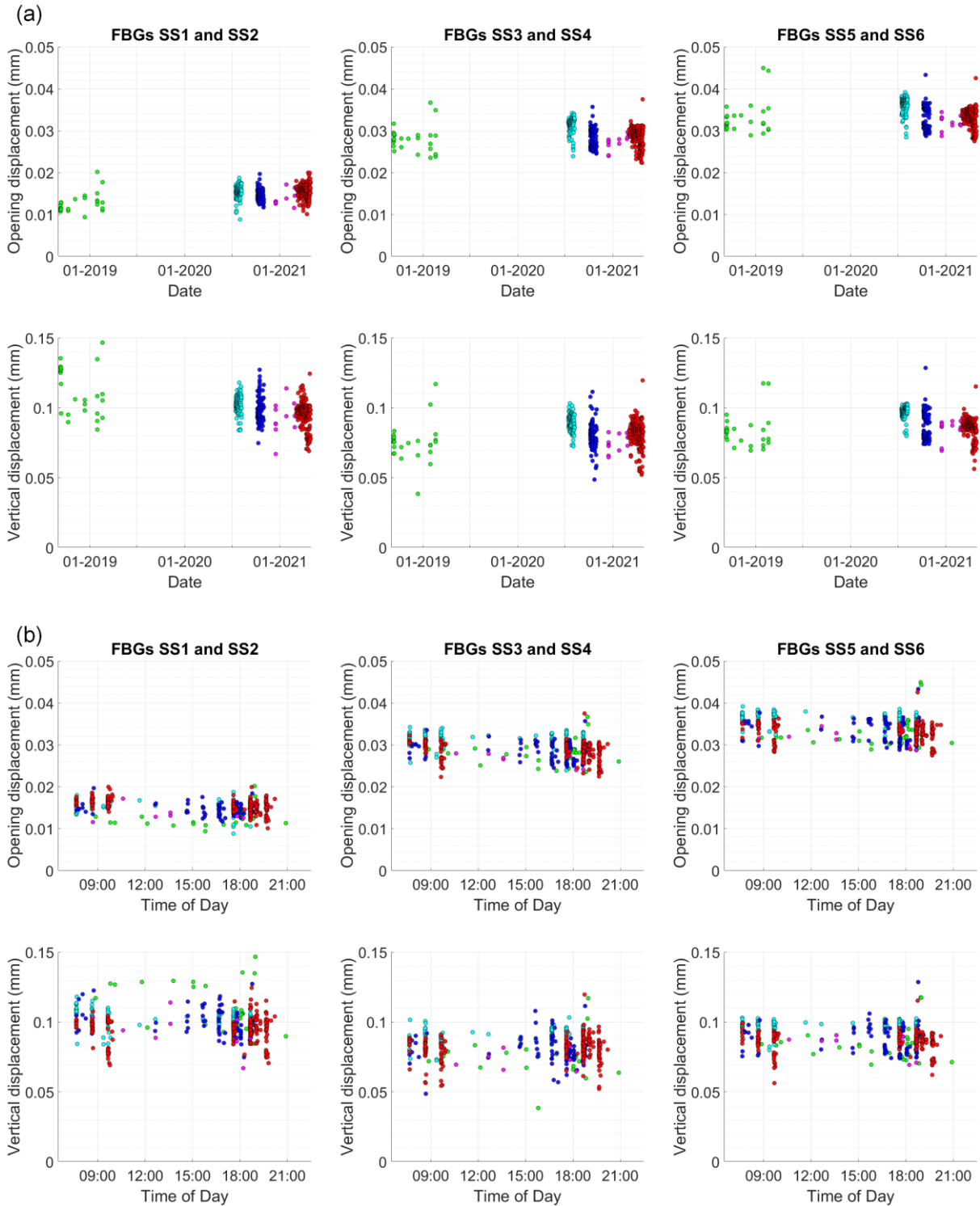


*Figure A.13: Variation of peak dynamic movements at the south spandrel separation crack with (a) date and (b) time of day, for all recorded Northern Rail trains passing on the north track*

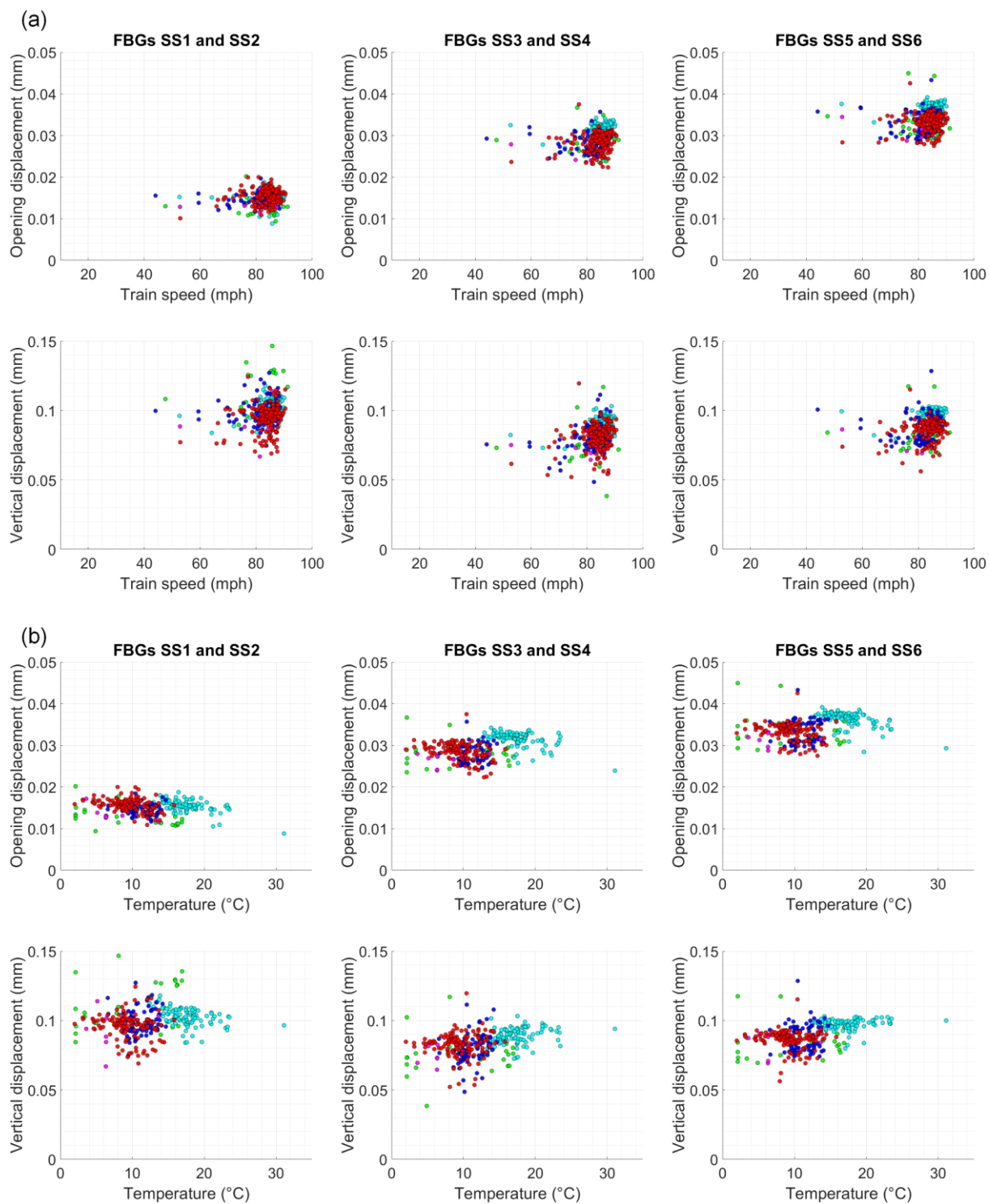


*Figure A.14: Variation of peak dynamic movements at the south spandrel separation crack with (a) train speed and (b) temperature, for all recorded Northern Rail trains passing on the north track*

## A4 The principal strain response in the arch

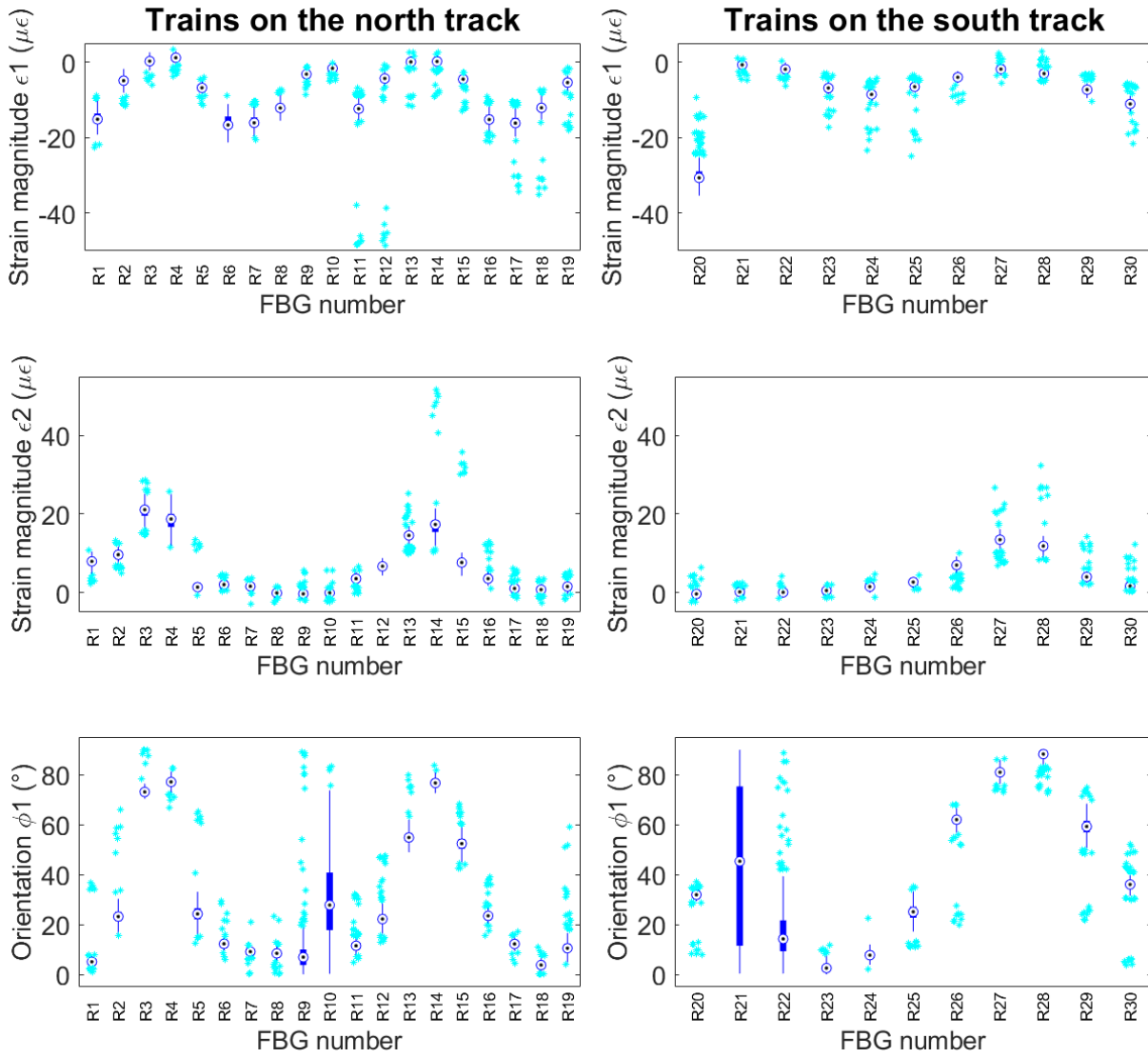


Figure A.15: Statistical variation of the principal strain measurements for each FBG rosette location, across all Northern Rail trains, when critical axle loads are applied at the western third point

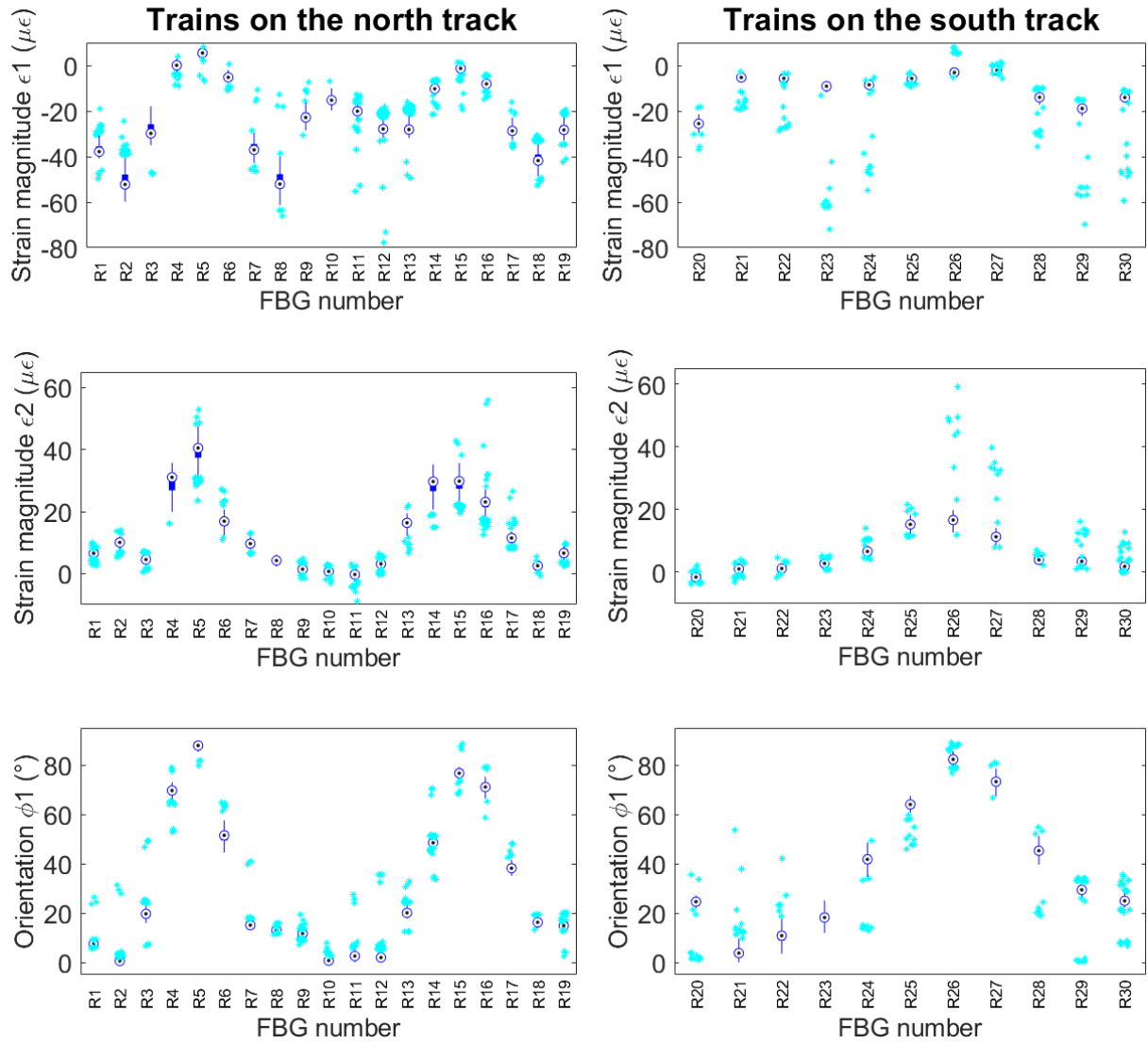


Figure A.16: Statistical variation of the principal strain measurements for each FBG rosette location, across all Northern Rail trains, when critical axle loads are applied just west of the arch crown

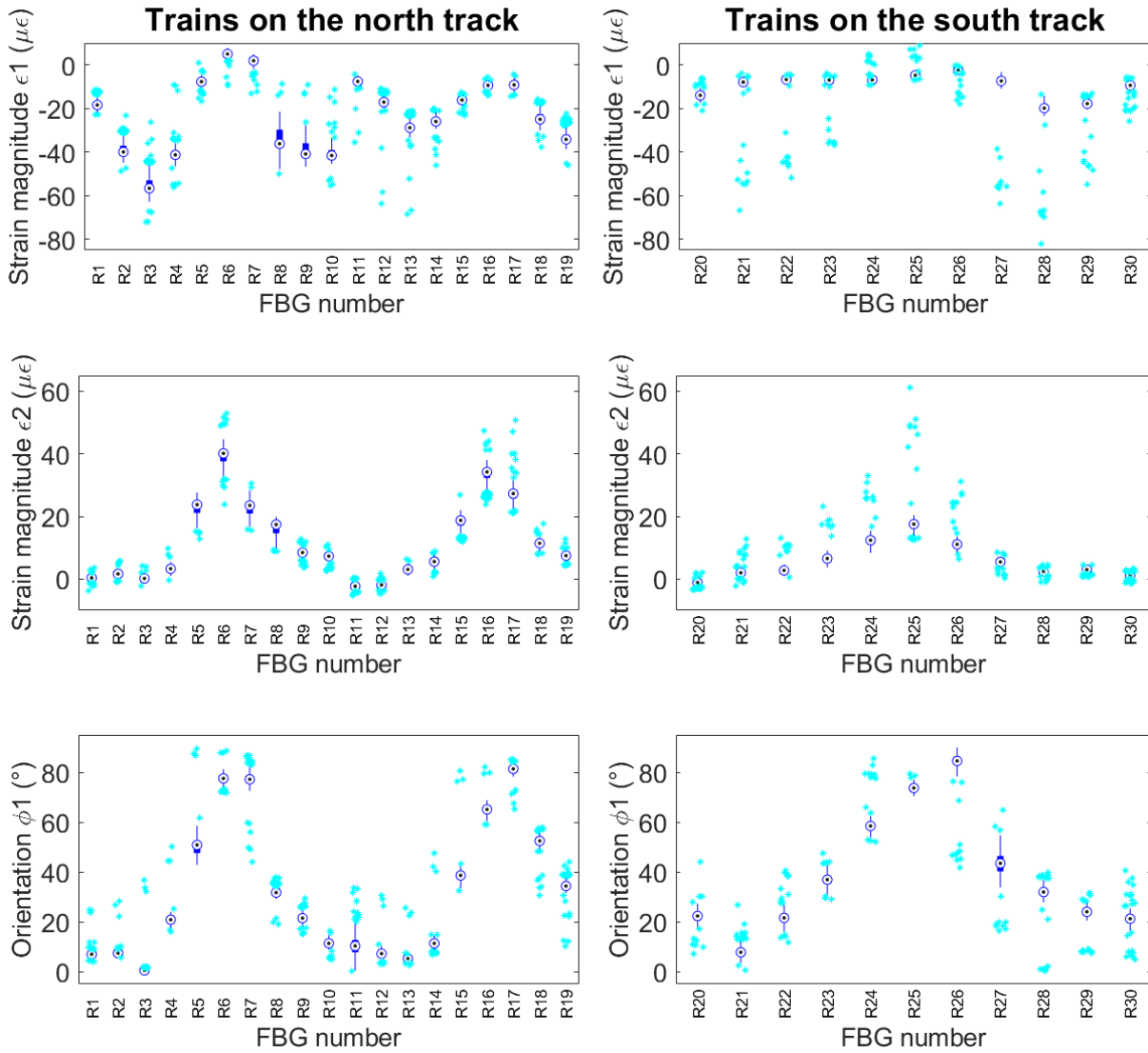


Figure A.17: Statistical variation of the principal strain measurements for each FBG rosette location, across all Northern Rail trains, when critical axle loads are applied just east of the arch crown

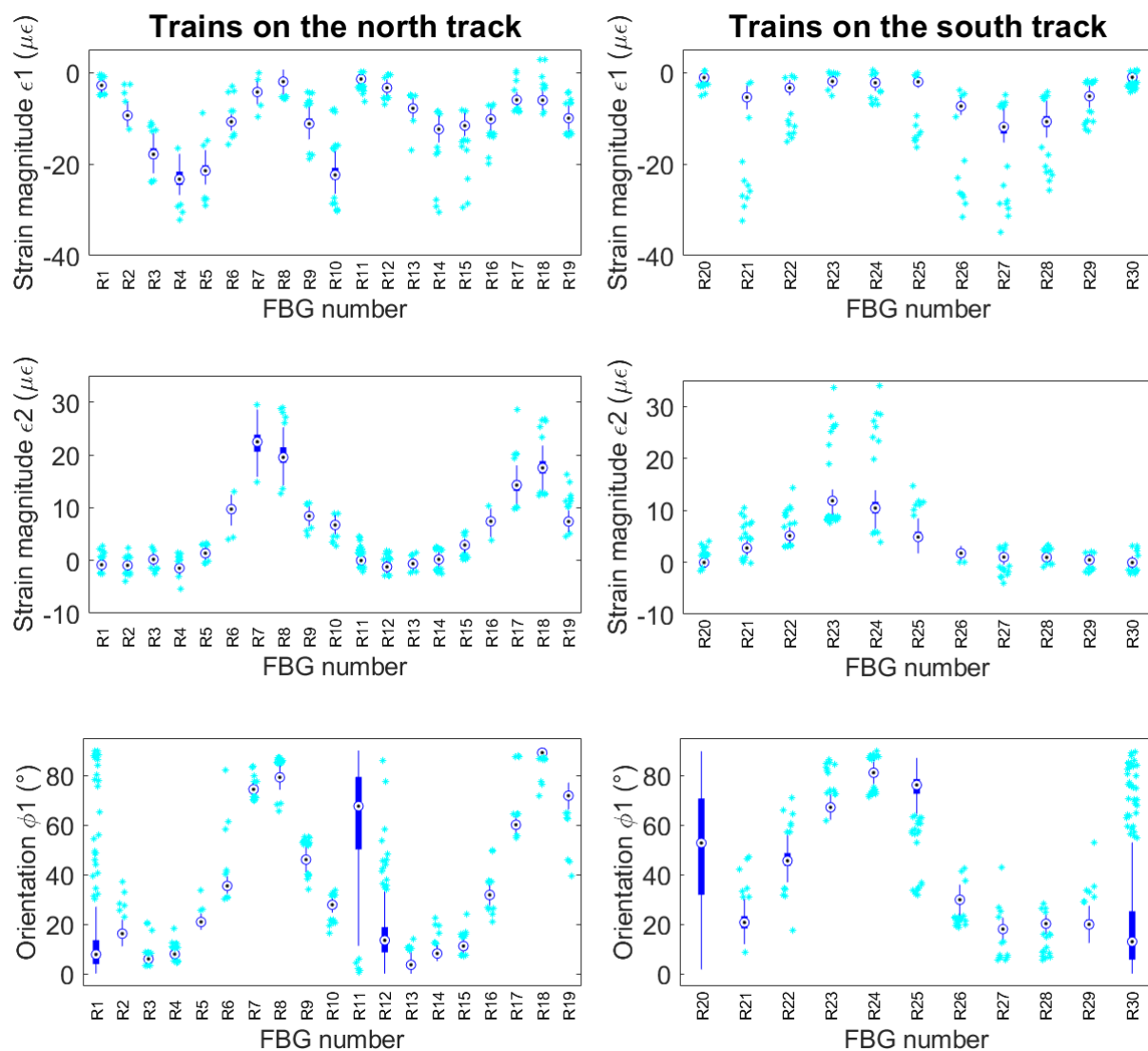


Figure A.18: Statistical variation of the principal strain measurements for each FBG rosette location, across all Northern Rail trains, when critical axle loads are applied at the eastern third point

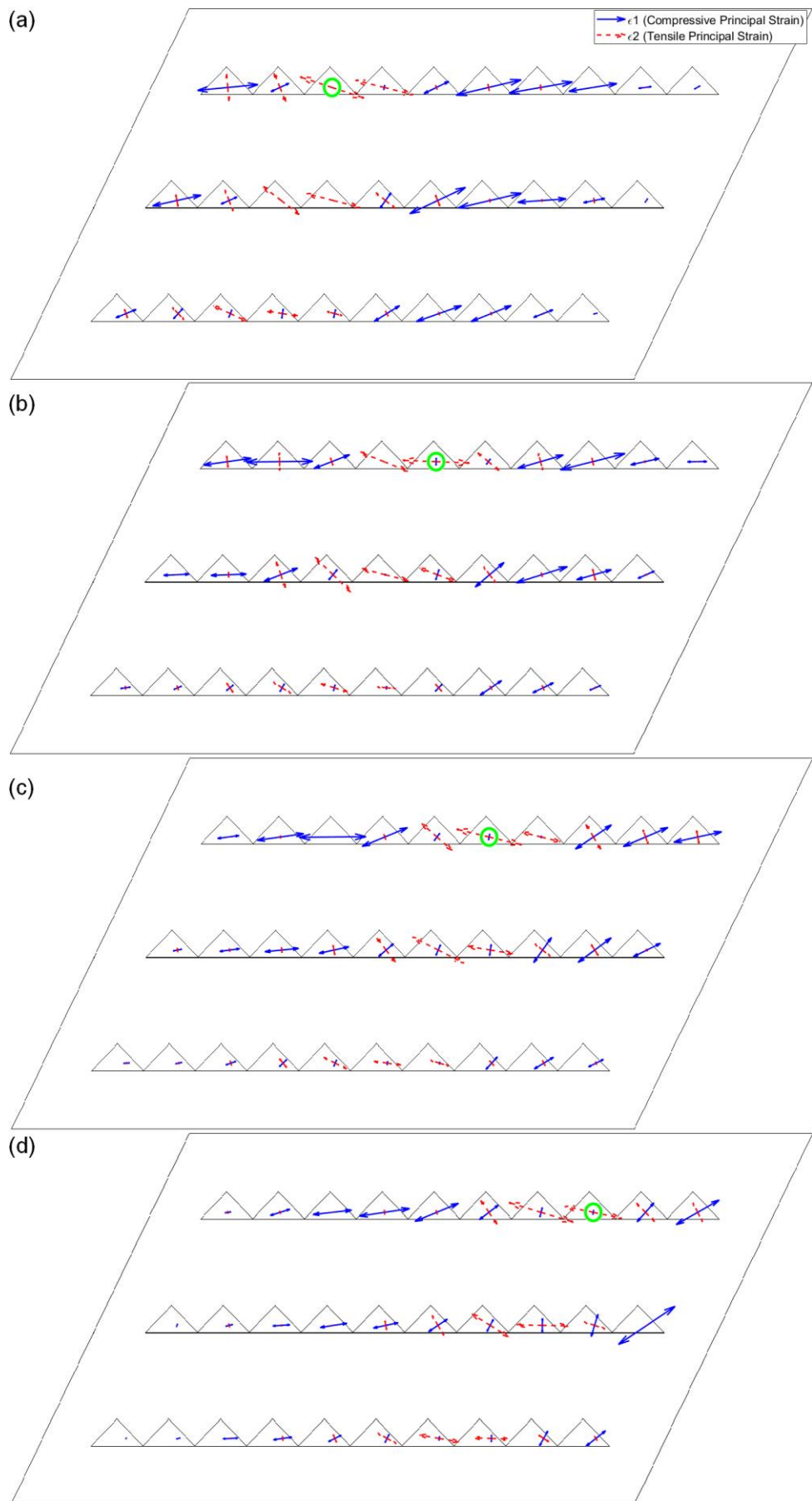


Figure A.19: Quiver plots showing the median principal strain response in the arch, across all Northern Rail trains, when critical axle loads are applied (a) at the western third point, (b) just west of the crown, (c) just east of the crown, and (d) at the eastern third point

# Appendix B

## Long-term FBG data: CrossCountry trains

This Appendix plots the data for all trains running on the CrossCountry route, recorded to date. These are assumed to be Class 222 trains, with the majority running in sets of either 4 or 9 carriages. However, some are likely to be Class 220 or 221 trains; these are highly similar, although they are sometimes deployed in sets of 5 carriages. Occasionally, sets of more than 9 carriages are used.

Plots are presented in the same sequence that was used in Chapter 8, for the First TransPennine trains. In the plots of the peak response (Figures B.3 to B.14), data points are coloured according to the time period in which they were measured, using the same convention described in section 8.3. In the quiver plots of the principal strain response (Figure B.19), tensile strains are plotted in red and compressive strains are plotted in blue.

### **B1 The instantaneous dynamic strain response in the arch**

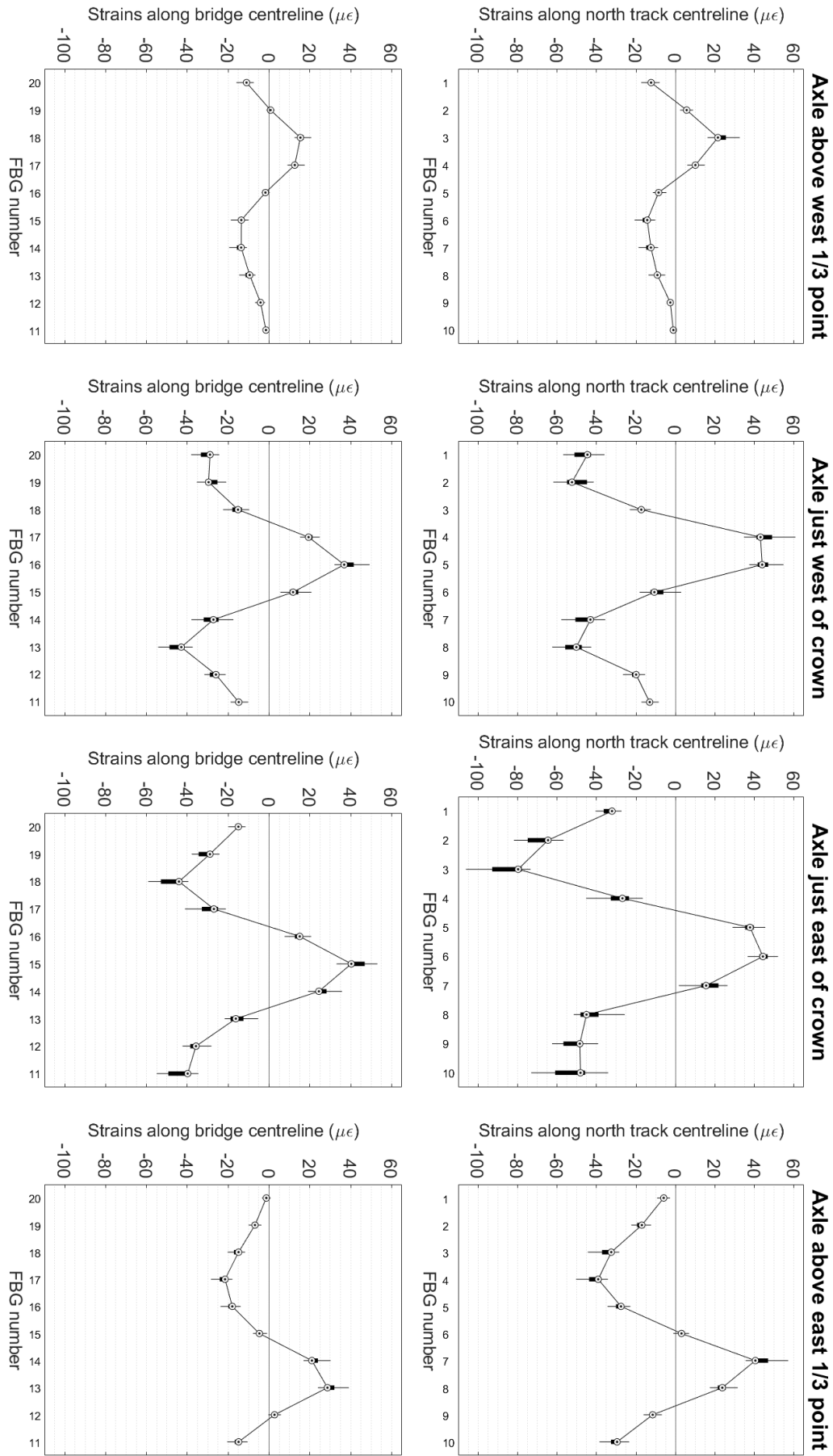


Figure B.1: Statistical variation of the instantaneous longitudinal strains over the northern half of the arch, when the critical axle loads are applied at key locations along the arch span, across all CrossCountry trains passing on the north track

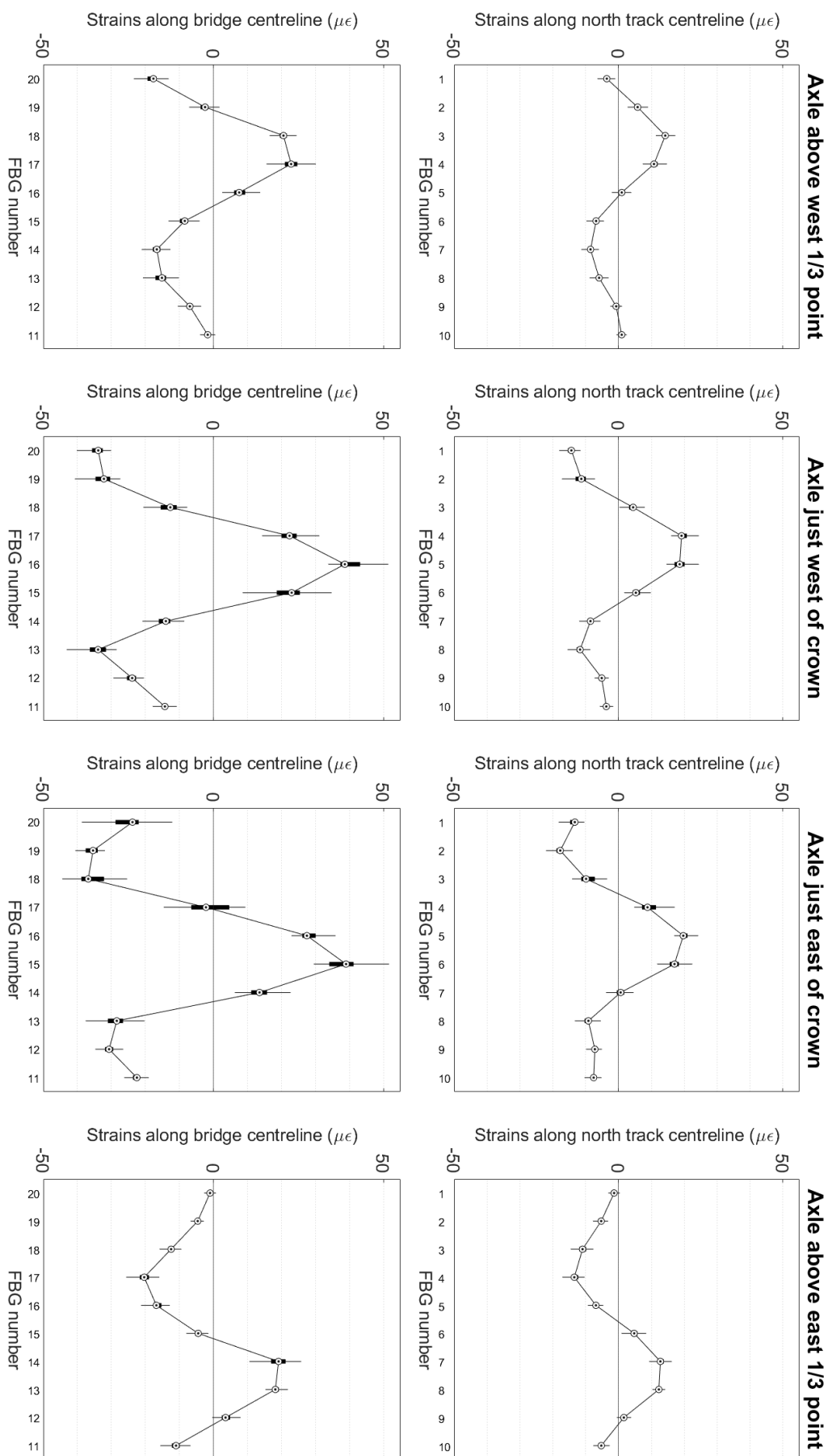


Figure B.2: Statistical variation of the instantaneous longitudinal strains over the northern half of the arch, when the critical axle loads are applied at key locations along the arch span, across all CrossCountry trains passing on the south track

## B2 The peak-to-peak dynamic strain response in the arch

### B2.1 Trains on the north track

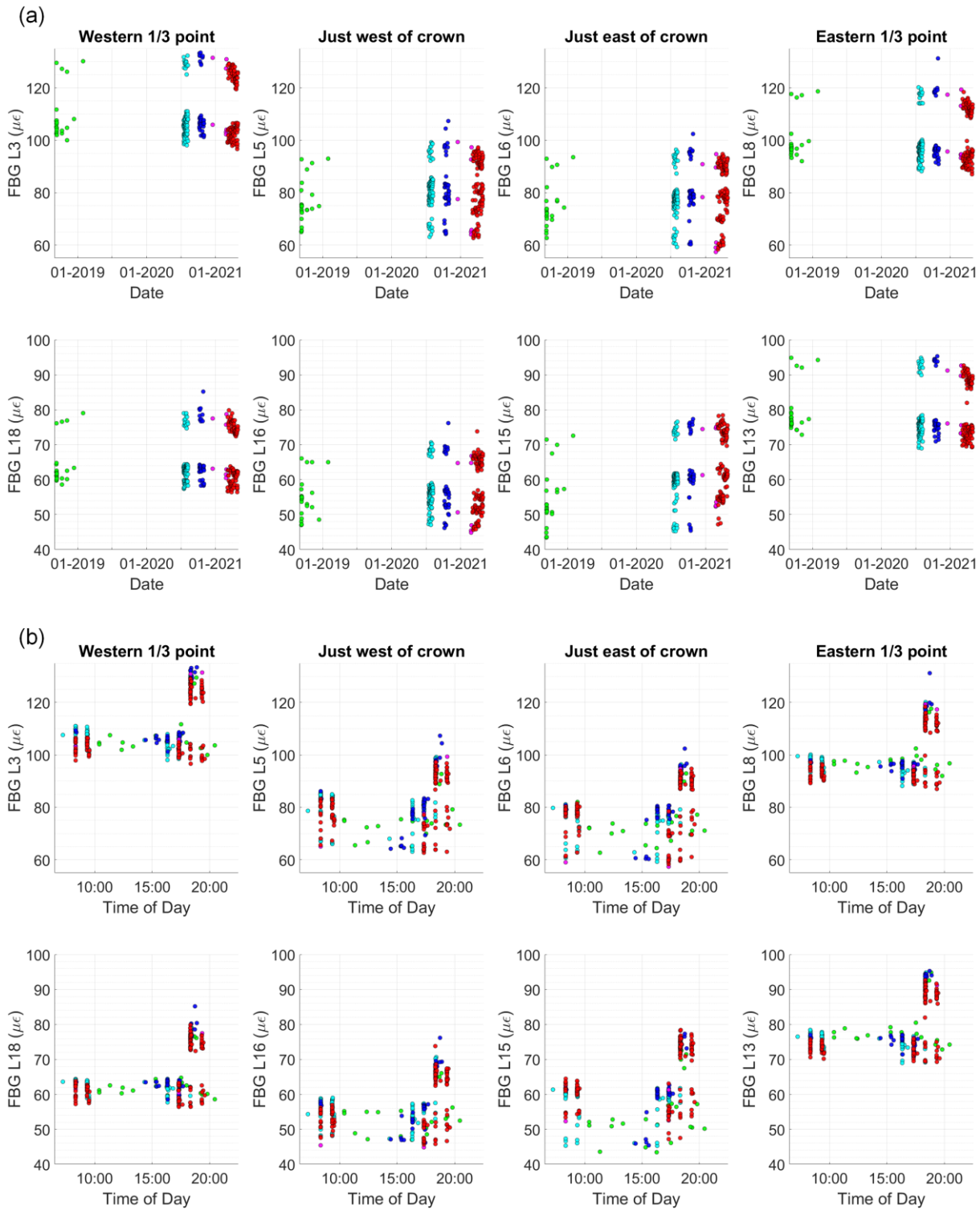


Figure B.3: Variation of peak-to-peak longitudinal strains over the northern half of the arch with (a) date and (b) time of day, for all recorded CrossCountry trains passing on the north track

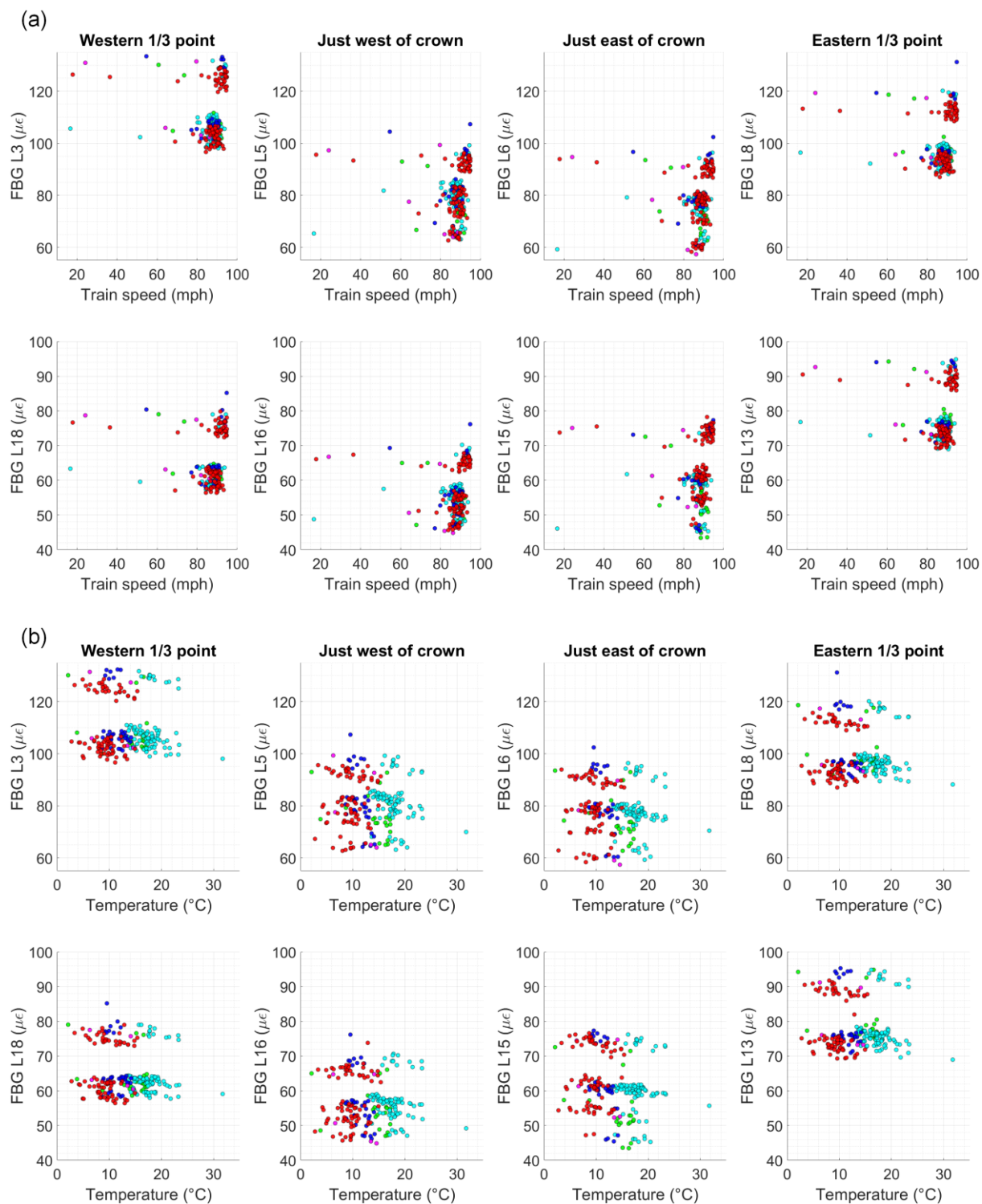


Figure B.4: Variation of peak-to-peak longitudinal strains over the northern half of the arch with (a) train speed and (b) temperature, for all recorded CrossCountry trains passing on the north track

## B2.2 Trains on the south track

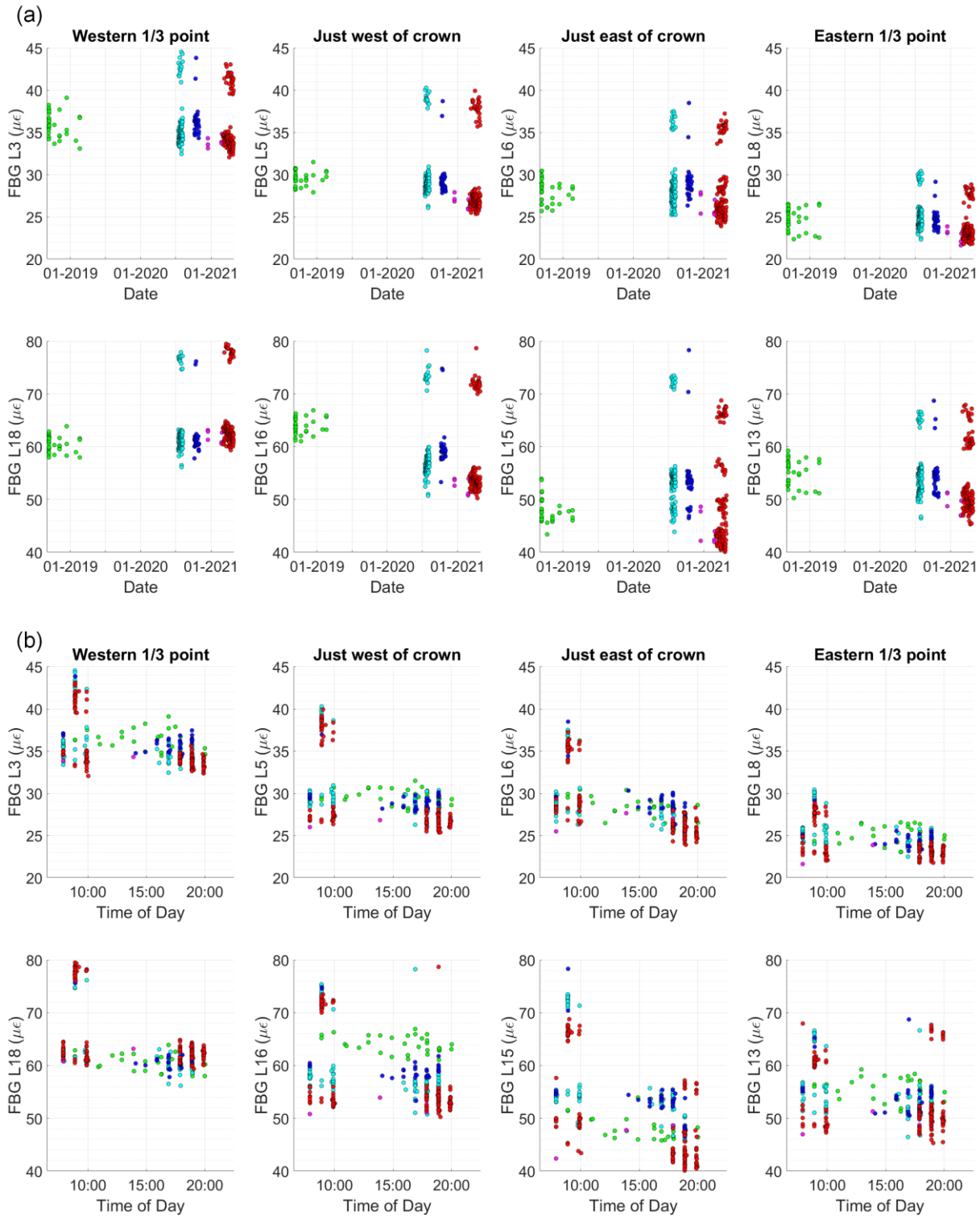


Figure B.5: Variation of peak-to-peak longitudinal strains over the northern half of the arch with (a) date and (b) time of day, for all recorded CrossCountry trains passing on the south track

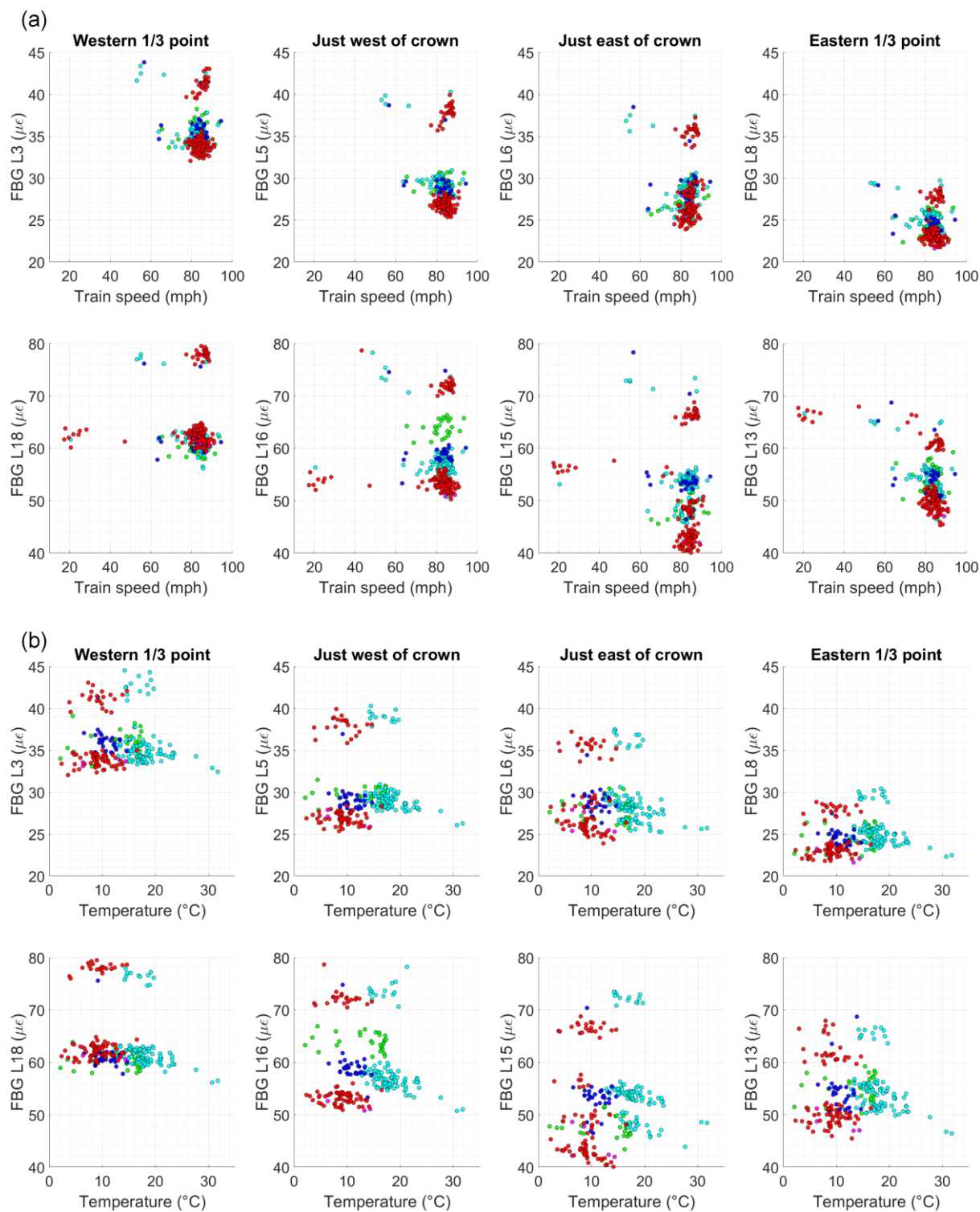


Figure B.6: Variation of peak-to-peak longitudinal strains over the northern half of the arch with (a) train speed and (b) temperature, for all recorded CrossCountry trains passing on the south track

## B3 The peak dynamic crack movements

### B3.1 Trains on the south track

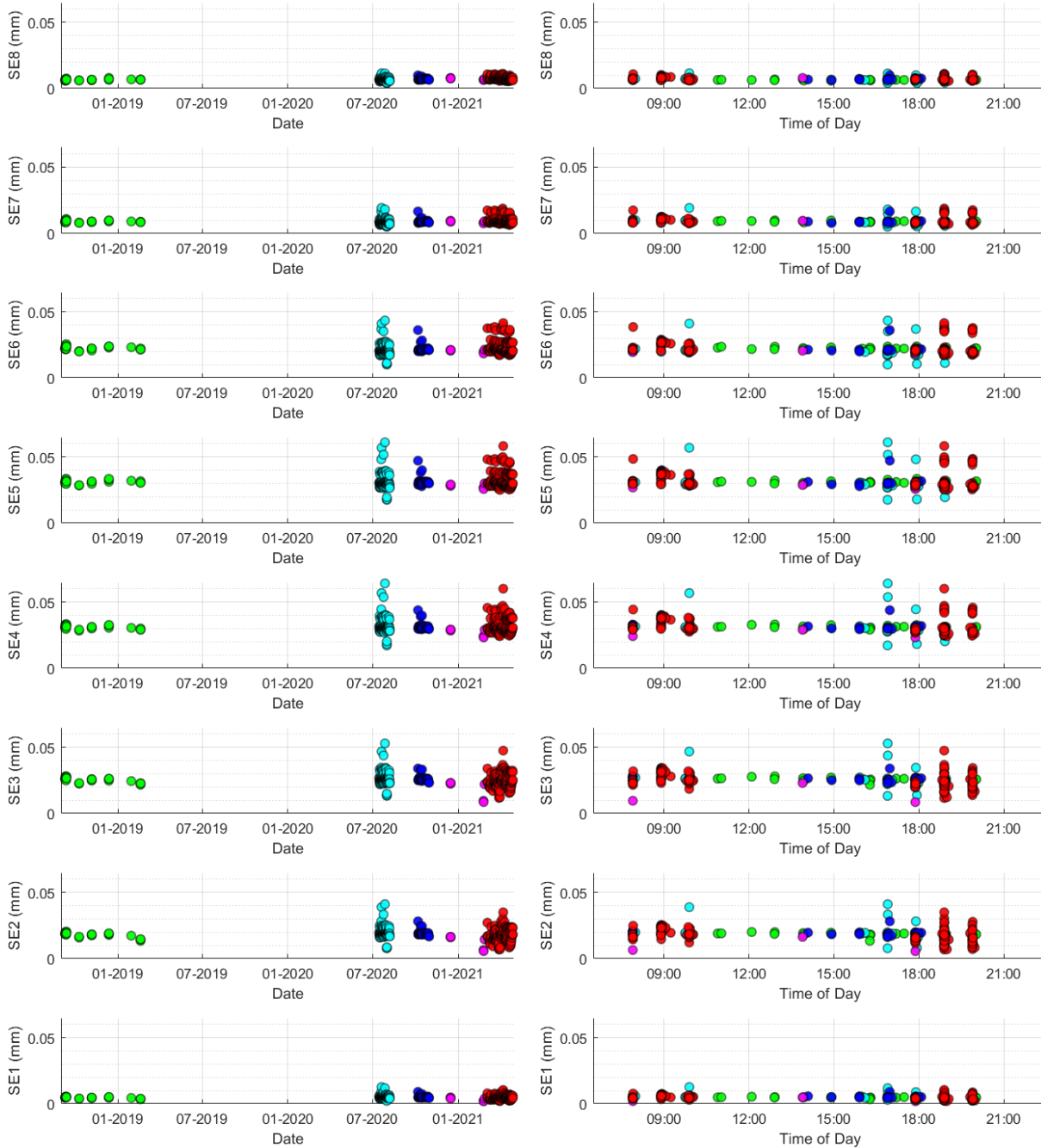
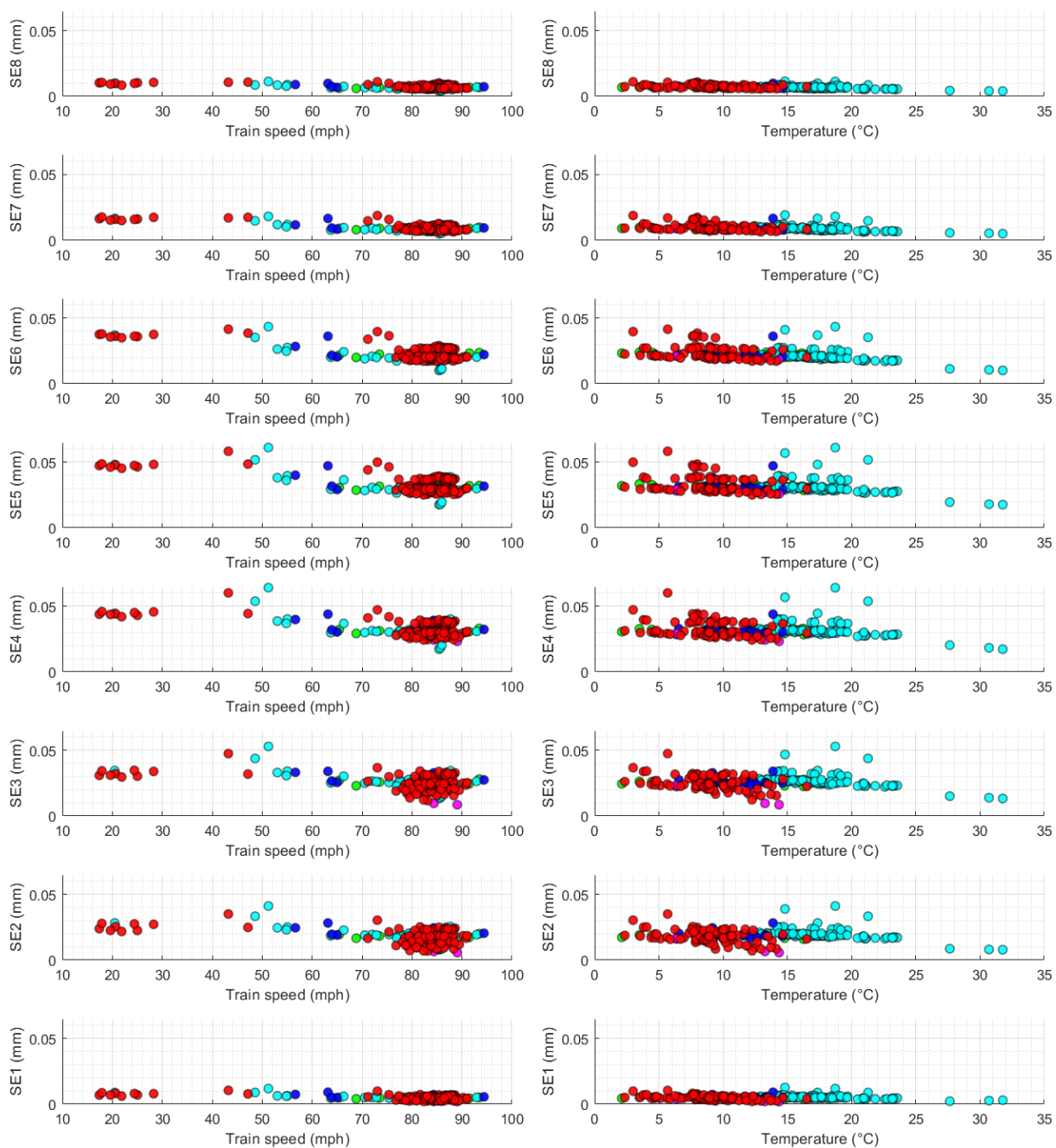
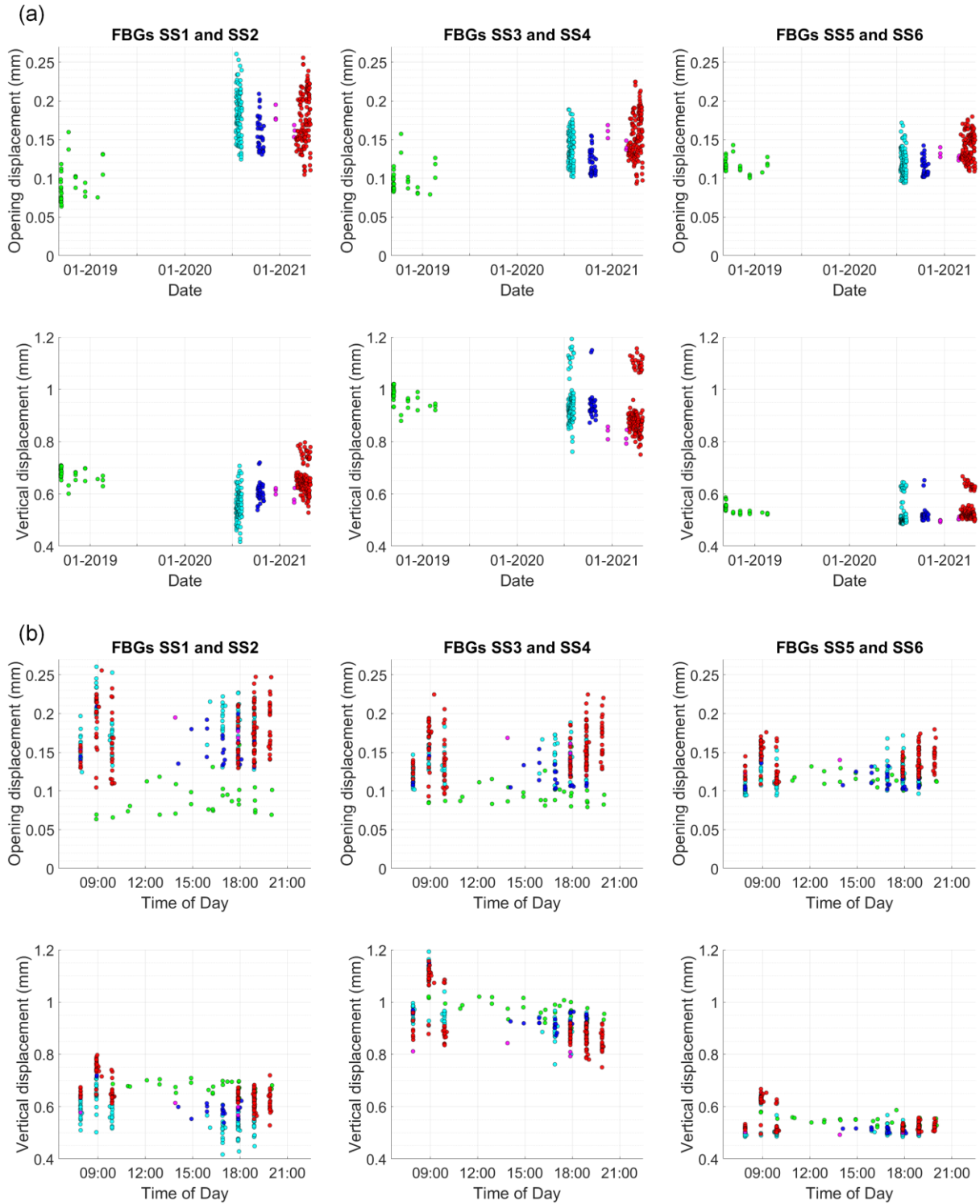


Figure B.7: Variation of peak dynamic movements at the south-eastern longitudinal crack with (left) date and (right) time of day, for all recorded CrossCountry trains passing on the south track



*Figure B.8: Variation of peak dynamic movements at the south-eastern longitudinal crack with (left) train speed and (right) temperature, for all recorded CrossCountry trains passing on the south track*



*Figure B.9: Variation of peak dynamic movements at the south spandrel separation crack with (a) date and (b) time of day, for all recorded CrossCountry trains passing on the south track*

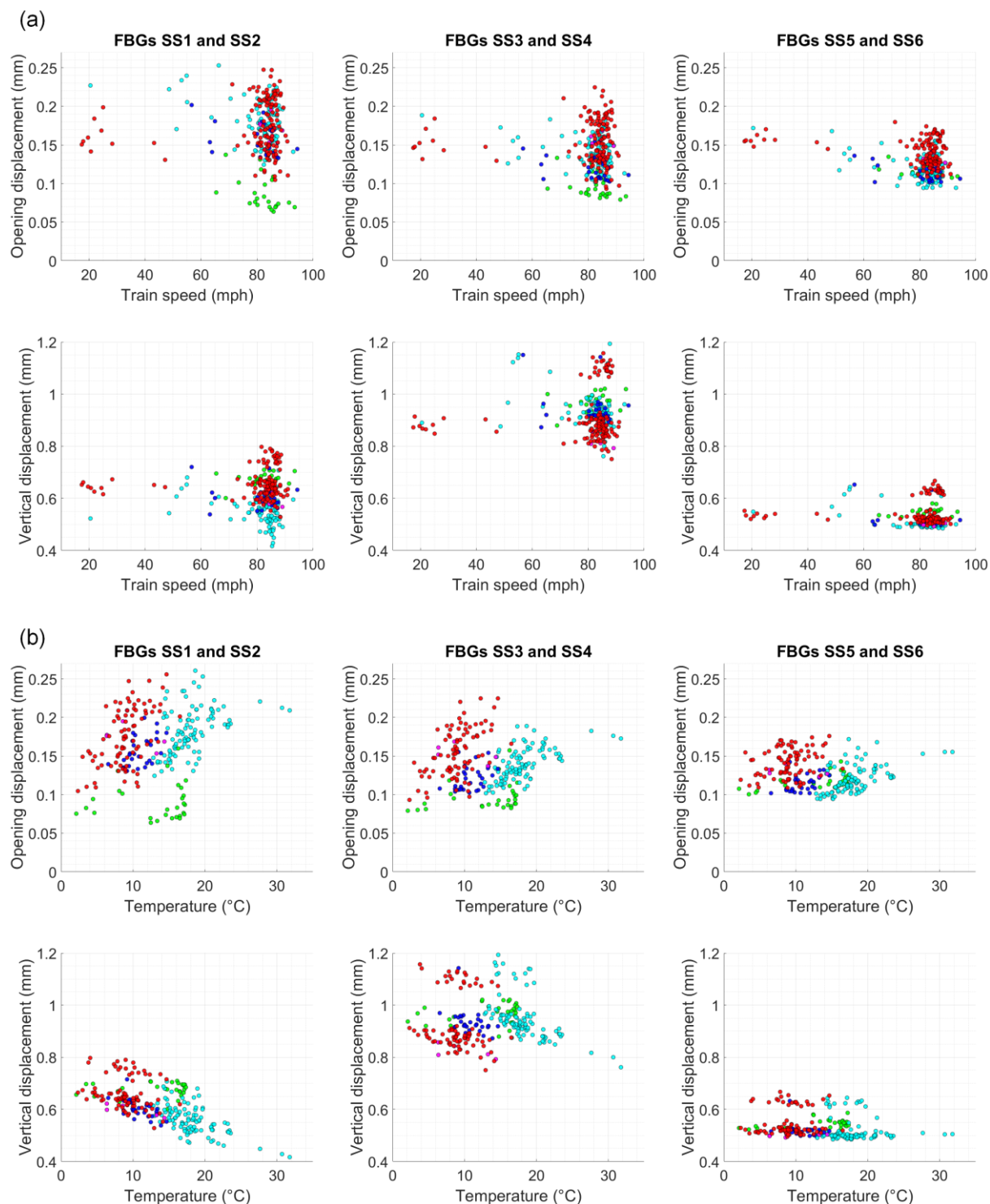
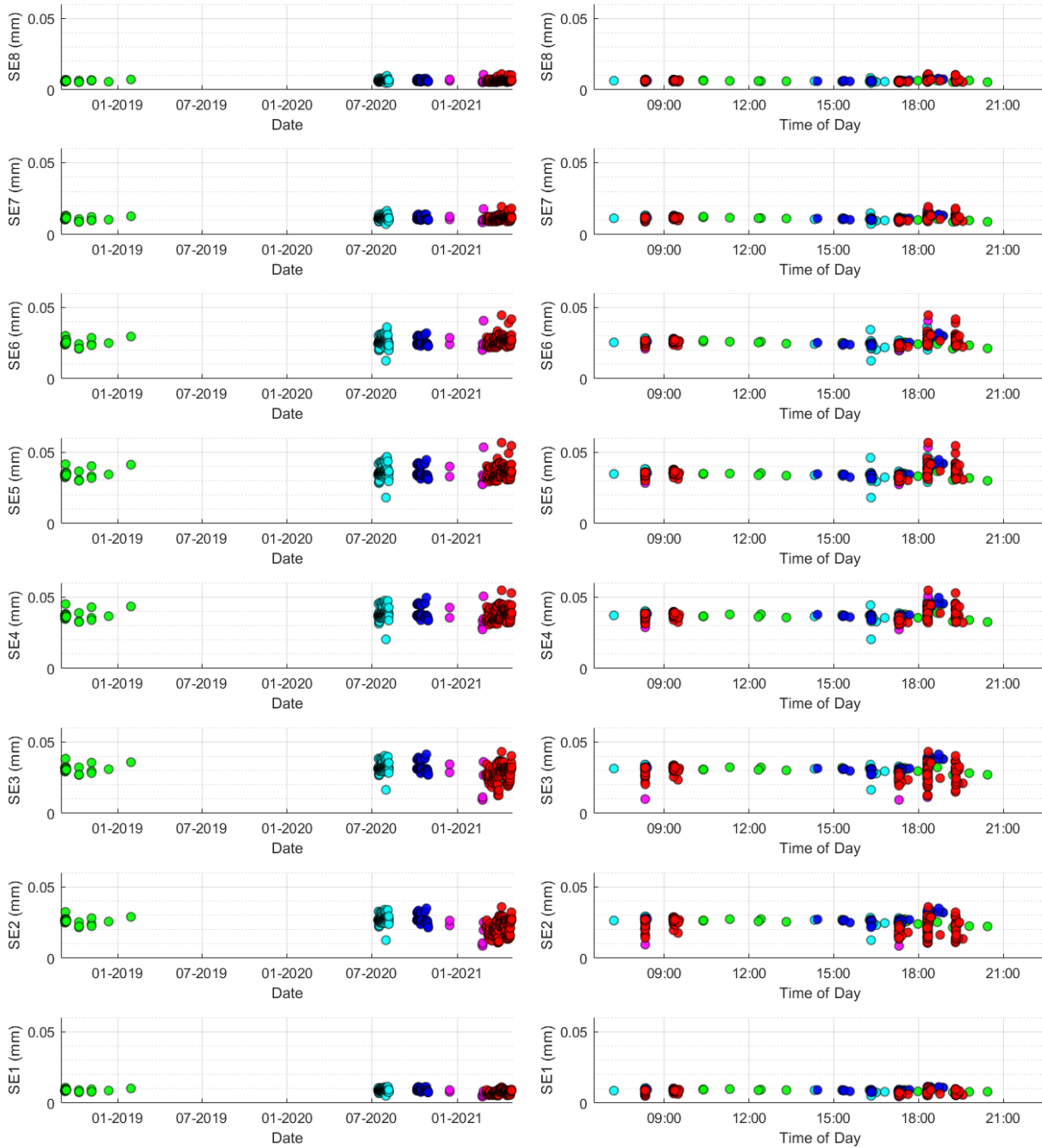
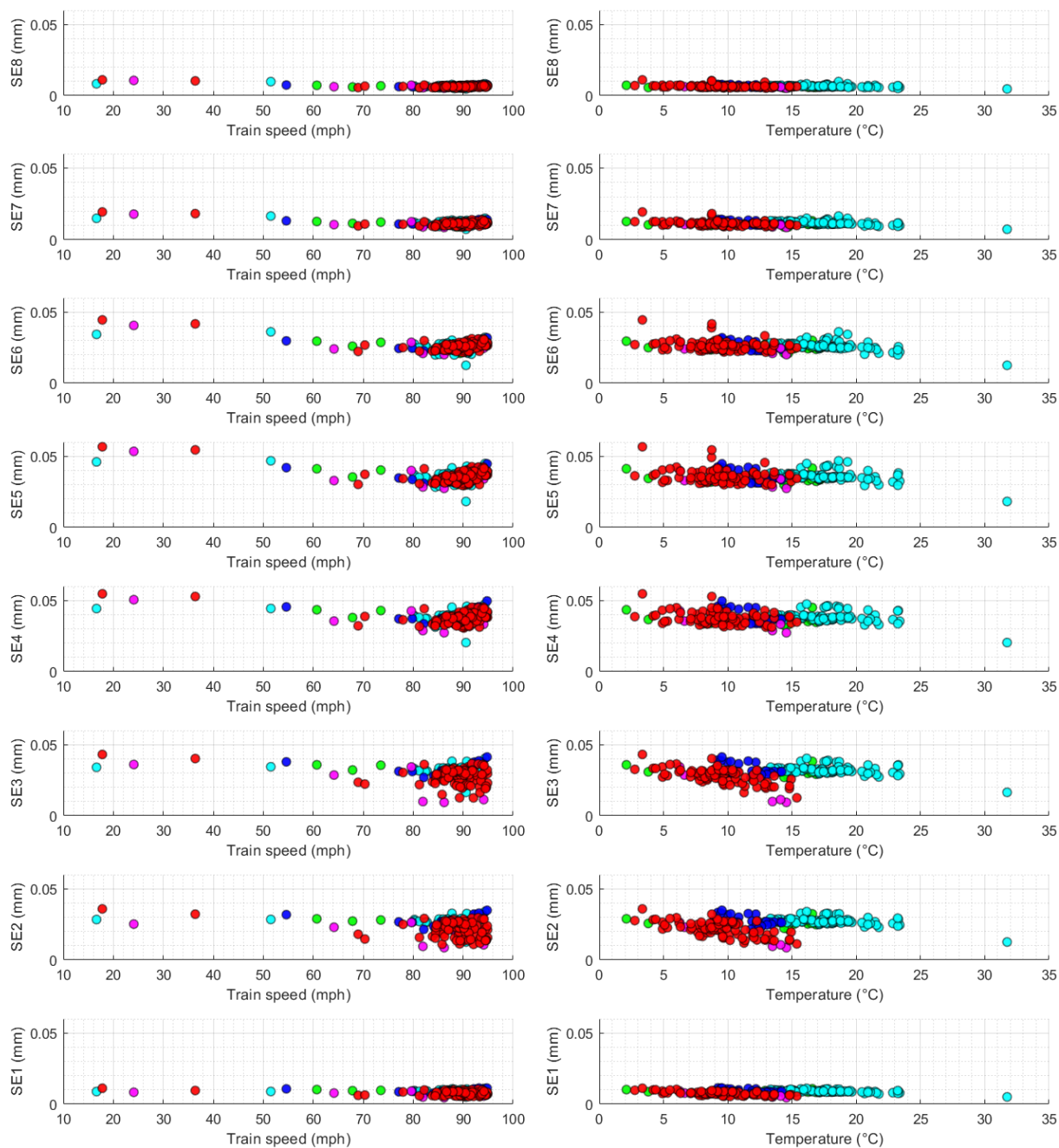


Figure B.10: Variation of peak dynamic movements at the south spandrel separation crack with (a) train speed and (b) temperature, for all recorded CrossCountry trains passing on the south track

## B3.2 Trains on the north track



*Figure B.11: Variation of peak dynamic movements at the south-eastern longitudinal crack with (left) date and (right) time of day, for all recorded CrossCountry trains passing on the north track*



*Figure B.12: Variation of peak dynamic movements at the south-eastern longitudinal crack with (left) train speed and (right) temperature, for all recorded CrossCountry trains passing on the north track*

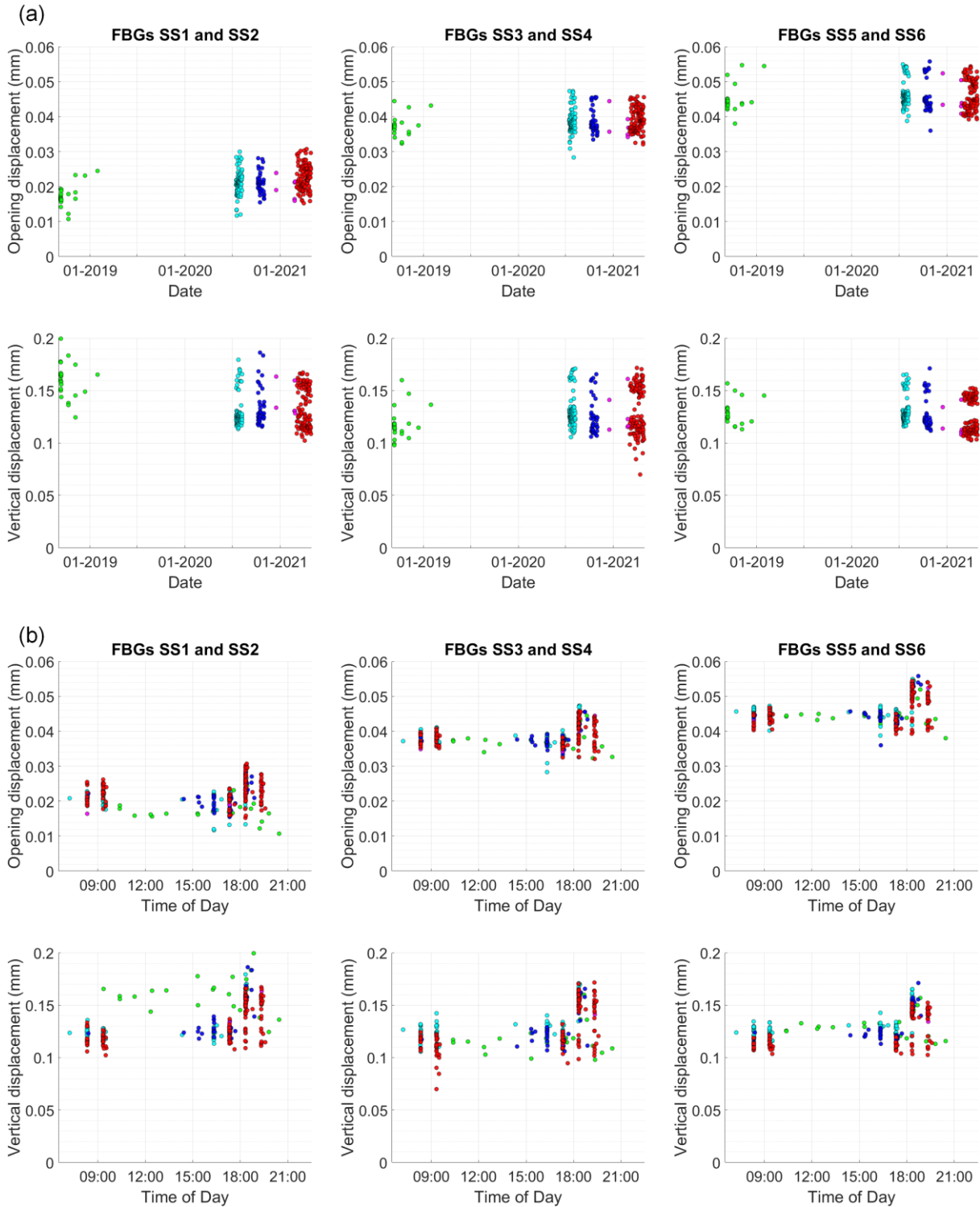


*Figure B.13: Variation of peak dynamic movements at the south spandrel separation crack with (a) date and (b) time of day, for all recorded CrossCountry trains passing on the north track*

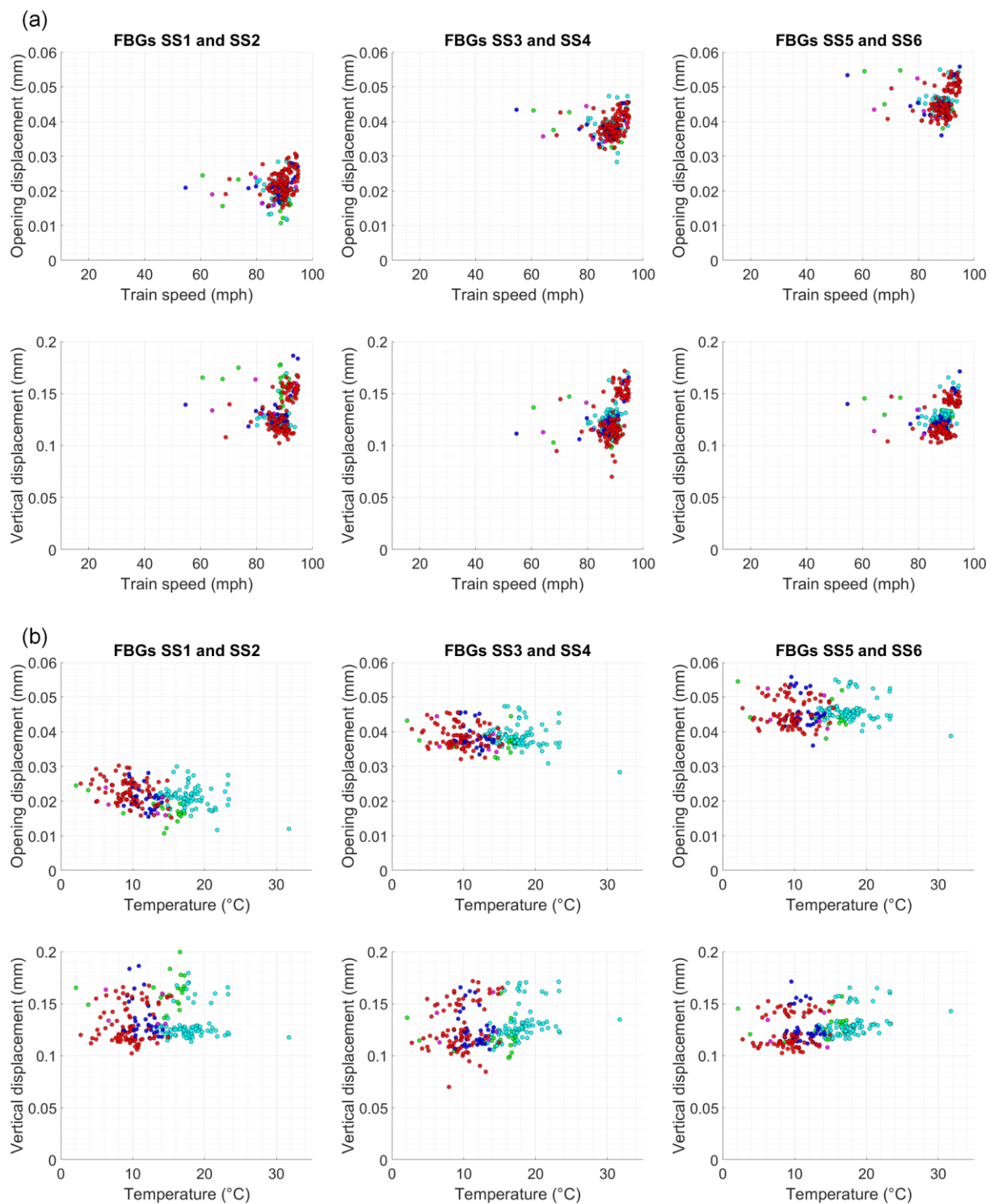


*Figure B.14: Variation of peak dynamic movements at the south spandrel separation crack with (a) train speed and (b) temperature, for all recorded CrossCountry trains passing on the north track*

## B4 The principal strain response in the arch

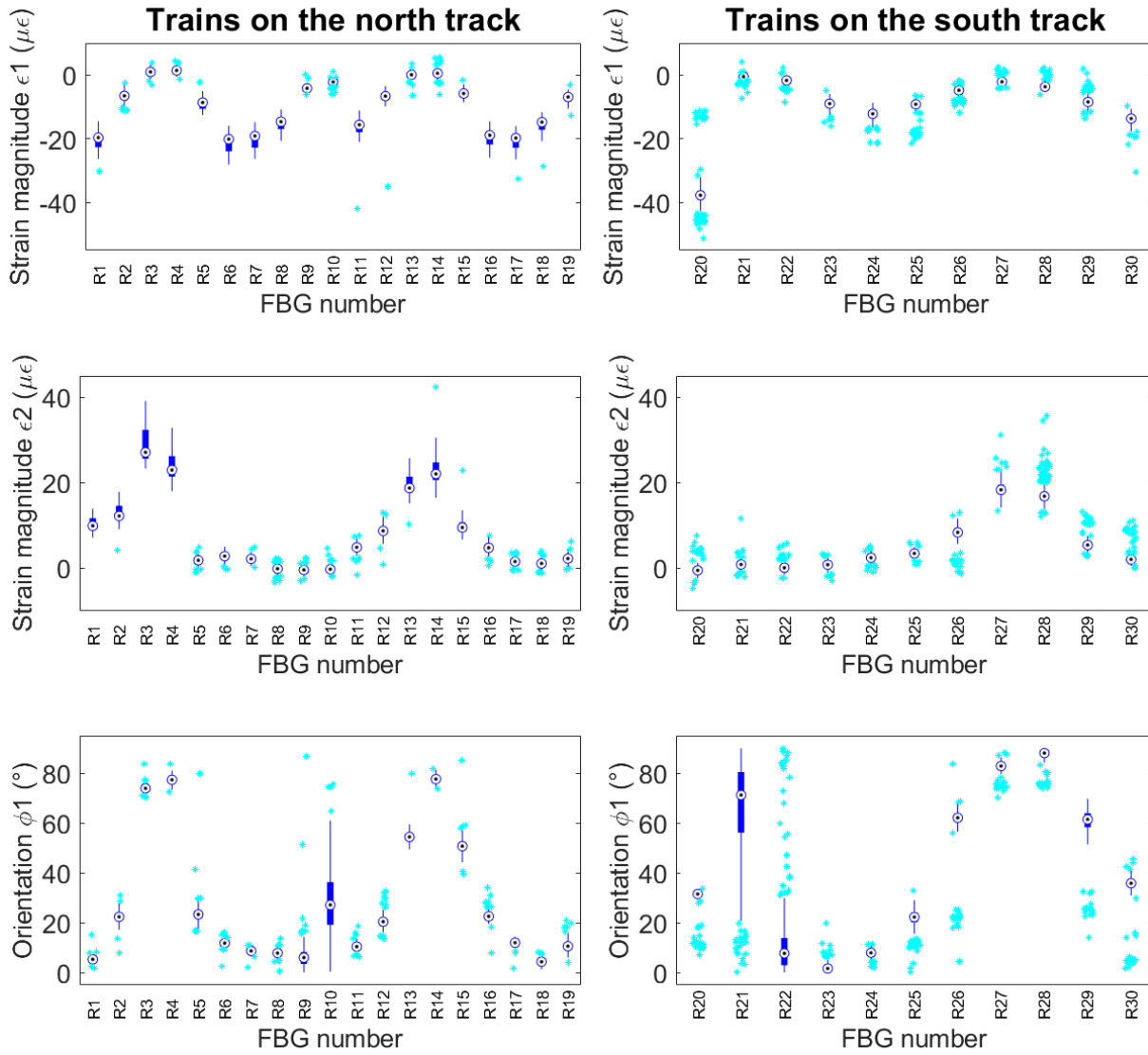


Figure B.15: Statistical variation of the principal strain measurements for each FBG rosette location, across all CrossCountry trains, when critical axle loads are applied at the western third point

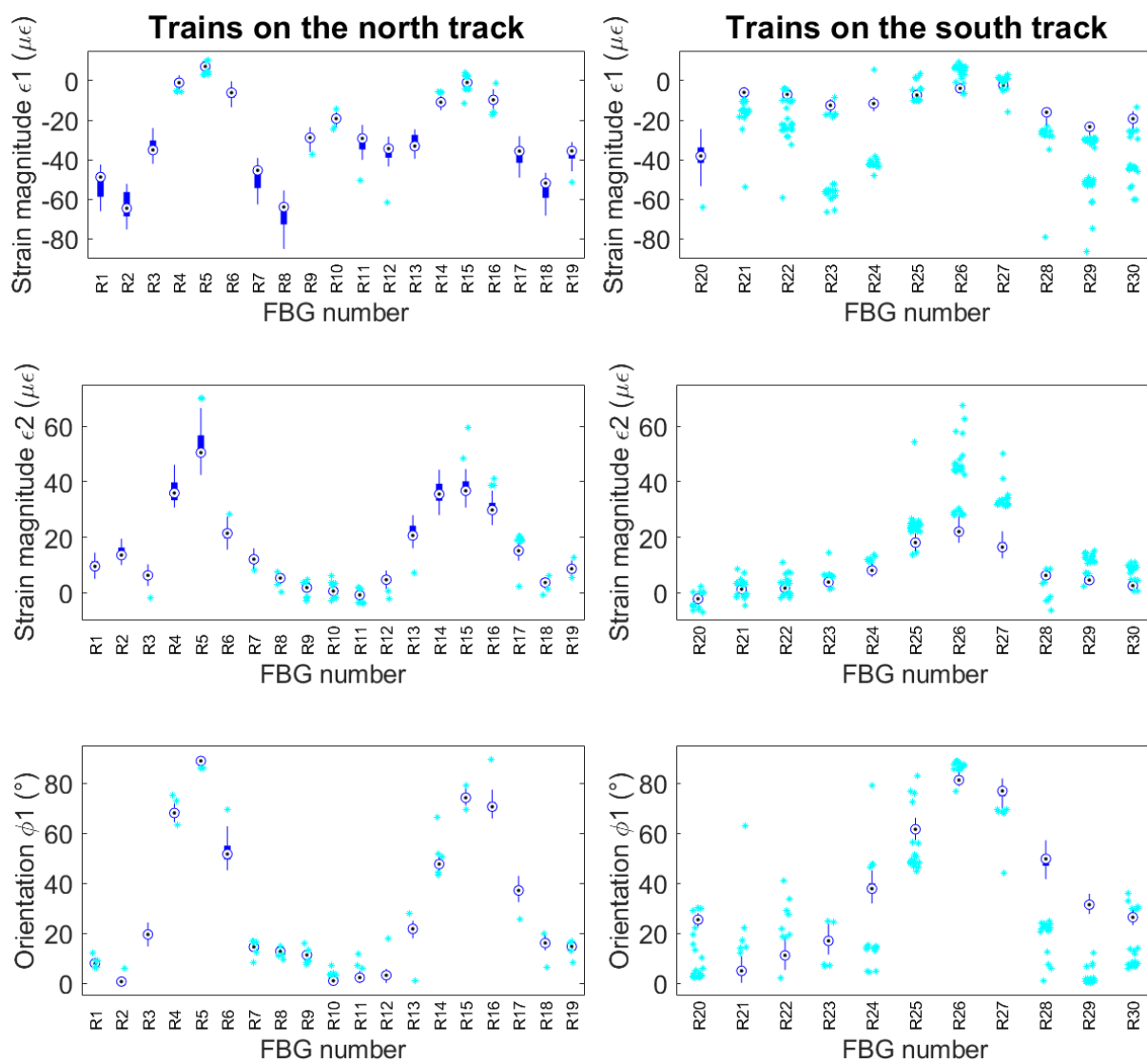


Figure B.16: Statistical variation of the principal strain measurements for each FBG rosette location, across all CrossCountry trains, when critical axle loads are applied just west of the arch crown

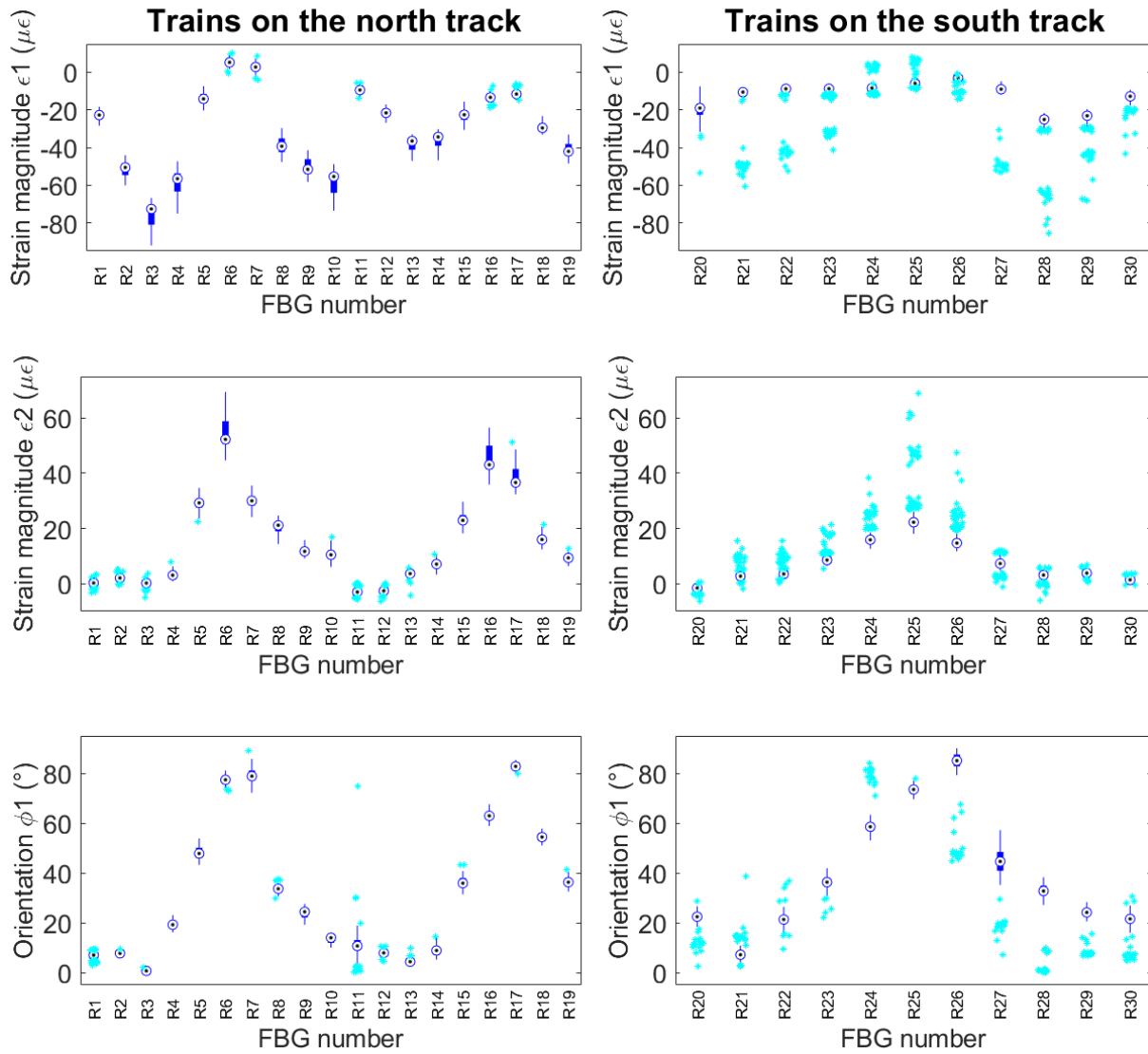


Figure B.17: Statistical variation of the principal strain measurements for each FBG rosette location, across all CrossCountry trains, when critical axle loads are applied just east of the arch crown

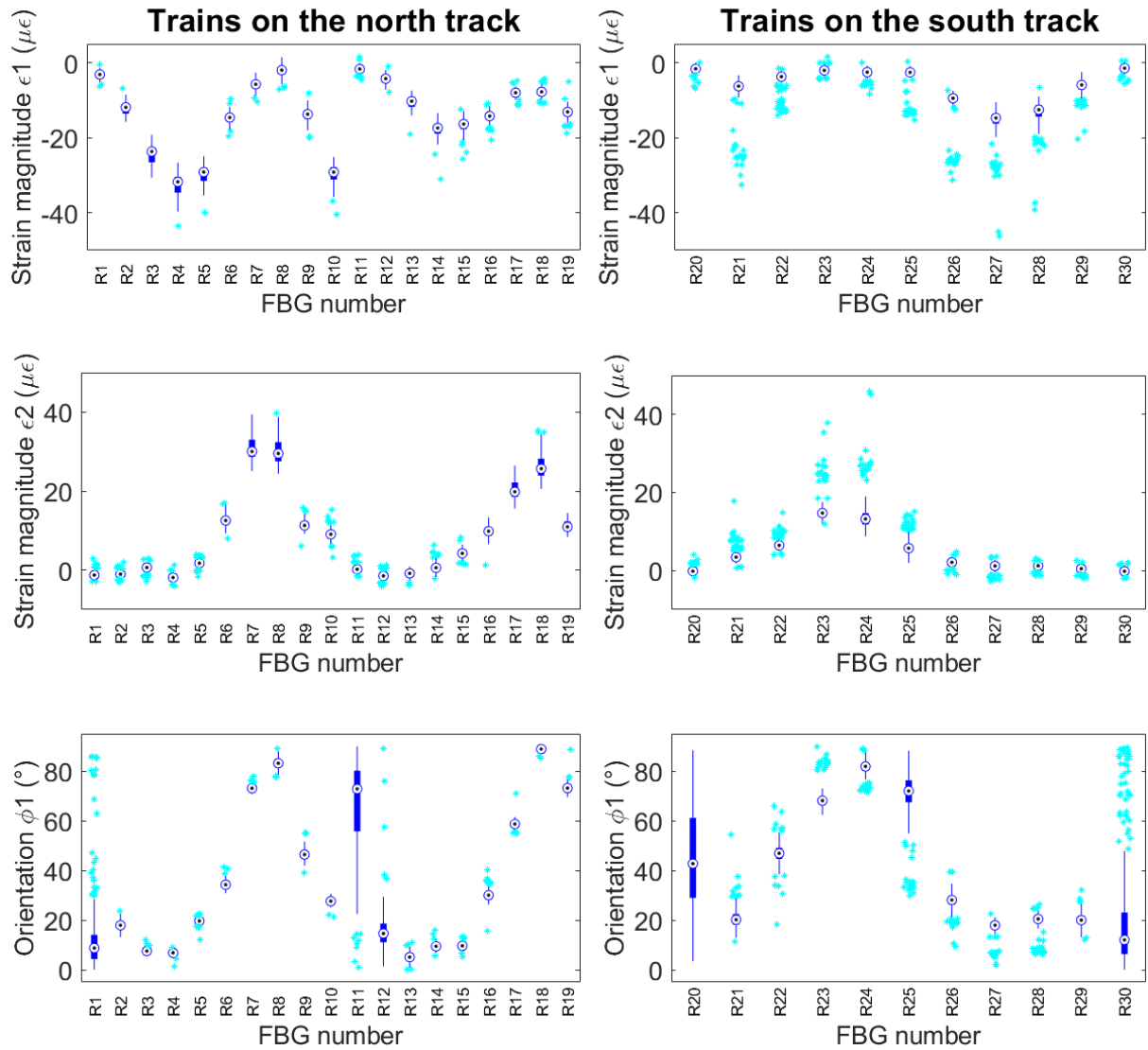


Figure B.18: Statistical variation of the principal strain measurements for each FBG rosette location, across all CrossCountry trains, when critical axle loads are applied at the eastern third point

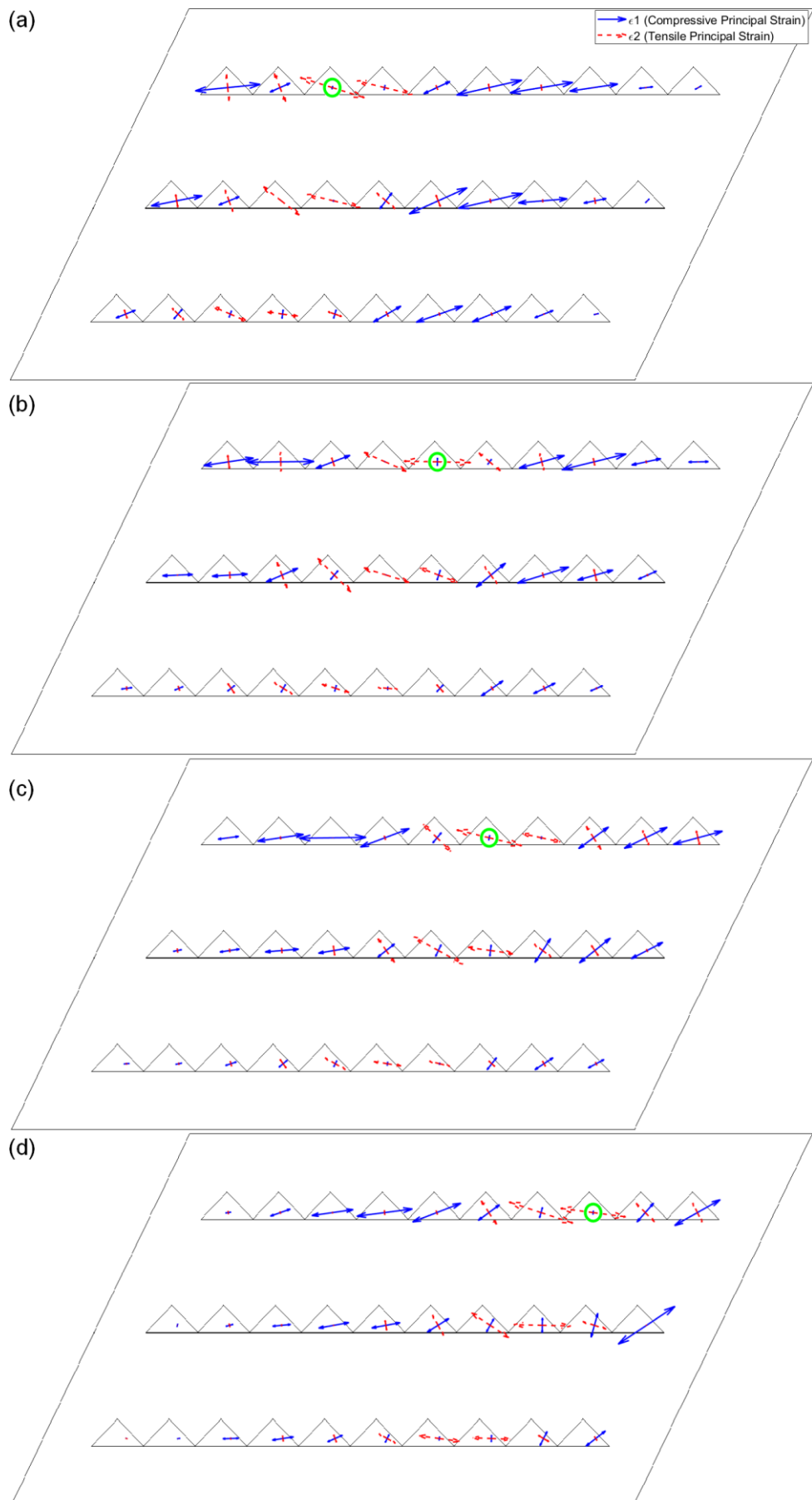


Figure B.19: Quiver plots showing the median principal strain response in the arch, across all CrossCountry trains, when critical axle loads are applied (a) at the western third point, (b) just west of the crown, (c) just east of the crown, and (d) at the eastern third point

